UNIVERSITY OF SOUTHAMPTON

FACULTY OF ENGINEERING, SCIENCE AND MATHEMATICS

SCHOOL OF CIVIL ENGINEERING AND THE ENVIRONMENT

TRACK BEHAVIOUR:

THE IMPORTANCE OF THE SLEEPER TO BALLAST INTERFACE

BY

LOUIS LE PEN

THESIS FOR THE DEGREE OF DOCTOR OF PHILOSOPHY

2008

ACKNOWLEDGMENTS

I would like to sincerely thank Professor William Powrie and Dr Daren Bowness for the opportunity given to me to carry out this research.

I'd also like to thank the Engineering and Physical Sciences Research Council for the funding which made this research possible.

Dr Daren Bowness worked very closely with me in the first year of my research and helped me begin to develop some of the skills required in the academic research community. Daren also provided me with some of the key references in this report, he is sadly missed.

Network Rail, Tarmac, Pandrol and Corus steel must also be acknowledged for their support in kind. In particular John Amoore of Network Rail has been instrumental in arranging for some of the field monitoring work to take place on the West Coast Main Line.

At the University of Southampton I have been able to benefit from the advice given by numerous members of academic and laboratory staff, in particular my thanks to Dr Jeffrey Priest, Harvey Skinner and Ken Yeates. I'd also like to thank all the general staff that I have come into contact with within the School of Civil Engineering who have made my stay here very enjoyable.

Professor William Powrie has been very diligent in reading through drafts of this report and other interim reports that I have provided him with. His comments and insights have been enormously beneficial.

Last but not least, I acknowledge the continual support of my parents, Sylvia and Patrick Le Pen, and my wife, Lisa Bernasek.

UNIVERSITY OF SOUTHAMPTON

FACULTY OF ENGINEERING, SCIENCE AND MATHEMATICS

SCHOOL OF CIVIL ENGINEERING AND THE ENVIRONMENT

PHD THESIS

TRACK STABILITY

ABSTRACT

The aim of this research is to develop a fuller understanding of the mechanical behaviour of the sleeper/ballast interface, related in particular, to the forces applied by high speed tilting trains on low radius curves. The research has used literature review, field measurements, and laboratory experiments on a single sleeper bay of track. Theoretical calculations are also presented.

Field measurements are carried out using geophones to record time/deflection for sleepers during passage of Pendolino trains on the West Coast Main Line. Calculations are presented to quantify normal and extreme magnitudes of vertical, horizontal and moment (VHM) loads on individual sleepers.

Results from laboratory experiments, on the pre-failure behaviour of the sleeper to ballast base contact area, show that lateral load/deflection behaviour is load path dependent and relations are determined for improved computer modelling of the sleeper/ballast interface. Further test results are used to establish the failure envelopes for combined VHM loading of the sleeper/ballast base contact area. Tests show that the sleeper/ballast base resistance at failure occurs at a load ratio (H/V) of about 0.45 (24°) at 2 mm of displacement tending to 0.57 (30°) at greater displacements. In addition, measurements from pressure plates within the testing apparatus are used to describe the development of confining stress within the ballast during 100 cycles of vertical load. The development of confining stress is assessed with reference to a finite element model of the laboratory apparatus and it is shown that the earth pressure ratio moves towards the active condition for peak load and the passive condition at minimum load per cycle.

The contribution to lateral resistance of the crib ballast and varying sizes of shoulder ballast is also established and it is found that the shoulder and crib resistance can best be characterised by taking the mean resistance over a range of deflection from 2 mm to 20 mm. Calculations are presented, supported by the experimental data, to quantify the resistance from different sizes of shoulder ballast and a chart is presented which can be used as the basis for shoulder specification in practice.

ABBREVIATIONS

BOEF	Beam On Elastic Foundation
BS	British Standard
CTRL	Channel Tunnel Rail Link (recently renamed to HS1; High Speed 1)
CWR	Continuously Welded Rail
DFT	Department For Transport
DSSS	Dynamic Sleeper Support Stiffness
DTS	Dynamic Track Stabilization
ERRI	European Rail Research Institute
FTSM	Flexible Track System Model
FWD	Falling Weight Deflectometer
LVDT	Linearly Variable Displacement Transducer
MGT	Mega Tonnes of Traffic
NR	Network Rail
RGS	Railway Group Standard
TGV	Train de Grand Vitesse
UIC	Union International des Chemins de fer
VHM	Vertical, Horizontal, Moment

SPECIALIST TERMS

Cant	For the purposes of this document, cant is expressed as the design difference in level, measured in millimetres, between rail head centres (generally taken to be 1500 mm apart) of a curved track (compare with 'cross level'). (Rail Safety and Standards Board GC/RT5021, 2003)
Cant deficiency	The difference between actual cant and the theoretical cant that would have to be applied to maintain the resultant of the weight of the vehicle and the effect of centrifugal force, at a nominated speed, such that it is perpendicular to the plane of the rails. For the purposes of this document, cant deficiency is always the cant deficiency at the rail head, not that experienced within the body of a vehicle. (Rail Safety and Standards Board GC/RT5021, 2003)
Maximum design service cant deficiency	The maximum cant deficiency at which a train is designed to travel. For conventional trains a cant deficiency of 6° is specified, for tilting trains this is increased to 12°(Railway Safety GC/RC5521, 2001)
Curving force	Centrifugal force horizontal to the Earth's surface
Dynamic load	Vertically any load effect above the static load of a train resting on the tracks and horizontally any load above the wind load and when curving the centrifugal force load.
Dynamic Sleeper Support Stiffness (DSSS)	The peak load divided by the peak deflection of the underside of a rail seat area of an unclipped sleeper subjected to an approximately sinusoidal pulse load at each rail seat; the pulse load being representative in magnitude and duration of the passage of a heavy axle load at high speed.
Lateral	The direction across the track whether horizontal or canted
Sleeper/ballast interface	All contact areas between the sleeper and ballast including base, shoulder and crib
Track modulus (***k***)	Spring support constant, always evaluated for a single wheel load on half the track.
Trackbed	Soil layers below the sleeper base

Track superstructure	Rails, railpads, sleepers.
Track substructure	Similar to the trackbed, soil layers supporting the superstructure.
Track system	Refers to the rails, pads, sleepers and trackbed
Low radius curves	Referring to curves where the curving force approaches and reaches the peak permitted. A lower limit for the radius of curves in this category can be taken from Railway Group Standards. These state that the maximum design limiting cant deficiency of 300 mm for a Pendolino is reduced on curves less than 700 m in radius (Rail Safety and Standards Board GC/RT5021, 2003). The upper limit depends on the operating cant deficiency of the train and the cant of the track. For a train travelling at 110 mph on 150 mm canted track the maximum radius of curve at which the vehicle can maintain an operating cant deficiency of 300 mm is 760 m. In reality few curves are of such low radius and curves evaluated on the WCML for this research had radii of 1025 m and 1230 m with 150 mm cant present. The phrase low radius curve will therefore be interpreted to incorporate curves in the range 700 m to 1230 m in this report.

DEFINITION OF SYMBOLS USED

$\boldsymbol{a}$	1. Sleeper spacing 2. Speed of sound in fluid
a	Angle of cant of the track
$\boldsymbol{b}$	1. Exponent 2. Sleeper width at base
$\boldsymbol{B}$	Sleeper length
$\boldsymbol{C_F}$	Dimensionless constant for wind loading
$\boldsymbol{C_L}$	Dimensionless constant for lifting wind load
$\boldsymbol{C_S}$	Dimensionless constant for sideways wind load
$\boldsymbol{C_R}$	Dimensionless constant for rollover wind load
d	Frictional resistance angle at interfaces (e.g. ballast to sleeper)
r	Density
$\boldsymbol{D}$	Shear force
$\boldsymbol{d}$	Distance between railheads centre to centre
$\boldsymbol{D_{degrees}}$	Operating cant deficiency in degrees
e_N	Strain in the ballast layer after N cycles of load
e_1	Strain in the ballast layer after cycle 1
$\boldsymbol{e}$	Eccentricity
$\boldsymbol{E}$	Young's modulus
$\boldsymbol{EI}$	Bending stiffness of the rail
$\boldsymbol{E_r}$	Stress state dependent vertical modulus (used by Geotrack)
f	Internal friction angle
$\boldsymbol{F}$	Force/Force on body moving through fluid medium
g	Bulk unit weight
$\boldsymbol{h}$	1. Reference height 2. Height of sleeper
$\boldsymbol{H}$	Horizontal (load)
$\boldsymbol{I}$	Second moment of area
$\boldsymbol{H_g}$	Height of centre of gravity above rail on level track
$\boldsymbol{k}$	Foundation coefficient (N/m/m) (also referred to as track modulus)
$\boldsymbol{K}$	Earth pressure ratio
$\boldsymbol{k_1}$ to $\boldsymbol{k_4}$	Experimental constants
$\boldsymbol{K_a}$	Active earth pressure coefficient`

K_0	Normally consolidated earth pressure coefficient`
K_p	Passive earth pressure coefficient`
l	Angle of heaped ballast
L	1. Sleeper width 2. Characteristic length for BOEF 3. Lateral
l	Characteristic length for wind loading
m	Viscosity
M	Moment
m	Lateral track modulus per metre of track
m_d	Lateral track modulus per sleeper spacing (=***am***)
N	Number of load cycles
N_g	Analogous to the bearing capacity factor found from Meyerhof formula
N_q	Bearing capacity factor
P	Lateral wheel load
Q	Vertical wheel load
q	The sum of initial and incremental bulk stress (i.e. maximum bulk stress)
q_w	the angle that provides the least resistance and is found by trial and improvement
$q(x)$	The variation in vertical load with longitudinal distance (***x***) which is replaced with ***Q***, the wheel load in the derivation process.
r	Density
s_f	Stress at failure
R_w	The reaction at the sleeper/ballast shoulder contact
R_b	The reaction on the base slip surface
s_g	Shape factor
s'_h	Effective horizontal stress
s'_v	Effective vertical stress
s	1. Sleeper spacing 2. Slope angle of the ballast as it falls away from the shoulder, the maximum value this can take is equivalent to the internal angle of friction for the ballast (estimated to be 45°)
t_h	Tangent to failure surface on graph of V against H when V=O
t_m	Tangent to failure surface on graph of V against M/B when V=0
t	The torsional resistance of the sleeper rail fastenings, which may be evaluated per metre run of track
u	Pore water pressure
$u(x)$	The lateral rail deflection at distance *x* from the applied load
m	Viscosity of fluid
V	1. Velocity 2. Relative velocity 3. Vertical (load)
V_{max}	Maximum bearing capacity
$w(x)$	Rail deflection with respect to longitudinal direction
$w(x)$	Rail vertical deflection at longitudinal distance ***x***
W	Weight
y	The height of the shoulder above the level of the sleeper top
x	1. The longitudinal distance from the load 2. Extent of ballast shoulder adjacent to sleeper top
y	Yaw angle

CONTENTS

List of Figures

List of Tables

LIST OF ACCOMPANYING MATERIAL

1. Introduction

"The Railways are a vital public service. They are an essential part of the transport system, supporting a growing economy. Last year they carried over a billion passengers for the first time since the early 1960s, they are carrying 45% more freight than in 1995." Rt Hon. Alistair Darling, MP, Secretary of State for Transport (2004).

The loads currently experienced by railway track systems are more complex and potentially damaging than in the past because of technologies such as tilting trains, longer trains, and higher intensities of use. It is also possible that future freight axle loads in the UK will increase from the current 25 tonnes to 30 tonnes on some sections of track; some sleepers, such as the G44 on the West Coast Main Line (WCML), have been designed with this in mind.

The aim of the proposed research is to develop a fuller understanding of the mechanical behaviour of the sleeper/ballast interface with particular emphasis to loading applied by Pendolino tilting trains curving at high speed on the West Coast Main Line (WCML). A secondary motivation is to look at the ultimate lateral force that may be available to resist track buckling, an issue that may become increasingly significant if climate change leads to increased seasonal and daily temperature ranges in the UK.

Chapter 1 includes brief sections on:

- Context: The state of the railway industry in the UK, high speed rail routes in general and high speed services on the WCML route.
- The problem being investigated: A description of track loading and how this is transferred to the sleeper/ballast interface.
- Knowledge gap: Justification for the research.
- The aim and objectives of the research.

Throughout this report the Pendolino train on the WCML is taken as the reference whenever train or track data are required.

1.1. *Context*

The majority of today's railway track throughout the world consists in principle of the same components as it did over 100 years ago. Rails are laid on sleepers which are themselves laid across some form of levelled, usually artificially placed, soil (ballast, sub ballast). The vehicles running on the track benefit from the minimal friction interface between steel wheel and steel rail to run very efficiently at relatively high speeds.

What has changed since the first railway track was laid is the quality of the materials used, as well as changes including refinements to the rail profile, the introduction of longer rail sections which are welded together (continuously welded rails, CWR), the specification of the formation and the quality of construction, as well as the greater axle loads and maximum speeds of the trains using the track.

Although high speed rail has been operating in various parts of the world for several decades, even now technical advances are continuing to increase maximum possible speeds. For example the high speed record for a train on conventional rails was recently advanced to 574.8km/h for a specially modified TGV, set in France on Tuesday 3rd April 2007 (BBC, 2007).

1.1.1. High Speed Lines

There are two types of conventional high speed lines operating in the world today.

- Dedicated
- Dual purpose

French TGVs operate on dedicated lines and are able to operate normally at 300kmph along relatively straight sections of track.

While some high speed train lines are specifically constructed dedicated lines, many, usually older routes, are dual purpose. Dual purpose lines carry combinations of high speed passenger trains, stopping services and slower freight trains. This has implications for the design of the track, particularly on curves.

This project focuses on the type of high speed rail offered by tilting trains on dual purpose lines.

For dual purpose lines the cant, which is the term for banking when applied to track and is defined in Figure 1-1, cannot be optimised for a single train speed. In practice this means that on curves a balance speed that is not optimal for all train types is chosen such that the resultant force, through the centre of gravity of the train is normal to the canted sleepers. The optimal cant angle for a chosen speed can be calculated from the force diagram shown in Figure 1-1.

For example for a speed of 100 km/hr on a curve of 1000 m radius, the optimum cant angle would be $\tan^{-1}(v^2/rg) = 4.5°$ corresponding to a height offset of $1500 \times \sin(4.5°) =$ 118 mm on standard gauge track assuming the rail centres are 1500 mm apart. In practice the cant is also limited to a maximum value. On Network Rail track, the cant is limited to 150 mm.

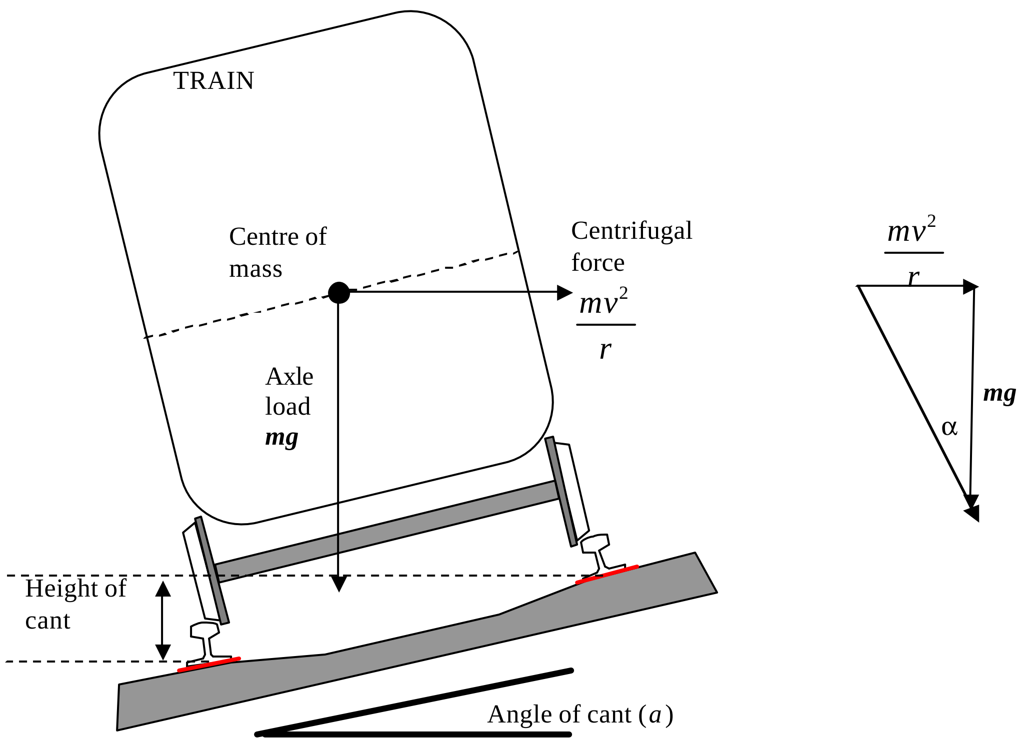

Figure 1-1: Calculation of optimal cant

When cant is not present, or is less than optimal for the speed of a conventional train; the vehicles and the passengers travelling on curves experience a sideways force. If this force becomes unacceptably large the train may be in danger of coming off the tracks due to the wheels climbing the outside rail or the vehicle overturning. This will not occur until long after the passengers’ tolerance limit is reached, and it is the latter that limits the acceptable maximum speed of a passenger train when curving.

Higher mean journey speeds may be obtained on dual purpose track by tilting trains because the tilt can compensate passengers for non-optimal cant. Provided the tilt/rotation is about a point close to the centre of gravity of the train, the global curving forces due to radial acceleration on the train are largely unaffected by the tilt. The speed of tilting trains on curves is then limited by safety considerations based on overturning of the vehicle.

The maximum operating speed for a train on a curve can be calculated by comparing the maximum likely overturning loads including wind and dynamic as well as centrifugal components with the rollover resistance of the train and incorporating a suitable safety margin.

Calculating maximum speed in this way is carried out using a parameter termed the operating cant deficiency. This is the angle away from normal to the (canted) track of the resultant train force, including components of curving and (static) axle loads. It does not include wind loading or other loading effects due to track misalignment and wheel/rail defects.

For conventional trains and tilting trains the maximum operating speed is limited to a cant deficiency of 6° and 12° respectively (Railway Safety GC/RC5521, 2001) under normal conditions, although restrictions can be applied under severe climatic conditions. Furthermore all trains are required to have a rollover resistance of 21°. This means that for conventional trains the safety margin against rollover is at least 15° and for tilting trains this reduces to at least 9°. These margins make allowance for potential wind load and loading effects due to misalignment of the track and wheel/rail defects. Because of the lower safety margin on tilting trains, track and vehicles need to be maintained to higher standards.

Note the inherent assumption that the track system is capable of safely supporting loading up to rollover. A more detailed description of tilting train behaviour can be found in Harris et al. (1998).

Because many rail networks are decades old and include low radius curves reflecting the maximum operating speeds of bygone eras, many countries, including Italy Germany, Finland, Switzerland, Czech Republic, Portugal, Spain, Slovenia and the United Kingdom have introduced tilting trains (Alsthom, 2008) as a way to reduce journey times on these “classic railway lines”.

1.1.2. Britain

In Britain today there is a great deal of pressure to improve journey times, capacity and quality of train ride. Following the Hatfield rail crash of October 17th 2000, train operating costs increased substantially and it is a matter of public record (DFT, 2004) that new reforms must reduce these costs so that the rail industry can operate within the public finances available to it.

Despite the increased costs, there has been a significant increase in train passenger numbers each year since 1995 (Green, 2005), with the likelihood that this will continue. Record levels of investment are being made in the industry, with several major projects recently completed or currently underway including the Channel Tunnel Rail Link parts one and two and the West Coast Main Line (WCML) modernisation, as well as high profile projects such as Thameslink and Crossrail planned for 2008/9.

In this context it was decided to refurbish the dual purpose WCML with the intention of introducing tilting passenger trains which would operate at speeds of up to 140 mph. However, the work ran into a number of difficulties and it has been well publicized that the cost, reported by the Office of Rail Regulation (2008) to be £7.4 billion by completion in December 2008, is much more than the £2.4 billion originally planned (Office of Rail Regulation & Railtrack, 2000). In addition, problems with the signaling have meant that, so far, the tilting trains have been limited to a maximum operating speed of 125 mph rather then the 140 mph of which they are capable. Notwithstanding this, the opening of the first phase of the work in September 2004 resulted in a record journey from London to Manchester in 1 hour 53 minutes, 15 minutes less than the previous record (BBC, 2004) with regular timetabled services currently covering the journey in around 2 hours 10 minutes, 35 minutes faster than previously.

The route of the WCML was set out many decades ago and incorporates many relatively low radius curves where the new tilting trains are travelling at greater speeds than any trains before.

1.2. The problem being investigated

Figure 1-2 shows the way in which, during curving on canted track, loads from a Pendolino train are transferred to the sleeper/ballast interface. Note that loading from sources other than static, curving and wind is not included in the diagram.

The lateral forces due to curving or wind loading act at the centres of mass and pressure of the vehicle respectively, and therefore a moment is applied to the track system in addition to a purely lateral force. The moment manifests itself in terms of an increased vertical load on the outer rail and a reduced vertical load on the inner rail (Figure 1-2B). Global normal loads on the rails may also be increased when the track is canted because the curving force can be resolved normal to the track; however, on canted track the weight of the vehicle is no longer normal to the track and so cant also acts to reduce force normal to the track.

The rail head is curved and the wheel rim is sloped so that contact occurs across a small area. The size of the wheel/rail contact patch varies depending on the curvature of the wheel and rail and their stiffnesses and may be estimated as about the size of a 5 pence piece or a 15/20 mm diameter circle. The slope of the wheel rim helps the vehicle to steer and remain safely within the rails. Under ideal conditions the lateral load is resisted on the railheads through the small frictional contact patches between the wheels and the rails, but when necessary this lateral force is also resisted at contact with the wheel-flange/outer-railhead. Flange/rail contact is undesirable as it leads to wear; such contact can be eliminated by appropriate design geometry with compatible train speed, i.e. operating at the balance speed on curved sections of track.

The loads on the rails cause them to rotate and deflect on their fastenings which in turn transfers load to the sleepers and below. Differences between the vertical loads on the two rails lead to a moment acting on the sleeper, which must be resisted at the sleeper/ballast interface. Collectively there is a simultaneous vertical, horizontal and moment (VHM) load about the base centreline of the sleeper/ballast interface (Figure 1-2C).

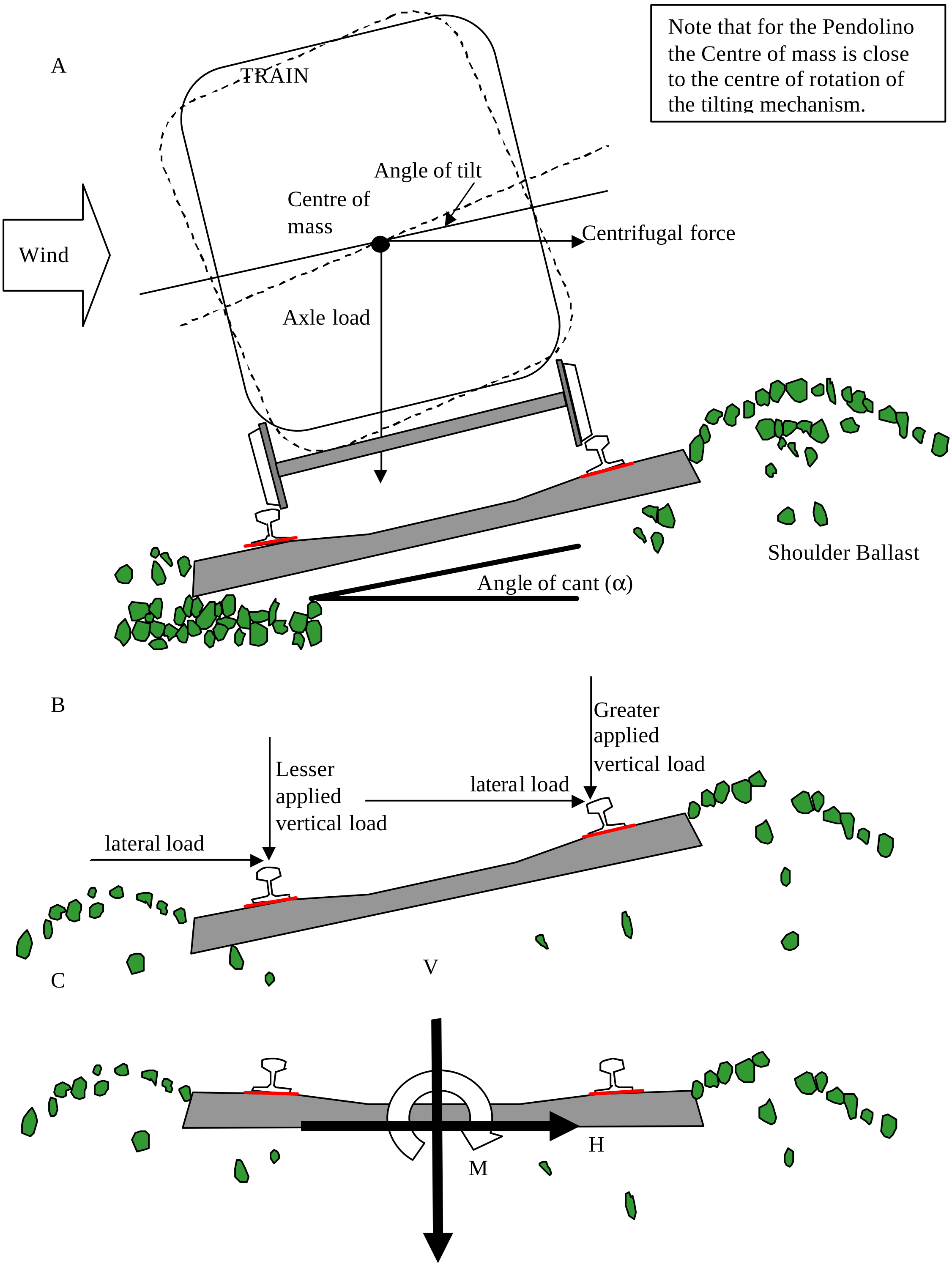

Figure 1-2: Transfer of forces through to sleeper/ballast interface

The magnitudes of forces and deflections at particular locations within the track system are related to the relative stiffnesses of the rails, the railpads, the sleepers and the trackbed support. These forces and deflections are extremely difficult to quantify accurately at all locations in the track system, particularly within the geotechnical layers.

The load at the sleeper/ballast interface passes to three distinct contact areas: the shoulder, crib and base (Figure 1-3). It is the behaviour of these three contact areas individually and collectively to resist train loading on curved sections of track which will be the main focus of the research.

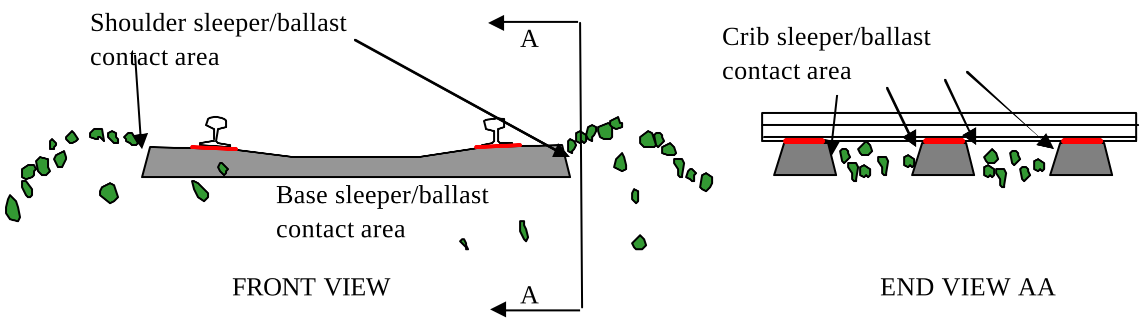

Figure 1-3: The sleeper/ballast interface

1.3. Knowledge gap

Existing computer models used to evaluate train and track performance do not account for individual components of lateral track resistance from each of the three sleeper/ballast contact areas. Different types of train/track-system models make different simplifications, partly related to the type of model and purpose. The most commonly used models within the rail industry are vehicle/track dynamic models, e.g. Vampire (DeltaRail, 2006) which focus on the behaviour of the wheel/rail interface. Vehicle/track dynamic models may be able to incorporate actual track alignment data from NR track recording vehicles to simulate the behaviour that occurs as given types of trains pass over track at certain levels of degradation prior to maintenance. The results can show whether forces and displacements outside of those permitted may be generated. Vehicle/track dynamic models can incorporate sophisticated representations of train suspension systems and have the ability to evaluate track load from new trains, before they have been allowed onto NR track by inexpensive computer simulation rather than expensive actual testing. However, such models simplify the behaviour of the sleeper/ballast interface to that of a linear elastic spring both vertically and laterally. Other types of computer models have been developed as design aids for trackbed specification, e.g. Geotrack (Chang et al., 1980). Models such as Geotrack typically represent short sections of track to evaluate the ability of ballast and deeper geotechnical layers to cope with vertical load on straight sections of track. These types of models can be used to specify appropriate depths of ballast beneath the sleepers so as to attenuate cyclic vertical load to a level the subgrade can withstand on a long term basis. However trackbed design models have not usually accounted for lateral or moment loading on canted curved sections of track, nor attempted to model the effects of crib and shoulder ballast.

Much actual testing of the resistance of track to vertical and lateral loads has been carried out; however, accessing such tests is problematic and there are limitations on the test data available which will be discussed later in this thesis.

Acceptable loading of track can be considered from two standpoints:

1. Design of the track.
2. Acceptance of vehicles to run on the track.

Various track design methods exist within respective national codes, and design methodologies have also been developed privately by individuals/organizations. The design of the track tends to focus on the ability of the formation to cope adequately with vertical loading from trains without considering lateral or moment forces.

From the perspective of acceptable loading of vehicles, in the UK, new track vehicles are required to demonstrate certain levels of safety and codes then govern their maximum operating speeds. In the UK, codes require new vehicles to meet two key criteria for track loading in that they need to demonstrate:

- No lateral loads in excess of W/3 + 10 where W is the axle load in kN, this relation is termed the Prud’homme relation. (British Railways Board GM/TT0088, 1993).

- An overturning resistance angle of at least 21° at all times. (Safety and Standards Directorate Railtrack PLC GM/RT2141, 2000).

The overturning resistance is the only place within UK codes that a moment loading of the track is considered. However it assumes that the track is able to cope with the load and, within the practicalities of vehicle design, it applies no upper limit to such loading.

While research continues, vehicle and track design and maintenance rely on safety standards in codes of practice which have evolved over many decades to become increasingly complex e.g. see the quantity of codes listed online by the Rail Safety and Standards Board (2008). Some of the track safety requirements such as the Prud'Homme limit for lateral track stability date back to the 1950's (Esveld, 2001); this relation is being applied today to Pendolino trains operating on infrastructure which, while still adhering largely to routes laid out many decades ago, has been wholly replaced and modernised.

Chapter two elaborates on the points made within this section and provides more detailed references.

1.4. Objectives

"*The superstructure is separated from the substructure by the sleeper-ballast interface, which is the most important element of track governing load distribution to the deeper track section*." (Indraratna and Salim, 2005).

The **aim** of the proposed research is to develop a fuller understanding of the mechanical behaviour of the sleeper/ballast interface, and specifically to:

- Quantify likely magnitudes of Pendolino train loading for normal and extreme conditions by summing the effects of curving forces, wind load and static axle loads on low radius curves of the WCML (Chapters 2 and 3).
- Characterise the in-service (pre-failure) behaviour of the sleeper/ballast interface due to likely Pendolino train loading (Chapters 5 and 7).

- Quantify the development of confining stress within the ballast at the end of an initial 100 Pendolino axle loads on freshly prepared ballast and assess its impact on sleeper/ballast interface behaviour (Chapter 6).
- Characterise single sleeper interface properties (pre-failure) for use with vehicle/ track dynamic models (Chapter 7).
- Quantify the failure envelope of the sleeper/ballast base contact for a single sleeper in combined VHM loading (Chapter 8).
- Quantify the resistance available from the crib and shoulder sleeper/ballast contact areas both experimentally and by calculation (Chapter 8).
- Address the implications of the findings of the research (Chapter 9).

The objectives will be achieved by:

- The use of the beam on elastic foundation (BOEF) analogy to estimate likely Pendolino track loading as it is transferred to the sleeper ballast interface (Chapters 2 & 3).
- The use of geophones to measure real sleeper movements on curves of the WCML during passage of high speed Pendolino trains (Chapters 5 and 7).
- The development, validation and use of a testing apparatus to measure the pre and post-failure lateral resistance available from the three sleeper/ballast contact areas, and able to measure confinement within the ballast. A description of apparatus and testing procedures are given in Chapter 4. In Chapters 5 and 7 a comparison is made with geophone data to validate the ability of the apparatus to reproduce satisfactorily actual track behaviour. In addition Chapter 5 examines the effect of loading rates on the lateral cyclic behaviour of the sleeper/ballast interface. Results for lateral resistance tests for different arrangements of crib and shoulder ballast are presented in Chapter 8.
- Development of a finite element model of the testing apparatus to use as a tool to interpret the measured confining stress in the laboratory experiments (Chapter 6).
- The application of wider geotechnical principles to the problem of rail track loading, in particular the effects of combined VHM loading on granular materials, and the application of limit equilibrium principles to the resistance provided by the shoulder ballast (calculations are presented in Chapter 8).

- The evaluation of testing and field data in conjunction with the results from geotechnical calculations, leading to an improvement in the fundamental understanding of the behaviour of the sleeper/ballast interface (key points are made in each chapter and all points are drawn together with conclusions presented in Chapter 9).

Chapter 2 of this report provides an evaluation of current background knowledge to identify gaps and support the current research. Although Chapter 2 incorporates the bulk of the literature review, much literature has been referenced and reviewed in later Chapters where it is relevant for comparison with results.

2. Background: justification for the research

Much research has been carried out around the world to improve knowledge of the behaviour of railway track systems e.g. Indraratna and Salim (2005), Esveld (2001), Selig and Waters (1994) and Alias (1984). However, there are still gaps in our knowledge, particularly from a geotechnical perspective.

Over the past century methods of modelling train/track interaction have advanced greatly. From the late 1970's computer models were developed for design use. Early computer models were often limited to two dimensions and provided results at only a small number of key locations. These simplifications were in part due to the need to limit the number of calculations and thus the computing time required. Today, there are a large number of models reported in the literature giving insights into various aspects of train/track interaction.

All track system models apply simplifications depending on what they are investigating. Models have first focused on the behaviour on straight sections of track with the result that the behaviour of the track system at the sleeper/ballast interface due to loading on ***curved*** sections of track is one of the least well understood aspects of track system behaviour.

By being familiar with the track system and the roles each component part plays in supporting train loading, it will be possible to evaluate the relative sophistication of the different types of model in common use. Such an understanding then provides a context to review the way in which models represent simplified behaviour of the sleeper/ballast interface to provide data for particular purposes. Later in this report comparisons will be made between the real behaviour at the sleeper/ballast interface and modelling simplifications. The real behaviour is assessed by the geophone track measurements and experimental measurements presented in Chapters 5, 6 and 7. In particular, it will be shown that pre-failure behaviour is load path dependent and may also vary significantly from sleeper to sleeper; aspects of behaviour which no commonly used models take into account.

This Chapter includes sections on:

- The track system: A look at the components that may need to be represented in a track system model.
- Some of the more important train/track interaction models. Models included are:
    - Beam on elastic foundation (BOEF): the simplest and oldest model of the track system, this static model offers insights into the load at the wheel/rail interface and the effects of global track stiffness. This model will be further used to estimate likely loading on the sleeper for a Pendolino on the WCML both in this chapter and Chapter 3.
    - Geotechnical static track system models (Geotrack), offering insights into the behaviour of the ballast.
    - Dynamic train/track interaction models which provide data at the wheel/rail interface. General principles and the basis for contemporary vehicle/track interaction models commonly used within the rail industry
    - Contemporary models (Vampire), widely used throughout the world and able to incorporate real track alignment data from track recording vehicles to run simulations of load response over great lengths of track at the wheel/rail interface.
- The current state of knowledge and design practice including a look at:
    - Load testing of the sleeper/ballast interface
    - Design practice for the trackbed
    - Acceptance of vehicles to run on the track

2.1. The track system

To investigate the effect of specific track loading, an appreciation of the roles of the different parts of the system is required. Modern conventional track can be subdivided into seven components (Figure 2-1) each of which has a specific role in supporting the train load:

- Rails
- Railpads/fastenings
- Sleepers

- Ballast
- Geosynthetic
- Subballast
- Subgrade

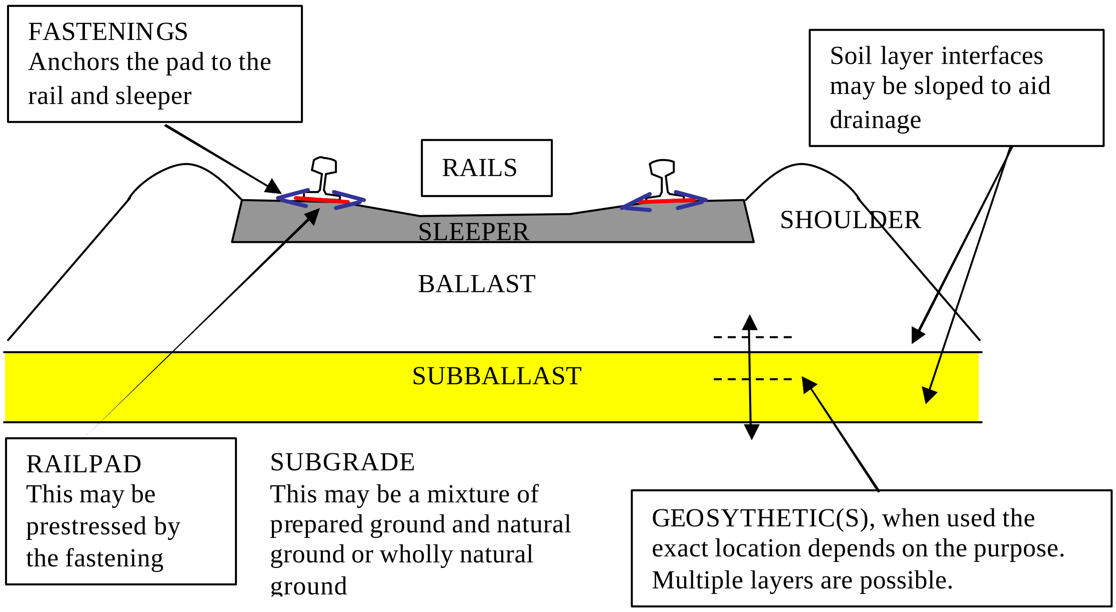

Figure 2-1: General track cross-section, UK

The magnitude of deflection of the rail at the wheel/rail interface is key to providing a stable track system able to support trains safely at their running speeds and collectively all the components of the track system and their load/response properties contribute to this. When a rail deflects less than a certain amount under loading, damage will occur to the wheel and suspension of a train vehicle as well as to the track; however, excessive deflection also results in track and vehicle damage. Design of track requires consideration of the load response behaviour of all components of the track system to provide acceptable load response, optimum maintenance regimes and overall lifetime performance.

We shall now briefly consider each of the rail track system components from the top down:

2.1.1. Rails

The basic steel rail cross-section has been refined over time. It can be manufactured to a high specification in terms of strength and geometry so as to provide as smooth a train ride as possible. On today's high performance lines, rails are welded together to create continuously welded rails (CWR) thus eliminating a potential cause of dynamic load: the discontinuity caused by traditional fishplate bolted joints. The length of rails has also increased so that welds are spaced further apart. The mass per metre of rail is known to contribute to the track stability and for high speed lines a mass of about 60 kg per metre (Specification: 60 E1) is the norm in Europe (British Standards Institution BS EN 13674-1, 2003) and is used on the WCML. The rails are placed on the sleeper at slightly inclined positions to point inwards; this aids the sloped wheel rims to steer within the rails and avoid flange contact. On a G44 sleeper, the type used on the WCML, the inclination is 1:20 (Tarmac, 2005). Throughout this report, rail section properties through ***xx*** and ***yy*** axes will be considered to be sufficiently close to the normal and lateral track axes. The wheel/rail interface has been extensively researched and rolling contact theory is well developed e.g. Kalker (1979). Typically rails experience wear during service and require grinding to maintain a smooth running service at regular intervals and, when necessary, replacement.

2.1.2. Pads/fastenings

A rail pad is placed between the rails and sleeper and the rail is fastened to the sleeper using a clip which may also pre-stress the pad. Research has indicated that the stiffness of the pad makes a significant contribution to the everyday quality of ride and to track service life and intervals between maintenance e.g. Fermer and Nielsen (1995). Without a pad the train loads would be more concentrated through the rigid contact of the rail to sleeper, causing more damage to track and vehicle. The pad and fastening permits limited vertical deflection and rotational movements of the rail relative to the sleeper. On the WCML Pandrol fastenings and pads are used with properties tested and reported on by Pandrol (2003).

2.1.3. Sleepers

The sleepers are often referred to as ties as they tie the rails together, preventing any dangerous relative lateral movement and providing support for the rails. Sleepers are, typically, made from reinforced, pre-stressed concrete and, again, their mass is known to contribute to the stability of the track. Two types of concrete sleeper are commonly used: mono or duo block sleepers. On the WCML type G44 mono block sleepers are used weighing 310kg each (Tarmac, 2005). However it is not clear which type of sleeper is most advantageous. Duo-block sleepers are used on TGV lines; here, concrete ends supporting the rails are joined by steel reinforcing rods permitting the omission of the middle section of concrete sleeper. This may reduce the weight and also improve the consistency of ballast contact. For mono-block sleepers, ballast tends to settle during service relative to the sleeper centre beneath both rail seats and periodic maintenance by tamping is required to correct this. If this is not done, ultimately *"failure to maintain the track causes the ties to break along the track centreline"* (Turcke and Raymond, 1979). This is known as centre binding. On the other hand, the lighter duo-block sleepers are less able to stabilise dynamic load. Duo-block sleepers are also considered to give better lateral resistance because they have four ends vertically normal to the ballast on horizontal track as opposed to the two ends of a mono-block.

The sleepers then transfer the more concentrated loads from the rails to the larger contact areas of the sleeper/ballast interface. However, it should be noted that the sleeper is supported by a finite number of small discrete contacts with the ballast.

2.1.4. Ballast

The main role of the ballast is to attenuate the relatively high stress immediately beneath the sleeper to an acceptable level that can be withstood on a long term basis by the subgrade. The weaker the subgrade the thicker the ballast layer needs to be; although if the subgrade is too weak, implying an excessive ballast layer thickness, other measures may need to be taken. When a subgrade is weak and/or the ballast layer is too thin, repeated loading can lead to localised ballast penetration into the subgrade. In the case of a low permeability subgrade (clay), water may accumulate in these pockets, leading to the eventual failure of the ballast and track. Variation of layer thickness also leads to a variable track resilient response to load. A wide range of load response over a short length of track will ultimately lead to early track failure (Hunt, 2000).

The ballast thickness in developed parts of the world is usually the main design criterion for a contractor evaluating the design of a new section of track, as the type of ballast material used has generally been incorporated into developed countries' standards. The choice of ballast material is based on its ability to provide uniform support to the rails and permit rapid drainage. This leads to a conflict in the specification of ballast. Uniform support may best be achieved by well-graded ballast whereas adequate drainage is best achieved by uniformly graded ballast. Around the world the ballast used may depend on the materials locally available. Various studies of rock types suitable for ballast, e.g. Boucher and Selig (1987), Watters et al (1987), Klassen et al (1987) and Raymond (1985b) have concluded that igneous or metamorphic rocks chosen for their angular shape and relatively uniform grading and strength provide the best type of ballast. More recently Indraratna and Salim (2005) compared current specifications of ballast throughout the world and proposed a new optimum grading of ballast to meet the conflicting requirements to provide uniform support and drainage.

Network Rail (Safety and Standards Directorate Railtrack PLC RT/CE/S/006, 2000) requires ballast to be well graded with particle sizes mainly between 32 mm and 50 mm in diameter and laid to a depth of 300 mm or more below the sleeper base.

Ballast is also piled up at the ends of the sleepers (shoulder) and between the sleepers, (crib). The main purpose of shoulder ballast is to protect the track from buckling due to temperature induced rail loads, with or without trains present. The crib ballast provides pressure on the ballast below and at contact with the sleepers to increase the stability of the track and prevent longitudinal movement of sleepers.

In the past ballast would rest on natural formation or fill material of varying quality and this is believed to be the case on the WCML where conversations with track engineers have indicated that the refurbishment work was carried out by removing the top 0.5m of existing ballast and re-laying fresh ballast to support the new track.

2.1.5. Geosynthetics

Geosynthetics are the most recent addition to the track system; ballast can be strengthened and various types of subgrade can benefit from the use of geosynthetics. There are several sub categories of geosynthetic commonly used (Corbet, 2003) and choice depends on function.

Geosynthetics in the form of geo***grids*** placed within the ballast layer but below the depth of tamping may be used to improve the strength and service life of ballast as a number of studies have indicated, e.g. Bathurst and Raymond (1987), Brown (1996), Indraratna et al. (2004), and McDowell et al. (2006).

A geo***textile*** may be placed between the ballast and subballast to provide filtration and/or increased strength (Raymond, 1982). As a filter a geotextile acts as a barrier against the migration of particles from the subballast/subgrade into the ballast while still permitting drainage (Chrismer and Richardson, 1986). Fouling of the ballast by subballast/subgrade migration is known as ballast pumping. It impairs ballast drainage capabilities leading to a long term decline in performance. Poor drainage leads to ballast saturation and some studies have shown that settlement rates may increase in wet ballast (Fair, 2003). Fouling is also associated with the development of ballast pockets and varied rates of settlement and resilient response.

Geosynthetics have also been used as a barrier locally to prevent groundwater from infiltrating the trackbed to maintain safe levels of drainage (Lacy and Pannee, 1987).

2.1.6. Subballast

The subballast layer (sometimes known as the capping layer) works, either solely or in conjunction with a geosynthetic, to prevent the relatively large sizes of ballast particles from penetrating the subgrade or vice versa. The subballast layer will typically consist of sand 100 mm thick and also helps to transfer the load evenly into the subgrade.

2.1.7. Subgrade

Ultimately all train loading reaches the subgrade. The subgrade may be the natural ground or a combination of fill material and natural ground at depth. Selig and Waters

(1994) wrote that the influence of traffic induced stresses may extend downward as much as 5 metres or more below the bottom of the sleepers. This was supported by large scale 3D finite element modelling of the track superstructure and substructure by Powrie et al., (2007) in which it was shown that the vertical stress reduced to 3% of the maximum stress between sleeper and ballast at 1.67$\boldsymbol{S}$ where $\boldsymbol{S}$ is the sleeper length in metres i.e the maximum surface stress reduced to less than 3% at a depth of ~4.1 m for a typical 2.5 m long sleeper. Depending on the stiffness of the subgrade, the penetration of stresses into the subgrade can lead to significant proportions of vertical sleeper resilient deflection and plastic displacement originating within the subgrade.

2.2. Train/track system interaction models

With an understanding of the track system it is possible to examine some of the more important track system models, and look at the insights some of these models give into track system behaviour.

2.2.1. Beam on Elastic Foundation Model (BOEF)

The simplest representation of the track is referred to as the BOEF model; it provides data at the level of the rail and allows calculations to be made based on tests that equate the track deflection for a known force with a foundation coefficient. Although referred to by some authors as a coefficient, the parameter has units of force per unit length of track per unit deflection and may more accurately be termed a modulus. The equations can be derived by considering Figure 2-2 and Figure 2-3.

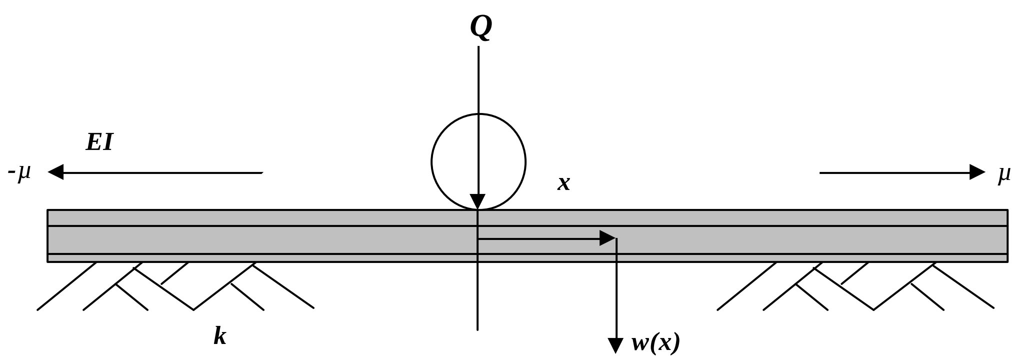

Figure 2-2: BOEF Model

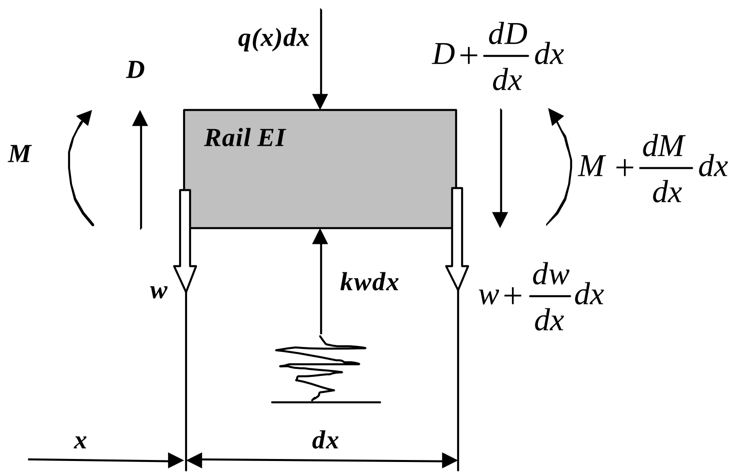

Figure 2-3: Beam element model

The most important equations that may be derived from Figure 2-2 and Figure 2-3 are summarised below (note that the equations are valid only for $x > 0$):

$$w(x)=\frac{Q}{2kL}e^{\frac{-x}{L}}\left[\cos\frac{x}{L}+\sin\frac{x}{L}\right]$$ **Equation 2-1**

$$\frac{4EI}{L^4}=k$$ **Equation 2-2**

$$M=-EI\frac{2Q}{2kL^3}e^{\frac{-x}{L}}\left[\sin\frac{x}{L}-\cos\frac{x}{L}\right]$$ **Equation 2-3**

Where

$$L=\sqrt[4]{\frac{4EI}{k}}$$ **Equation 2-4**

With notation defined:

EI =	Bending stiffness of the rail
k =	Foundation coefficient[1] or track modulus
w(x) =	Rail vertical deflection at longitudinal distance ***x***
D =	Shear force
M =	Moment
q(x) =	The variation in vertical load with longitudinal distance (***x***) which is replaced with ***Q***, the wheel load in the derivation process.
L =	Is termed the characteristic length and arises from the derivation process.
Q =	Wheel load

These types of relation appear in the literature at least as far back as 1927 (Timoshenko, 1927) and have more recently been presented in varied forms by Raymond (1985a) and Esveld, (2001). A full derivation is presented in Appendix A which also incorporates additional track parameters (see Chapter 3).

When using these equations all the parameters should be known except for ***k*** which is found from experiment. ***E*** and ***I*** are for the rail and should be available from design data. Taking realistic values for a Pendolino train on the WCML (Table 2-1), a graph of deflection (Figure 2-4) and moment (Figure 2-5) with distance from the wheel load can be plotted.

Variable	**Value**	**Units**	**Description**	**Notes**
Q	72,560	N	Wheel load	Pendolino train average 180% tare (Harwood, 2005)
E	205,000	N/mm^2	For Rail	Assumed typical value for steel
I	30,383,000	mm^4	For Rail	60 E 1 (British Standards Institution BS EN 13674-1, 2003)
k	Varied	N/mm/mmm	Track Modulus	Range of values chosen based upon literature e.g. Bowness et al (2005b) measured 38N/mm/mm at Crewe UK.

Table 2-1: Data used to create the graph of moment and deflection in the rail

[1] Hereafter referred to as ***track modulus***, although in later chapters the term ***vertical track modulus*** may be used to distinguish it from ***lateral track modulus***. Vertically, the track modulus will always be evaluated for half of the track for a single wheel load, whereas horizontally it is evaluated for the full track by summing rail stiffness about the ***yy*** axis.

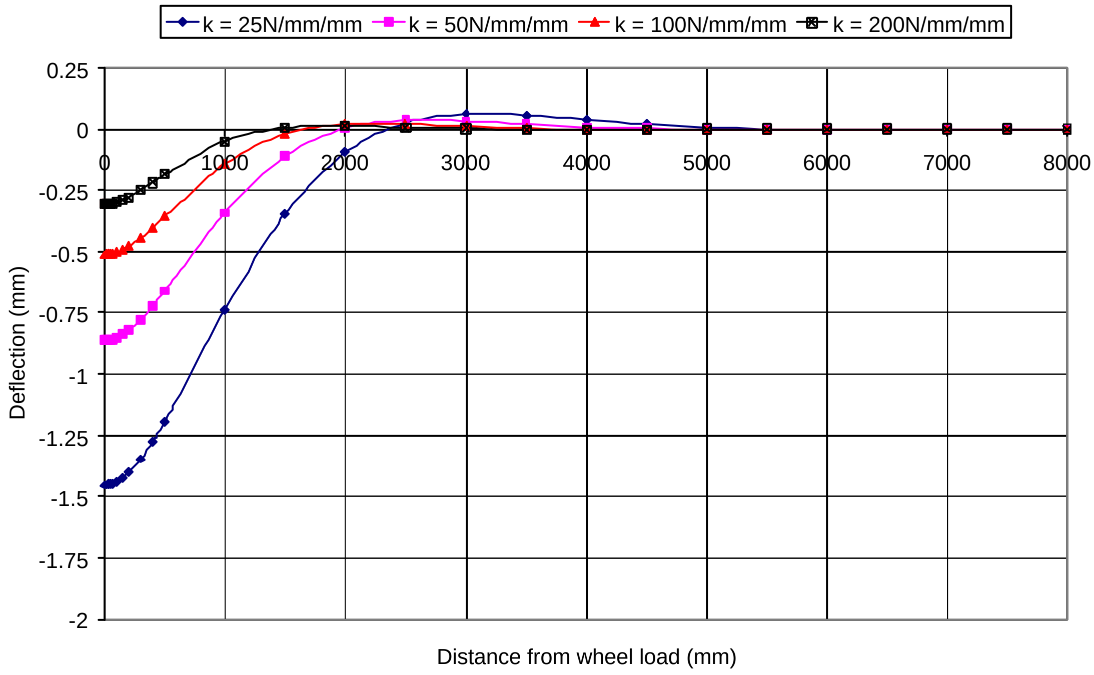

Figure 2-4: BOEF model: Graph of deflection of the rail for a Pendolino wheel load and varying track modulus

Note the marginal uplift that occurs in the deflection before the rail returns to its normal position as the wheel load passes. It is arguable whether this actually happens because in the BOEF model the self weight of the rails and weight of the sleepers attached to them is ignored. It is perhaps more likely that the load at the sleeper/ballast interface due to self weight locally reduces prior to and after the passage of a bogie. Such a reduction in normal force on the sleeper/ballast interface is potentially dangerous as it may lead to the occurrence of rail buckles when pre-existing track misalignment and raised temperatures are also present (ERRI committee D202 report 3, 1995).

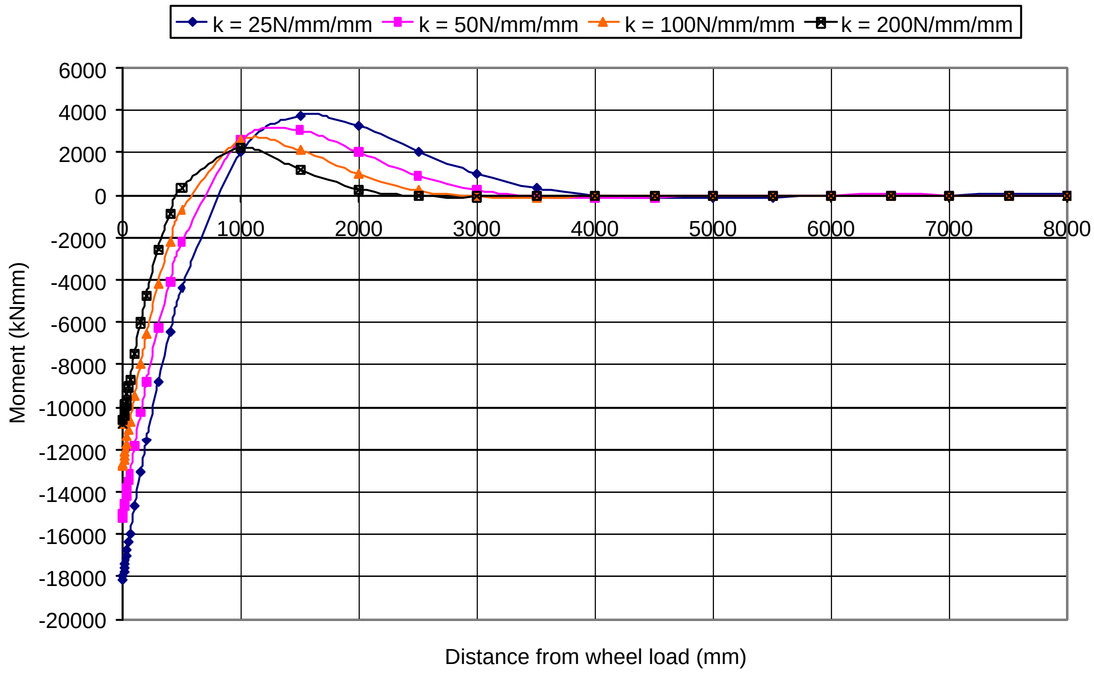

Figure 2-5: BOEF model: Graph of moment in the rail for a Pendolino wheel load and varying track modulus

It is sometimes convenient to use the track modulus per sleeper spacing instead of per unit length of track, k is then replaced by:

$$k = \frac{k_d}{a}$$ **Equation 2-5**

Where a = sleeper spacing as shown in Figure 2-6

With this substitution made it is possible to determine:

- load per sleeper (railseat load) in relation to track modulus
- deflection of sleepers and track modulus,

as Raymond (1985a) showed:

$$k_d w(x) = \frac{aQ}{2L} e^{\frac{-x}{L}} \left[\cos\frac{x}{L} + \sin\frac{x}{L} \right]$$ **Equation 2-6**

$$w(x) = \frac{aQ}{2k_d L} e^{\frac{-x}{L}} \left[\cos\frac{x}{L} + \sin\frac{x}{L} \right]$$ **Equation 2-7**

Where x is evaluated in multiples of sleeper spacing, however note that no fundamental change has taken place in the underlying assumptions of the BOEF model. All that has been done is to evaluate the displacement at sleeper intervals. Provided the sleepers are reasonably close and the rails reasonably stiff this does not introduce significant error. However, as the sleepers become further apart the discrete nature of the support renders the BOEF model more and more invalid.

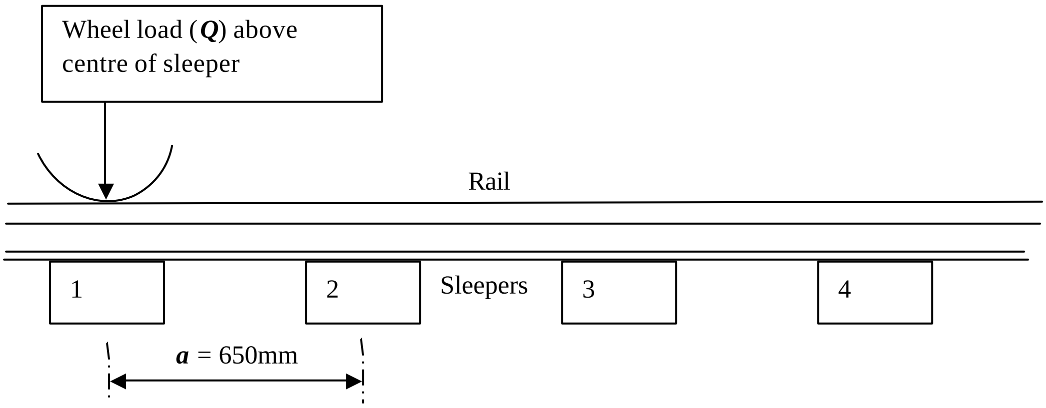

Figure 2-6: Track diagram for evaluation of railseat loads and deflections

Figure 2-7 and Figure 2-8 show the railseat load (the load reaching the sleeper) as a percentage of the applied load and the deflection on the first sleeper immediately below the wheel and for three further sleepers to one side. Sleepers on opposite sides of the wheel receive equal loading.

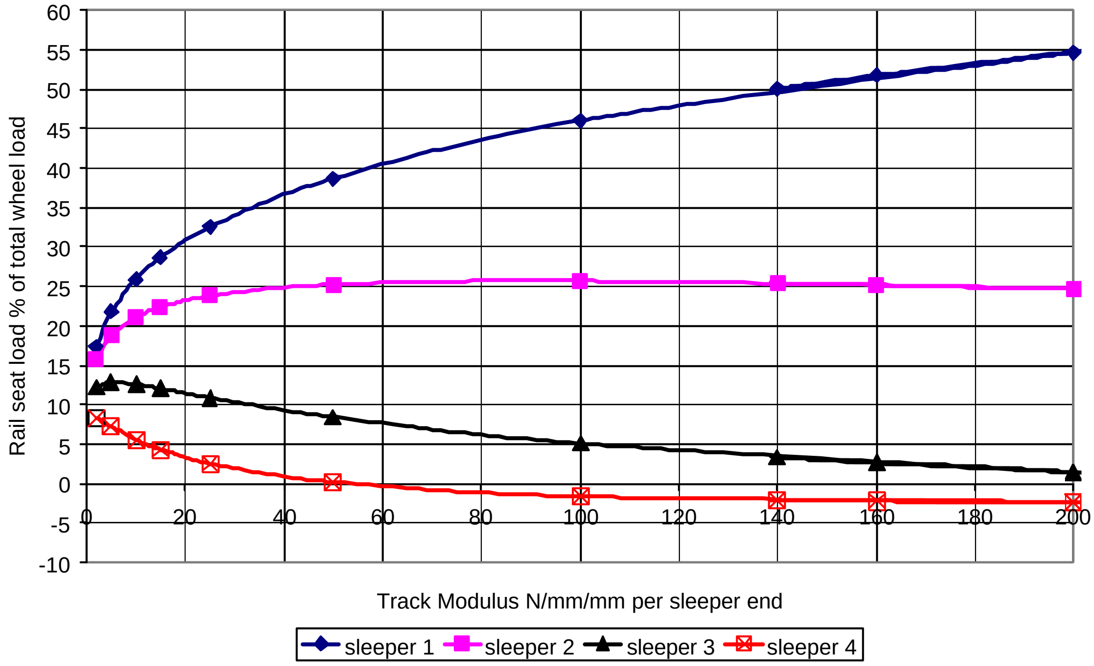

Figure 2-7: Rail seat load as a % of wheel load with increasing track modulus, sleepers at 650mm centres on 60 E 1 rails

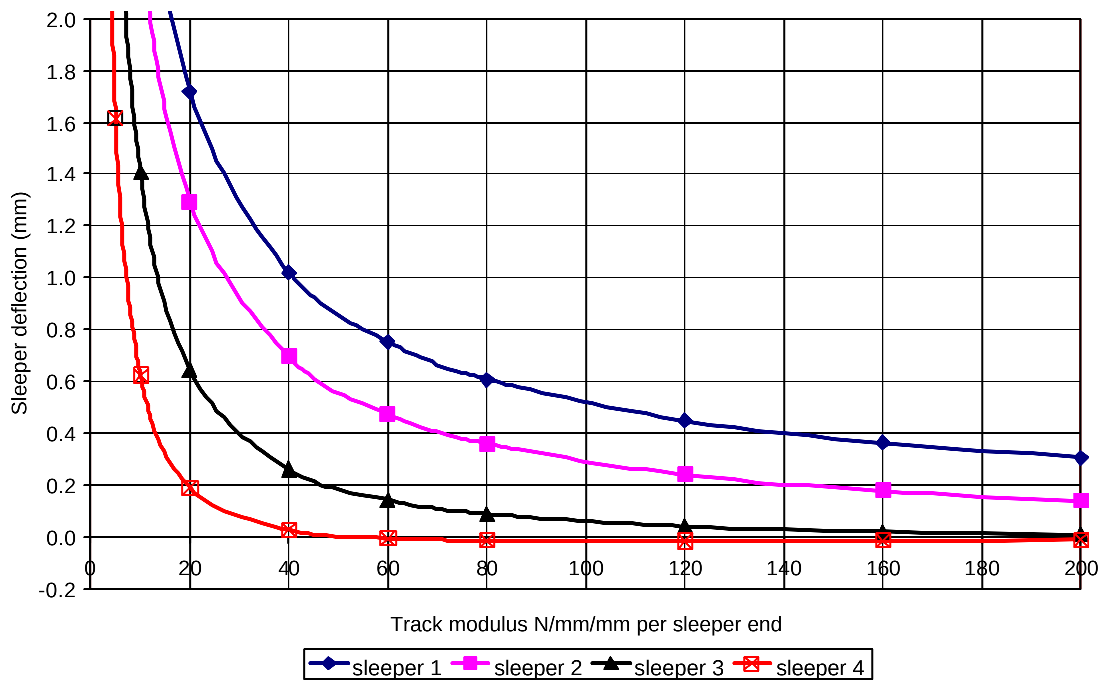

Figure 2-8: Variation of rail displacement with distance from the load and increasing track modulus for a Pendolino wheel load

The BOEF model can be useful when considering the vertical track behaviour at the level of the rail. However, the geotechnical aspects of the railpad, the sleeper, the ballast and the subgrade are oversimplified, being lumped into a single linearly elastic variable: the track modulus. Despite this simplification the BOEF model can be used to provide estimates of load reaching the sleeper/ballast interface provided realistic deflection ranges are known and can be used to set the track modulus to a realistic level. In chapter 3 this model will be extended and used to examine the lateral load reaching the sleeper. An appropriate range of track moduli can be found by using geophones to measure sleeper deflections during Pendolino passage as described in Chapters 5 and 6. With the appropriate range of track moduli identified by the geophone measurements, estimates of vertical and lateral load reaching the sleeper were used to inform the laboratory experiments reported in Chapters 4 to 8.

2.2.2. Static Track System Models (Geotrack)

Static models of the track system can be constructed in two ways (O'Reilly and Brown, 1991):

1. Finite element methods, significant early examples include: SENOL (Brown and Pappin, 1981), PSA (1968) reviewed by Adegoke et al (1979), ILLI-TRACK (Tayabji and Thompson, 1976).
2. Layered elastic systems, significant early examples include: MULTA (Kennedy and Prause, 1978), Geotrack (Chang et al., 1980), ARTS (Turcke and Raymond, 1979).

Perhaps the most well known static track system model is named Geotrack. Geotrack is a design aid for railway track. It adopts an elastic multi-layered stress state dependent approach to modelling the ballast, subballast and subgrade with beams representing the sleepers and rails (Figure 2-9). Geotrack also permits separation of the sleeper from the ballast and variation of sleeper length, size and spacing.

Geotrack was developed at the University of Massachusetts, Amherst, USA in the late 70s and early 80s; considering the advances in computing since then it would seem that Geotrack is somewhat outdated. However, despite its age in computing terms, a design method for ballast layer thickness was published in the late 90s based on results from Geotrack, (Li and Selig, 1998a) (Li and Selig, 1998b), which one group of reviewers rated as the most analytically advanced in the world (Burrow et al., 2007a).

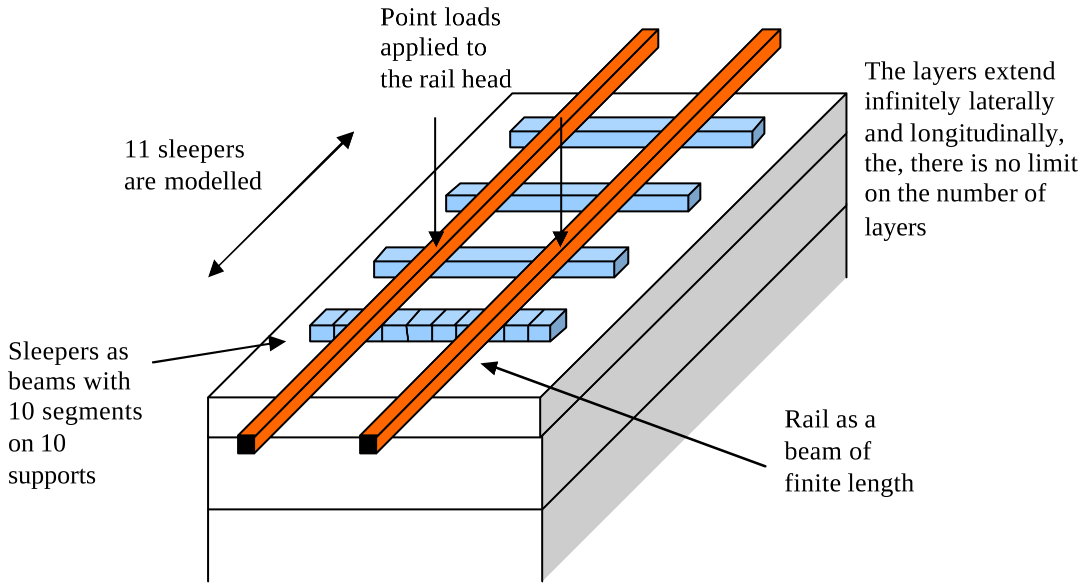

Figure 2-9: Idealization of Geotrack model

Geotrack provides outputs for forces, bending moments, stresses and displacement at key locations including at the rail seats, between the ties and ballast and between the ties and rails.

Geotrack was developed after consideration of the other programs available at the time (1979) and grew from improvements to a program known as MULTA (Multi Layer Track Analysis). Validation was provided by comparing Geotrack outputs with data taken from tests carried out at The (US) Department of Transportation's Facility for Accelerated Service Testing (FAST) in Pueblo, Colorado, USA.

A key validation of Geotrack was its ability to reproduce test results of the pressure distributions at the interfaces between sleeper and ballast, as shown in Figure 2-10, and between ballast and subgrade.

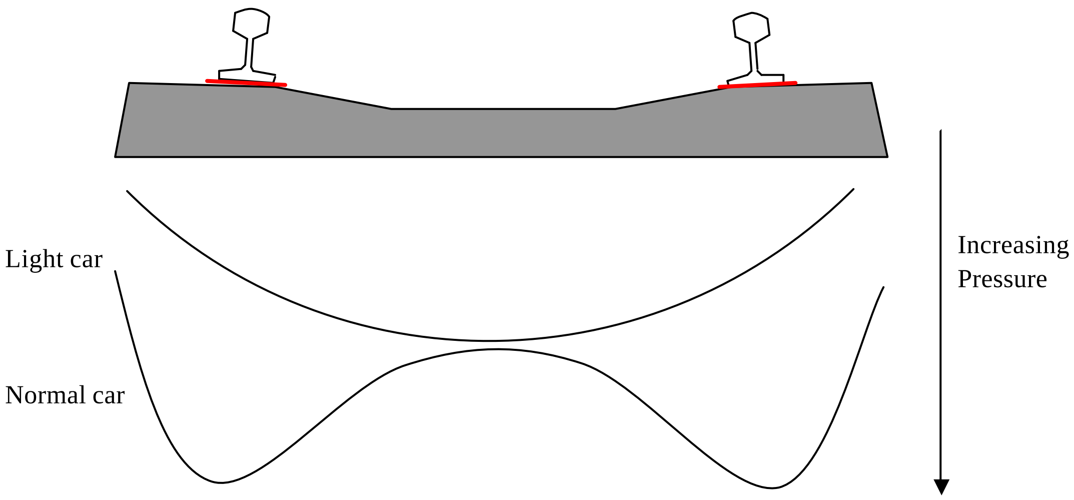

Figure 2-10: Idealized pressure distributions sleeper/ballast interface after Kennedy and Prause (1978), not to scale

The development of the w-shaped pressure distribution for a normal car occurs theoretically when a flexible sleeper is supported continuously by an elastic layer of uniform stiffness. In practice this is a gross simplification because sleeper support is highly erratic due to the relatively large size of ballast particles and the development of structure within the ballast. Shenton (1975) reported data from British Rail tests in which pressure plates fitted to the base of the sleeper were able to identify a w-shaped pressure distribution from a locally highly varied pressure line (Figure 2-11).

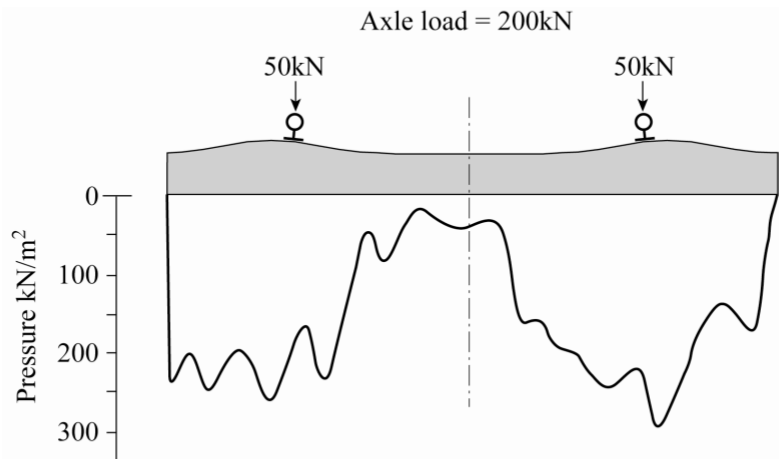

Figure 2-11: Pressure beneath sleeper, after Shenton (1975)

Finite element modelling carried out as part of this research (reported in chapter 5) idealising the ballast as an elastic finite depth layer on flexible elastic support also confirmed the development of the w-shaped distribution.

The w-shaped pressure distribution causes differential settlement of the ballast beneath the sleeper so that maintenance operations are required to restore the sleeper to ballast contact beneath the railseats where the pressure is highest.

Geotrack utilizes the work of Burmister (1945) which put forward a general theory of stresses and displacements in layered systems to set up the multiple layer stress dependent elastic system. In conjunction with this the material properties for each layer are calculated based upon a relation in the form of:

$$E_r = k_1 q^{k_2}$$ **Equation 2-8**

Where:

$\boldsymbol{E_r}$ =	the vertical resilient modulus
q =	the sum of initial and incremental bulk stress (i.e. maximum bulk stress)
$\boldsymbol{k_1, k_2}$ =	Parameters determined experimentally

Many researchers specialising in pavement/highway engineering have endorsed a relation of this form which is often termed the *k*-theta model (e.g., Gonzola (1981)).

The parameters in the *k*-theta relation are not dimensionless. Because of this Geotrack modifies Equation 2-8 to the form:

$$E_r = k_3 \left(\frac{s_{oct}}{P_a} \right)^{k_4}$$ **Equation 2-9**

Where:

$\boldsymbol{P_a}$ =	atmospheric pressure
s_{oct} =	mean stress [defined in Chang (1980) as (σ_1 σ_2 σ_3)/3]
$\boldsymbol{k_3, k_4}$ =	Parameters determined experimentally

Since the model is elastic, Poisson's ratio is also a required input parameter and because the formulations require each layer of the system to have a single elastic modulus a weighted average at the mid depth value for each layer is assigned. Such simplifications reduce computing power requirements, albeit at the expense of accuracy,

2.2.3. Dynamic track system models

The word dynamic can easily be misinterpreted. For clarity it is useful to define what is meant by dynamic loading in so far as this report is concerned:

- Vertically, any load effect above the static load of a train resting on the tracks
- Horizontally, any load above the wind load and when curving the centrifugal force load.

Dynamic loads are due to accelerations which arise because of irregularities in the geometry of the wheels and rails and variability in the load/response of the support.

Dynamic models of the track take a very different approach from static models. Commonly, material properties are assigned to a track representation and an excitation frequency function is applied to the system to represent a train passing. Different loading functions can be incorporated to model the effects of rail corrugation, wheel flats, gaps or dips in the track as well as missing sleepers. Damping functions are assigned and properties such as acceleration, velocity and deflection at key locations can be found during and after a train has passed. These models are often more concerned with the performance of the train, and train representations include suspension and roll properties while the track system is often modelled with spring support.

Many examples of dynamic models can be found in the literature, Figure 2-12 illustrates the way in which a typical dynamic model (Cox and Grassie, 1983) represents the track.

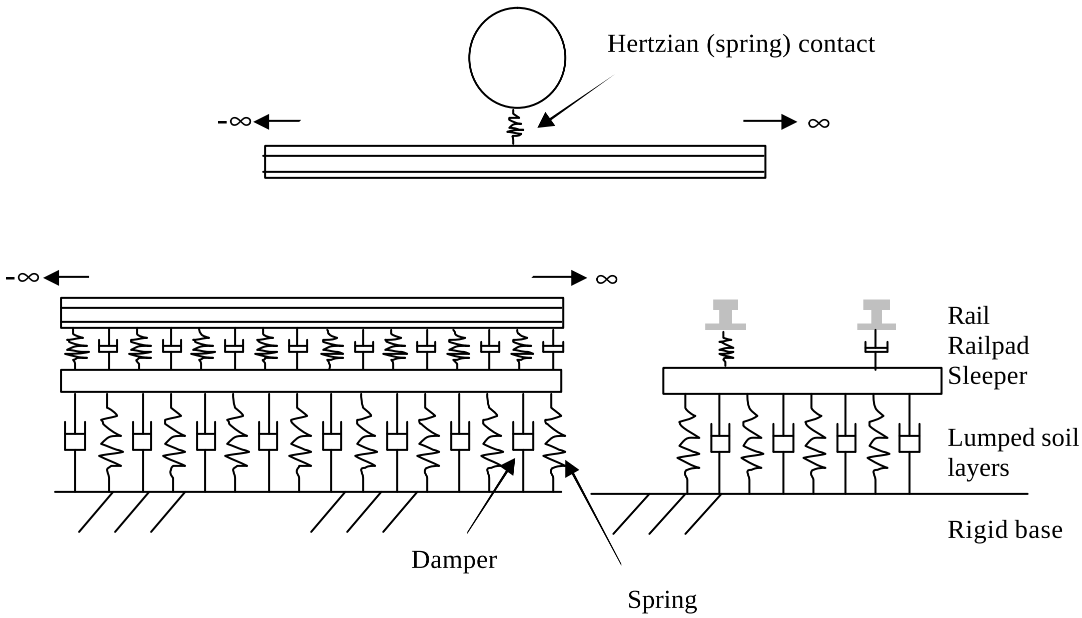

Figure 2-12: Continuous track model by Cox and Grassie (1983)

In dynamic models the masses of the components as well as the bending stiffness are important. In Cox and Grassie's model the ballast and sub-layers are represented by a single layer of springs and dampers.

Although this model can provide data at the rail and sleeper, from a geotechnical perspective it also suffers from similar drawbacks as the beam on elastic foundation mode; the behaviour of the geotechnical support is oversimplified and the model is not capable of providing data within the supporting soil layers.

2.2.4. Contemporary dynamic models (Vampire)

There are many papers and reports on dynamic train/track interaction. The large volume of published work is in part a reflection of the relative ease today with which a model can be prepared using general FE software. The models often specialise in analyzing train/track behaviour under specific conditions, for example train/bridge interactions (Song et al., 2003), (Yau et al., 2000). Some models have attempted to analyze behaviour when track parameters vary with length, for example Oscarsson (2002) varied track structure parameters on the basis of real track data.

Many of the models, particularly those which rely on finite elements, are CPU intensive and it is not possible to model long lengths of track using real track alignment data. Because of this commercially available non finite element software packages have been developed within the rail industry to focus the modelling effort on key track system features. These are able to evaluate train/track interaction over many miles of track using real track alignment data from track recording vehicles.

Network Rail and other companies worldwide commonly rely on a software package known as Vampire (DeltaRail, 2006) which was originally developed by British Rail and is now licensed and maintained by Delta Rail. Vampire is primarily a vehicle dynamics package. Within Vampire, real track data from track alignment recording vehicles can be input and simulated vehicles, defined from real vehicle parameters, pass over the track. Track recording vehicles are required to run across the track within set time periods depending on the required maintenance standard of the particular track and can identify how much the track has degraded from the design geometry using a number of different measurement criteria. These may include measurements of variations in:

- Vertical profile
- Lateral alignment
- Crosslevel/cant/superelevation
- Dynamic crosslevel
- Gauge
- Curvature

Note that these measurements are generally specified every 35 metres and are in a sense a rolling average, able to characterise the location of the rail profile but without specifically identifying its location to the precise millimetre.

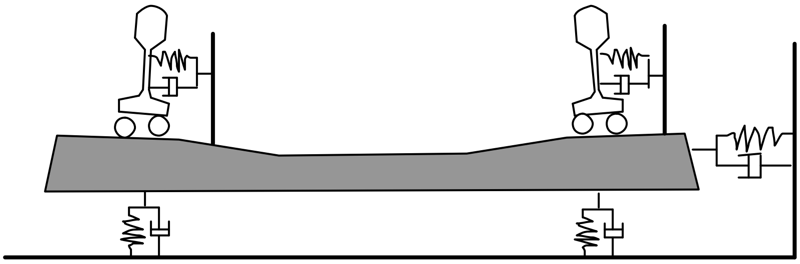

Figure 2-13: Track representation used within Vampire

Vampire lumps together the vertical stiffness of the rail pads with that of the ballast while permitting relative lateral movement of the rails on the sleepers (Figure 2-13). While useful for vehicle designers working to validate the maximum loads on the track at the wheel/rail interface, this type of model cannot provide data on loading in the trackbed. Also, it does not permit variation of lateral and vertical stiffness along the length of the track although that is something the developers (confirmed by telephone conversation, 2006) are considering for the future.

2.3. Current knowledge sleeper/ballast interface behaviour

Having examined the different types of track system models that exist, how they represent different parts of the track system and the strengths and weaknesses of these models, attention is turned to current understanding of the way in which the sleeper/ballast interface behaves. This section is in three parts

1. Testing: published results from tests on the behaviour of the sleeper/ballast interface
2. Design of the track: design criteria relating to the sleeper/ballast interface.
3. Acceptance of vehicles to run on the track: the loads vehicles impart to the track.

2.3.1. Published tests of the sleeper/ballast interface

A great deal of strength testing of track has been carried out over many decades in many countries. Internal reports of British Rail tests have been identified which date back at least as far as 1958 (BR, 1958). However, poor archiving and the break-up of British Rail means that finding such reports is problematic and in any case these early tests may not be relevant to today's track and rolling stock. In addition, test results may be held by research institutes and private companies and therefore not readily in the public domain.

Notwithstanding this, there are a number of tests reported in the literature, although, from the point of view of evaluating the sleeper/ballast interface, many have shortcomings in methods and are not reported in a consistent way, making comparison between tests problematic.

The behaviour of the sleeper/ballast interface is often tested and reported from a purely vertical or purely lateral load standpoint and, whereas the vertical behaviour is often tested for in-service non-failure behaviour, the lateral behaviour is often tested only for static failure.

The behaviour due to vertical loading can be quantified in terms of a resilient deflection from a Falling Weight Deflectometer (FWD) test. FWD data can be checked against design requirements for specifications of track (Network Rail RT/CE/C/039, 2003) and may also used to back calculate elastic moduli for subgrade soil layers (Burrow et al., 2007b). In such a calculation the thickness of all soil layers must be known and a rigid boundary at depth identified (e.g. ballast, subballast, subgrade, bedrock). Without high confidence in the location of soil layer boundaries and the likely strength of each layer the success of such back calculations can be questionable as there are an infinite number of possible solutions obtainable simply by varying layer thickness and strength parameters.

Lateral sleeper resistance tests are scarce in published literature and data are rarely presented so as to isolate resistance due to base, crib, and shoulder contact areas. Tests take different forms, and while some investigate the global resistance of the sleeper/ballast interface others report data on the resistance provided by the track system as a whole (including the ability of the rails to spread the load). In reported data it is often impossible to isolate the resistance due to the 3 sleeper/ballast contact areas or to be sure of the type of sleeper and the arrangement and type of ballast.

Committee D202 of The European Rail Research Institute (ERRI) carried out a review of lateral pull tests. The committee had access to unpublished reports and reports held by private companies and research organisations, the review provides a useful summary of test types and data as follows:

There are two types of lateral sleeper test commonly in use (ERRI committee D202 report 3, 1995):

1. Single sleeper push test: A sleeper is detached from the rails pushed sideways by a machine attached to the rails and its load/deflection response is recorded (e.g. Selig and Waters (1994)).
2. The panel pull method: A section of in-service track is pulled sideways from the rail head and its load/deflection behaviour is recorded. From this the individual sleeper resistance can be estimated. It can be performed with the section either isolated (cut) or attached to the rest of the line (uncut) (e.g. Esveld (2001)).

Individual push tests show a wide variation in load resistance, meaning that many tests are necessary to characterise the resistance for a given sleeper/ballast arrangement. A test on an uncut panel gives data from which it is difficult to obtain a characteristic individual sleeper response as it is difficult to quantify the effect of the rails in spreading the load. The cut panel pull test allows an averaging of individual sleeper contributions.

Table 2-2 summarises the results of various lateral resistance tests accessed by ERRI. Lateral resistance is reported per sleeper, and is quoted for unloaded track (ERRI committee D202 report 2, 1995). Tests report the maximum or ***peak*** lateral resistance reached within a deflection of about 20 mm. However, the peak lateral resistance can be misleading. Lateral resistance at the sleeper/ballast interface varies with deflection as shown in Figure 2-14.

	Peak lateral resistance/sleeper (kN) within 20 mm deflection			
	Minimum	**20% less than**	**50% less than**	**Maximum**
Loose tamped/relay	4.2	5.2	5.9	6.9
Just tamped (undisturbed)	5.9	7.1	8.3	11.8
Trafficked	5.4	8.1	10.3	15.7

Table 2-2: Summary of lateral resistance data on unloaded track on concrete sleepers (ERRI committee D202 report 2, 1995)

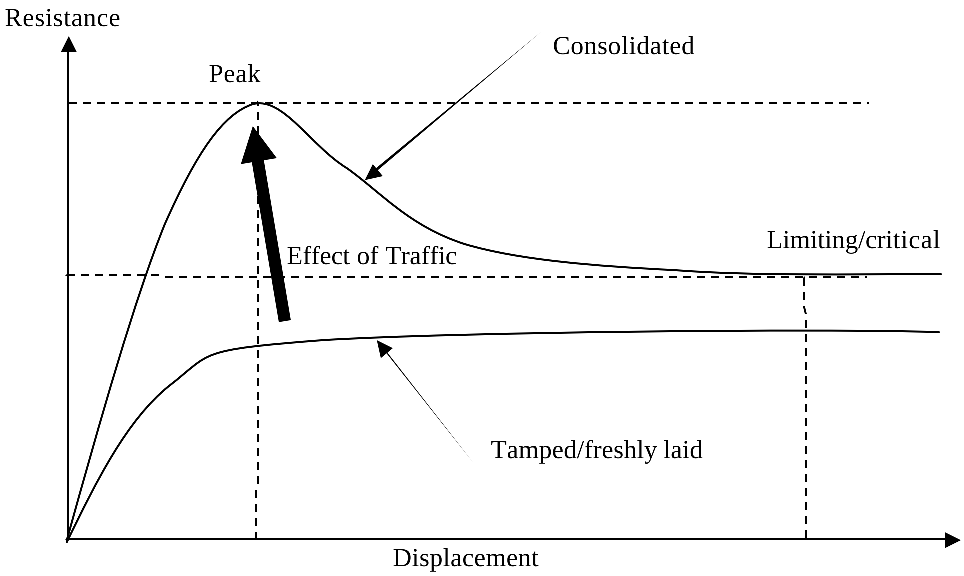

Figure 2-14: Characteristic sleeper lateral resistance/displacement response schematic not to scale (ERRI committee D202 report 3, 1995)

In Table 2-2 there is an almost fourfold increase in resistance from the worst to best case. This could be due to differences between test sites with different specifications and levels of fatigue of ballast and/or sleepers. Some of the variation may be due to differences between panel or single sleeper tests. ERRI committee D202 (1995) reported that the lateral resistance per sleeper was often less when testing a panel of sleepers; a result attributed to interaction between sleepers. It is also possible that some of the panel tests incorporated hanging sleepers. Without access to the original test data it is difficult to assess the quality of the results. However; Table 2-2 indicates that the consolidation of the ballast by tamping and trafficking has a large influence.

The data provided in Table 2-2 for static failure of the sleeper/ballast interface relates to large movements and is therefore more suited to evaluating resistance to buckling than performance characteristics during in-service loading. In this context the data can be interpreted in conjunction with other factors which influence the formation of rail buckles such as:

- Increased rail temperature
- Pre-existing track misalignment
- Vehicle passage

Vehicle passage is included because bow and precession waves (ERRI committee D202 report 3, 1995) provide a vertical lift to the track in front of and behind vertical loads (see Figure 2-4). The lifting force reduces the available frictional resistance at the sleeper base, meaning that lateral resistance from the crib and shoulder gain added significance in resisting buckling forces.

The values quoted in Table 2-2 are not able to describe the behaviour under pre-failure in service levels of loading, for which it is necessary to know the load/deflection response in the pre-failure region of likely train loading.

From this short study of available sleeper/ballast interface data, it is concluded that lateral sleeper/ballast behaviour tests are deficient in a number of factors. In particular it does not appear that in-service lateral response of the sleeper/ballast interface has been extensively investigated, while even static failure tests rarely report explicitly the:

- Type of sleeper
- Type of ballast
- Spacing of sleepers
- Presence of crib ballast
- Presence and size of shoulder ballast
- Quality of contact between sleeper and ballast.

This makes it difficult to assess the component of resistance from each of the three sleeper/ballast contact areas.

In terms of the base contact area, it would be more logical to report the behaviour in terms of a friction angle or a vertical to horizontal load ratio that would account for the effect of vertical load. In contrast, the resistance from the crib and shoulder contact areas should be substantially independent of vertical load.

This summary of available test data justifies the need for tests that:

1. Characterise the pre-failure load/deflection behaviour of the sleeper/ballast interface using loading that represents likely in-service situations
2. Evaluate the contributions from each of the three sleeper/ballast contact areas and make allowance for vertical load during static failure.

Further comparisons with tests in the literature will be made in Chapter 8, after the results from the tests carried out for this research are presented in Chapters 6, 7 and 8.

2.3.2. Design practice for the trackbed

British Rail developed a method of specifying an appropriate depth of ballast for the subgrade strength based on measurements of the reduction in pressure with increased ballast layer depth made in the 1970s (Shenton, 1975). The weaker the subgrade, the greater the depth of ballast needed. The method essentially treated the ballast as a continuum with uniform load transfer properties. In fact, the load transfer behaviour of ballast is highly dependent on its structure due to the large particle sizes in relation to typical sleeper footprint and ballast layer depth. The principles of this research survive in Network Rail codes of practice today that specify the depth of ballast layers below the sleeper for ***existing*** lines based on the undrained subgrade modulus and a parameter to describe the desired vertical stiffness of the track for different uses, where critical velocity (i.e. where the train speed approaches the speed of sound in the subgrade) is not likely to be a problem (Network Rail RT/CE/C/039, 2003). The parameter of stiffness used is known as the Dynamic sleeper support stiffness[2] (DSSS). The DSSS is different from the track modulus and is defined as:

- *The peak load divided by the peak deflection of the underside of a rail seat area of an unclipped sleeper subjected to an approximately sinusoidal pulse load at each rail seat; the pulse load being representative in magnitude and duration of the passage of a heavy axle load at high speed.*

The DSSS can be characterised by FWD tests, with stiffer track needed for higher speed trains.

---

2 In practice the definition of DSSS is interpreted in different ways. It appears that FWD test data are sometimes interpreted to determine the DSSS by taking the difference between the values of deflection at d0 and d1000 (below the load and 1000 mm away). The removal of the d1000 deflection may be intended to isolat e the deflection due to the ballast, i.e. it is considered the deflection due to the subgrade. Although this method contradicts the NR code of practice this is explained by considering the code as an advisory document rather than a standard. Furthermore it also appears that in this light the “advice” that the DSSS be greater than 100 kN/mm for track where trains run in excess of 100 mph is not enforced and, in practice, measured values are typically lower.

For ***new*** trackbed layers the depth of ballast is not specified. Instead a desired vertical DSSS is specified (Rail Safety and Standards Board GC/RT5014, 2003) and the factors that a justification for a design of trackbed must address are listed:

- distribution of loads on the subgrade
- prevention of overstressing of the subgrade
- prevention of premature deterioration of the ballast and track components
- provision of uniform, adequate sleeper support stiffness

This then permits the use of other methods to justify a trackbed design.

In addition to the vertical load deflection criterion (DSSS), track systems may be required to resist certain other forces. On the WCML, the track system was required to have performance characteristics capable of sustaining:

- A maximum static axle load of 250 kN
- A vertical dynamic force, generated by the static wheel load and the low frequency dynamic forces of 350 kN per wheel and an occasional isolated load of 500 kN per wheel
- A longitudinal force of 1200 kN per rail, to allow for train acceleration and braking, and for thermal forces within the rail
- A lateral force generated by the train of 100 kN over a length of 2 m

(Rail Safety and Standards Board GC/RT5021, 2003)

The occasional 500 kN vertical load is to account for wheel flats. The length of 2 m specified for the maximum lateral load of 100 kN can allow for hunting forces (developed as the train moves laterally relative to the rails) which have a short duration. A 2 m length can incorporate 3 sleepers but the track has the potential to spread the resistance to a 100 kN load over a greater distance depending on the lateral stiffness of the rails and pads and the ballast/sleeper response to loading.

The design process for new track changes the emphasis from meeting a coded specification (e.g. the old BR method) to meeting performance requirements such as vertical stiffness and ability to resist certain maximum loads. However, there remain aspects of the track design which are specified. In particular, minimum limits for the size of shoulder ballast on curves are given as shown in Table 2-3.

Type of track	Minimum width of shoulder measured at the top of the sleeper (m)	Minimum height of shoulder above top of sleeper (m)
CWR straight track and curved track over 2000m radius	0.375	0.125 in all cases
CWR curved track over 800m radius	0.450	
CWR curved track less than 800m radius	0.525	
Jointed track	0.300	level

Table 2-3: Minimum ballast shoulder dimensions (Rail Safety and Standards Board GC/RT5021, 2003)

Such specifications incorporate and build on the results of many tests carried out over many years, but it is difficult to determine how they were reached, or to understand why they differ from those in other countries. The American Railway Engineering Association (AREA) manual gives no specification for ballast above the level of the sleeper top face for shoulder ballast (AREA, 2003) but it does state that *"the condition of the ballast section and the amount of ballast at the ends of the ties is considered very important to the lateral stability of the track"*. The American approach seems to be to widen the shoulder ballast without any additional ballast height above the sleeper surface. This apparent inconsistency between the NR and AREA approaches raises questions about optimum shoulder profile for maximum benefit to the track.

Research carried out for the Association of American Railroads (AAR) in the late 1990s led to the publication of articles on railroad design (Li and Selig, 1998a) and (Li and Selig, 1998b). The method was used by Ove Arup for the design of the Channel Tunnel Rail Link (CTRL), and specifies a procedure for determining the granular layer thickness after consideration of (amongst other things):

- Axle load
- Train speed
- Annual tonnage
- Cumulative tonnage

- Resilient modulus.

Burrow et al. (2007a) compared design procedures by British Rail, UIC, NR and West Japan railways for the determination of granular layer thickness for the above criteria. They concluded that Li and Selig's method was the only one to consider each category. Although some differences between national design methods may be due to different prevalent geologies, these discrepancies imply that design methods have yet to be optimised internationally.

2.3.3. Acceptance of vehicles to run on the track

In the UK, Railway Group Standards require new rolling stock to meet acceptance criteria on track loading before being permitted to operate on the network. The process is easiest explained by taking the Pendolino as an example:

Prior to the arrival of the tilting train, standards had dealt with conventional, non-tilting trains, (British Railways Board GM/TT0088, 1993) (Safety and Standards Directorate Railtrack PLC GM/RT2141, 2000). However, tilting trains can curve at greater speeds and so new standards were developed to describe maximum operating speeds for the Pendolino (Railway Safety GC/RC5521, 2001). Having established standards for higher operating speeds (enhanced permissible speeds) it was then necessary to ensure that these greater speeds remained within previous standards for safe loading of the track. RGS's (British Railways Board GM/TT0088, 1993) state that a vehicle shall not subject the track to lateral forces greater than (W/3 + 10) kN where W is the axle load in kN. This simple relation is often termed the Prud'Homme limit, it was originally developed in the 1950s by the SNCF and it is intended to guarantee the lateral stability of the track (Esveld, 2001) (Prud'homme and Weber, 1973).

The Prud'Homme limit for car 6 of a Pendolino is:

- Axle 1 56.95kN
- Axle 2 56.84kN
- Axle 3 57.33kN
- Axle 4 57.74kN

(Dyson, 2005)

To meet the loading acceptance requirements, testing, both by computer simulation and practically was undertaken to quantify the likely lateral load from a Pendolino. Dyson (2005) and (2006) gives the key results and conclusions from these tests which were as follows:

Vampire simulations of Pendolino passes were prepared using measured track data. Certain features of track misalignment were found to cause high lateral loads, but in all cases the train (just) met derailment and overturning criteria in Vampire simulations on track of lower specification to that intended to be experienced by a Pendolino on the WCML.

In real track testing, strain gauge measurements from the rail were taken for a Pendolino traveling at 125 mph on 150 mm canted track operating at a 265 mm cant deficiency (approx.) on curves with radius of the order of 1200 metres. (Dyson, 2006).

This test gave:

- 30 kN on the outward rail
- 10 kN on the inward rail

These values are the peaks for the test run and do not occur simultaneously.

A centrifugal/centripetal force calculation (mv^2/r) resolved into the sleeper plane for 150 mm of cant gives a 39 kN load outward for a 15 tonne axle; the cant means that there is also a 15 kN resolved weight acting inward. The resultant force anticipated on the sleeper is therefore 24 kN. The difference between the calculated 24 kN and the 30 kN measured is probably due to dynamic loads.

Further test runs in which wheelsets were instrumented and readings taken while the train was travelling at 125 mph and a 265 mm cant deficiency (10°) gave a peak 2 m sustained force of around 43 kN. This value probably incorporates some misalignment of the track at a particular location, resulting in dynamic contributions to the overall lateral load.

These tests did not take account of wind loading, and it can be considered that wind loading was minimal in these tests. Wind loading is accounted for in other standards

(Railway Safety GC/RC5521, 2001), where considerations of local topography can be used to apply speed restrictions when the wind speed reaches certain values.

2.4. Summary of Chapter 2

In Chapter 2, different aspects of the track system that models may need to incorporate have been considered, and it has been shown that different track models use different methods depending on the desired outputs. Furthermore, the most widely used track system models make simplifications to the behaviour at the sleeper/ballast interface which may either ignore lateral behaviour or use linear elastic simplifications, and do not consider the three contact areas (base, shoulder and crib) separately.

It has been shown that actual testing of the sleeper/ballast interface has generally not considered pre-failure lateral behaviour and that lateral static failure tests do not share a common framework for reporting the results.

Design of the trackbed does not explicitly consider lateral and moment loading, but design loading from vehicles assumes that the track will provide adequate support for lateral loads from vehicles and moments up to rollover of vehicles.

We have also seen how a relatively simple model (BOEF) can be used to estimate the proportion of vertical load reaching the sleeper. In Chapter 3 this model will be extended and used to evaluate the lateral load passing to the sleeper.

3. An exploration of track loading

In this chapter we will calculate loads from a Pendolino train curving at high speed in line with the first objective set out at the end of Chapter 1; i.e. to

- Quantify likely magnitudes of Pendolino train loading for normal and extreme conditions by summing the effects of curving forces, wind load and static axle loads on low radius curves of the WCML.

The Chapter begins with a section to describe train loading and track behaviour on a curve. Following this background, the Chapter is divided into three main sections; each focusing on a particular aspect of train/track loading:

1. Maximum load on the rails due to wind and curving forces for level and 150 mm canted track.
2. Normal[3] loads likely to reach a sleeper.
3. Lateral loads likely to reach a sleeper.

It will be shown that loading at the wheel/rail interface can be transferred to individual sleeper loading using a BOEF analogy adapted to both vertical and lateral representations of the track. In doing so, key features of the interaction between the relative normal and lateral stiffness of the track system will be highlighted.

No account will be taken of dynamic load in this report, although if needed dynamic loads can be taken into account for track and trackbed design by relating the train speed, and measures of track and train quality (including wheel diameter and trackbed stiffness) to dynamic amplification factors. For example, using typical north American track and train data and the relations set out in Raymond (1978) a dynamic amplification factor for the load on sleepers of about 1.25 for a train travelling at 125

[3] On horizontal track the vertical and normal planes coincide. However, because track is sometimes canted the direction perpendicular to the plane of the track is not always vertical. Thus the term “normal” will be used to apply to the (axis) perpendicular to the track. The term “lateral” will always describe the direction across the track whether horizontal or canted.

mph is obtained. More detailed consideration of dynamic effects can be found in Esveld (2001).

The methods presented and the loads calculated in this Chapter will be used to inform the laboratory testing methods detailed in Chapter 4 and to evaluate laboratory test results and geophone monitoring data in Chapters 5, 6, 7, and 8.

3.1. Background: Description of train loading and track behaviour on a curve

The transfer of load through the track system and how far the load spreads away from an axle along the rails and into adjacent sleepers is related to the global track system stiffness and the relative contributions of the component parts (rails, pads, sleepers, trackbed) along the normal and lateral axes of the track

Vertically, if the trackbed support stiffness (track modulus) is increased while the track superstructure stiffness remains constant a greater proportion of axle load is transferred into a sleeper immediately beneath an axle, as can be seen in Figure 2-7.

The potential for lateral resistance of the sleeper/ballast interface is due mainly to the normal force at the sleeper/ballast base contact area. The normal force at the sleeper/ballast base contact area relative to the position of a wheel load on a rail is determined by the vertical stiffness of the track system, including contributions from the rails (***xx*** axis), pads, sleepers, ballast and subgrade. The potential for lateral resistance is therefore largely governed by the vertical stiffness of the track. In contrast to this the lateral applied force is determined by the lateral stiffness of the track, including contributions from the rails (***yy*** axis), fastenings (rotations), and sleeper/ballast base contact. This means that, if the track superstructure stiffness remains constant, a worst case scenario for lateral track loading occurs when low normal trackbed stiffness combines with high lateral trackbed stiffness. The implications of this are explored in this Chapter.

To estimate the load transferred to individual sleepers immediately below and adjacent to axles the BOEF model (detailed in Chapter 2) can be used provided the necessary track component stiffnesses are known. The stiffness of the track superstructure components can be calculated from manufacturer's information and Standards. To estimate the trackbed stiffness (track modulus) knowledge of the range of normal and lateral sleeper movement can be used to back calculate appropriate ranges of track modulus

Figure 3-1 shows data of sleeper displacements on the WCML as a Pendolino train passes travelling at 110 mph around a 1230 m radius curve on 150 mm canted track. A more detailed explanation of how these data were obtained together with more comprehensive results is presented in Chapters 5 and 7. In Figure 3-1, nine carriages comprising 36 axles pass; these can be identified in the peaks and troughs of the deflection/time plots. The data show the range of vertical deflections at each end of the sleeper and laterally. The deflections are about a zero millimetre average due to the way in which geophones work. Also because of the way in which the geophone data are processed it is common practice to neglect the first and final bogie sets in evaluating track movement (Bowness et al., 2007). From Figure 3-1 it can be seen that as a Pendolino curves the outer (high) end of the sleeper deflects vertically over a range of about 0.8 mm, while the inner sleeper (low) end only deflects over a range of about 0.3 mm. This difference is due to curving forces exerting a moment on the sleeper. The lateral deflection is shown on the right-hand scale of Figure 3-1; this is over a range of approximately 0.5 mm. It is useful to keep these values in mind throughout Chapter 3 as a comparison to the deflection ranges in the calculations presented.

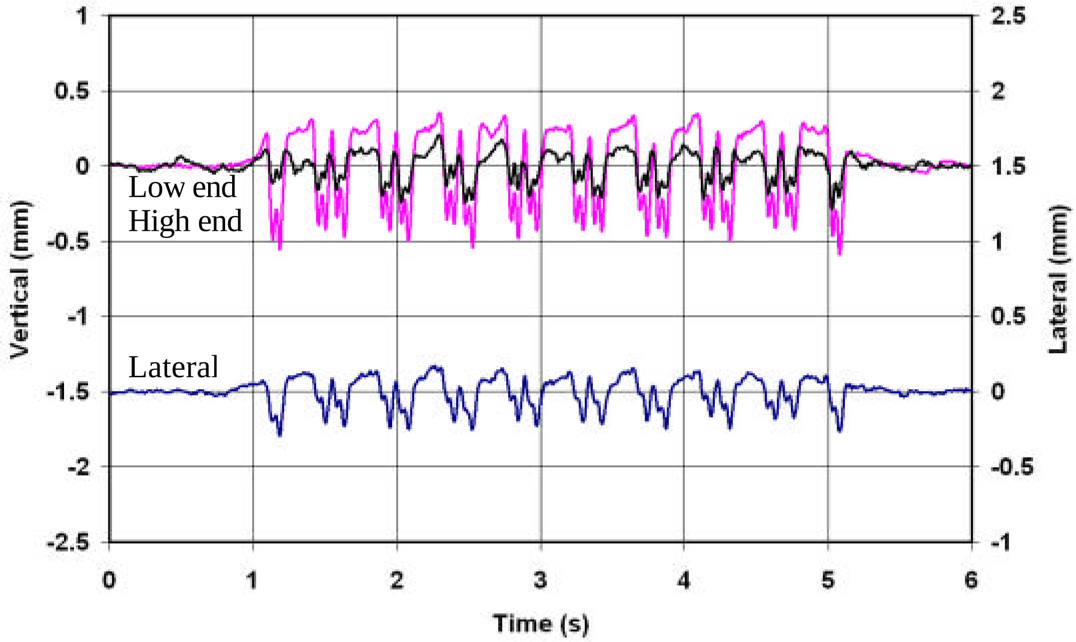

Figure 3-1: Deflection/time graph for passage of a Pendolino train curving at 110 mph on a 1230 m radius curve with 150 mm cant at Weedon, Northampton, February 2007

3.2. Maximum load on the rails due to wind and curving forces

The maximum moment that a train may impart to the track occurs at rollover. On level track this is reached when the moment is such that all the vertical force passes through the outer rail, i.e. the moment is half the rail spacing multiplied by ***mg***. For this to happen a lateral load of sufficient magnitude and lever arm is required. If this force is due to curving the lever arm passes through the centre of gravity of the vehicle. However, it is more likely to occur due to a combination of curving and wind forces. Wind forces have a different lever arm, corresponding to the centre of pressure on the vehicle.

On canted track the cant acts to increase the rollover moment and to calculate the rollover moment it is necessary to know the location of the centre of gravity of the train. For a Pendolino train the rollover angle on level track is known to be 24.4° (Harwood, 2005), which (as shown later in Figure 3-4) may be used to calculate the centre of gravity of the train.

In the following subsection the objective is to calculate wind loading and curving force in a severe scenario for a Pendolino train, and compare these loads to the maximum rollover resistance. The calculation will be carried out for both level and canted track. In carrying out these calculations it will be shown that rollover is a real possibility given moderately severe wind conditions.

3.2.1. Wind Loading

The force on a body moving through a fluid is a function of the size, shape and orientation of the body and the density, viscosity and elasticity of the fluid. The elasticity is also related to the fluid density and speed of sound through the fluid. Kuethe and Chow (1998) provide a more comprehensive explanation of such loading.

$$F = f(r, V, l, m, a)$$ **Equation 3-1**

Where:

F=	Force on body moving through fluid medium
r =	density of fluid
V =	relative velocity
l =	characteristic length dimension of body
m =	viscosity of fluid
a =	speed of sound in fluid

If it is assumed that a and m have no influence on the force F it can be shown that:

$$F = 0.5 C_F r V^2 l^2$$ **Equation 3-2**

Where C_F is a dimensionless constant (note: 0.5 is sometimes included within C_F).

For a particular body the parameters of size, shape and orientation can be simplified into a global characteristic dimension. It is possible to assign a characteristic dimension to a body by means of wind tunnel tests. In the case of a Pendolino train the characteristic dimension squared (l^2) has been found to be 78.7 m^2 for the lead vehicle (Baker et al., 2003). The Pendolino's trailing cars have not been tested, but it is reasonable to take the value of a Mark 3 vehicle, for which extensive data exist, as 75.9 m^2, (Baker et al., 2003).

Equation 3-2 is further split into three versions which account for side force (***S***), uplift force (***L***) (caused by the low pressure above the train), and moment (***R***) as shown in Figure 3-2. In the last case the equation includes a reference height ***h*** (thus maintaining consistency of units), which for a Mark 3 vehicle is 3.36 m.

$$S = 0.5 C_S r V^2 l^2$$ **Equation 3-3**

$$L = 0.5 C_L r V^2 l^2$$ **Equation 3-4**

$$R = 0.5 C_R r V^2 l^2 h$$ **Equation 3-5**

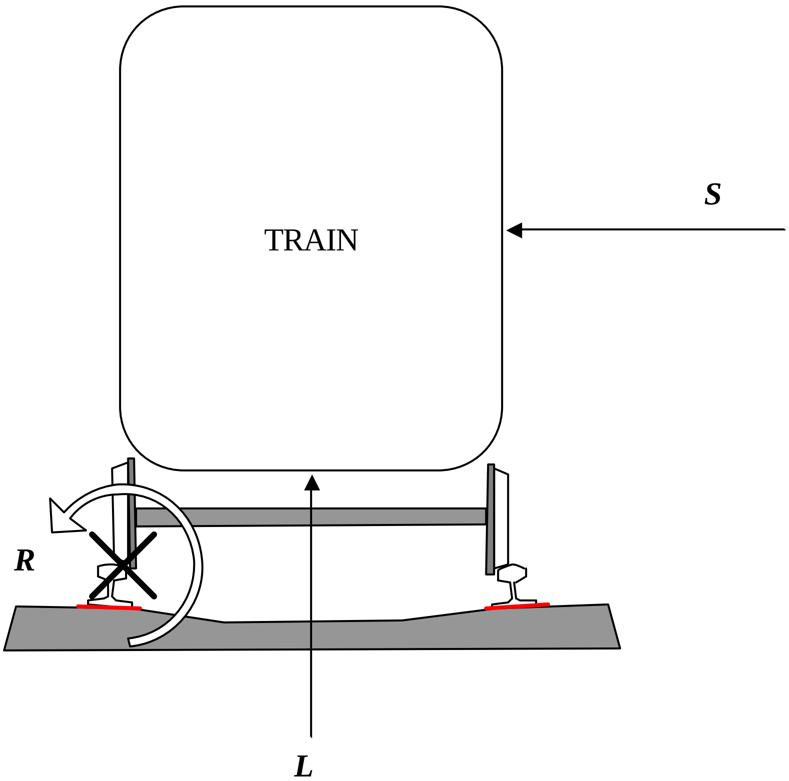

Figure 3-2: Force diagram for wind load equations

The coefficients, $\boldsymbol{C_S}$, $\boldsymbol{C_L}$, and $\boldsymbol{C_R}$ are a function of the yaw angle (y) defined in Figure 3-3. Full scale tests have been conducted to produce charts relating the yaw angle to each of the three coefficients based on the Mark 3 as a reference vehicle (Baker et al., 2004).

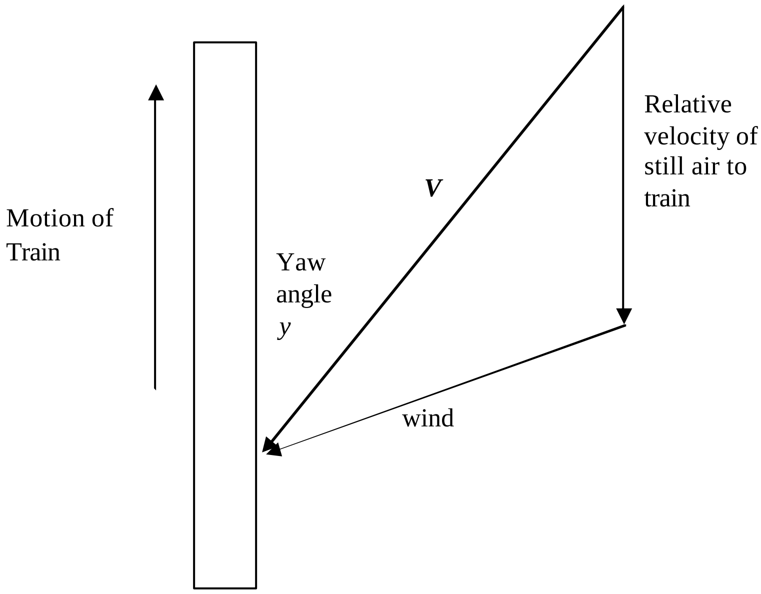

Figure 3-3: Yaw angle

Although the wind imparts all of its force laterally when the wind direction is side on to the train, this will not provide the greatest force unless the train is stationary. The force is increased if account is taken of the relative motion of the train, and the worst case depends on the wind and train speed and their relative orientation.

Complications also arise when a train is on a curve. In this case each vehicle may be at a different yaw angle. However, Railway Group Standards apply reduced values for permissible limiting design cant deficiency for trains operating on curved track less than 700 m in radius (i.e. the maximum speeds are reduced). The standard (Rail Safety and Standards Board GC/RT5021, 2003) states that the exceptional limiting design values for cant deficiency at enhanced permissible speed shall be:

- 150 mm for curves under 400 m radius (5.7°)
- 225 mm for curve radii less than 700 m but greater than or equal to 400 m (8.5°)
- 300 mm for curve radii greater than or equal to 700 m. (11.3°)

This means that the maximum overturning forces due to trains curving occur on curves greater than 700 m in radius where trains are capable of reaching speeds that mobilise the full operating cant deficiency. Therefore this research does not consider curves less than 700 m in radius and, for curves greater than 700 m in radius, differences in orientation of the vehicles may be neglected due to the large radii compared to train length.

It is difficult to quantify a likely maximum wind speed and hence resultant wind speed (***V***). Railway group standards set out calculations to find maximum permissible speeds based on probabilities of winds and train speeds with topographical features combining to create an overturning moment greater than an acceptable level of risk (Railway Safety GC/RC5521, 2001). Within these standards a contour map of the UK indicates that the maximum mean hourly wind speed with a 50 year return along the WCML route ranges from 20 to 24 m/s. The standard sets out a methodology to find a 3 second gust wind speed using the mean hourly wind speed with a 50 year return and applying speed up factors for specific conditions of exposure. The 3 second gust wind speed is then used along with considerations of the risk of overspeeding, deviation from design cant and curvature of the track, and the minimum rollover resistance angle for the train to decide on an appropriate allowable operating cant deficiency for an acceptable level of risk. The calculation of the 3 second gust is complex and site specific. However, it will be shown that relatively low wind speeds are sufficient to put high speed trains on low radius curves at risk of overturning.

To carry out the calculation the following assumptions are made:

- The coefficients C_S , C_L and C_R have been calculated by applying the approximate relations inferred from design charts (Baker et al., 2004) shown in Equation 3-6, Equation 3-7 and Equation 3-8 below. These relations are approximately true for yaw angles in the ranges calculated and are considered adequate for estimating the maximum wind load.

$$C_S = \frac{0.4y}{30}$$ **Equation 3-6**

$$C_L = \frac{0.08y}{20}$$ **Equation 3-7**

$$C_R = \frac{0.6y}{60}$$ **Equation 3-8**

- The density of air is approximately 1.22 kg/m^3, and the characteristic dimension squared (l^2) for a Pendolino lead car is 78.7 m^2.

- The wind speed is assumed to be 24 m/s the highest mean hourly wind speed in the UK with a 50 year return.
- The train is at a speed of 56 m/s (125 mph) on a 1045 m radius curve. Such a train speed on a 150 mm canted curve corresponds to the maximum design service cant deficiency of 11.3° for a tilting train (Railway Safety GC/RC5521, 2001). The reason for choosing these magnitudes of speed and radius are explained more fully later in the Chapter.

The calculation relies on trialling different wind angles to find the critical case. In Table 3-1, Table 3-2, and Table 3-3 the results are shown for a narrow range of wind angles near to the critical.

Wind angle from train	**Wind speed**		**Resultant relative wind towards train**	**Overall Resultant wind *V***	**Yaw *y***	**Side Force coeff from graph C_S (Baker et al., 2004)**	**$0.5 r V^2 l^2$**	**Side Force *S***
	Toward train	**Side onto train**						
°	m/s	m/s	m/s	m/s	°	C_S	kN	kN
60	12.00	20.78	68.00	71.11	17.00	0.23	242.72	55.00
70	8.21	22.55	64.21	68.05	19.35	0.26	222.34	57.37
80	4.17	23.64	60.17	64.64	21.45	0.29	200.61	57.36

Table 3-1: Side force calculation for wind speed of 24 m/s and Pendolino train speed at 56 m/s

Wind angle from train	**Wind speed (m/s)**		**Resultant relative wind towards train**	**Overall Resultant wind *V***	**Yaw *y***	**Uplift Force coeff from graph C_S (Baker et al., 2004)**	**$0.5 r V^2 l^2$**	**Uplift Force *L***
	Toward train	**Side onto train**						
°	m/s	m/s	m/s	m/s	°	C_L	kN	kN
60	12.00	20.78	68.00	71.11	17.00	0.07	242.72	16.50
70	8.21	22.55	64.21	68.05	19.35	0.08	222.34	17.21
80	4.17	23.64	60.17	64.64	21.45	0.09	200.61	17.21

Table 3-2: Uplift force calculation for wind speed of 24 m/s and Pendolino train speed at 56 m/s

Wind angle from train	**Wind speed (m/s)**		**Resultant relative wind towards train**	**Overall Resultant wind *V***	**Yaw *y***	**Rolling Moment coeff from graph C_R (Baker et al., 2004)**	**$0.5 r V^2 l^2$ *h***	**Rollover moment *R***
	Toward train	**Side onto train**						
°	m/s	m/s	m/s	m/s	°	C_R	kN	kNm
60	12.00	20.78	68.00	71.11	17.00	0.17	815.55	138.61
70	8.21	22.55	64.21	68.05	19.35	0.19	747.05	144.58
80	4.17	23.64	60.17	64.64	21.45	0.21	674.05	144.56

Table 3-3: Rolling moment calculation for wind speed of 24 m/s and Pendolino train speed at 56 m/s

If the calculation of rollover *R*, shown in Table 3-3, has been carried out correctly it should agree with the moment load that would be generated by applying the lateral and uplift loads from Table 3-1 and Table 3-2. Therefore by taking moments about the lee rail (Figure 3-2) it is possible to check for consistency within the calculation. However, it is not known where the lateral wind load has been applied. The lever arm will therefore be adjusted so that the rollover moment is in agreement with that found in Table 3-3 and the solution considered for practicality.

Description	Force (kN)	Lever arm (m)	Moment (kNm)	Notes
Side	57.4	2.3 (adjusted)	132	The lever arm has been fixed to give the right answer
Uplift	17.2	0.75	13	Assume rail contacts 1.5 m apart and neglect cant
Total			145	Same as Table 3-3 to nearest kN

Table 3-4: Check on calculation

Therefore a lever arm for the side force of 2.3 m satisfies the calculation. Such a lever arm is within the bounds of possibility being lower than the reference height h (3.36 m) but above the midpoint (3.36/2 = 1.68).

3.2.2. Curving forces

Over the length of the train the maximum lateral curving force generated can be found using the relation:

$$F = \frac{mv^2}{R} \qquad \textbf{Equation 3-9}$$

Where $\boldsymbol{R}$ is the radius of curve, $\boldsymbol{m}$ is the mass of the train and $\boldsymbol{v}$ is the velocity. The curving force can then be divided equally between each axle.

The worst case values of train speed and curve radius are determined from the maximum permitted operating cant deficiency of the Pendolino.

It can be shown that the angle of operating cant deficiency ($\boldsymbol{D_{degrees}}$) can be found from:

$$D_{degrees} = \tan^{-1}\left[\frac{mv^2 / R}{mg}\right] - a$$ **Equation 3-10**

Or

$$D_{degrees} = \tan^{-1}\frac{v^2}{Rg} - a$$ **Equation 3-11**

Where:

***R*=**	Radius of curve
a =	Angle of cant
v **=**	Speed of train

By adjusting the speed of the train and radius of the curve it is possible to manipulate Equation 3-11 to obtain the maximum operating cant deficiency (300 mm or 11.3°) on 150 mm canted track (5.7°). If this is done using the maximum permitted speed of the train (125 mph or 56 m/s) a curve of radius 1045 m is required. Hence this justifies the train speed used to calculate wind loading and these values will also be used to calculate curving force and rollover moment presented in the next section.

3.2.3. Calculation of rollover forces on a car due to wind and curving forces

Harwood (2005) provided data on axle mass for the Pendolino train:

	Axle mass (mass at wheel/rail interface)		
	Minimum (kg)	**Average (kg)**	**Maximum (kg)**
Tare	11,521	12,944	14,919
180% Passenger load	14,122	14793	15,306
240% Passenger load	14,083	15,112	16,060

Table 3-5: Pendolino axle loads (Harwood, 2005)

It is not clear how these totals were calculated and obtaining further clarification has not been possible. There is a significant variation in axle mass ranging from 11,521 kg to 16,060 kg. The risk of rollover due to wind loading is greater for lighter cars when the centre of gravity of the vehicle remains the same, however; greater absolute magnitudes of lateral train loading due to curving forces occur for heavier cars.

For the lightest car the rollover resistance on level track is 339 kNm this is found by multiplying axle mass by the number of axles on a car, by gravity and half the width between rail centres ($11521 \times 4 \times 9.81 \times 0.5 \times 1.5$). Similarly the rollover resistance for the heaviest car is 473 kNm. On canted track the rollover moment increases because increasing cant increases the horizontal distance from the centre of gravity to the high rail. In this case the lever arm for rollover resistance can be shown to be:

$$\left[\frac{d}{2} + H_g \tan a\right]\cos a \qquad \textbf{Equation 3-12}$$

Or

$$0.5d\cos a + H_g \sin a \qquad \textbf{Equation 3-13}$$

Where:

***H_g*=**	Vertical height to centre of gravity on level track
a =	angle of cant (e.g. $\tan^{-1}150/1500$)
d =	Distance between centres of wheel/rail contact points (e.g 1500 mm)

The height of the centre of gravity of the vehicle measured vertically from the high (outer) rail head is also altered by cant and this dimension is required to apply the centrifugal force at the appropriate level. This can be found from:

$$H_g \cos a - 0.5d\sin a \qquad \textbf{Equation 3-14}$$

Alsthom (Harwood, 2005), indicated the normal distance above the railheads of the centre of gravity (***H_g***) of a Pendolino carriage varied:

- at tare the range is 1.621-1.811 m and
- at 180% passenger tare this can rise marginally to1.651-1.811 m.

It is also possible to back-calculate the centre of gravity from the rollover angle of 24.4° also supplied by Alsthom (Harwood, 2005). This is done geometrically by drawing a line at 24.4° from the railhead through the the train and then drawing a line vertically through the centre of the train (Figure 3-4). The centre of gravity is where these two lines intersect and is found to be at 1.65 m vertically on horizontal track from the wheel to rail contact.

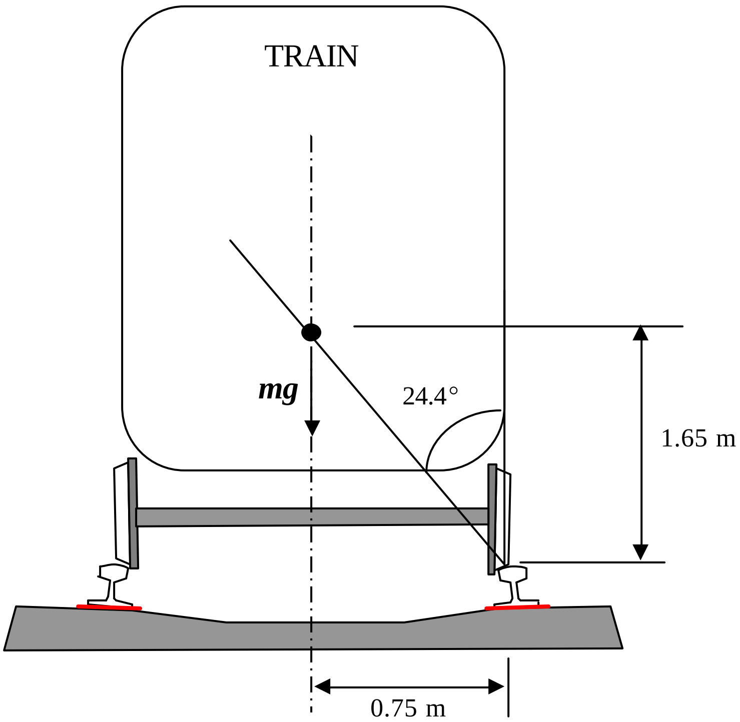

Figure 3-4: Back estimate of centre of gravity

Taking a centre of gravity at 1.65 m above the wheel/rail contact the force diagram on horizontal track is shown in Figure 3-5.

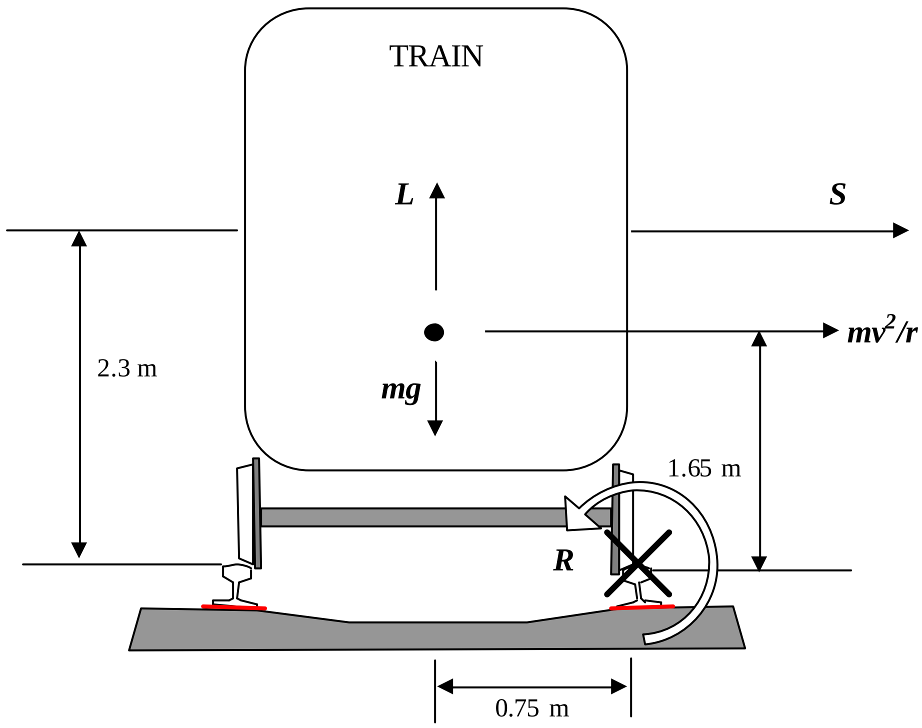

Figure 3-5: Force diagram of curving and wind forces on horizontal track

Taking moments about the lee (outside curve) rail contact:

Description	Force (kN)	Lever arm (m)	Moment kNm	Notes
Centripetal (mv2/r)	138	1.65	228	1045 m radius curve at 125 mph
Side force from wind (S)	57	2.3	131	Table 3-4
Self weight (mg)	-452	0.75	-339	4× axle load
Uplift from wind (L)	17	0.75	13	Table 3-4
Total overturning			372	
Total resisting			-339	
Overall Moment			33	+ive: failed
Ratio of Moments			0.91	<1 failed

Table 3-6: Results of wind loading and curving force calculation for the lightest single vehicle on horizontal track

Description	Force (kN)	Lever arm (m)	Moment kNm	Notes
Centripetal (mv2/r)	193	1.65	318	1045 m radius curve at 125mph
Side force from wind (S)	57	2.3	131	Table 3-4
Self weight (mg)	-630	0.75	-473	4× axle load
Uplift from wind (L)	17	0.75	13	Table 3-4
Total overturning			462	
Total resisting			-473	
Overall Moment			-11	+ive: failed
Ratio of Moments			1.02	<1 failed

Table 3-7: Results of wind loading and curving force calculation for the heaviest single vehicle on horizontal track

Table 3-6 and Table 3-7 show that, for the case of the lightest vehicle, the overturning resultant moment is significantly greater than the resisting moment; whereas the heaviest vehicle is marginally safe against overturning. However, it would only take a small increase in the wind speed, or marginal deviation from design cant and radius to overturn the heaviest vehicle.

The calculation has been for horizontal track, it can also be applied to canted track as shown in Figure 3-6. Note that Figure 3-6 exaggerates the cant, which at 5.7° is much less noticeable.

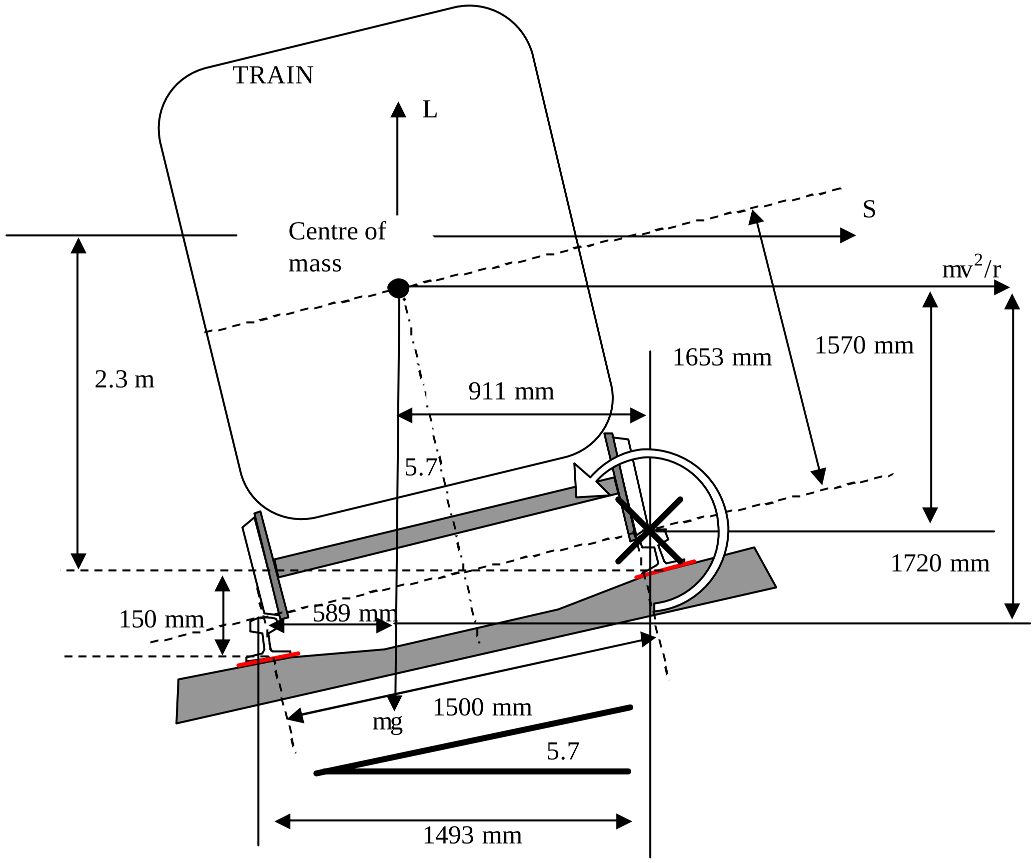

Figure 3-6: Force diagram of curving and wind forces on 150 mm canted track

Description	Force (kN)	Lever arm (m)	Moment kNm	Notes
Centripetal (mv2/r)	138	1.57	217	1045 m radius curve at 125mph
Side force from wind (S)	57	2.3	131	Table 3-4
Self weight (mg)	-452	0.91	-411	4× axle load
Uplift from wind (L)	17	0.91	15	Table 3-4
Total overturning			364	
Total resisting			-411	
Overall Moment			-48	+ive: failed
Ratio of Moments			1.13	<1 failed

Table 3-8: Results of wind loading and curving force calculation for the lightest single vehicle on 150 mm canted track

Description	Force (kN)	Lever arm (m)	Moment kNm	Notes
Centripetal (mv2/r)	193	1.57	303	1045 m radius curve at 125mph
Side force from wind (S)	57	2.3	131	Table 3-4
Self weight (mg)	-630	0.91	-573	4× axle load
Uplift from wind (L)	17	0.91	15	Table 3-4
Total overturning			449	
Total resisting			-573	
Overall Moment			-124	+ive: failed
Ratio of Moments			1.28	<1 failed

Table 3-9: Results of wind loading and curving force calculation for the heaviest single vehicle on 150 mm canted track

Table 3-8 and Table 3-9 show the important role the cant plays in ensuring the train remains on the track, in particular due to the large increase in resisting moment that results from increasing the lever arm for the axle weight from 0.75 m on horizontal track to 0.91 m on canted track.

3.3. Normal loads likely to reach a sleeper

Having established that it is possible for loading to reach extreme levels which place the trains at risk of overturning provided the track remains structurally sound, attention is now turned to evaluating the proportions of load that are likely to be transferred to the sleepers. In this section the normal load on the sleepers is considered, while the following section will consider the lateral load on the sleepers. By calculating appropriate ranges of sleeper loading it will then be possible to test the sleeper/ballast interface using the laboratory apparatus described in Chapter 4 to demonstrate the ability of the interface to cope with both likely in-service and extreme levels of loading.

In Chapter 2 the BOEF model for track support was outlined. It is possible to use this model to determine the normal load on a sleeper due to the axle load on the rails above, provided the track modulus is known. Unfortunately evaluating the track modulus is problematic particularly as it is not normally used to describe track properties within Network Rail. Instead NR company codes of practice (Network Rail RT/CE/C/039, 2003) specify that new track for trains running in excess of 100 mph should have a DSSS above 100 kN/mm per sleeper support end.

Network Rail standards (Network Rail RT/CE/C/039, 2003) specify a method of measuring the DSSS using a FWD. In summary: a sleeper is unclipped from the rails and a load pulse representing a mass of 12.5 tonnes is applied to the sleeper and the deflection recorded. A seating load, to ensure the sleeper is in contact with the ballast across its base, may also be present. This effectively assumes that the maximum axle mass is 25 tonnes and the rails spread 50% sleepers on either side. For a DSSS in excess of 100 kN/mm per sleeper end the deflection resulting from a 12.5 tonne mass on an unclipped sleeper end should be less than $(6.25 \times 9.81)/100 = 0.62$ mm. (Note that the deflection is calculated for the load due to a 6.25 tonne mass, half of the 12.5 tonnes in the test as the sleeper stiffness is per sleeper end).

The DSSS is evaluated for unclipped sleepers, whereas the track modulus incorporates a measure of the ability of the rails to spread the force over a deflection basin. With an unclipped sleeper this spreading of the load into a deflection basin does not occur.

Despite these difficulties, it is possible to estimate the track modulus corresponding to a DSSS of 100 kN/mm per sleeper end. In Chapter 2 it was shown that the sleeper deflection could be plotted in relation to the track modulus for a specific axle load. If this is now done for a load from a 25 tonne axle (12.5 tonnes per wheel), Figure 3-7 shows the deflection for different track moduli. Reading from Figure 3-7 the track modulus for a deflection of 0.62 mm is then ~160 N/mm/mm. In fact this method of back calculation is imperfect because such a track modulus would transmit about 52% (not 50%) of the axle load through to the sleeper immediately below the axle load (Figure 2-7); however this is sufficiently close. Furthermore, no allowance for the deflection due to the railpad has been made, which would increase the deflection at the rail (by about 0.18 mm, Pandrol, (2003)) compared to that at the sleeper and lead to a reduced overall track modulus and larger deflection from a BOEF calculation with the trackbed and railpad stiffness lumped together.

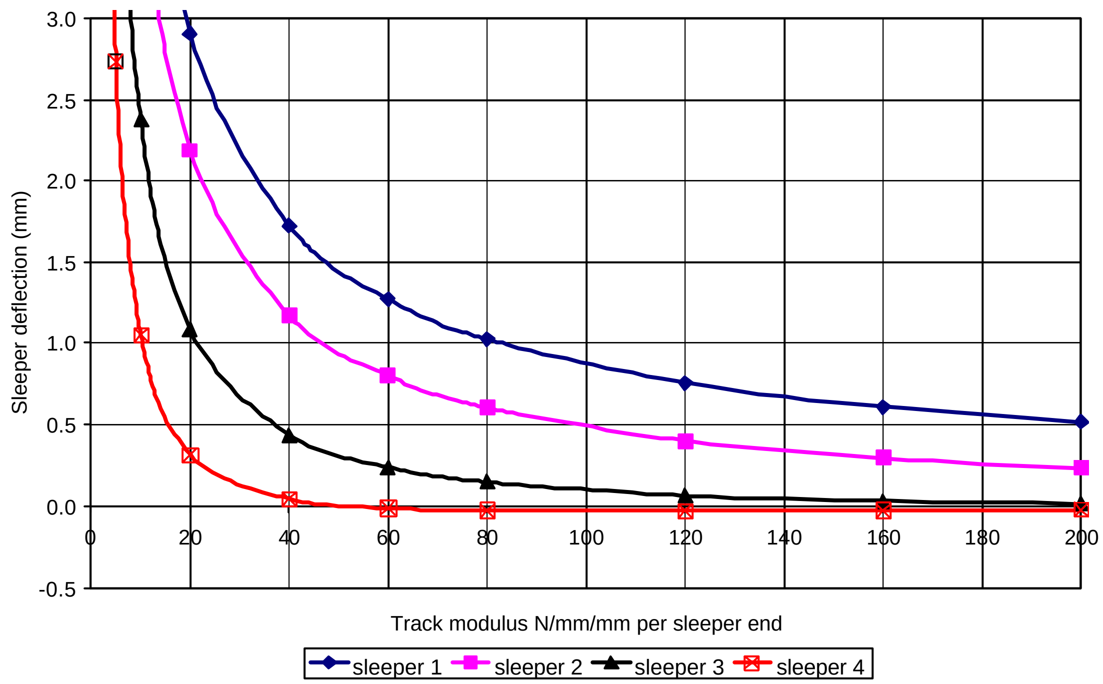

Figure 3-7: Track modulus and sleeper deflection for a 25 tonne axle load

For a given value of track modulus normal loads on an individual sleeper can be estimated. In practice measurement of sleeper deflections on the WCML during Pendolino train passage (Chapter 5 and 7) has shown a range in measured deflections. The vertical load is unlikely to vary as much as the measured deflection, so this implies a large variation of track modulus between sleepers. It is therefore important to evaluate the effect of a varying track modulus on the proportions of load reaching sleepers.

The effect of increasing the track modulus on the proportion of vertical load reaching sleepers when an axle is placed immediately above a sleeper on horizontal track is shown as a bar chart in Figure 3-8 for certain values of track modulus. Note that for a given track modulus the total proportion of load reaching the sleepers must add to 100%. When adding the proportion of load on sleeper one to 2× the proportion of load on sleepers two to six in Figure 3-8 it may appear that more than 100% of load is being transferred. However, the BOEF model spreads small proportions of load along into sleepers beyond sleeper six and these small, often negative (uplift), proportions of load ensure the summed proportions of load add to 100% in each case.

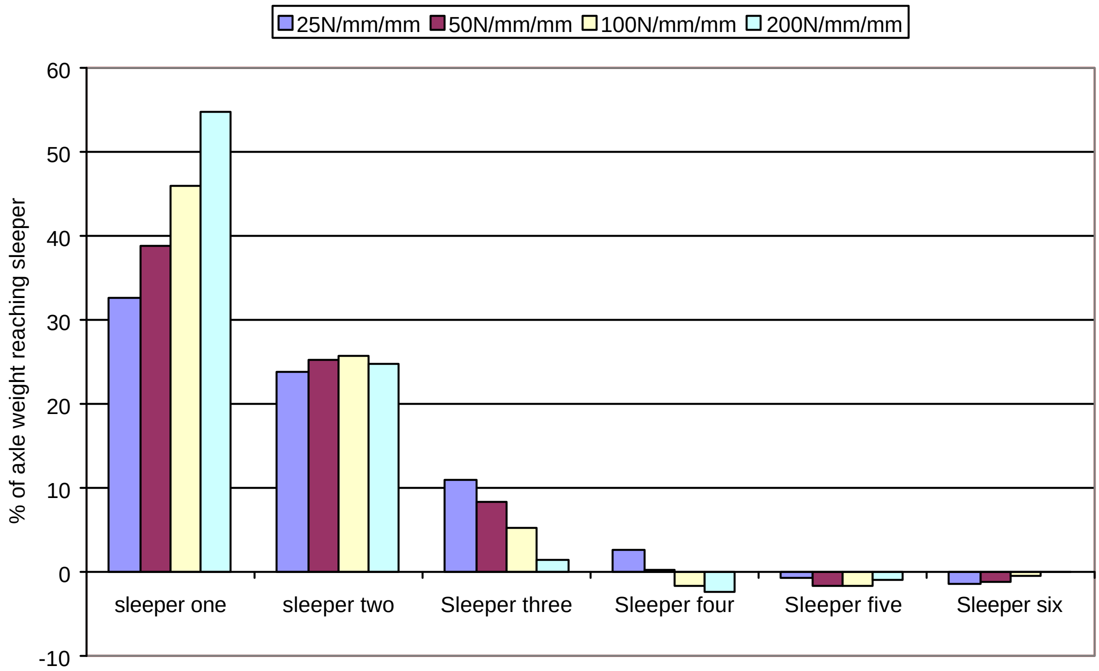

Figure 3-8: Sleeper/ballast vertical load due to Pendolino load on horizontal track

Figure 3-8 shows that, although the track modulus has increased eightfold, the proportion of axle load reaching sleeper one, immediately below the axles, is relatively insensitive to this and shows a much less marked increase from 33% to 55% of axle load.

So far only one axle has been considered but other axles also exert influence. These effects can be summed to find the peak vertical load. The BOEF model can be evaluated from a reference axle as shown in Figure 3-9.

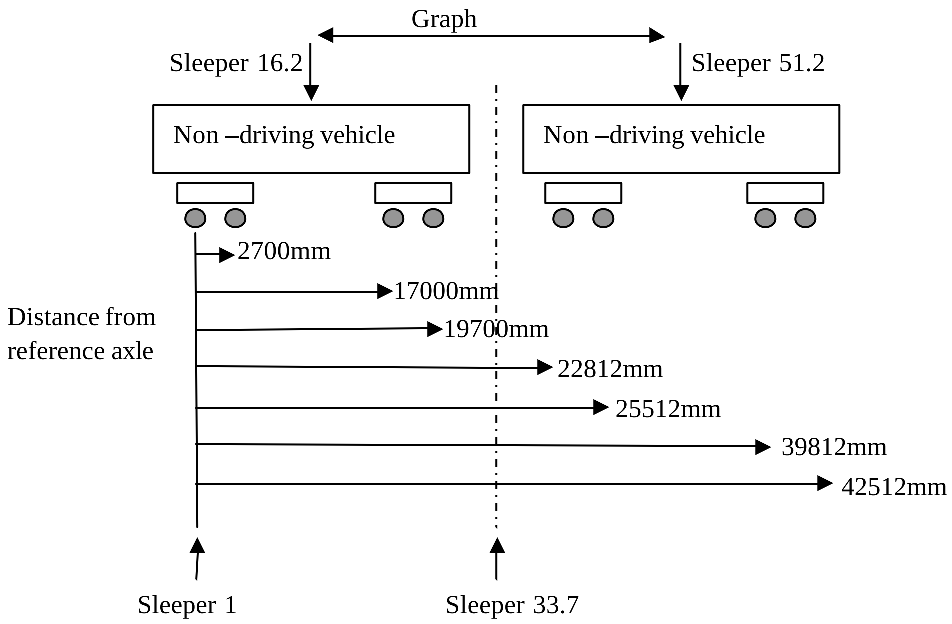

Figure 3-9: Axle layout for non-driving vehicles on a Pendolino train

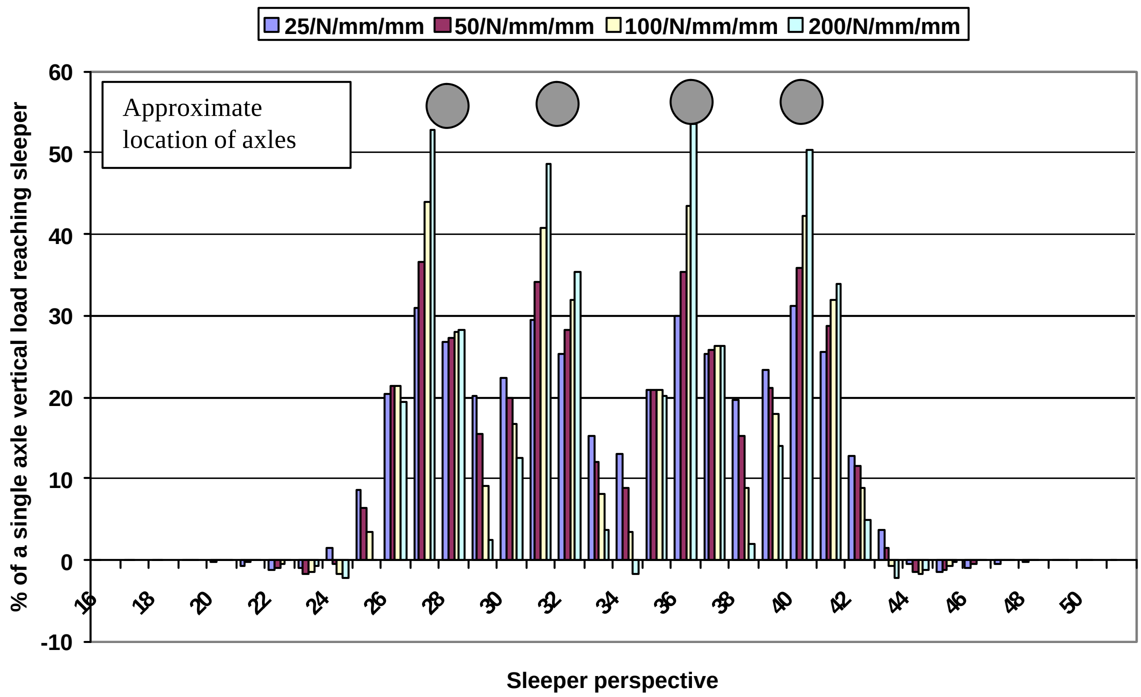

Figure 3-10: Vertical load expressed as a percentage of single axle force for mid section of two Pendolino non driving vehicles

The slight asymmetry about each wheel position is because the sleeper spacing and the axle spacing differ.

Comparison of Figure 3-10 with Figure 3-8 shows that adjacent axles have no significant effect on the maximum vertical load experienced at the sleeper level for the range of track moduli evaluated.

3.4. Lateral loads likely to reach a sleeper

To estimate lateral loads due to curving a simple model will be adopted assigning lateral load from curving forces equally to all axles. In Chapter 7 further consideration of geophone data will describe more fully reasons for possible variation in lateral load from axle to axle.

In a similar way to that by which the vertical load was estimated on a single sleeper, an estimate of lateral load can be made using a BOEF analogy. However, the track is more complex laterally. Modifications to the BOEF model can account for some of the increased complexity. To make these modifications it is assumed that:

- The lateral supports are elastic and of constant stiffness.
- The Pandrol fastclip fixings between the rails and sleepers provide additional torsional stiffness about a vertical axis.

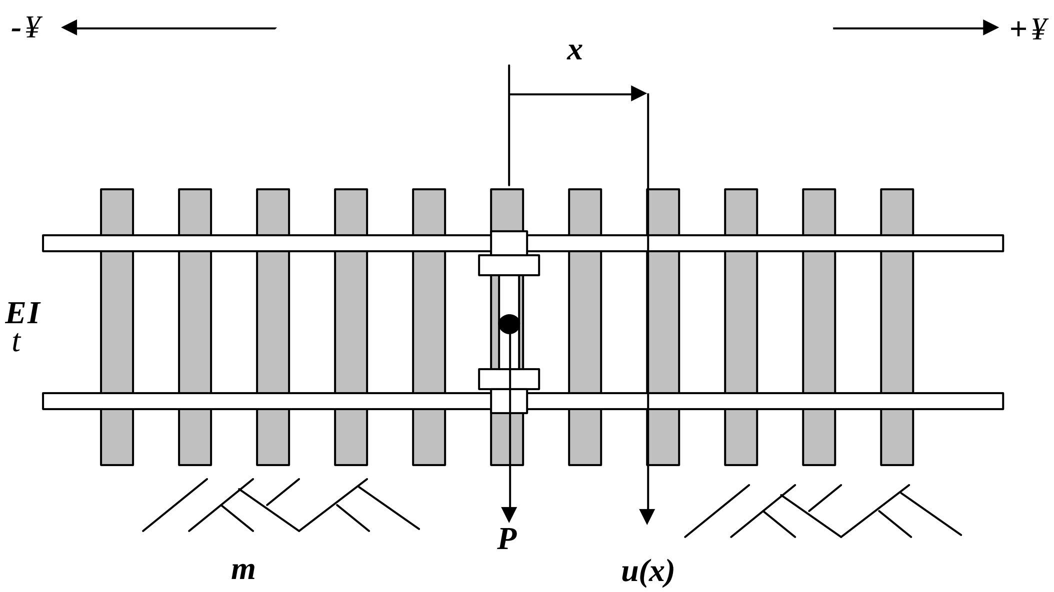

Figure 3-11: Lateral beam with elastic and torsional support

Where:

***P* =**	the lateral load which may be evaluated at each axle and summed for the carriages and train
***EI* =**	the bending stiffness of the track in the lateral plane
***m* =**	the lateral track modulus assuming a linear lateral response to load from the ballast/sleeper interface made up from the base, shoulder and side contacts.
***u(x)* =**	the lateral rail deflection at distance x from the applied load
***x* =**	the longitudinal distance from the load
t =	the torsional resistance of the sleeper rail fastenings, which may be evaluated per metre run of track

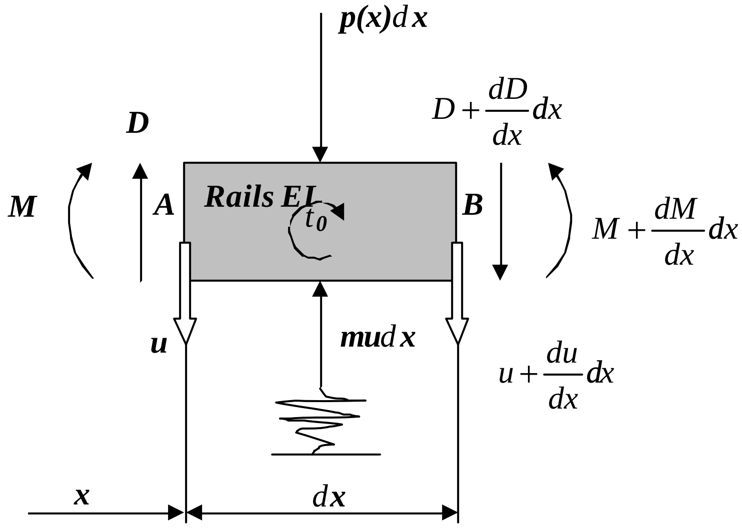

Figure 3-12: Beam element model, plan view

By applying a similar method to that used for the BOEF model, equations for the deflection and moment when $x > 0$ can be derived (Appendix A):

$$M = \frac{-P}{4\left(L_1 L_2^2 + L_1^3\right)} e^{-L_1 x}\left(\left[-L_2^2 - L_1^2\right]\cos L_2 x + \left[L_1 L_2 + \frac{L_1^3}{L_2}\right]\sin L_2 x\right) \qquad \textbf{Equation 3-15}$$

$$u(x) = \frac{P}{4EI\left(L_1 L_2^2 + L_1^3\right)} e^{-L_1 x}\left(\cos L_2 x + \frac{L_1}{L_2}\sin L_2 x\right) \qquad \textbf{Equation 3-16}$$

$$L_1 = \sqrt{\frac{\sqrt{4mEI} - t_0}{4EI}}$$ **Equation 3-17**

$$L_2 = \sqrt{\frac{\sqrt{4mEI} + t_0}{4EI}}$$ **Equation 3-18**

Using the values shown in Table 3-10 it is now possible to calculate a likely lateral bending moment in the rail and deflection of the rail and sleeper due to a lateral load. For this calculation a lateral load of 30 kN will be used. This would correspond to a train at 180% average passenger axle mass curving at 110 mph (49 m/s) on a curve of radius 1070 m resolved into the plane of 150 mm cant (where axle weight would act to reduce the lateral load). This is similar to sites on the WCML where field measurements, reported in Chapters 5 and 7, were taken.

Symbol	Description	Value	Units	Notes
E	Young's Modulus	205000	N/mm^2	
		2.05E+11	N/m^2	
I	Second moment of area	10,246,000	mm^4	Calculated by adding both rails for rail section 60E1(British Standards Institution BS EN 13674-1, 2003)
m	Lateral Elastic modulus	10 to 100	N/mm/mm of track	Range adjusted to provide realistic deflections (Chapter 5 monitoring data) and comprises both sleeper and railpads lateral stiffnesses
t_0	Torsional stiffness of rail sleeper fastenings	340249	Nmm/rad/mm of track	From manufacturer's tests (Pandrol Rail Fastenings Limited report No: 41174, 2003)
		111	kNm/rad per fastener	
P	Applied lateral laod	30	kN	Estimate of likely in service load on a sharp curve
a	Sleeper spacing	650	mm	

Table 3-10: Lateral beam on elastic support model: values used

As with the vertical case, the lateral track modulus is unknown. However, from monitoring data on the WCML a movement of about 0.5 mm (Figure 3-1) seems reasonable.

Figure 3-13 and Figure 3-14 compare the effect of the torsional resistance of the track for probable extremes of lateral track moduli.

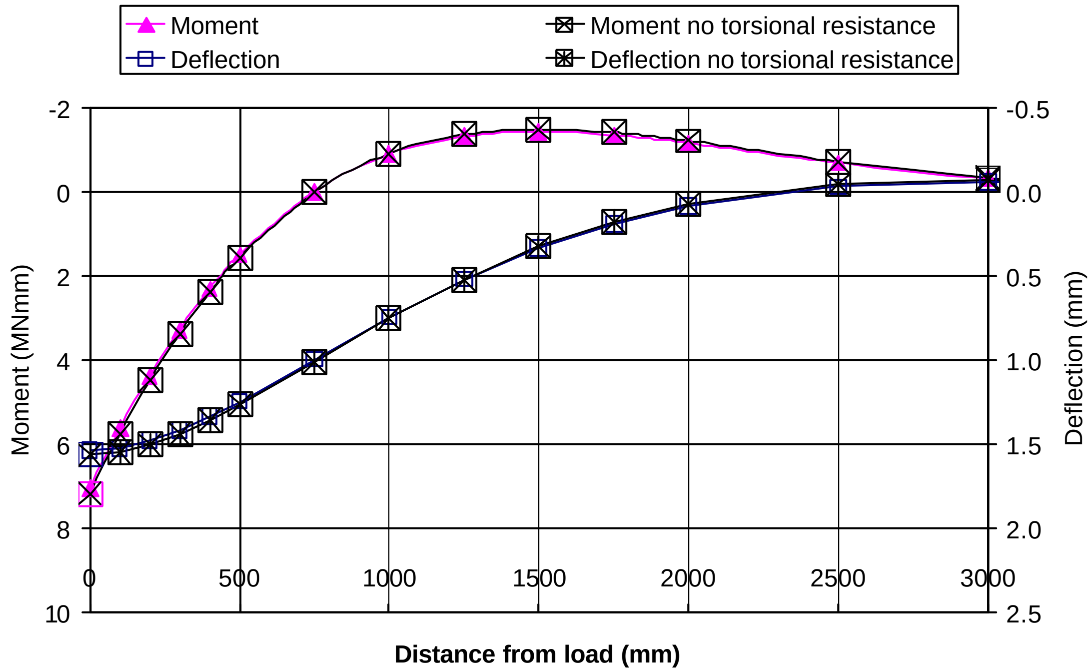

Figure 3-13: Track moments and deflections using the lateral beam model with a lateral stiffness of 10 N/mm/mm track

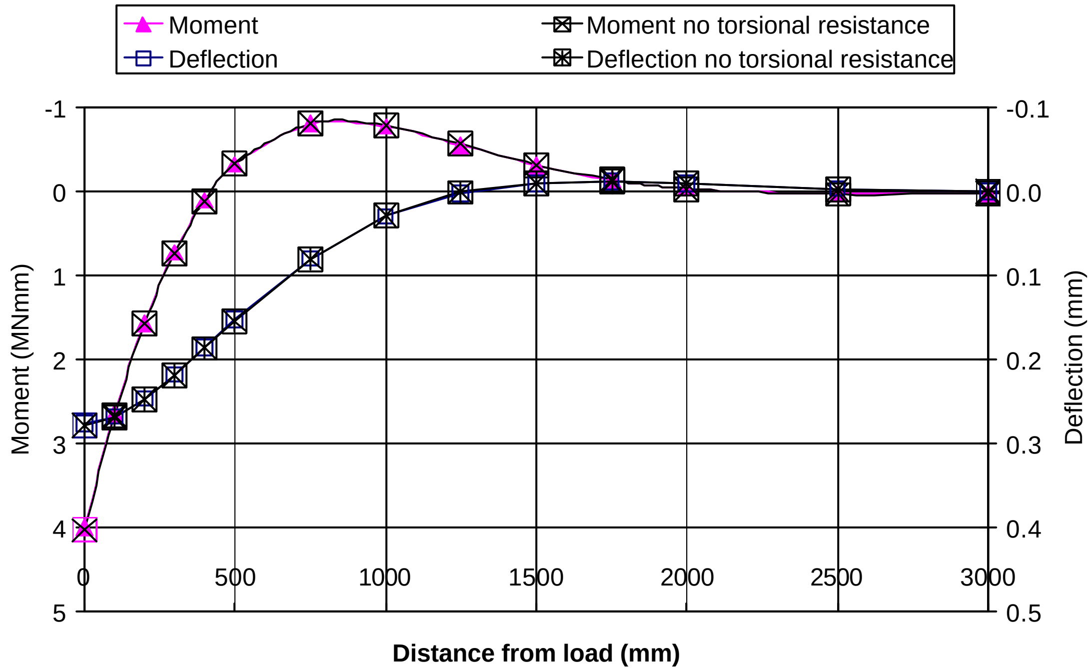

Figure 3-14: Track moments and deflections using the lateral beam model with a lateral stiffness of 100 N/mm/mm track

It can be seen that the inclusion of torsional resistance at the magnitude specified in Table 3-10 has negligible impact on the resulting moments and deflections. To simplify further calculations, the torsional stiffness will be ignored.

With this simplification the deflection may be evaluated for different lateral track moduli:

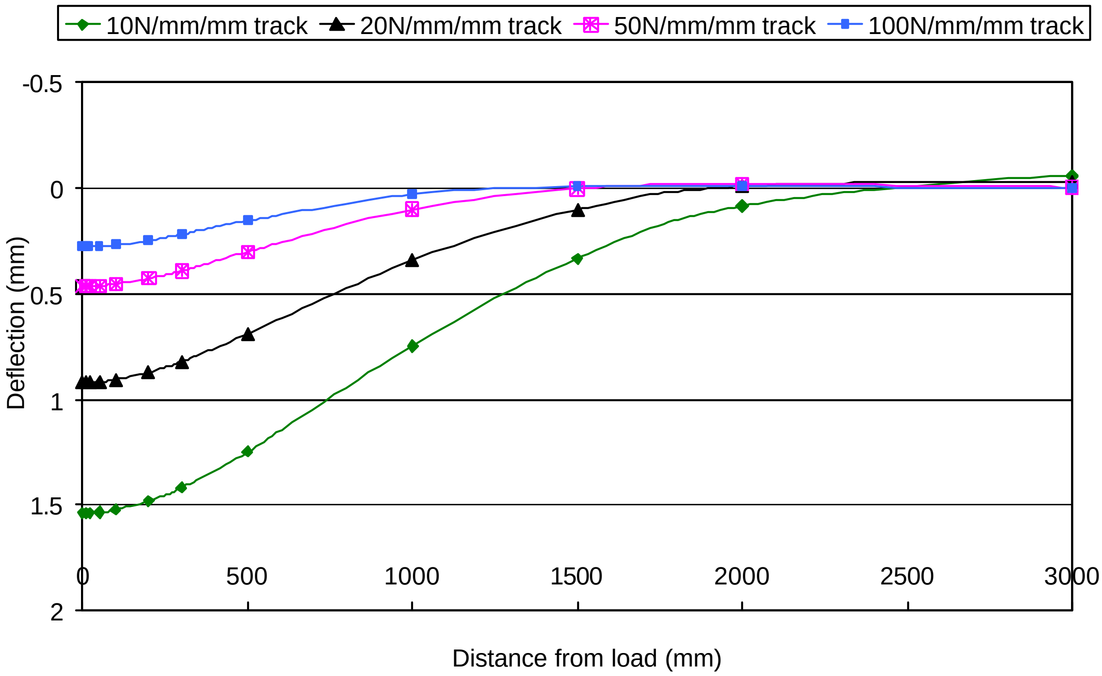

Figure 3-15: Sleeper lateral deflection with varied lateral modulus for 30 kN load on E1 60 rails

A lateral track modulus of about 50 N/mm/mm gives a reasonable match to the lateral deflection shown in Figure 3-1. However, further field measurements reported in Chapter 7 will show that the deflection range and hence lateral stiffness of the track can vary significantly from sleeper to sleeper.

Attention is now turned to the load reaching individual sleepers. This is achieved by simplifying and rearranging Equation 3-16 with t_0 of zero and $\boldsymbol{m} = \boldsymbol{m_d}/\boldsymbol{a}$ such that:

$$L = L_1 = L_2 \quad \textbf{Equation 3-19}$$

$$m_d = am \quad \textbf{Equation 3-20}$$

Substituting into Equation 3-16 gives:

$$SleeperLoad = u(x)m_d = \frac{aPL}{2} e^{-Lx} (\cos Lx + \sin Lx)$$ **Equation 3-21**

Where a is the sleeper spacing and m_d is the lateral track modulus per sleeper.

It is then possible to plot the % of applied lateral load reaching sleepers from a single axle load for different track moduli:

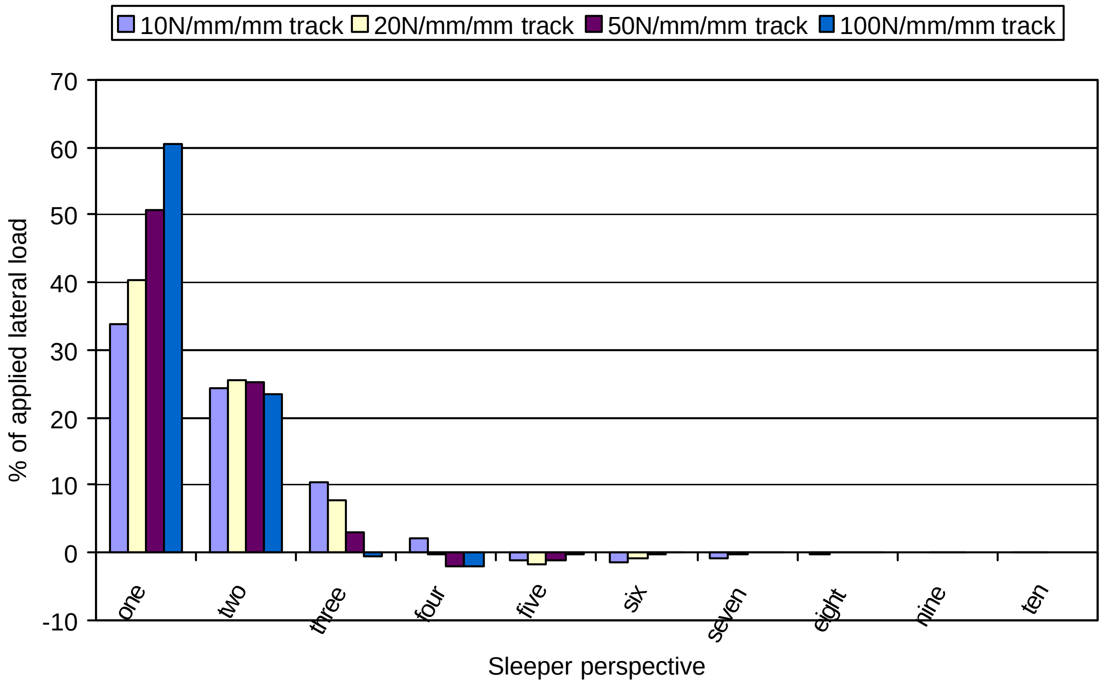

Figure 3-16: Sleeper lateral load as a % of applied axle force, sleeper spacing 650mm

Figure 3-16 indicates that for this simple model, within the range of lateral track moduli evaluated, the maximum lateral load on a sleeper below an axle force will vary between 34 and 60 percent of the applied lateral load from one axle. By carrying out a further calculation (the same as for the vertical load) the effects of axles from two carriages can be summed as indicated in Figure 3-17.

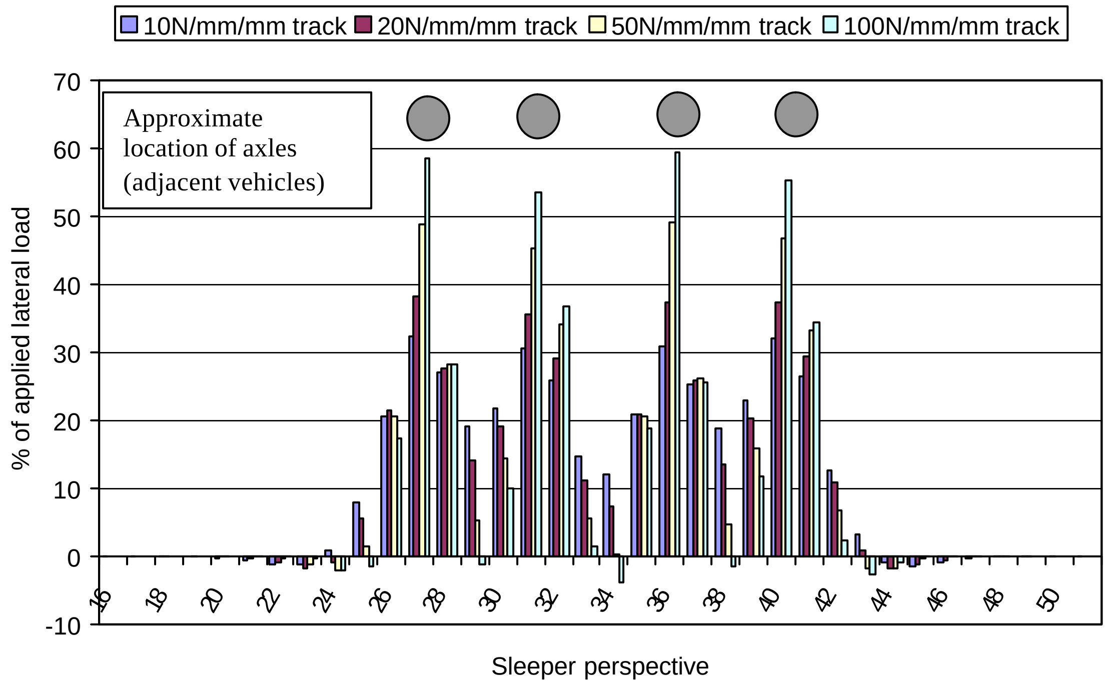

Figure 3-17: lateral load expressed as a percentage of single axle force, middle of two adjacent non-driving Pendolino carriages

As in the vertical case (Figure 3-10) the asymmetry in Figure 3-17 is caused because the axles are out of alignment with the sleeper spacing and, by comparing Figure 3-17 with Figure 3-16, it can be seen that adjacent axles do not have a significant influence on the maximum load reaching the sleeper.

So far the BOEF analogy has been used to assess the pre-failure behaviour of the sleeper. However it can also be used to assess the development of resistance at the sleeper/ballast interface at the base contact.

The load required to cause failure at the sleeper/ballast base contact area is expected to be proportional to the applied vertical load. Figure 3-8 shows that the lower the vertical track modulus the lower the proportion of vertical load reaching a sleeper immediately beneath an axle and hence the lower the lateral resistance at failure. Figure 3-16 shows that the greater the lateral track modulus the greater the proportion of load reaching a sleeper immediately below an axle.

Therefore failure is most likely when a low vertical track modulus and high lateral track modulus are present. An illustration of this is shown in Figure 3-18.

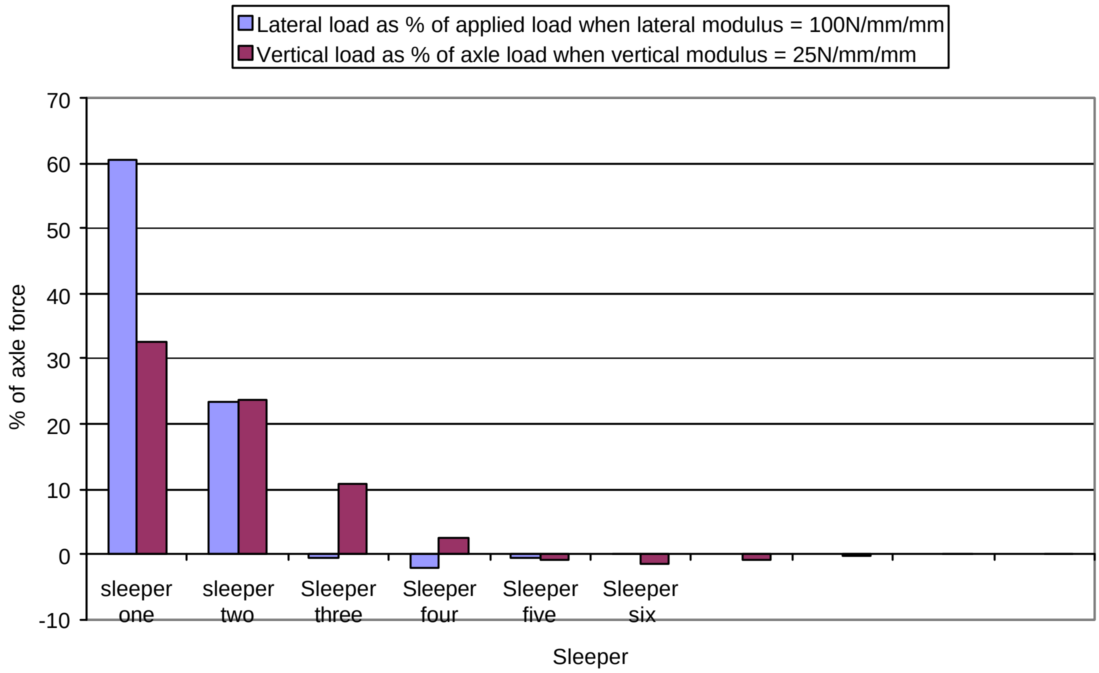

Figure 3-18: Comparison of load transfer vertically and laterally of axle load into sleepers

It can be seen from Figure 3-18 that the lateral load and vertical load are not equally distributed. The vertical load is dispersed along a greater length of track than the lateral load.

This implies that, theoretically, in extreme cases it may be possible for localized lateral failure of a single sleeper to occur. However, it is important to note that if a sleeper does tend to fail locally the load will be transferred to the rest of the system and global failure may be far from imminent.

Ideally, design would ensure that lateral and vertical track moduli are identical so that the failure resistance would remain at the same ratio to the actual load on each sleeper.

At this stage, beam on elastic support models have been taken as far as they can in evaluating the load reaching the sleeper/ballast interface. To develop fundamental understanding further requires practical experiments and 3D models which account for the effects of the component parts of the whole track system.

3.5. *Summary of Chapter 3*

It has been shown that on a curve of 1045 m radius with moderately extreme wind averaging 24 m/s, a train travelling at 56 m/s on 150 mm canted track at 80° yaw to the wind could be at risk of rollover. On horizontal track the ratio of resisting to overturning moment could be as low as 0.91 and on 150 mm canted track the ratio could be as low as 1.13 where a ratio less than 1 indicates rollover. On canted track modest increases in wind speed for a 3 second gust, and dynamic load are likely to mean that overturning could occur.

It has been shown that over a range of possible track moduli:

- The typical vertical load reaching a single sleeper immediately beneath an axle is likely to be in the range 33% to 55% of the weight of the axle.
- The lateral load reaching a sleeper immediately adjacent to an axle may be in the range 34% to 60%.

These percentages of load likely to reach a sleeper will be used to justify laboratory loads.

Vertical and lateral deflections for different track moduli were shown in Figure 2-4 and Figure 3-15 where the ranges of moduli evaluated were chosen based on WCML field data such as that shown in Figure 3-1. Further results shown in Chapters 5 and 7 will support these ranges as typical. Note however that the WCML data incorporates moment loading which was not considered in the BOEF anology.

4. Test set-up

In Chapter 3, calculations were presented to estimate normal and lateral axle load and the probable proportions of these loads reaching the sleeper during the passage of a Pendolino train on a curved section of track. The calculations relied on elastic assumptions about the behaviour of the track system, and assumed that the sleeper/ballast interface would support the loading.

To understand better the behaviour of the sleeper/ballast interface, a testing rig was designed and constructed, representing a slice of the track incorporating one sleeper bay under (near) plane strain conditions.

The testing rig enabled tests to:

- characterise the behaviour of the three sleeper/ballast contact areas, base, shoulder and crib due to likely Pendolino train loading,
- explore the failure envelope for a single sleeper in combined VHM loading,
- measure the development of confining stress within the ballast during initial train passage, and
- characterise single sleeper interface properties (pre and post failure) for use with dynamics models,

in line with the objectives set out at the beginning of Chapter 1.

In this chapter there are sections to:

- describe the testing apparatus,
- describe the test preparation procedures,
- describe the method of cyclic loading, and
- summarise the testing carried out.

Chapter 5 provides support to the testing procedures adopted by comparing results with field data and by making comparisons with the literature.

4.1. Description of testing apparatus

A slice of the track was re-created in the laboratory as closely as possible. A photograph of the testing apparatus used is shown in Figure 4-1.

Figure 4-1: Testing apparatus

Two vertical sides 5 metres long and 0.65 metres high were constructed from heavy steel sections and panels bolted together. These were held at a fixed distance of 0.65 m apart, equal to one sleeper spacing on the WCML, by steel ties at the base and at various other locations as shown in Figure 4-2.

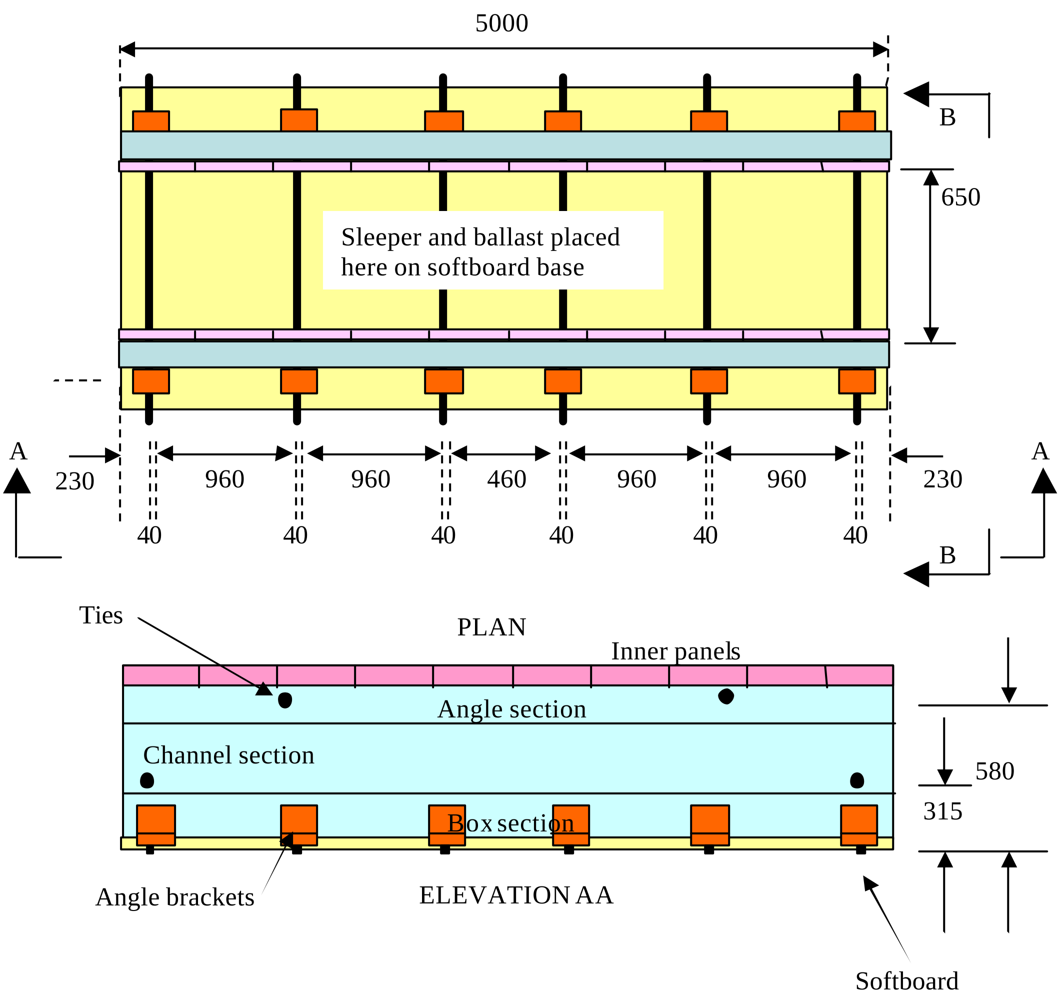

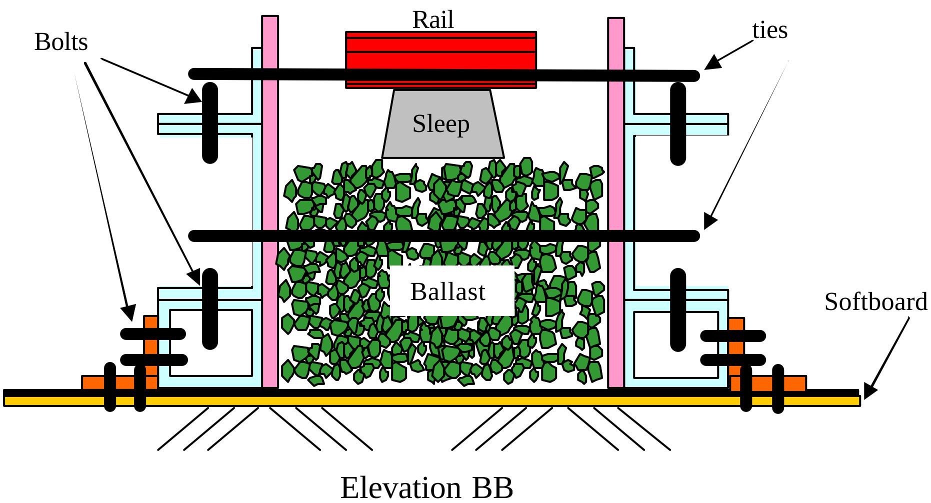

Figure 4-2: Laboratory track section, plan and side views, not to scale

The test rig was constructed from heavy stiffened steel sections to prevent any significant flexure of the rig during testing and maintain the test conditions as near as practicable to plane strain.

Wooden and steel panels 500 mm by 650 mm were firmly attached on the inside walls of the testing rig, using tapped countersunk bolts as shown in Figure 4-3. The wooden fronts to these panels were removable to allow placement of pressure plates to measure confining stress as shown in Figure 4-4.

The pressure plates, shown in Figure 4-5, comprised 10 mm thick load cells attached to 12 mm thick steel. Therefore the total thickness was nearly the same as for the 25 mm thick wooden panels being replaced. The pressure plates did not fill the same area as the wooden panels being replaced so this was made up with dummy steel panels where no load cells were attached. Wooden battens 10 mm thick attached to the dummy panels ensured they were flush and allowed cabling for the load cells to pass behind them. Ideally the panels would all be of the same stiffness, however this was not possible and it is recognised that the stiffness of the instrumented and dummy steel panels is greater than the wooden panels.

During each test, four pressure plates were placed along the inside wall of one side of the testing rig. The location of pressure plates was varied, initially these were placed as shown in Figure 4-6. Each load cell consisted of a model 53, 250lb (1.1 kN) compression load cell with +/-0.25% linearity purchased from RDP electronics Ltd (RDP Electronics Ltd, 2008) and was connected to a data logger.

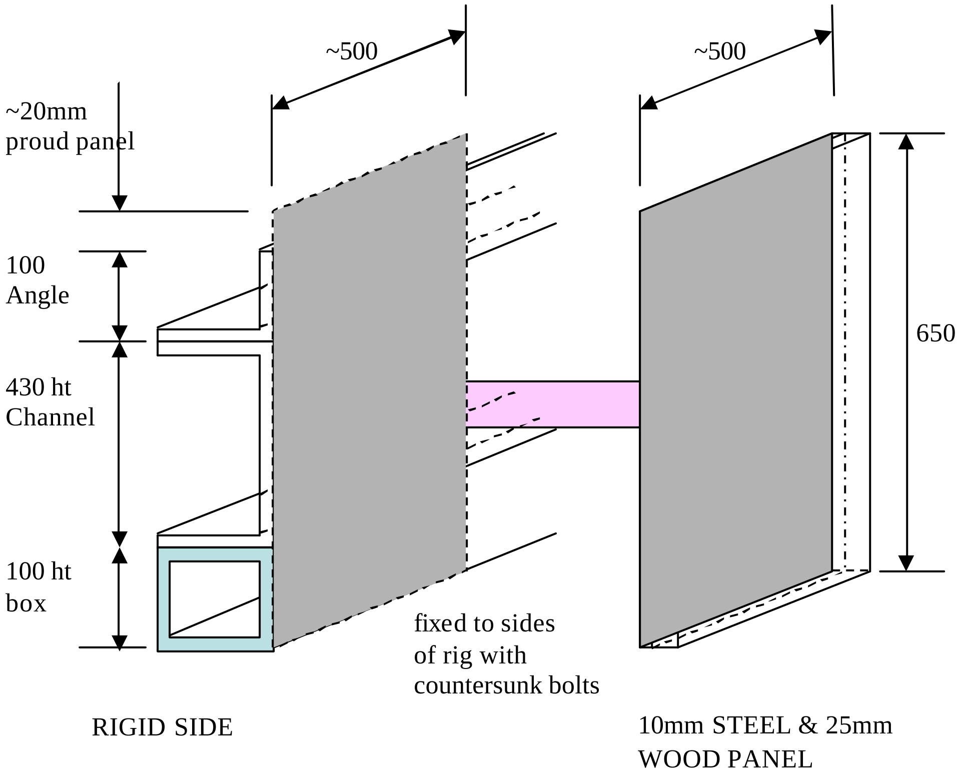

Figure 4-3: Panels fixed to inner sides of rig, dimensions in mm, not to scale

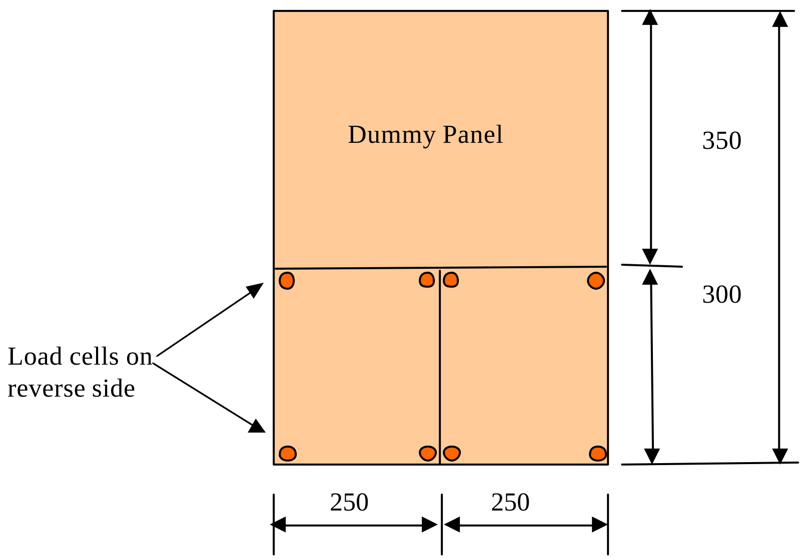

Figure 4-4: Pressure plates: front face view, dimensions in mm, not to scale

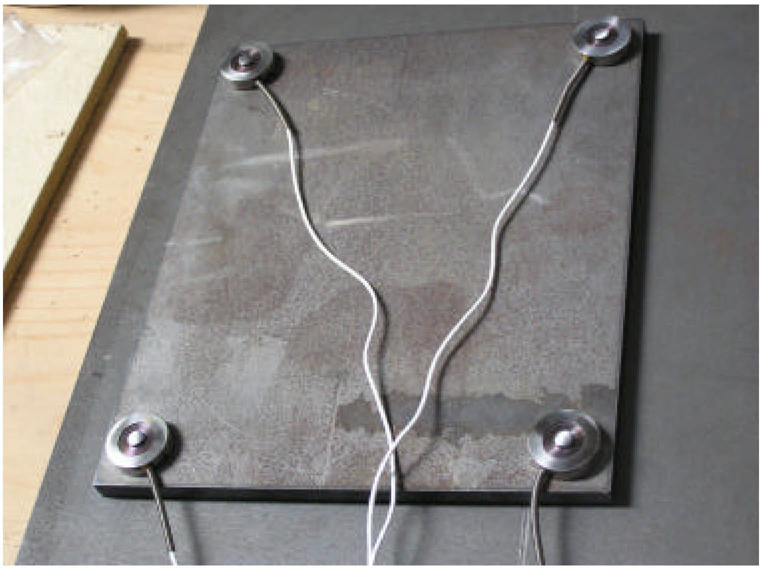

Figure 4-5: Photo of pressure plate showing the load cells on the rear

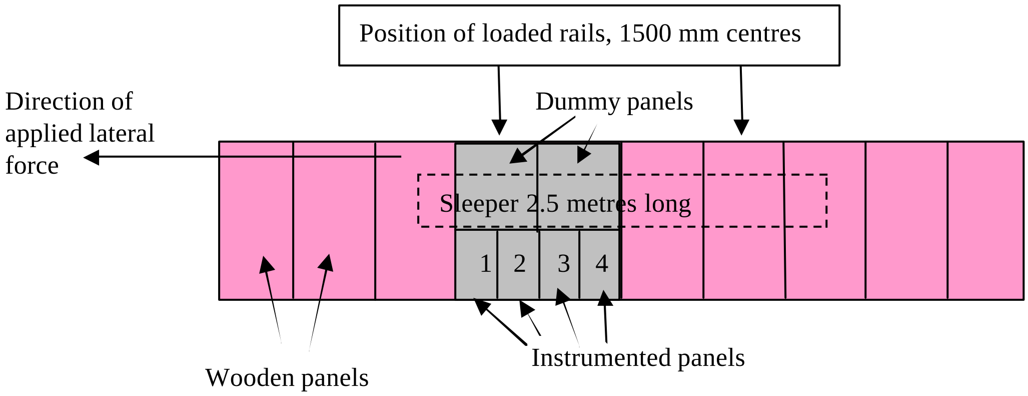

Figure 4-6: Instrumented inside wall of test rig, view from inside the assembly

A double layer of plastic sheeting was placed on the inside walls of the testing rig to minimise friction at the contact with the ballast. On the base a double layer of wooden softboard was placed having a thickness of 20 mm to represent a slightly compressible subgrade and ensure a frictional contact.

Although it was not an objective of this research to investigate the vertical resilient behaviour, it was considered important that the testing apparatus should reproduce as closely as possible actual track behaviour. The softboard, in addition to providing a frictional contact also contributed to the vertical resilient deflection of the sleeper above. This was important because the majority of resilient deflection of actual track can be from deflection within subgrade. The resilient deflection of the sleeper on the ballast in the laboratory experiments was evaluated to ensure the apparatus was able to reproduce realistic levels measured on the WCML, the results of this comparison are presented in Chapter 5.

Both the plastic sheeting and softboard are visible in Figure 4-7 in which ballast filling has begun. The ballast is placed to a depth of 300 mm, a minimum thickness that would be expected on actual track in the UK (Network Rail RT/CE/C/039, 2003). Ballast was sourced from stockpiles at Southampton docks and was determined to be made up of crushed granite. Sieve tests were also carried out prior to and during testing and these proved that particle distribution conformed to Network Rail specification (Safety and Standards Directorate Railtrack PLC RT/CE/S/006, 2000) with no measureable difference in particle distribution occuring as a result of the tests carried out for this research.

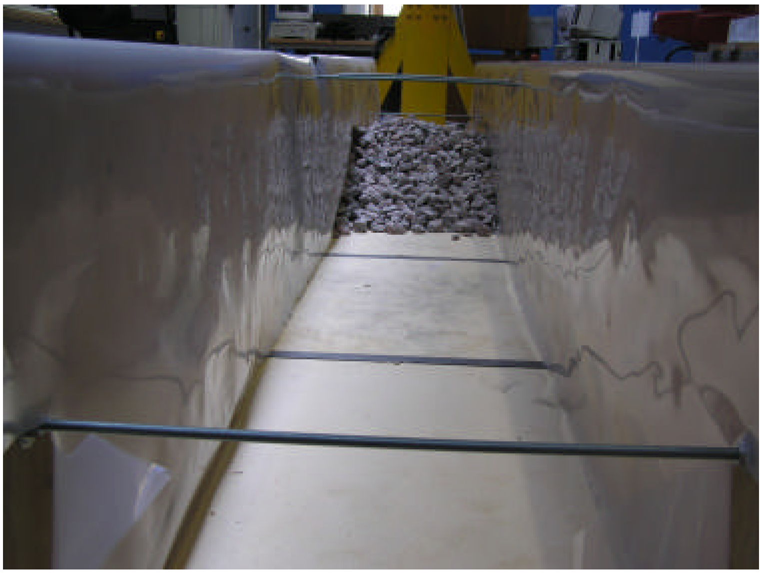

Figure 4-7: Photo inside testing rig during ballast filling

After the ballast was placed and a level surface prepared, a G44 sleeper with 0.4 m part lengths of BS113A rails attached by Pandrol fastenings (Pandrol Rail Fastenings Limited: Report No. 45111, 2000) was placed centrally on top. Finally a loading beam was placed across the railheads and hydraulic jacks were connected as shown schematically in Figure 4-8.

The vertical hydraulic jack was capable of loading up to 250 kN either in tension or in compression and had a stroke length of +/- 125 mm. The lateral hydraulic ram was capable of loading at +/- 150 kN and had a stroke length of +/- 75 mm. Both rams were manufactured by INSTRON and, although the rams were decades old were controlled using 2 No. recently purchased type 8400 INSTRON controllers, which in addition to controlling the rams, provided continuous output for the load and deflection to the data logger. According to INSTRON the accuracy of the rams is to 1% of stroke length and 1% of actual load. The controllers were automatically tuned so that loading signals were compatible with the response of the testing apparatus.

It had been intended to obtain E1 60 rails as used on the WCML. This proved difficult, however, so BS113A rail sections were used instead. This was possible because the G44 sleeper can accept either specification provided the Pandrol fastenings are correctly set up. BS113A rails are a British specification of rails weighing 56 kg/metre, slightly less than the 60 kg/m of E 1 60 rails.

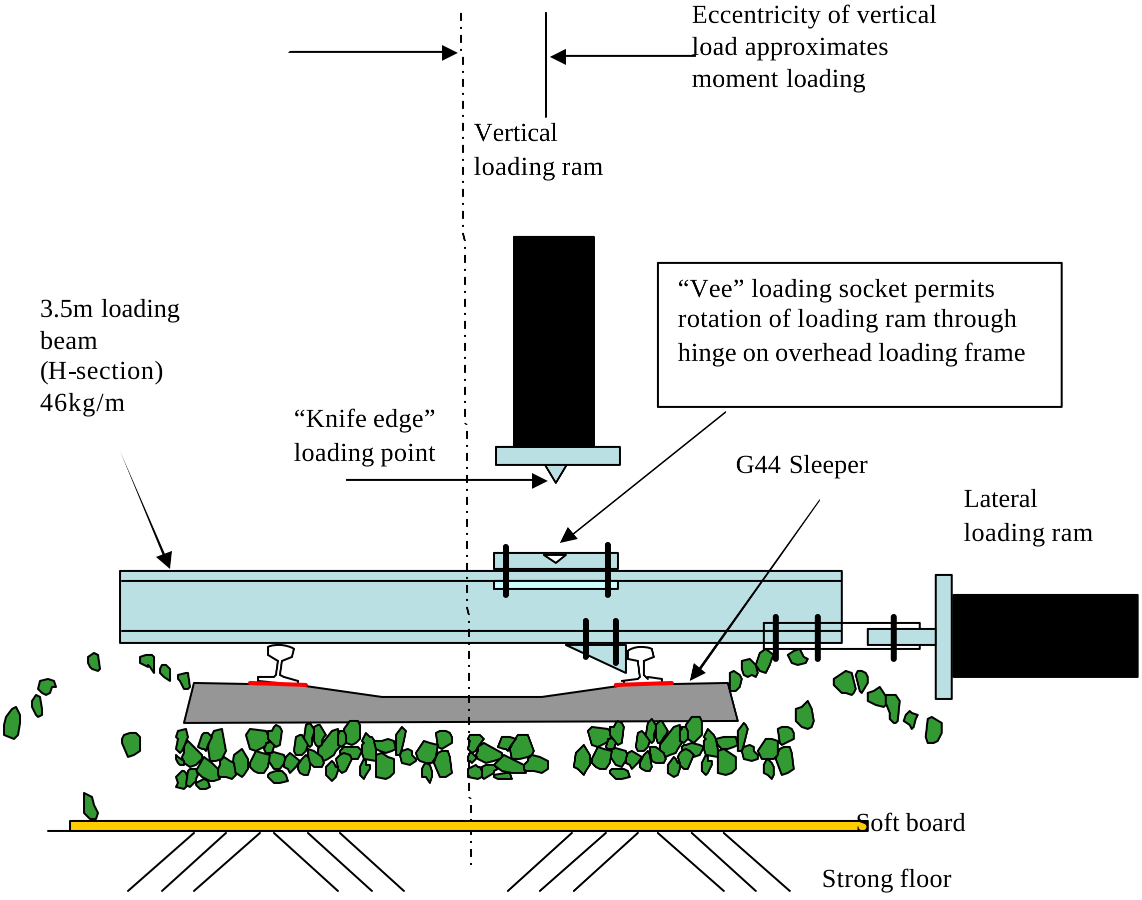

Figure 4-8: General arrangement of sleeper/ballast testing rig: Elevation

The vertical loading ram was attached to a portal frame above by a hinge at a height of approximately 1500 mm above the loading point. This allowed the vertical ram to follow the vee loading point when the loading beam and sleeper were moved sideways by the lateral ram. It was also possible to move the vertical ram along the portal frame to an eccentricity relative to the centre of the sleeper so as to apply a moment loading. The lateral load was transferred through the loading beam onto the inside flange of the near railhead by a bolted steel section as shown in Figure 4-8.

After the ballast, sleeper and loading arrangement had been set up, instrumentation to measure the vertical and horizontal deflection of the sleeper during testing was installed. The vertical movement of the sleeper was measured at both sides of either end during testing by means of four LVDTs. These were fixed to brackets firmly clamped to the sides of the testing rig and positioned so as to measure the vertical deflection of a level plate glued to the sleeper (Figure 4-9). Therefore all measured movement of the sleeper was relative to the testing apparatus walls.

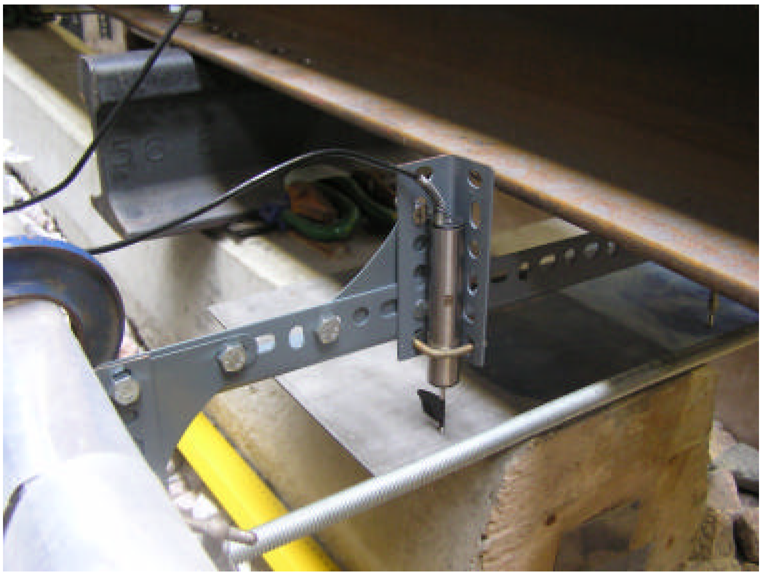

Figure 4-9: Photo of vertical LVDT on sleeper

The controllers for the hydraulic rams provided a continuous stream of load/deflection data. However, as the rams were not directly connected to the sleeper it was necessary to use an LVDT to measure the sleeper lateral movement as shown in Figure 4-10.

Figure 4-10: Photo of lateral LVDT on sleeper

All instrumentation was connected to a single data logging system consisting of a Vishay 5100B scanner of two modules containing multiple channels on strain gauge and high level cards. The load cells were connected to strain gage cards and the LVDT's and the hydraulic ram displacement and load were connected to high level cards. The Vishay data logger was used at frequencies of 1, 5, 10, and 50 Hz.

The properties of the LVDTs used are described in Table 4-1. The data logger was able to measure the signal to the nearest tenth of a millivolt and the accuracy of the data logger is therefore taken as accurate to the nearest millivolt. The accuracy of these LVDTs is then, in all cases, at least accurate to the nearest 67th of a mm and for the shorter LVDTs is accurate to the nearest 333rd of a mm.

Range	**Calibration used**	**Deflection per mV**	**Use**
(mm)	mV per mm	(mm)	
+/-50	64.74	0.015	Vertical
+/-25	194.05	0.005	Vertical
+/-15	293.12	0.003	Vertical
+/-15	306.96	0.003	Vertical
+/-75	65.07	0.015	Lateral
+/-15	292.75	0.003	Vertical and lateral

Table 4-1: LVDTs used

The large range LVDT (+/- 75 mm) was used to measure the lateral movement of the sleeper during failure tests. However because it has the lowest resolution, lateral measurements were also taken from a low range LVDT (+/- 15 mm) for lateral cyclic loading tests where the lateral deflection was small.

4.2. Testing Procedure

A range of tests was carried out to investigate pre-failure and failure behaviour of the sleeper/ballast interface for different arrangements of sleeper/ballast. Initially tests were carried out with only base ballast present, with later tests being used to assess the effect of adding in different sizes of shoulders and crib ballast on the behaviour of the sleeper/ballast interface.

It was intended that tests would represent a condition of freshly laid track ballast. This meant that to assess the variability of failure behaviour a number of different test set-ups were required. This meant that after each failure test the sleeper was removed and the entirety of the ballast within the testing rig was shovelled over to re-create a loose initial unaltered state and the surface re-levelled for the (re)placement of the sleeper. Levelling of the top was achieved by use of a wooden board of similar dimensions to the sleeper footprint.

3 different phases took place within each test set-up:

1. Initial 100 vertical cyclic loads applied
2. Pre-failure cyclic loading tests, initially static and then at higher frequencies
3. A failure test

Initially tests took place to justify the testing procedures; these were required to check such things as:

- Safety; to check that no unexpected behaviour occurred
- LVDT data; to check that the LVDTs gave consistent and correct data
- The effects of loading frequency on load/deflection response

It is also known that traffic can increase the lateral resistance of the sleeper/ballast interface (Esveld, 2001). Therefore the number of cycles permitted in lateral cyclic loading tests was kept small, the largest number of cyclic lateral loads applied was 160 in one test set-up, however in the subsequent failure test, no significant difference from the other tests was observed

These preliminary tests, identified a number of apparatus issues and resulted in modifications to the testing procedures which were incorporated into the tests that are reported in Chapters 6, 7, and 8.

The following subsections detail:

- justification of loading,
- the general method of test preparation, and
- the general method of lateral cyclic loading testing and failure testing.

Validation for the testing methods is presented in Chapter 5.

4.2.1. Justification of loading in tests

In Chapter 3 track loading was explored and it was shown that a train on a 1045 m radius curve travelling at 125 mph mobilised its full operating cant deficiency of 300 mm (11.3°). It is equally possible to mobilise full operating cant deficiency on lower radius corners at slower speeds or on higher radius curves at greater speeds when the cant of the track is equal. Therefore the maximum loading from curving force may be calculated solely from knowledge of the axle mass, the maximum operating cant deficiency of the train and the maximum permitted cant of the track.

Restating Equation 3-10:

$$D_{degrees} = \tan^{-1}\left[\frac{mv^2 / R}{mg}\right] - a$$ **Equation 4-1**

Where $D_{degrees}$ is the operating cant deficiency

Rearranging Equation 3-10, the maximum curving force $\boldsymbol{F}$ ($\boldsymbol{mv^2/r}$)is then:

$$F = mg\tan(D_{degrees} + a)$$ **Equation 4-2**

For an axle mass of 14793 kg (180% passenger tare) travelling on track of cant angle 5.7° (150 mm) at its maximum permitted operating cant defficiency of 11.3° (300 mm) using, Equation 4-2, the maximum horizontal curving force is 44 kN. If this is resolved into the plane of cant together with the vertical load and moments are taken about the railheads (using the dimensions shown in Figure 3-6) the forces across and normal to the railheads are as shown in Figure 4-11

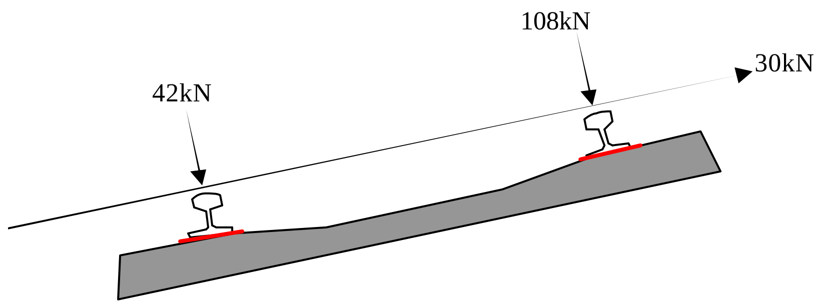

Figure 4-11: Loading magnitudes for 180% average passenger tare at maximum operating cant deficiency

For the case shown in Figure 4-11 the total normal load applied at the rail heads is 150 kN. In Chapter 2 it was shown that between 33% and 55% of normal load is transferred to a sleeper beneath an axle. Therefore it has been decided that for all tests the peak applied normal load at the sleeper ballast interface will reach 80 kN (~50%). This also includes the dead weight from the loading beam rails and sleeper of 5 kN (comprising. (310×9.81)N from the sleeper, (56×9.81)N from the rails and (42×3.5×9.81)N from the loading beam).

In the laboratory the sleeper was placed level. Although actual track is canted, reproduction of cant in the laboratory would cause significant experimental complications for minimal benefit. Also, by maintaining the same ultimate normal load on a level sleeper the effect of moment can be more easily evaluated simply by adjusting the eccentricity of the application point for the vertical load.

In Figure 4-11 the normal load on the railheads is in the ratio 42:108 or 1:2.5.

It is also desirable to test the sleeper/ballast interface for rollover loading. At rollover the normal railhead load is entirely through the outer railhead, however reproducing such a situation in the laboratory is potentially unstable. Therefore a compromise for safety reasons means that the tests carried out have the vertical ram placed either centrally or at an offset of 0.5 m.

Using a simply supported beam analogy a vertical load at 0.5 m offset loads the railheads in the ratio 250:1250 or 1:5.

In Chapter 3 the proportion of lateral load from an axle reaching a sleeper immediately beneath was estimated to be in the range 34% to 60%. If the total lateral load is 30 kN this corresponds to a loading range of 10kN to 18 kN. However, this research is also investigating the failure behaviour, so lateral load has been applied within this range and above.

4.3. Summary of testing procedures

4.3.1. Method of test preparation

After careful consideration and some preliminary tests (some of which are reported in Chapter 5) it was decided that all test set-ups would share the following common features:

1. Zero readings for the load cells were taken prior to filling in the ballast.
2. The ballast was prepared to the desired dimensions (shoulder, crib) and the top carefully levelled by hand with a wooden board to provide an even support.
3. The sleeper was placed and allowed to settle until it stabilised (at least overnight).
4. The loading beam was placed and the hydraulic rams were attached to the beam via their respective fixings. In some cases the lateral ram was connected later after an initial 100 vertical load cycles were applied.
5. The LVDTs were placed and tested to ensure they were within range and had sufficient travel in anticipated directions of movement during loading.
6. A vertical load was applied in increments (5, 40, 75) up to 75 kN and the assembly monitored for safe performance.
7. A cyclic vertical load was applied from 5 kN to 75 kN for 100 cycles at a frequency of 0.2 Hz or 0.3 Hz. A 5 kN dead load from the rails, sleeper and loading beam was also present. The vertical load was applied either centrally or 0.5 m to one side of the centreline of the sleeper on the side where the lateral ram was located.

8. A minimum of 10 lateral load cycles at not more than 1/3 of the vertical load was applied before further non failure combined vertical, lateral and moment load testing was carried out (method of pre-failure cyclic load testing described in following section).
9. Finally the sleeper was pulled laterally in displacement control over a distance of at least 80 mm while a vertical load was maintained. Different tests had different levels of constant applied vertical load applied at different eccentricities from the centreline of the sleeper.

During the failure lateral pull tests the vertical loading ram rotated about a pin attached to the portal frame as the sleeper was pulled sideways so that the ram head reached a lateral offset relative to the overhead pin. This meant that after 100 mm of lateral movement of the sleeper, the vertical load reduced by approximately 0.2% while the lateral load increased by 7% of the vertical load. The vertical reduction in load is considered insignificant. However, the increase in the lateral load is significant and is accounted for in all results included in this report.

Also note that the testing arrangement meant that for safety it was important to maintain the vertical hydraulic ram in a compression only condition (i.e. no lifting). This is why a seating load of at least 5 kN was maintained throughout the application of the vertical cyclic loads.

The vertical loading cycles were applied at a frequency of 0.2 or 0.3 Hz. This avoided dynamic effects such as resonant frequencies of the test rig and was practical because 0.3 Hz can be data logged at 10 Hz satisfactorily.

The 100 vertical load cycles allow the sleeper some opportunity to settle and stabilise onto the ballast while remaining a relatively low and practical number to permit rapid testing for the several dozen tests carried out in total. Although 100 might seem a relatively small number of cycles of axle load compared to reality (where this might occur in a single day), it is well documented that vertical settlement in ballast follows a logarithmic relation e.g. (Selig and Waters, 1994), therefore, the first 100 cycles are as important as the following 9,900. Comparison will be made between expected and actual vertical settlement in Chapter 5.

4.3.2. Methodology for pre-failure cyclic loading tests

After the applicarion of the 100 vertical load cycles and prior to failure testing, tests were carried where lateral and sometimes vertical load was cycled as follows:

1. Vertical load was carefully increased to 10, 25, 40, 55 or 70 kN and was maintained throughout testing, in addition a dead load of 5 kN was present.
2. The lateral ram was adjusted to apply and maintain 2 kN in tension.
3. From 2 kN the lateral load was carefully increased to be equal to 1/3 of the total vertical load either by adjusting the position of the ram slowly of by applying a slow rate of loading up to the desired level (e.g. 2 kN or 4 kN per second), so that the maximum vertical to lateral loading ratio would be 15:5, 30:10, 45:15, 60:20 or 75:25 and cycled back to 2 kN.
4. A further 9 cycles were applied of increasing/decreasing load between 2 kN and 1/3 vertical load.
5. Following the application of the 10 pseudo static load cycles different combinations of cyclic lateral load were applied using different wave forms either triangular or sine. Usually this was with a vertical load held constant but some tests were carried out with lateral and vertical load applied using sine wave forms simultaneously to represent more realistic train loading.

4.4. Tests carried out

A total of 23 tests divided into 5 groups were carried out as shown in Table 4-2 . In each test pre-failure and failure behaviour of the sleeper/ballast interface was assessed for specific arrangements of load and ballast. Following test group X changes were made to the arrangement of LVDT instrumentation; the lateral deflection data for test group X have been neglected from the results presented in following Chapters.

Test Group	Number of test set-ups	Main purpose to:
X	5	Check testing methods. (improvements were made to the instrumentation after these tests).
A	3	Investigate behaviour of the sleeper base to ballast contact area with vertical and lateral load.
B	4	Investigate behaviour of the sleeper base to ballast contact area with moment load included.
C	9	Investigate behaviour of the sleeper base to ballast contact area and the additional resistance to failure provided by the presence of different sizes of shoulder ballast.
D	2	Investigate behaviour of the sleeper base to ballast contact area and the additional resistance to failure provided by the presence of crib ballast.

Table 4-2: Test groups

4.5. Summary of Chapter 4

In chapter 4 a testing apparatus has been described. Applied loads on the testing apparatus have been justified with reference to the BOEF analogy set out in Chapters 2 and 3 and testing procedures have been outlined. Results from these tests will be presented in Chapters 5, 6, 7 and 8.

5. Validation of testing apparatus

The purpose of Chapter 5 is to demonstrate the validity of the testing equipment and the procedures adopted by:

1. Determining that the vertical laboratory behaviour is realistic during the initial 100 cycles of applied vertical load compared with real track behaviour.
2. Justifying that the lateral cyclic loading procedures adopted optimise the comparability and quality of the results obtained.

This Chapter will involve statistical comparison and detailed discussion of the behaviour observed from the geophone field measurements and the laboratory testing results.

This Chapter is divided into three main sections:

- Geophone monitoring on the WCML; this section characterises vertical sleeper movement on low radius curves of the WCML during passage of Pendolinos at high speed.
- Vertical plastic and resilient response; this section examines laboratory data for changes in the plastic strain and resilient response during the initial 100 load cycles and makes a comparison with the geophone data and other reported track measurements from the literature.
- Evaluation of results of tests to assess the appropriate range of loading frequency required to represent train lateral cyclic loading. The results of this evaluation were adopted into the testing procedures presented in Chapter 4. This section includes an assessment of the importance of stress relaxation (creep) in the test data.

At the end of the Chapter a summary draws together key points.

5.1. Geophone monitoring on the WCML

5.1.1. Background

The University of Southampton has developed two independent, innovative techniques for measuring sleeper deflections. One system combines remote video monitoring with particle image velocimetry (PIV), using a high speed digital camera and a small telescope. The second uses sleeper mounted geophones that give a voltage output proportional to the velocity of motion, which can be filtered and integrated to calculate deflections. A full description of the monitoring systems is given in Bowness et al., (2007).

This section presents vertical geophone monitoring data obtained during site visits to curves on the WCML, and characterises vertical sleeper movements caused by Pendolino trains curving at high speed.

The lateral deflection data will be presented later, in Chapter 7.

5.1.2. Methods; geophone monitoring

Geophones are small seismic sensors that produce an output voltage proportional to velocity. The Sensor Nederland LF-24 low frequency geophones used have a sensitivity of 15 V/m/s. Two variants of the geophone were used, one which may be aligned vertically and one which may be aligned in the horizontal plane normal to gravity. This meant that sleeper movement relative to the canted sleeper base was not directly measured. However the minimal slope (~6°) meant that horizontal and vertical movements provided sufficiently accurate indications of sleeper lateral and normal movement relative to the sleeper base.

The remote video monitoring technique uses a high speed digital camera to video a target attached to the sleeper end. The camera captures digital video directly to a laptop computer at up to 150 frames per second. To avoid the video being affected by ground borne vibration immediately adjacent to the track, the webcam is coupled to a telescope and mounted on a tripod such that the target may be videoed from a distance.

The use of both PIV and geophone methods simultaneously to capture sleeper movements provides independent validation of the data obtained.

Both the video monitoring targets and the geophones were attached to an aluminium L-bracket and an angled wedge plate to align them vertically and horizontally, which was fixed to the sleeper ends with fast setting glue as shown in Figure 5-1.

Figure 5-1: Geophone attached to a bracket glued to one sleeper end

The remote video monitoring data are not presented in this report for two reasons. First, in this case, the data were subject to ground borne vibrations due to the difficulty of locating the camera stand sufficiently far from the track and secondly, because it operates at a lower frequency to the geophones the system is less able to produce high resolution deflection/time plots for trains travelling at over 100 mph (Bowness et al., 2005a). However, although no results are presented here, the data obtained corroborated the general trends shown in the geophone measurements. All data from the geophones were gathered using a calibrated Campbell Scientific CR-9000 high speed datalogger set to record at 500 Hz. Matlab was then used to process the data using methods decribed in Bowness et al (2007), and deflection data were pasted into a spreadsheet to produce the charts shown in this report. One limitation of using geophones is that the deflection is always determined from the motion of the geophone, i.e. no motion or very slow motion is not detected and the geophone always indicates it has returned to its at rest position when motion has stopped. Therefore any relative movement of the sleeper from its position prior to passage of a train to its position after the train has passed is not evident in the processed deflection geophone data.

The monitoring sites were located on a length of track of the WCML near Weedon Bec, Northampton as shown in Figure 5-2. Three sections of track were monitored on a length of track incorporating a reverse curve (i.e. an S-shaped curve). The geophones were located on two sections of constant curvature (i.e. not on transition zones), labelled:

- Site 1 (LEC1 69m40ch Dn, Curve radius=1230m; Cant=150mm),
- Site 2a (LEC1 69m70ch Up, Curve radius=1025m; Cant=150mm)
- Site 2b (LEC1 69m78ch Dn, Curve radius=1025m; Cant=150mm)

Site 1 had been tamped approximately 6 months prior to the data reported here being taken. Site 2a and 2b were on the same curve.

Two monitoring trips were carried out at all three sites approximately 4 months apart, November 2006 to February/March 2007, some of this data are reported in Priest et al., (2008). Since the current research is not concerned with comparing the relative data from the two trips, only data from the second monitoring trip in February/March 2008 is presented in this report.

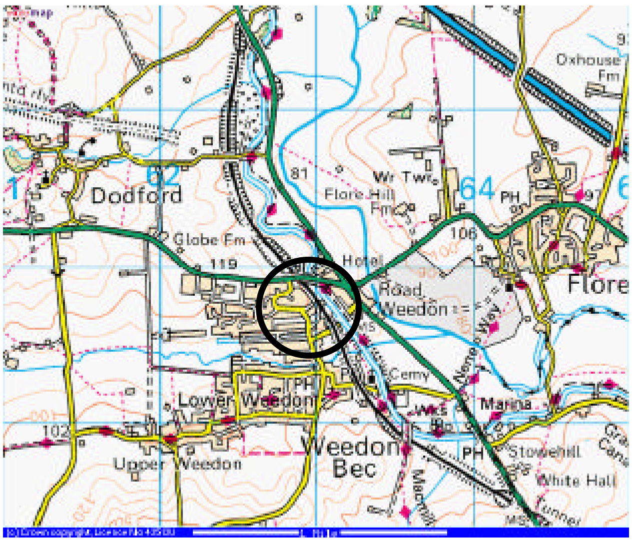

Figure 5-2: Location of monitoring sites at Weedon Bec (located in circle)

Figure 5-3: Photograph of Pendolino curving at high speed near Site 2a, the tilt is active

Several different arrangements of geophones were used to obtain deflections in different orientations using up to ten data logging channels. All the different arrangements indicating the number and the type of trains captured are shown in Appendix B. Each of the 14 set-ups encompassed the passage of between 1 to 7 trains. In total, data from 47 trains were recorded. Most of the trains were Pendolinos travelling at approximately 110 mph, these are the data that will be presented here.

5.1.3. Results; geophone monitoring

To examine the vertical behaviour, selected characteristic results will be taken from site 1 which was tamped approximately 6 months prior to the data being taken and sites 2a and 2b which are not thought to have undergone major maintenance for several years. The data from site 1 are thought to represent more closely the initial state of ballast represented by the laboratory results, presented in later sections.

Ideally, deflection/time results from different sleepers and opposite sleeper ends are compared for the same train passage. However, comparisons of deflection/time results are sometimes made using data from different Pendolino trains. This is necessary because, with the limited number of geophones and data logging channels available, the geophones had to be moved around to capture all the data of interest across a number of sleepers. The velocities for all the Pendolino trains were similar and the axle loads would also be broadly similar. Therefore comparison of different geophone measurements between different Pendolino trains is not expected to introduce significant error and this will be shown in this section. Figure 5-4 shows the key to the site 1 data presented.

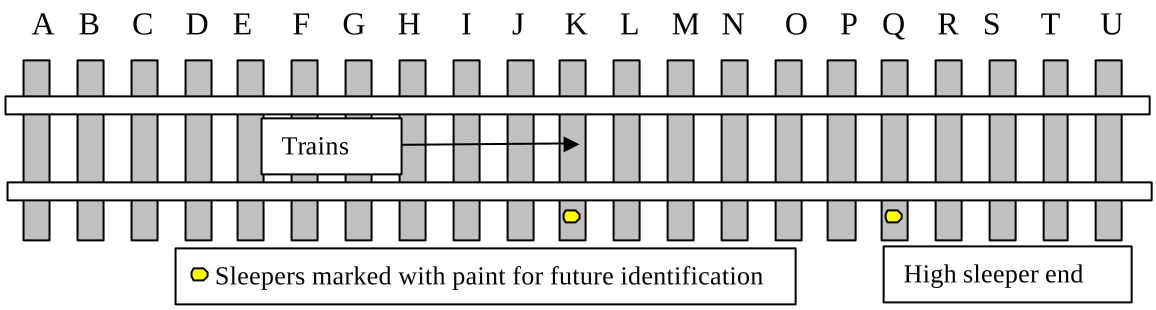

Figure 5-4: Site 1 with sleeper labels, (Curve radius=1230 m; Cant=150 mm)

Figure 5-5 shows typical data of vertical sleeper deflections at the high rail end from sleepers E and G. The Pendolinos are set up in their nine car configuration comprising 18 bogies and 36 axles; these can be clearly identified in the peaks and troughs of the time deflection plots which are about a zero deflection mean for the data set. In either graph of Figure 5-5, reading from left to right, as the first axle approaches the sleeper the geophone begins to record upward and then downward relative deflection. However, the video monitoring data has shown that any upward deflection is minimal and the apparent upward deflection shown in the geophones is an artefact of the equipment and the filtering methods. For the initial axle, the downward deflection appears larger than for subsequent axles until the final axle produces a similar result. This is not the case, however, when considering the absolute range of movement from the first positive peak to the first negative trough which is no greater than subsequent absolute ranges of movement.

To obtain a range of movement representing the resilient deflection for a single axle load, the 7th axle is taken as typical. These are used to produce Figure 5-6 and Table 5-1 using the data from two Pendolino trains curving at ~110 mph.

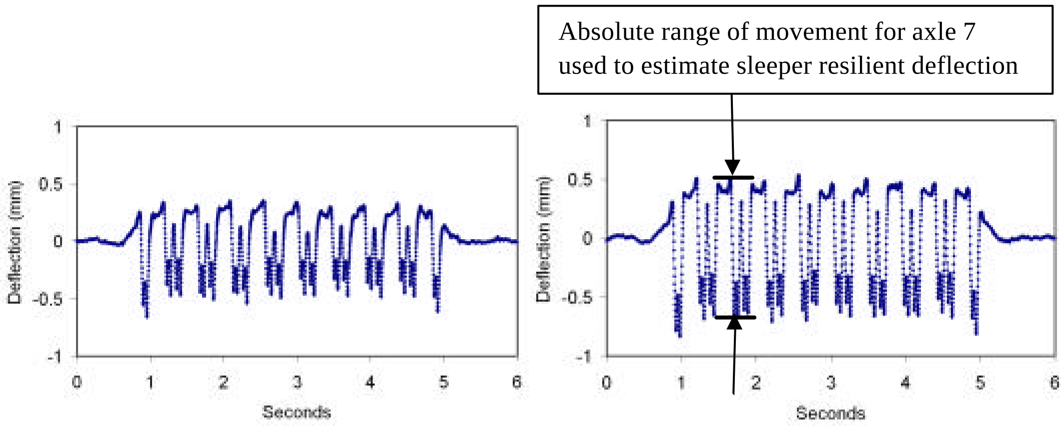

Figure 5-5: Vertical deflection data at high sleeper end during passage of a Pendolino train at 110 mph, sleepers E, G, set-up 1[4], same train run

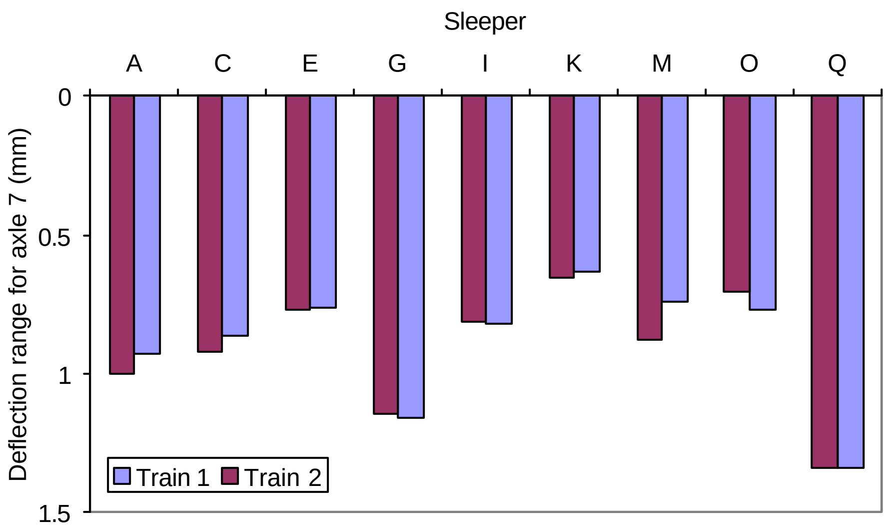

Figure 5-6: Vertical range for axle 7 for a single pass of a Pendolino travelling at ~110 mph, site 1, set up 1, all geophones located on the high sleeper end, train run 1 and 2

	Minimum (mm)	**Maximum (mm)**	**Mean (mm)**
Train 1	0.63	1.34	0.89
Train 2	0.65	1.34	0.91
Mean train 1 and 2	0.64	1.34	0.90

Table 5-1: Summary of deflection range for high sleeper end for axle 7 across 9 sleepers at site 1 during two different Pendolino train passages

[4] See appendix B for details of the geophone arrangements for each set up.

At site 1 it was relatively simple to set up geophones at the high sleeper end. However gaining access to the low sleeper end was more problematic due to the need to run cables beneath the track. In addition although the key in appendix B may indicate that geophones were present on both sleeper ends, the sensitivity of the equipment, the difficulty of working on in-use track and the need to continually adjust the arrangement of equipment in sometimes difficult weather conditions meant that some data was inevitably found to be erroneous. For these reasons there were relatively few sleepers for which data on the low and high sleeper end were recorded simultaneously. Figure 5-7 shows the high and low end sleeper time/deflection plots for the same sleepers for data from two train runs. Both train runs had one geophone position in common at the high end of sleeper K, results from this geophone gave similar magnitudes of deflection implying that both trains had similar axle loads as well as nearly identical speeds. The speed can be estimated by dividing the length of the train (217 m) less the distance to the first axle and from the last axle (2.725 m each) by the time from the first axle to the last taken from the geophone deflection data. In each set of data shown here this is very close to 110 mph.

It can be seen in Figure 5-7 that the high end sleeper deflections are much greater than those at the low end. Also, the high end sleeper movements can be used to identify more clearly the passage of bogies and axles, with the low end deflections being more erratic.

It can also be seen in Figure 5-5 and Figure 5-7 that a common feature of the vertical deflections of each sleeper end was that for each bogie the high sleeper end has a tendency for the second axle to deflect more than the first axle, whereas, in contrast to this, the low sleeper end shows the reverse tendency. The reasons for this will be explored further in Chapter 7.

Figure 5-8 and Table 5-2 compare the range of deflection for axle 7 as it passes two different sleepers at the high and low ends at site 1.

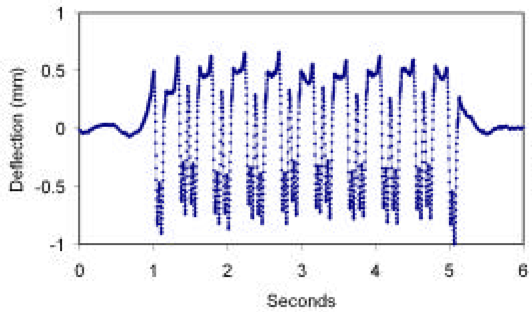

Sleeper Q high end (setup 1, run 1)

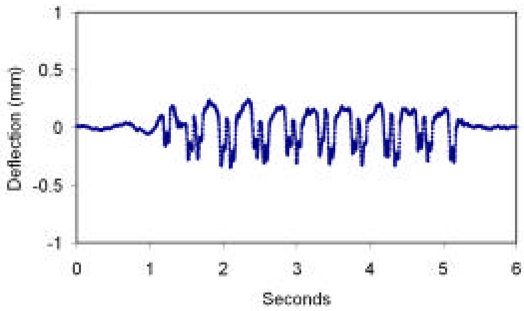

Sleeper Q low end (set up 3, run 14)

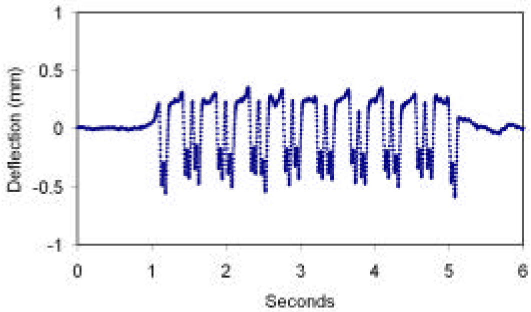

Sleeper K high end (set up 3, run 14)

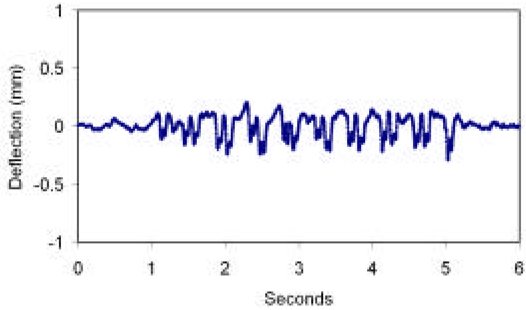

Sleeper K, low end (set up 3, run 14)

Figure 5-7: Comparison of vertical deflection at opposite sleeper ends during passage of Pendolino trains at site 1 for runs 1 and 14

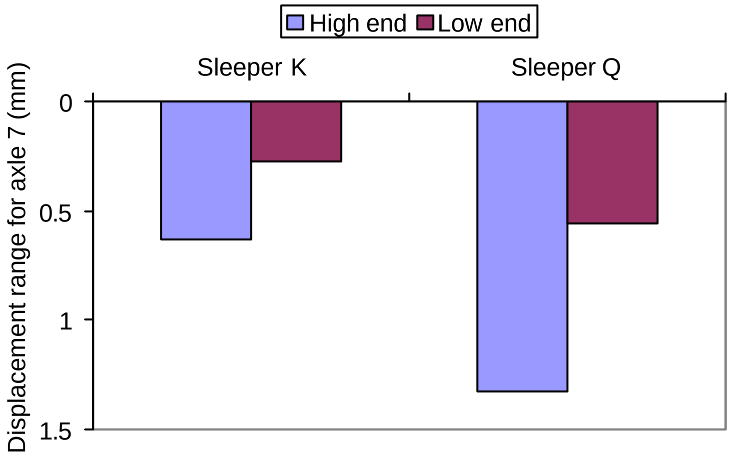

Figure 5-8: Sleeper vertical deflections at opposite ends for axle 7 of a Pendolino using data from set up 1 train runs 1 and 14, , trains travelling at ~110 mph on a 1230 m radius curve

Sleeper end	K (mm)	Q (mm)	Mean (mm)
Low	0.28	0.56	0.42
High	0.63	1.33	0.98
mean	0.46	0.95	0.70
Ratio, low to high	1:2.25	1:2.38	1:2.31

Table 5-2: Summary of deflection range data for both sleeper ends of axle 7 across 2 sleepers at site 1 during Pendolino train passage, trains travelling at ~110 mph on a 1230 m radius curve

Figure 5-9 and Table 5-3 compare the vertical range of deflection for axle 7 at either end of a sleeper each from site 2a and site 2b.

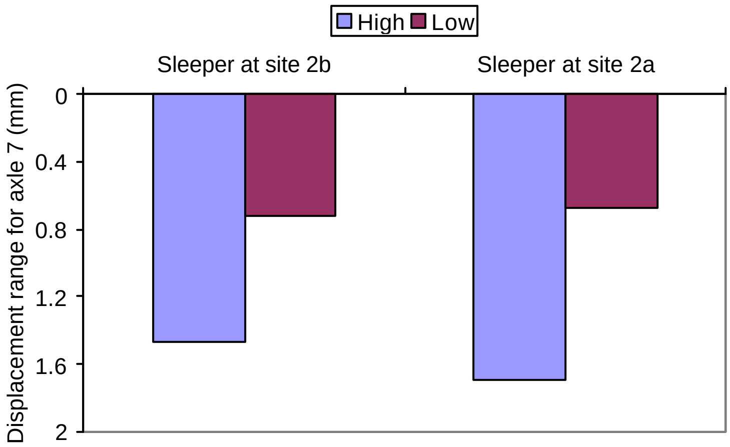

Figure 5-9: Sleeper vertical deflections at opposite ends for axle 7 of a Pendolino using data from sites 2a and 2b[5], trains travelling at ~110 mph on a 1025 m radius curve

Sleeper end	2b (mm)	2a (mm)	Mean (mm)
Low	0.72	0.66	0.69
High	1.47	1.71	1.59
Mean	1.10	1.19	1.14
Ratio, low to high	1:2.04	1:2.59	1:2.30

Table 5-3: Summary of deflection range data for both sleeper ends of axle 7 across 2 sleepers at site 2a and 2b during Pendolino train passage, trains travelling at ~110 mph on a 1025 m radius curve

[5] Site 2b data from run 8, set up 3, channels 3 and 1. Site 2a data from set up 4 run 14 channel 6 and set up 5 run 12 channel 10.

5.1.4. Interpretation, geophone monitoring data

In Figure 5-6 the bars indicate the deflections for two trains. The Pendolino trains that are recorded in the geophone data are travelling at similar speeds and are likely to be of similar weight. Figure 5-6 and Table 5-1 show that for similar loading events individual sleepers deflect over similar ranges but their behaviour in relation to nearby sleepers can be quite different in range of deflection. Although it is not shown here data from dozens more trains give the same characteristic behaviour. Site 2 also shows variation between the two sleepers instrumented, and although no data is shown here, again sleepers showed consistent behaviour due to similar loading events.

Several trends are apparent from the geophone data shown from sites 1 and 2:

- The range of movement for the same sleepers was consistent for different Pendolino trains passing at ~110 mph.
- There was a significant range in the deflection response between sleepers over a relatively short length of track. For the nine high end sleeper deflection data shown in Figure 5-6 the movement range more than doubles from 0.63 mm to 1.35 mm.

Given that the cant of the track and speed of the trains is known and the load may be estimated, the geophone data may also be compared to expected behaviour based on a calculation of normal forces on the railheads.

For an average Pendolino car at 180% passenger tare the axle mass is known to be 14793 kg. Using the geometry shown in Figure 3-6 the lateral and normal forces on the rail heads may be calculated. If this load is considered proportional to the deflection beneath the sleeper, the ratio of deflection for a point 100 mm from either end of a sleeper (about where the geophones were located) may be estimated, the results are shown in Table 5-4.

		Curving force		Normal force		Ratio of deflection	
Site	**Curve Radius**	**Horizontal**	**In cant plane**	**Inner railhead**	**Outer railhead**	**Rails**	**Sleeper ends**
	m	**kN**	**kN**	**kN**	**kN**	**1.5 m apart**	**2.3 m apart**
1	1230	28.9	14.2	59.8	89.5	1:1.50	1:2.29
2	1025	34.7	20.0	54.1	96.1	1:1.78	1:2.72

Table 5-4: Proportioning of deflection to sleeper ends for 14793 kg axle mass on 150 mm canted track travelling at 110 mph

The geophone results for the four sleepers, two from site 1 and one each from site 2 shown in this section are summarised in Table 5-5.

	Ratio, low to high sleeper end deflection			
Site	**1**		**2b**	**2a**
Sleeper	**K**	**Q**		
Measured from geophone data	1:2.25	1:2.38	1:2.04	1:2.59
Calculated from an elastic proportioning of the load	1:2.29		1.:2.72	

Table 5-5: Vertical deflection ratio from geophone data

The results in Table 5-5 show that the measured ratio of deflection is in reasonable agreement to an estimate due to a proportioning of the normal force on the rail heads. Although there is some variation in the data, i.e. the ratio for the sleeper at site 2b is lower than expected.

5.2. Vertical plastic strain and resilient range, laboratory data

5.2.1. Background

The measured vertical deflection of the sleeper in the laboratory experiments included a component from the softboard present at the base of the ballast. Therefore the measured resilient response of the sleeper on the 300 mm ballast layer cannot be used to quantify the resilient response of the ballast. However, if the deflection from the softboard is assumed constant, the sleeper deflection may be used to evaluate plastic strain occurring in the ballast layer and changes to the resilient range of movement over the 100 load cycles.

In this section the vertical deflection measurements from the laboratory experiments taken during the first 100 load cycles are considered in respect of:

- Vertical plastic strain
- Changes to the resilient deflection range

It will be shown that the testing apparatus behaves in a similar way to real track in key characteristics of behaviour.

5.2.2. Methods, laboratory data vertical strain and resilient range

In the laboratory, 21 tests in test runs X, A, B and C were carried out without crib ballast present and are therefore appropriate for comparison of vertical deflection behaviour. Note that the 5 tests in test run X are included as they are considered suitable for comparisons of vertical behaviour, although they are not used to evaluate lateral behaviour in Chapter 7 due to inadequacies in the instrumentation arrangement which were corrected prior to the other test runs. Each test was prepared and the 100 cyclic vertical loads applied as detailed in Chapter 4.

These tests examine the behaviour of the base sleeper/ballast only. However, it is recognised that crib ballast would influence the vertical response although this would not be expected to have a significant influence on individual cylces of load.

For test runs X and A the rails were loaded equally, for test runs B and C the load was placed at an eccentricity of 0.5 m from the centreline towards the sleeper end where the sleeper was attached to the lateral hyrdualic ram. The railhead closest to the two rams is referred to as the "near end" with the opposite sleeper end referred to as the "far end". (i.e. the near end received the greater vertical loading in the eccentric loading tests). The vertical deflection was measured within about 100 mm from each end of the 2.5 m long sleeper, so that the vertical LVDTs were in similar locations relative to the sleeper ends as the geophones.

5.2.3. Results, laboratory data vertical strain

The plastic vertical strain in the ballast layer is defined as the change in the measured vertical deflection of the sleeper over a load cycle divided by the depth of ballast (300 mm). The change in vertical deflection is evaluated as the load returns to the minimum point in each sinusoidal load cycle (from 10 kN to 80 kN and back to 10 kN). Graphs produced from some of the tests, considered to show behaviour representative of all tests, are presented in Figure 5-10 with individual test strain data and a summary of plastic strains after 100 load cycles in Table 5-6 and Table 5-7 respectively. Note that N/A indicates that some inconsistency in the data or a mistake in test preparation and execution resulted in the data being discarded, a negative strain indicates a reduction in ballast layer thickness.

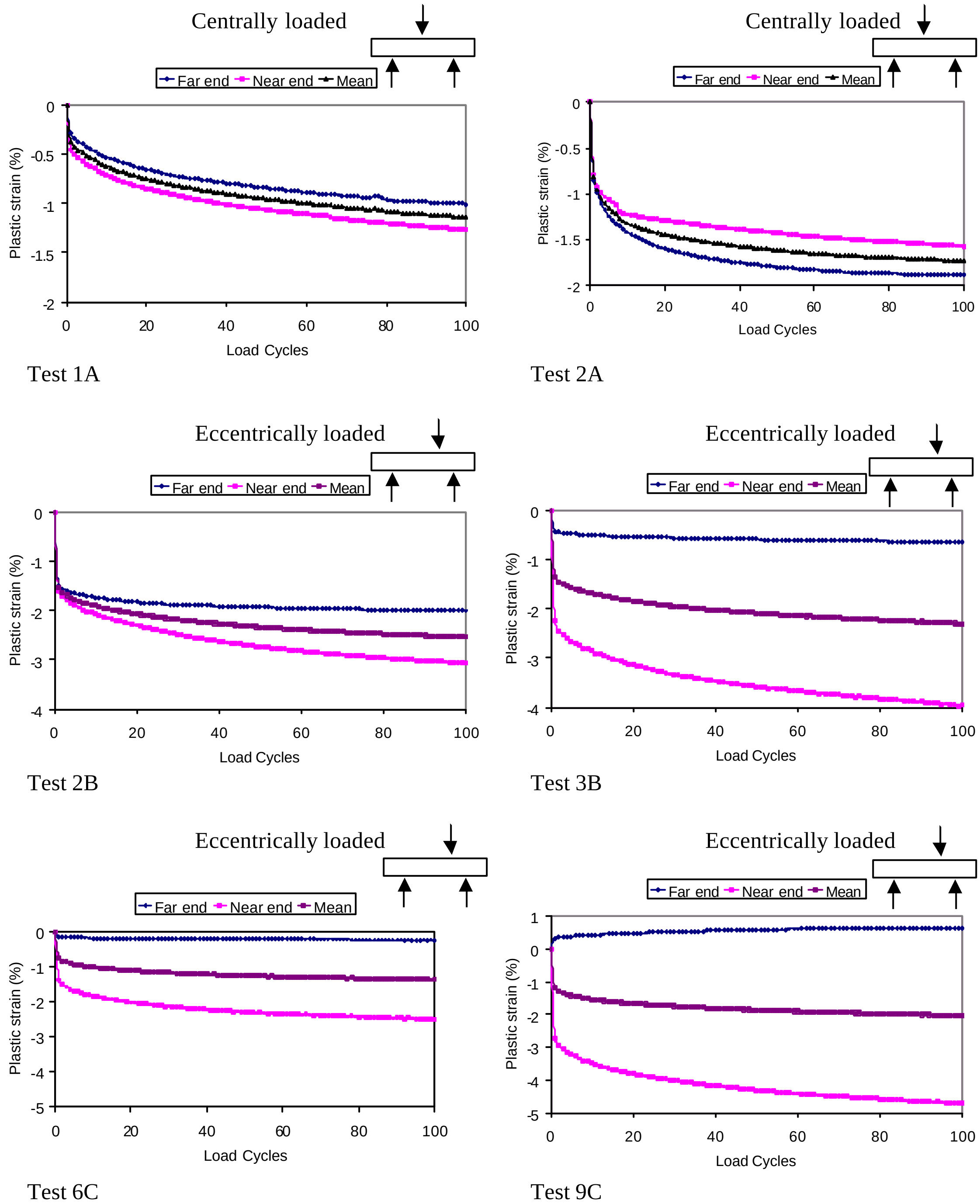

Figure 5-10: Vertical strain[6] during 100 vertical load cycles for selected tests, the load is cycled from 10 to 80 kN

---

[6]In test 2a the initial 7 load cycles were from 10 kN to 85 kN (not 10 kN to 80kN). When this error was corrected a kink in the graph for the near and far end measurements occurs; this represents a differential settlement at the sleeper/ballast contact. The mean plastic strain appears largely unaffected and the data is considered sufficiently accurate for trends to be observed.

		Plastic strain (%)		
Test	**Loading**	**Far**	**Near**	**Mean**
1X	Central	N/A	N/A	N/A
2X	Central	1.62%	1.26%	1.44%
3X	Central	3.94%	2.05%	3.00%
4X	Central	3.60%	1.09%	2.34%
5X	Central	2.88%	1.33%	2.10%
1A	Central	1.97%	2.53%	2.25%
2A	Central	1.89%	1.58%	1.73%
3A	Central	N/A	N/A	N/A
1B	Eccentric	0.99%	3.44%	2.22%
2B	Eccentric	2.01%	3.06%	2.53%
3B	Eccentric	0.64%	3.92%	2.28%
4B	Eccentric	-0.28%	3.16%	1.44%
1C	Eccentric	0.13%	3.33%	1.73%
2C	Eccentric	0.45%	3.44%	1.95%
3C	Eccentric	0.49%	2.89%	1.69%
4C	Eccentric	0.57%	3.26%	1.92%
5C	Eccentric	-0.15%	3.79%	1.82%
6C	Eccentric	0.24%	2.39%	1.32%
7C	Eccentric	-0.22%	2.88%	1.33%
8C	Eccentric	-0.42%	4.20%	1.89%
9C	Eccentric	-0.64%	4.70%	2.03%

Table 5-6: Vertical plastic strains[7] for all tests over 100 cycles of load from 10 kN to 80 kN

Test run	**Far end plastic strain (%)**			**Near end plastic strain (%)**			**Both sleeper ends mean plastic strain (%)**		
(number of tests)	**Max, single test**	**Min, single test**	**Mean all**	**Max, single test**	**Min, single test**	**Mean all**	**Max, single test**	**Min single test**	**Mean, all**
X (5-1)	-3.94	-1.62	-3.01	-2.05	-1.09	-1.43	-3.00	-1.44	-2.22
A (3-1)	-1.97	-1.89	-1.93	-2.53	-1.58	-2.05	-2.25	-1.73	-1.99
B (4)	-2.01	0.28	-0.84	-3.92	-3.06	-3.4	-2.53	-1.44	-2.12
C (9)	-0.57	0.64	-0.05	-4.7	-2.39	-3.27	-2.03	-1.32	-1.74
All (21-2)	-3.94	0.64	-1.04	-4.7	-1.09	-2.81	-3.00	-1.32	-1.92

Table 5-7: Summary of vertical plastic strains for all tests over 100 cycles of load from 10 to 80 kN

Consideration of Figure 5-10, Table 5-6 and Table 5-7 reveals that the plastic strain varies significantly from test to test. This is thought to have been due to the variability of structure within the ballast and variability in the consistency of the sleeper/ballast contact.

[7] Tests omitted due to data inconsistencies/experimental error/human error: 3A, 1X

5.2.4. Interpretation, vertical strain data

Following placement or maintenance, ballast initially undergoes rapid plastic settlement (Selig and Waters, 1994). This is clearly identifiable in all the tests shown here. The plastic strain during the first loading cycle in the laboratory tests was sometimes as great as in the following 99 cycles (e.g. test 3B). By comparing the strain at each sleeper end in Figure 5-10 it can be seen that, across the full footprint of the sleeper, strain is often highly biased to one end, even when the sleeper is loaded centrally as in the case of tests 1A and 3A. When the sleeper is loaded eccentrically as for tests 2B, 3B, 6C and 9C the ballast beneath the "near" sleeper end closest to the load strains by a greater amount. Also, it is sometimes possible for the sleeper end farthest from the load to rise over the course of the 100 loading cycles as indicated by a positive strain relative to its initial level as in test 9C. The rise is probably caused partly by an inconsistent sleeper/ballast contact. However, despite the differences in the plastic strain at opposite sleeper ends, the mean plastic strain for both sleeper ends, regardless of whether the load was centrally or eccentrically applied was more consistent. These trends are illustrated in the box and whisker plots shown in Figure 5-11.

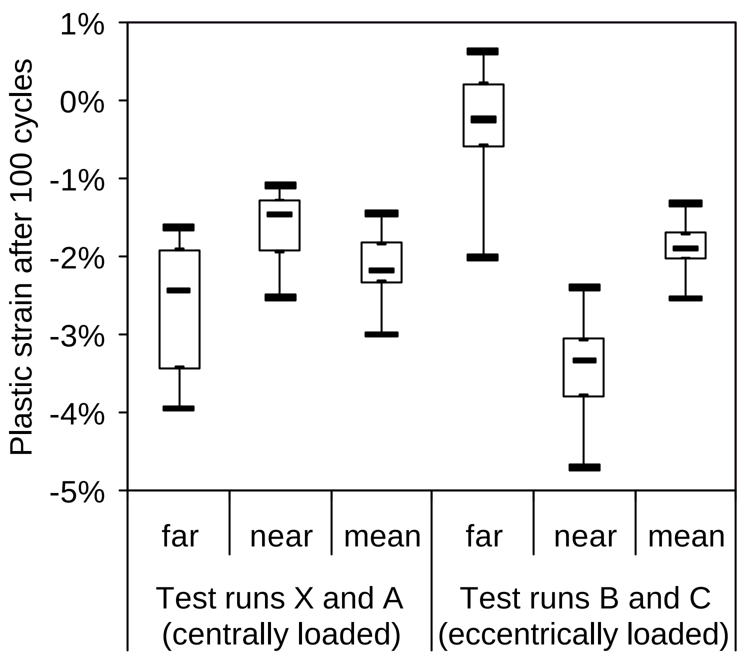

Figure 5-11: Comparison of plastic strains for test runs with central and eccentric load, far, near and mean of sleeper ends

The laboratory plastic strains can be compared with actual track measurements. Following placement or maintenance the plastic strain in the ballast layer can be represented by a power relation (Selig and Waters, 1994):

$$e_N = e_1 N^b \qquad \textbf{Equation 5-1}$$

Where:

$e_{\boldsymbol{N}}$ =	strain in ballast layer after N cycles of load
$\boldsymbol{N}$ =	number of cycles of load
$e_{\boldsymbol{1}}$	ballast strain after the first cycle
$\boldsymbol{b}$ =	exponent

In this relation the number of load cycles may be changed to cumulative tonnes of load (usually quoted in Mega Tonnes; MGT) and the values $e_{\boldsymbol{1}}$ and $\boldsymbol{b}$ adjusted accordingly. Provided some experimental data are available this relation can be used to estimate ballast settlement with traffic. Selig and Waters (1994) reported that a particular granite ballast's plastic strain beneath a wooden sleeper ($e_{\boldsymbol{T}}$) immediately after construction for the first 300 MGT on a test track could be matched by a best fit power equation:

$$e_{\boldsymbol{T}} = -0.026\boldsymbol{T}^{0.21} \qquad \textbf{Equation 5-2}$$

Where $\boldsymbol{T}$ is MGT of cumulative load

In the tests for this research 100 cycles of load for a 15 tonne axle correspond to a cumulative load of 0.0015 MGT and applying Equation 5-2 gives -0.66% of plastic strain after the first 100 cycles as shown in Figure 5-12 where the mean strain from test 3B is also plotted for comparison. -0.66% is about 1/3 of the mean result (-1.92%) from all tests carried out for this research.

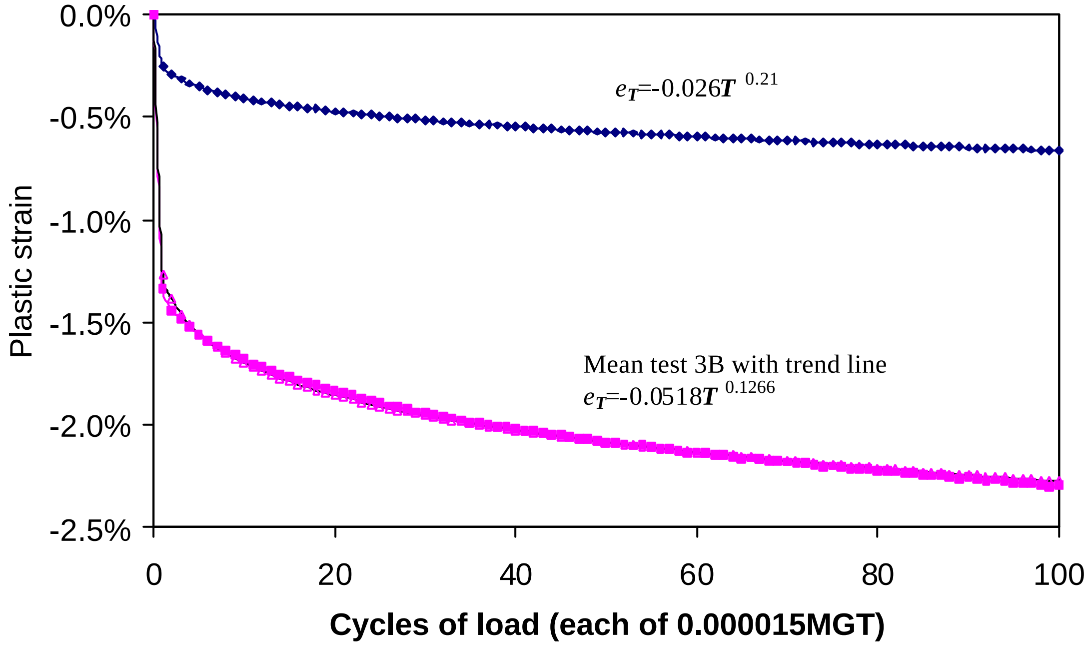

Figure 5-12: Comparison of plastic strain between that calculated from Equation 5-2 and the measured mean strain from test 3B

The difference from the strain predicted by Equation 5-2 to the much greater strain measured in the tests could be due to a combination of circumstances including that:

- The test track had been previously loaded by construction traffic.
- There are differences in the type of ballast.
- The laboratory ballast was placed more loosely.
- The superstructure of the track was different.

Wooden sleepers may develop more consistent sleeper/ballast interface contact because of the ability of particles to penetrate into the softer wooden base and transfer the load through a greater number of initial contact locations. Also, any differences in track component stiffnesses will give rise to a different track modulus and different proportions of axle load reaching sleepers.

It is interesting to note that fitting a power relation using a regression analysis to test 3B ($e_T = -0.0518\boldsymbol{T}^{0.1266}$ with $\boldsymbol{R}^2$=0.9936) results in an equation that implies an initially very much greater magnitude of strain with loading cycles represented by the greater coefficient (0.0518 as opposed to 0.026). However, the rate of plastic strain reduces faster represented by the lower power (0.1266 as opposed to 0.21). This is perhaps because in the laboratory there is no contribution to strain from subgrade.

To end this section several general observations can be made:

- The laboratory behaviour shows similar trends to real track data but larger initial plastic strains, probably due to a looser initial structure.
- There is variation between the plastic strains measured at opposite sleeper ends and between different tests for both central and eccentrically loaded tests. However, the mean for both sleeper ends is more consistent.
- The 100 cycles of load in the tests carry out an important role in bedding in the ballast so that by the end the ballast is more likely to correspond to freshly tamped track ballast. This improves consistency and comparability between test set-ups for subsequent tests to investigate the effects of combined cyclic vertical lateral and moment loading.

The procedures are therefore considered adequate.

5.2.5. Results; vertical resilient data

On real track the strain per load cycle in the ballast layer reduces very rapidly so that after a certain number of load cycles the plastic strain per cycle is barely discernable between individual and tens or hundreds of load cycles. This is a very important feature of track system behaviour because if it didn't happen differential settlement between sleeper ends and relative to adjacent sleepers would necessitate maintenance at uneconomic intervals.

While the plastic strain may vary little over many load cycles so that it is unimportant so far as an individual train is concerned, there is a resilient range of deflection per load cycle which is very important for the performance of the train.

In the laboratory experiments, the majority of the deflection during cycle one is non-recoverable. Therefore the resilient deflection per cycle is evaluated from the start of load cycle two and is defined as the difference between the deflection at the peak of one cycle and the deflection at the start of the following cycle. For some tests, the minimum measured deflections for each cycle did not precisely correspond to minimum load at one sleeper end. It was thought that this may have been due to inconsistent sleeper/ballast contact resulting in an effective pivot point beneath the sleeper base, active at the lower end of each loading cycle. The mean sleeper resilient deflection as an average of the measurements taken at each sleeper end for all tests was more consistent.

Figure 5-13, Figure 5-14, Figure 5-15 and Figure 5-16 compare the resilient deflection per cycle for the 100 load cycles for centrally loaded tests 1A and 2A and eccentrically loaded tests 2B and 3B.

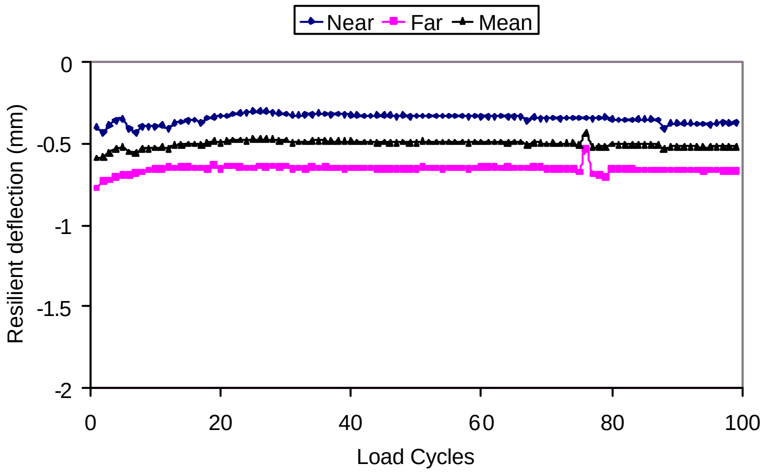

Figure 5-13: Resilient deflection for test 1A

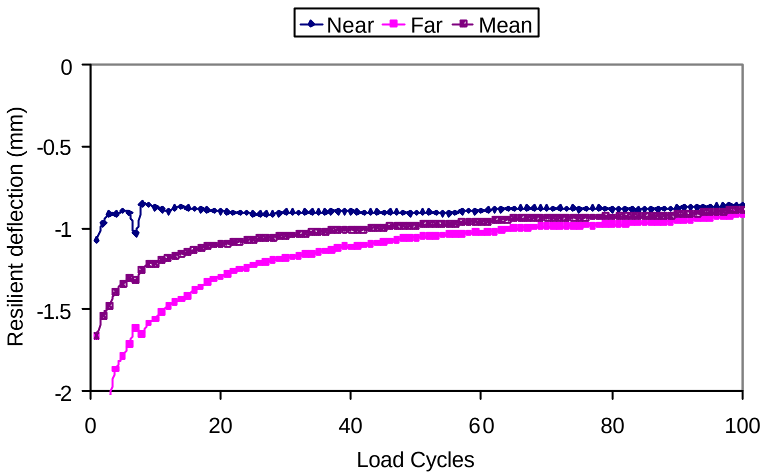

Figure 5-14: Resilient deflection for test 2A

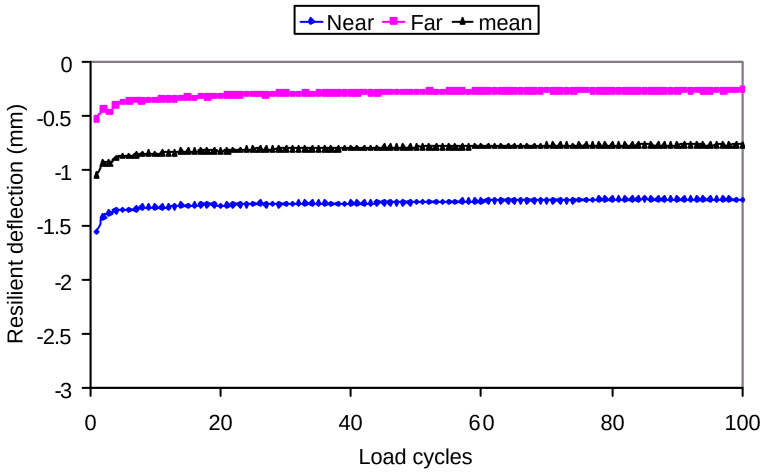

Figure 5-15: Resilient deflection for test 2B

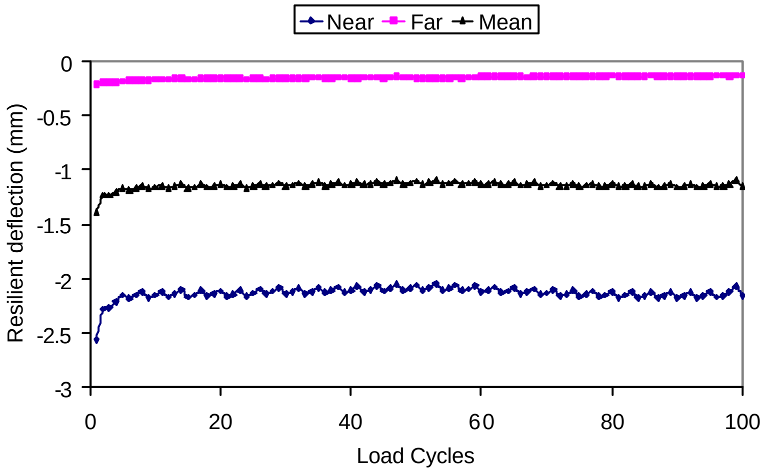

Figure 5-16: Resilient deflection for test 3B

Table 5-8 shows the resilient movement at cycle 2 and cycle 100 for all tests, Table 5-9 and Table 5-10 summarise the resilient range for cycle 2 and cycle 100 respectively for the different test runs with means of comparable data runs also provided.

		Resilient range cycle 2			Resilient range cycle 100		
Test set-up	**Loading**	**far**	**near**	**mean**	**far**	**near**	**mean**
1X	Central	N/A	N/A	N/A	N/A	N/A	N/A
2X	Central	1.78	0.43	1.10	1.71	0.55	1.13
3X	Central	0.87	0.83	0.85	0.65	0.76	0.70
4X	Central	1.80	0.12	0.96	0.99	0.39	0.69
5X	Central	1.04	0.59	0.81	0.65	0.44	0.55
1A	Central	0.64	0.26	0.45	0.66	0.37	0.51
2A	Central	1.85	0.68	1.27	0.90	0.85	0.87
3A	Central	N/A	N/A	N/A	N/A	N/A	N/A
1B	0.5 m eccentric	0.33	1.03	0.68	0.24	0.79	0.52
2B	0.5 m eccentric	0.34	1.19	0.76	0.26	1.28	0.77
3B	0.5 m eccentric	0.16	1.99	1.08	0.14	2.26	1.20
4B	0.5 m eccentric	0.55	1.95	1.25	0.43	2.23	1.33
1C	0.5 m eccentric	0.24	1.72	0.98	0.18	1.77	0.98
2C	0.5 m eccentric	0.18	1.46	0.82	0.11	1.87	0.99
3C	0.5 m eccentric	0.33	1.67	1.00	0.18	2.16	1.17
4C	0.5 m eccentric	0.25	1.59	0.92	0.15	1.87	1.01
5C	0.5 m eccentric	0.24	1.55	0.90	0.22	1.65	0.94
6C	0.5 m eccentric	0.24	1.36	0.80	0.22	1.43	0.83
7C	0.5 m eccentric	0.25	2.01	1.13	0.07	2.69	1.38
8C	0.5 m eccentric	0.11	2.09	1.10	0.68	1.62	1.15
9C	0.5 m eccentric	0.28	1.48	0.88	0.19	1.72	0.96
Max	All	1.85	2.09	1.27	1.71	2.69	1.38
Min	All	0.11	0.12	0.45	0.07	0.37	0.51
Mean	All	0.64	1.25	0.93	0.49	1.42	0.93

Table 5-8: Summary data for resilient response cycles 2 and 100 all tests

In Table 5-8 the cells of maximum, minimum and overall mean resilient deflection for cycle 2 and cycle 100 are shaded. These will later be used for comparison to the geophone data.

Test run	**Loading**	**Far end (mm)**			**Near end (mm)**			**Both (mm)**		
		max	**min**	**mean**	**max**	**min**	**mean**	**max**	**min**	**mean**
X (5-1)	Central	1.80	0.86	1.37	0.83	0.12	0.49	1.10	0.81	0.93
A (3-1)	Central	1.85	0.64	1.25	0.68	0.25	0.47	1.27	0.45	0.86
B (4)	0.5 m ecc.	0.55	0.16	0.35	1.99	1.03	1.54	1.99	0.68	1.24
C (9)	0.5 m ecc.	0.33	0.11	0.24	2.09	1.36	1.66	1.13	0.80	0.95
AX(6)	Central	1.85	0.64	1.33	0.83	0.12	0.48	1.27	0.45	0.91
BC (13)	0.5 m ecc.	0.55	0.11	0.27	2.09	1.03	1.62	1.25	0.68	0.95
All (19)	Both	-	-	-	-	-	-	1.27	0.45	0.93

Table 5-9: Summary data for resilient response cycle 2

Test run	Loading	Far end (mm)			Near end (mm)			Both (mm)		
		max	**min**	**mean**	**max**	**min**	**mean**	**max**	**min**	**mean**
X (5-1)	Central	1.71	0.65	1.00	0.76	0.39	0.54	1.13	0.55	0.77
A (3-1)	Central	0.90	0.66	0.78	0.84	0.37	0.61	0.87	0.51	0.69
B (4)	0.5 m ecc.	0.43	0.14	0.27	2.26	0.79	1.64	1.33	0.52	0.95
C (9)	0.5 m ecc.	0.67	0.07	0.22	2.69	1.43	1.86	1.38	0.83	1.04
AX(6)	Central	1.71	0.65	0.93	0.84	0.37	0.56	1.13	0.51	0.74
BC (13)	0.5 m ecc.	0.67	0.07	0.24	2.69	0.79	1.80	1.38	0.52	1.02
All (19)	Both	-	-	-	-	-	-	1.38	0.51	0.93

Table 5-10: Summary data for resilient response cycle 100

5.2.6. Interpretation; vertical resilient data

Figure 5-17 and Figure 5-18 show box and whisker plots for cycle 2 and cycle 100 respectively. It is important to bear in mind that these graphs represent relatively few tests but some trends can be identified.

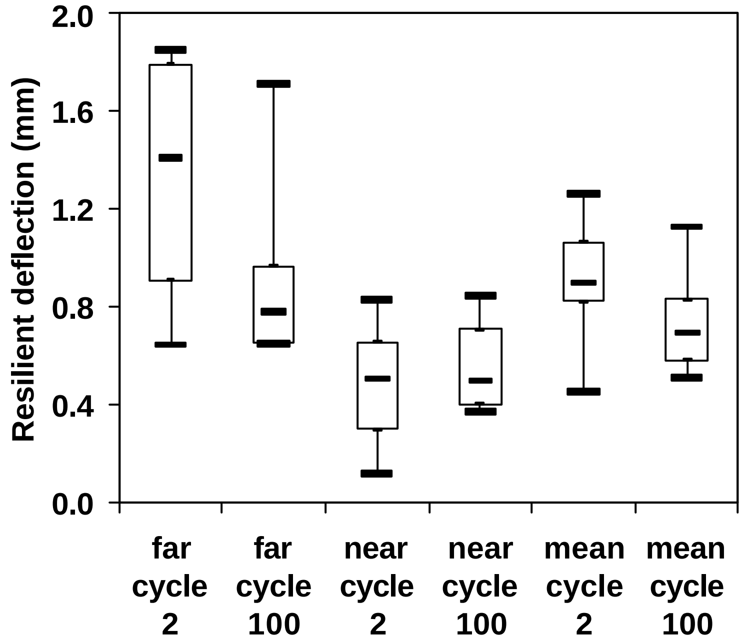

Figure 5-17: Box and whisker diagram of resilient response for centrally loaded tests

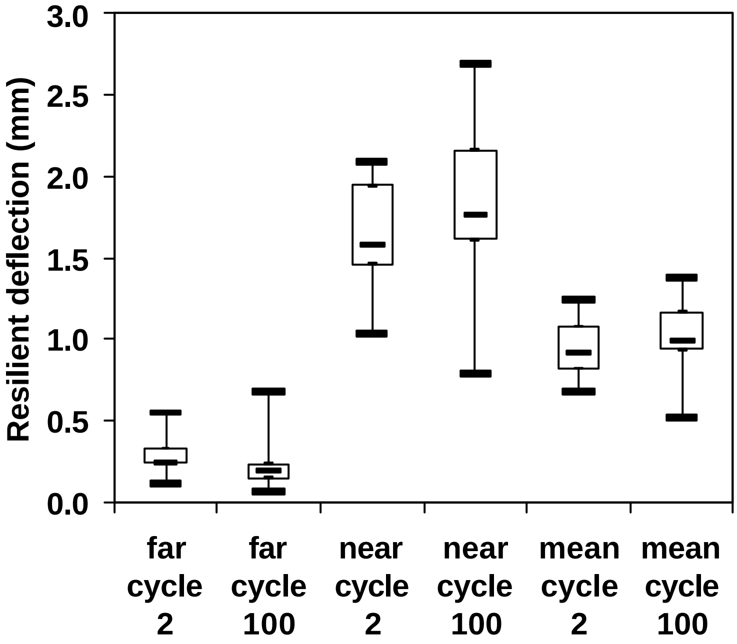

Figure 5-18: Box and whisker diagram of resilient response for 0.5 m eccentrically loaded tests

Although the terms near and far should have no meaning in the context of centrally applied load, in centrally loaded tests (Figure 5-17) there is some indication that the near sleeper end deflects over a lesser resilient range than the far sleeper end but that the difference reduced with load cycles. This could be caused by random variation in the data or a systematic effect of the testing apparatus. The near sleeper end corresponds to the location where the lateral hydraulic ram is connected and is also closer to where the load cells were located on the inside walls of the testing apparatus in test runs X and A. It is thought that these two non-symmetric features of the rig may have caused a small attraction of the load towards the near sleeper end and/or a stiffer ballast response despite the load being applied centrally.

Figure 5-18 shows the eccentrically loaded tests. As expected a greater resilient range is apparent at the sleeper end receiving the greater proportion of load (the near end). Furthermore, the range of response also increases, whereas at the opposite sleeper end the range narrows. Overall the mean resilient range increases slightly. The median ratio of deflection for test runs B and C is 1:6.4 at cycle two and 1:9.2 after 100 cycles, perhaps indicating that the higher proportion of load leads to a greater resilient response with increasing load cycles. However further experiments of more load cycles would be required to determine if this behaviour continued in the longer term.

The purpose of evaluating the resilient response of the laboratory tests was to compare it to the geophone measurements and to confirm that, although some differences exist because of difficulties in reproducing field conditions in the laboratory, the general behaviour is similar in key aspects.

The proportion of load on each railhead in the laboratory experiments and at the two sites where the geophone data on the WCML was taken varied, therefore it is considered that it is most appropriate to compare the mean deflection for both sleeper ends. In the laboratory experiments the mean sleeper deflection has been shown to be consistent regardless of the eccentricity of the vertical load.

Restating the geophone results where data was available for both sleeper ends of the same sleeper, site 1:

- the mean deflection was 0.70 mm for sleepers Q and K with individual sleeper response in the range 0.46 to 0.95 mm (Table 5-2).

At sites 2a and 2b:

- the mean deflection was 1.14 mm with all results in the range of 1.07 to 1.22 mm (Table 5-3).

The laboratory tests showed a range of mean resilient deflection for both sleeper ends from 0.45 mm to 1.38 mm with an overall mean of 0.93 mm (see Table 5-8). This is considered to place the laboratory tests well within the bounds of possibility for actual track.

5.3. Effect of loading rate on lateral response in the laboratory experiments

5.3.1. Background

It has been long known that train speed, i.e. the rate of loading, has an impact on recorded vertical deflection behaviour of the sleeper/ballast interface e.g. Raymond (1978). It is also well known amongst geotechnical researchers that amplitude of strain and rate of loading influence the shear behaviour of soils, e.g. Hardin and Drnevich (1972), Lo Presti et al., (1997).

The measured deflection of a soil medium subject to a shear force includes components of plastic and elastic strain. However, it is difficult to make a distinction between the magnitudes of each of these two components within globally measured deflections (Hardin, 1978), and the issue is further clouded when creep (also termed stress relaxation) is considered.

Kuwano (1999) showed that, for a sand, creep (d_c) obeys a log time ($\boldsymbol{t}$) relation for shear (t) so the longer a force is present and the greater that force the more creep. This may be expressed:

$$d_c = At\ln(t) \qquad \textbf{Equation 5-3}$$

Where $\boldsymbol{A}$ is a constant

This expression is only valid when the shear stress is maintained at a constant level; for dynamic loading Equation 5-3 may be evaluated over small increments and the results summed.

This research aims to characterise the lateral pre-failure behaviour of the sleeper ballast interface. To that end, it is important that loading rate effects, i.e. the contribution of stress relaxation is assessed and testing procedures adopted to minimise any impact on both the comparability and quality of testing results.

Since stress relaxation is a function of time, at higher rates of loading (i.e. train speeds) stress relaxation has less time to develop. In this section the sensitivity of stress-relaxation to loading rate is investigated and appropriate procedures adopted so that its influence on results is minimised and the applicability of results to the real track environment with rapid rates of loading from high speed trains is optimised.

It is not possible to determine the magnitude of plastic and elastic strains from the globally measured strains in the laboratory experiments. However the laboratory experiments differ from the real track environment where, after train loading, restorative forces in the form of tension in the rails may act to recover lateral displacement in addition to restorative forces from the ballast. As such it is considered that the purpose of this research is to prepare the way for further 3 dimensional models to be developed which can couple the sleeper/ballast behaviour to the behaviour of the whole track system.

5.3.2. Assessment of loading rate effects based on laboratory tests

After the application of the vertical loading cycles, all test set-ups were subject to an initial 10 pseudo static lateral load cycles as detailed in Chapter 4. Figure 5-19 shows a typical deflection and load/time graph for this. The vertical applied load was maintained at 70 kN (5 kN dead load is also present) and the lateral load then cycled from 2 to 25 kN. The sleeper deflection is re-set relative to zero when both the vertical load reaches its maximum and a 2 kN lateral seating load have simultaneously been achieved. The lateral load is applied through the railhead and the rail deflects relative to the sleeper through the Pandrol fastening and pad. Both the rail and sleeper lateral deflection show a drift over the loading cycles, this includes components of stress relaxation and plastic strain.

Applications of an initial 10 pseudo static cyclic loading tests on other test set-ups were sometimes accompanied by sudden slips of the sleeper on the ballast, a potentially dangerous behaviour. This behaviour did not usually occur after the ten pseudo static load cycles and this stage of test preparation was considered critical in ensuring that subsequent tests were able to evaluate pre-failure behaviour without dangerous slippage at higher frequencies of loading.

Further justification for the application of an initial 10 cycles of load comes in that it has been shown that the shear response of a granular medium stabilises after 10 cycles of load (Lo Presti et al., 1997).

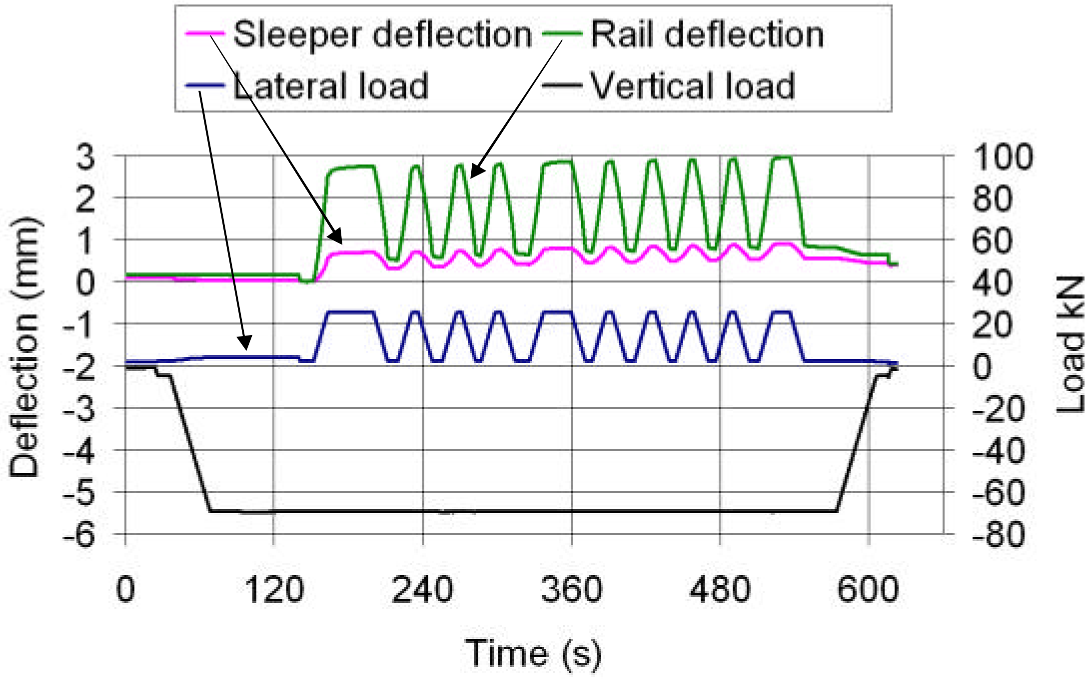

Figure 5-19: Deflection/time and load/time graph typical to all tests for an initial ten load cycles (set-up 1A)

To evaluate the contribution of stress relaxation to lateral sleeper deflection, three tests were carried out on the same test set-up where the lateral load was maintained at a high and then low constant level in the presence of a uniform vertical load of 75 kN on the sleeper/ballast interface. The maximum lateral load was maintained for approximately 4 minutes and the load was then reduced back to 2 kN and maintained for 8 minutes to observe any recovery. Load/deflection graphs are shown in Figure 5-20, Figure 5-21, and Figure 5-22; and a load and displacement/time graph for one of the tests is shown in Figure 5-23. The proportion of lateral to vertical load at failure will later (Chapter 8) be shown to have occurred by a ratio of lateral to vertical load of about 0.45 as an average of a number of tests at 2 mm of deflection, therefore in these Figures the proportion of load to failure is as shown in Table 5-11.

Figure	Vertical Load on sleeper/ballast interface (kN)	Likely Failure Lateral Load [0.45 ´ vertical load] (kN)	Maximum Lateral Load Applied (kN)	Maximum applied lateral load as a proportion of failure load (%)
5-20	75	34	10	29
5-21	75	34	15	43
5-22 & 5-23	75	34	20	58

Table 5-11: Proportion of lateral load to failure load in stress-relaxation evaluation tests

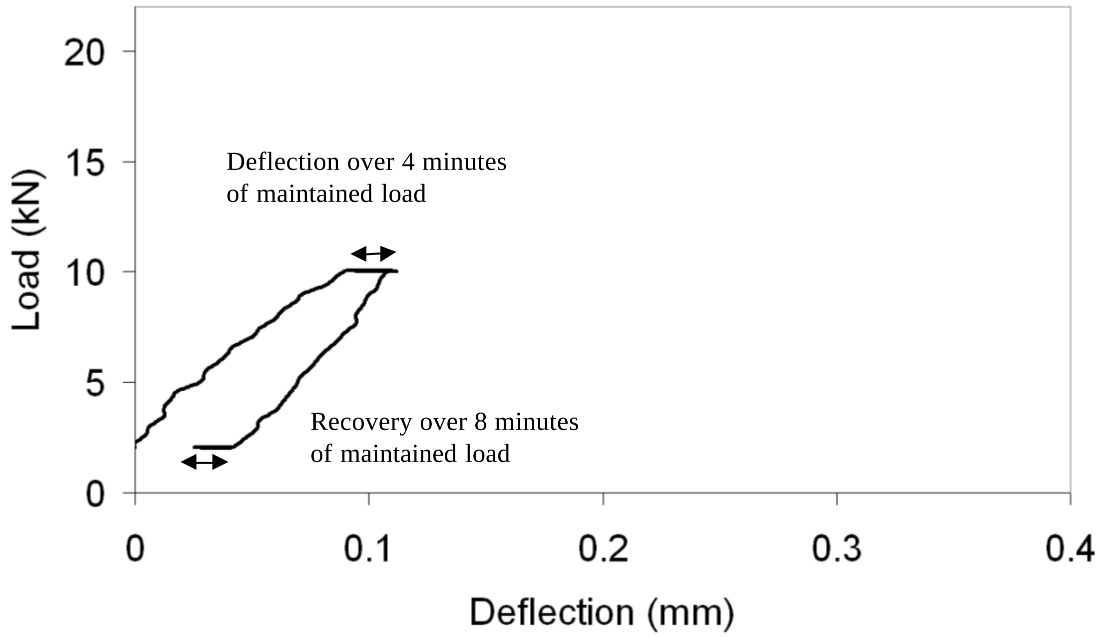

Figure 5-20: Lateral load/deflection graph to show creep, vertical load 75 kN, lateral load 2 to 10 kN

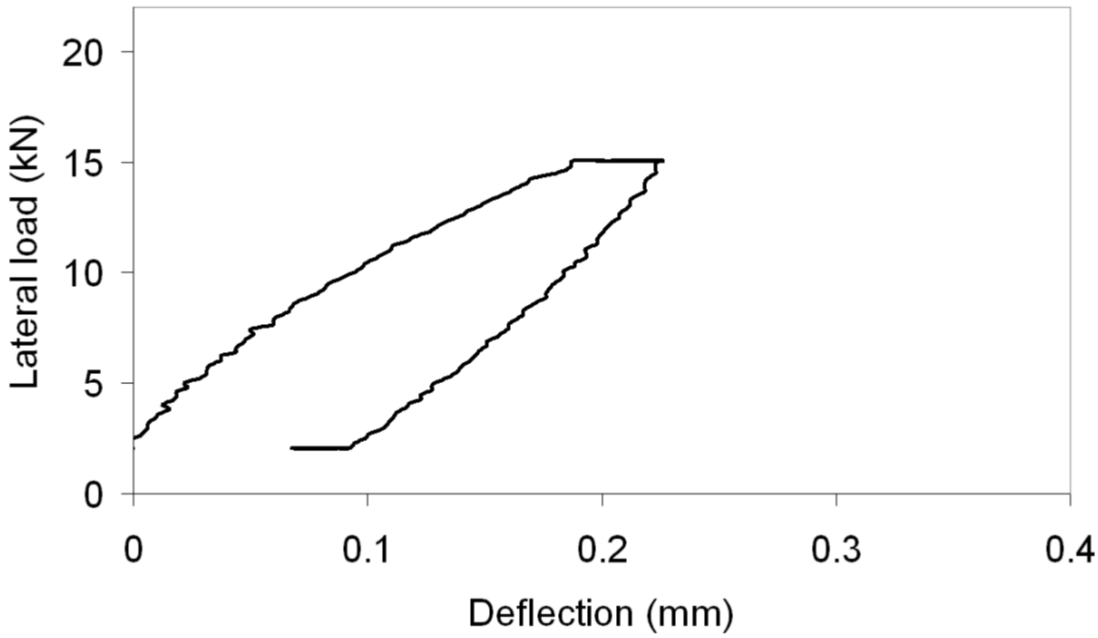

Figure 5-21: Lateral load/deflection graph to show creep, vertical load 75 kN, lateral load 2 to 15 kN

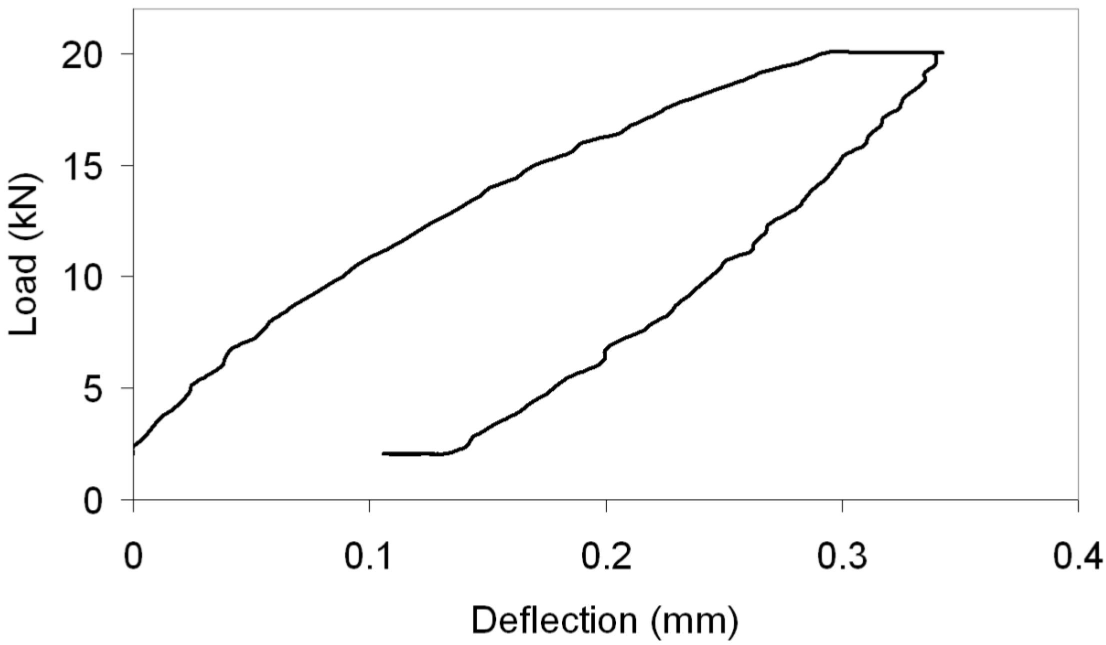

Figure 5-22: Lateral load/deflection graph to show creep, vertical load 75 kN, lateral load 2 to 20 kN

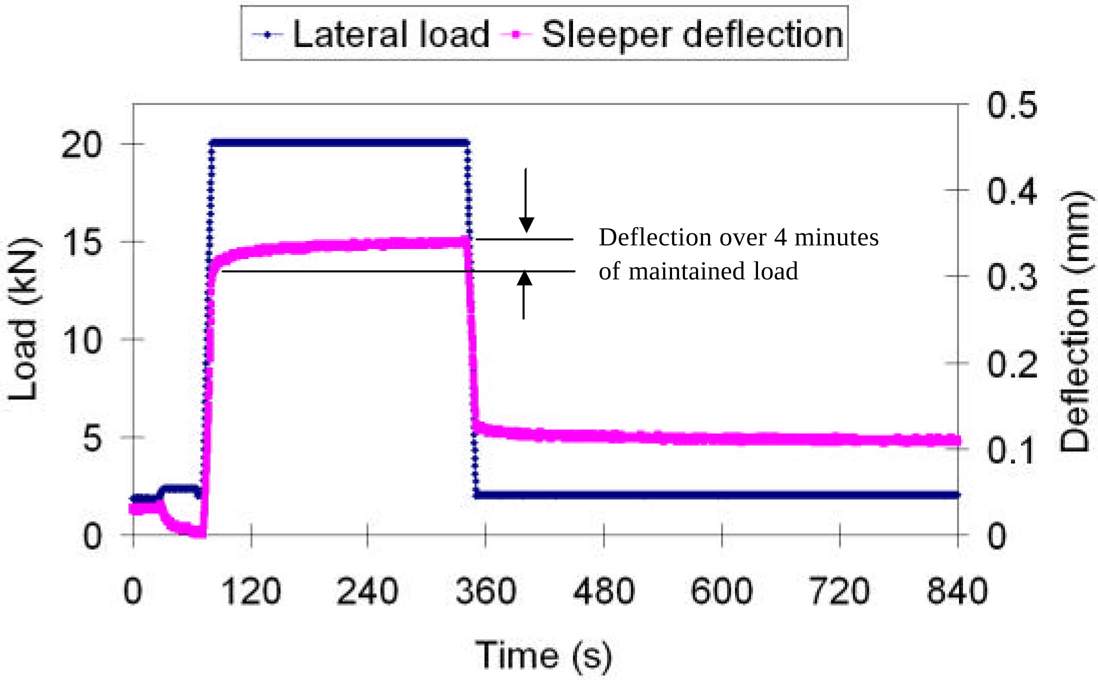

Figure 5-23: Lateral load and deflection/time graph to show creep, vertical load 75 kN, lateral load 2 to 20 kN

Table 5-12 shows the magnitudes of creep and the creep as a proportion of total deflection at maximum load.

		Creep at peak load			
Peak lateral load (kN)	**Proportion of failure load**	**From**	**To**	**Range**	**Creep as a proportion of maximum deflection**
20	58%	0.291	0.343	0.052	18%
15	43%	0.187	0.226	0.039	21%
10	29%	0.091	0.112	0.021	23%

Table 5-12: Summary of creep data

The proportion of creep in relation to the maximum deflection is similar in all three tests and appears insensitive to the changes in proportion of failure load.

After these relatively slow tests more rapid tests were carried out to ascertain if stress relaxation was apparent at more realistic rates of loading using a sinusoidal lateral loading waveform that could represent trains passing at slow speeds (although the loads would be representative of trains curving at high speed). Figure 5-25, Figure 5-26 and Figure 5-27 show load/deflection graphs for increasingly rapid rates of loading from 0.2 to 0.5 Hz where the vertical load is maintained at 75 kN and the lateral load is cycled from 2 to 20 kN over 5 cycles. Table 5-13 summarises the change in deflection at peak lateral load between cycle 1 and cycle 5.

Note that in the cyclic tests carried out it is not possible to evaluate the magnitudes of elastic strain, stress-relaxation and plastic strain separately although it is possible to observe and measure their combined effects. This is partly because the lateral load has not been cycled from 0 kN, instead, because the testing apparatus was designed only for tension (pulling) lateral loading, a minimum lateral load of 2 kN is always applied.

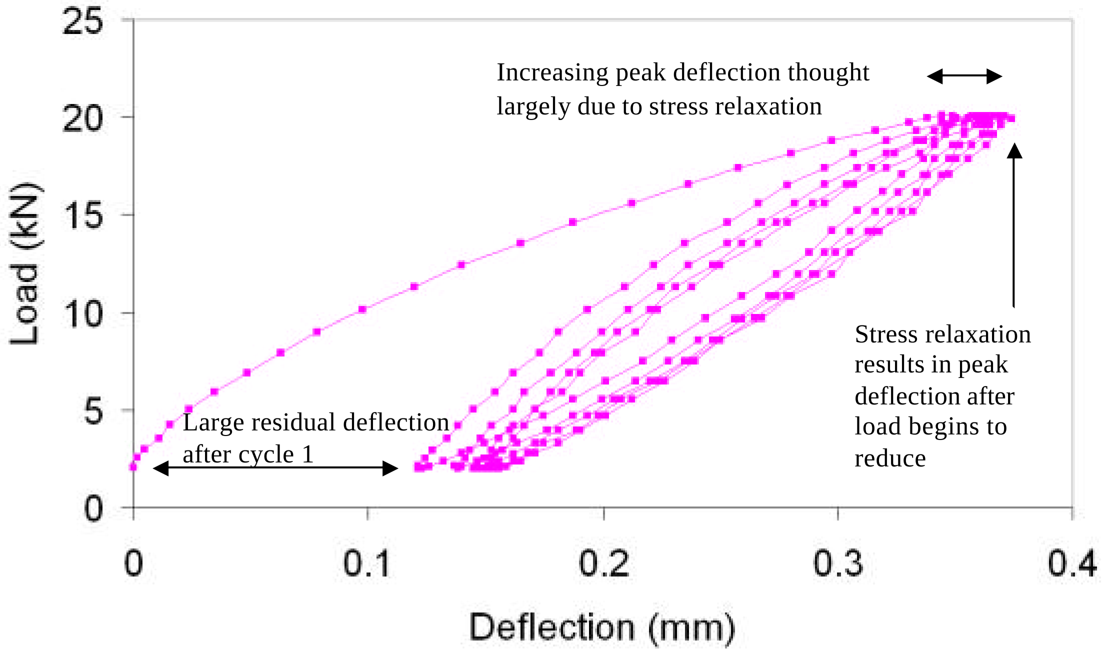

Figure 5-24: Lateral load/deflection graph, lateral load cycled from 2 to 20 kN in sine form over 10 cycles at 0.2 Hz

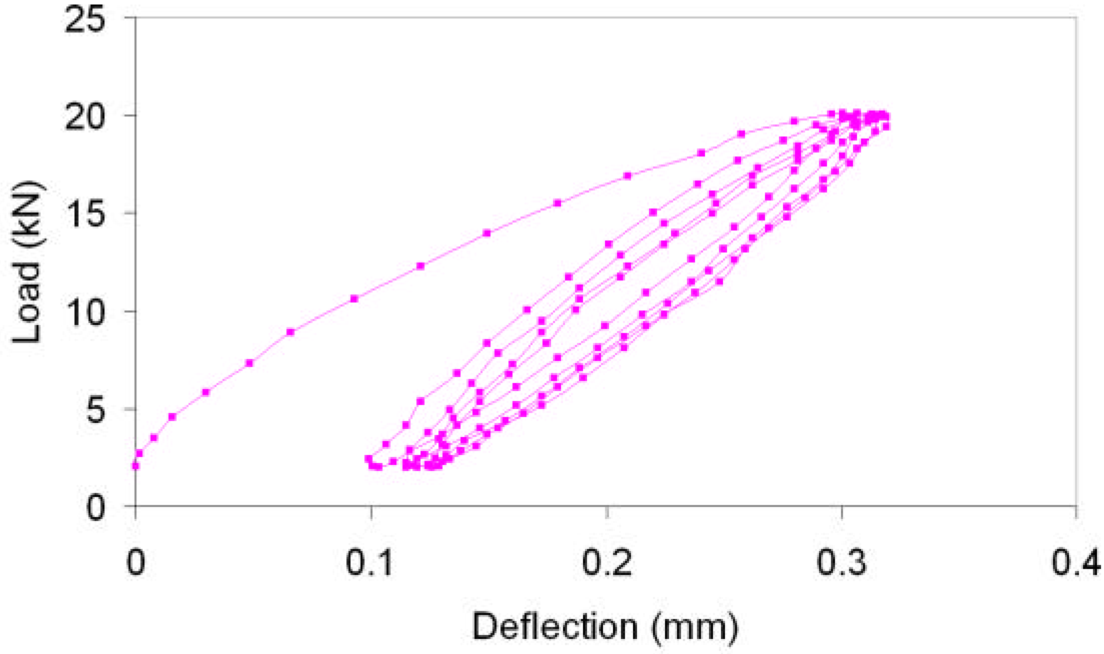

Figure 5-25: Lateral load/deflection graph, lateral load cycled from 2 to 20 kN in sine form over first 5 cycles at 0.3 Hz

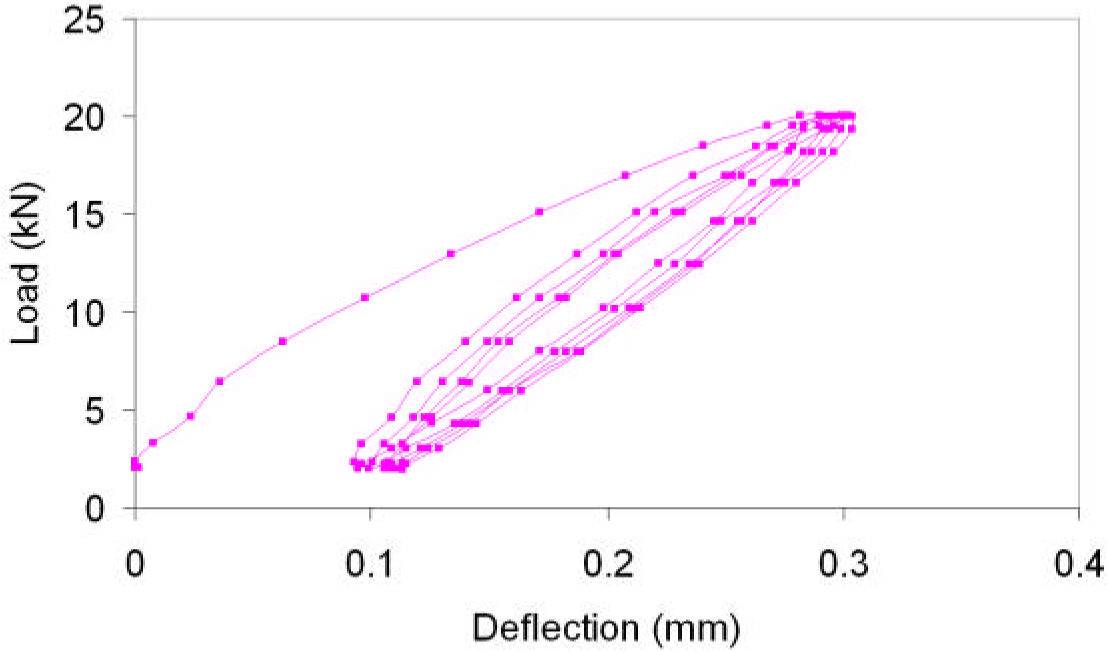

Figure 5-26: Lateral load/deflection graph, lateral load cycled from 2 to 20 kN in sine form over 5 cycles at 0.4 Hz

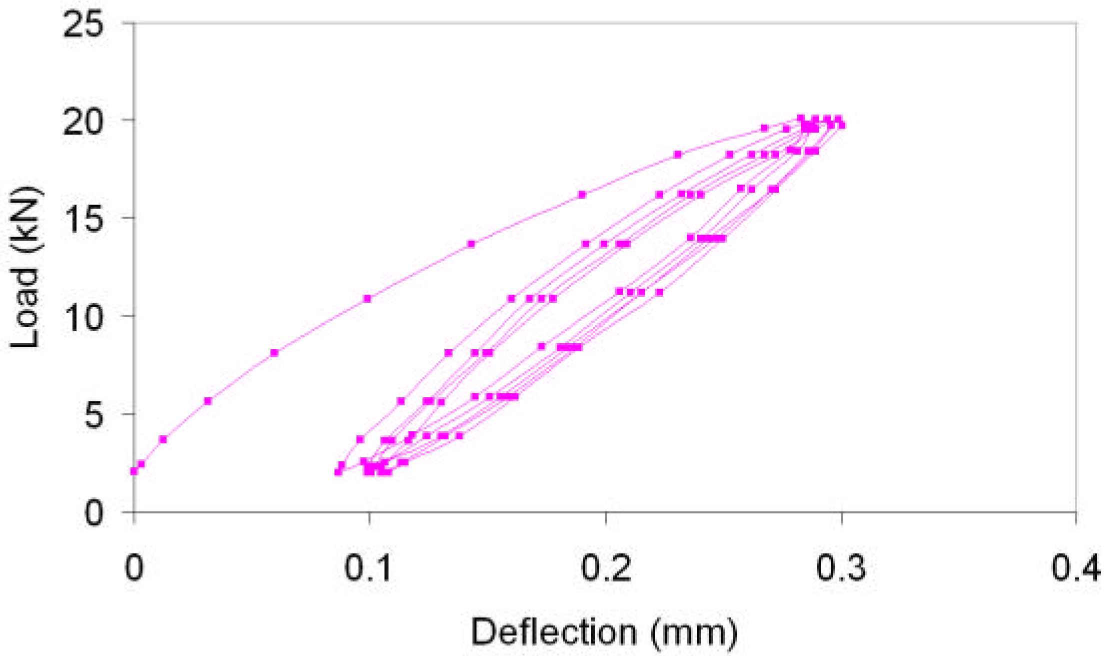

Figure 5-27: Lateral load/deflection graph, lateral load cycled from 2 to 20 kN in sine form over 5 cycles at 0.5 Hz

The load/deflection graphs show hysteresis caused by energy dissipation. A large difference in lateral deflection from the initial position to after the first cycle at 2 kN is also apparent.

Direct evidence for stress relaxation can sometimes be seen in the load/deflection graphs where the peak deflection for a load cycle occurs after the load has begun to reduce from its maximum value.

Loading rate (Hz)	**First cycle peak (mm)**	**Fifth cycle peak (mm)**	**Time interval: first cycle peak to fifth cycle peak (s)**	**Range: first cycle peak to fifth cycle peak (mm)**
0.2	0.349	0.369	20.0	0.020
0.3	0.300	0.317	13.3	0.017
0.4	0.281	0.302	10.0	0.021
0.5	0.283	0.299	8.0	0.016

Table 5-13: Summary of sleeper movement for increasing loading frequencies between first and fifth cycles

In producing Table 5-13 it was difficult to ascertain exactly the point at which the displacement reaches a peak for given load due to a too slow sampling rate. This error is minimised when considering the greater deflections corresponding to the fifth cycle, where the slower tests have greater fifth cycle peaks indicating greater proportions of stress-relaxation and plastic strain.

The geophone data shows that in-service Pendolino speeds of about 110 mph mean that the 36 axles typically pass within 6 seconds, which is an average of one axle every 1/6 of a second or 6 Hz, with axles on the same bogie passing in ~0.05 seconds or 20 Hz. Such high loading frequencies were not possible with the hydraulic rams available in the laboratory, although some tests, not reported here, were carried out at up to 5 Hz. In these tests the lateral ram was not able to apply the loading exactly, falling short over each cycle by a small proportion (5 to 10%) of the maximum and minimum loads commanded. However, these tests did confirm that little change in the load/deflection response was apparent over individual cycles whether the loading rate was at 0.5 Hz or 5 Hz.

Following these tests it was decided that the resulting behaviour would be comparable to real track conditions and stress relaxation could be minimised for test data over single cycles of load provided the loading rate was relatively fast (e.g. ≥ 0.5 Hz) and provided all tests were at the same rate.

5.4. Summary of Chapter 5

Geophone data were used to characterise the likely vertical range of resilient deflections occurring on actual track at the high and low sleeper ends as Pendolinos travelled around relatively sharp curves on canted track of the WCML:

- A range of resilient movements was measured over a short track length of sleepers, identifying the variability of the resilient range of deflection.
- The relative deflections of the high end and low end of sleepers were shown to be significantly biased towards the end receiving the greatest load, similar to a proportioning of load.

The test preparation procedure was validated by comparison to geophone data and actual plastic strain data reported in the literature:

- In the field a range of resilient deflections was observed across different sleepers and in the laboratory different tests showed a range of results despite the similarity of test preparation and the same depth of ballast.
- The plastic strain in the laboratory was generally higher for each test than from a test track in the USA. However general behaviour was similar, following a power relation trend line, and differences can be explained by the mechanical preparation procedure used on real track and differences in the superstructure and substructure between the test track and the laboratory.
- The rapid initial strain rates also showed the importance of an initial 100 vertical load cycles to bed in the sleeper/ballast contact prior to cyclic lateral, vertical and moment loading tests.

Lateral loading rate effects were also assessed and:

- Appropriate loading frequencies and appropriate ratios of vertical and lateral load were identified to minimise stress relaxation effects as far as possible and to optimise comparability between different test results.

These practices were adopted in the methods set out in Chapter 4.

6. The impact on confining stress within the ballast from cyclic vertical loading

This Chapter relates to the objective set out at the end of Chapter 1 to:

- Quantify the development of confining stress within the ballast at the end of an initial 100 Pendolino axle loads on freshly prepared ballast and assess its impact on sleeper/ballast interface behaviour.

This Chapter is divided into two main sections:

1. A review of the known behaviour of ballast: this section provides a context of how the results fit into known ballast behaviour and provides justification for the use of pressure plates within the testing rig developed for this research.
2. Confining stress within the ballast layer, this section examines pressure plate laboratory data during the first 100 load cycles and uses results from a finite element model of the experiment to investigate changes in ballast earth pressure ratio during load cycles.

At the end of the Chapter a summary draws together results from each section and links in with the objectives set out in Chapter 1.

6.1. A brief overview of the known characteristics of ballast material behaviour

In this section it will be demonstrated that while tests used on ballast to measure material properties can be used to show that ballast behaves in a similar way to other granular materials such as sand, typical soil mechanics tests have several drawbacks when compared to the railway environment and, despite recent advances, e.g. Indraratna and Salim (2005), are unable to adequately explain certain features of track lateral behaviour.

It is well known that the lateral resistance of the sleeper/ballast interface improves during trafficking after placement or maintenance tamping e.g. Sussman et al., (2003); Wood, (1993a); Wood, (1993b); Esveld, (2001); Selig, (1980); Selig and Waters, (1994). In some cases the loss of lateral resistance during tamping means that speed restrictions are applied until sufficient traffic has restored lateral resistance to acceptable levels. However, speed restrictions are costly to train operators and so Dynamic Track Stabilisation (DTS) systems have been developed to simulate the effect of traffic to reduce the need for speed limits. Esveld (2001) reported research by Deustche Bahne, carried out in the 80s, comparing the lateral resistance for track where a DTS had been applied to track where no DTS had been applied. Test data of mean individual sleeper resistance indicated that a DTS could simulate the effect of over 100,000 cumulative tonnes of traffic and typically increased individual mean sleeper lateral resistance from just under 6 kN to just under 8 kN.

The reasons behind the increase in lateral resistance are not clear. It may be supposed that trafficking causes structural changes within the ballast layer enabling it to better withstand lateral loads. It may further be deduced that these changes are driven by vertical cyclic loading because increases in lateral resistance are reported on straight sections of track where lateral cyclic load is minimal.

Structure in granular materials may be classified according to whether it results from bonds between the particles (bonded structure), or from particle interlocking, as in the case of ballast, when it is termed fabric structure (Barton, 1994). However, structural changes to ballast do not sit well within elastic models of material behaviour, and compared to other granular materials (clay, sand) ballast presents particular problems in commonly used tests to determine material properties due to the relatively large grain size. Despite the difficulties, several researchers have used large scale triaxial tests to show that the behaviour of ballast is highly influenced by stress state. Raymond and Davies (1978) carried out triaxial tests on a tough dolomite railroad ballast, in a large cell measuring 225 mm in diameter and 450 mm in height. Test samples were saturated, drained and tests performed at a constant rate of strain. Grain sizes were from 4 mm to 40 mm with over 50% in the range 10 mm to 20 mm. This is finer than NR's UK specification, (Safety and Standards Directorate Railtrack PLC RT/CE/S/006, 2000). Findings indicated that the shear strength and tangent modulus varied significantly with both confining pressure and density as shown in the scanned images reproduced as Figure 6-1, Figure 6-2 and Figure 6-3.

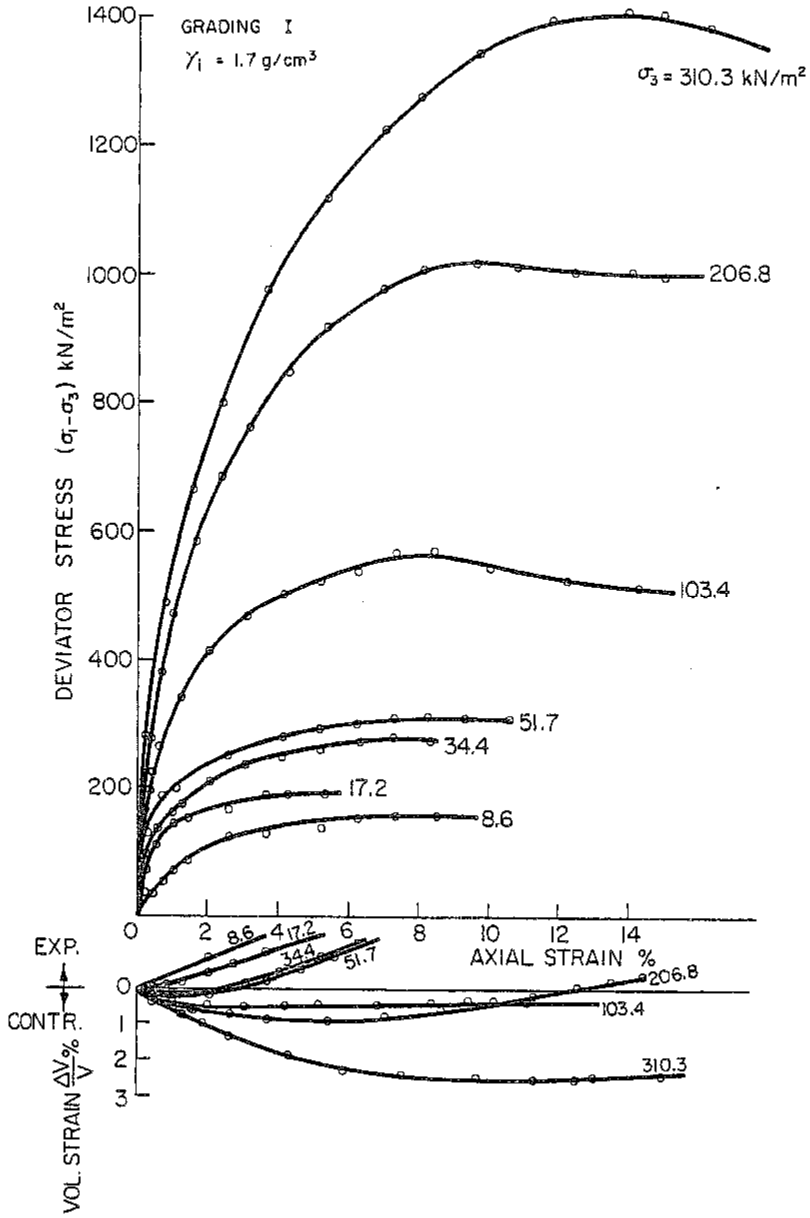

Figure 6-1: Triaxial tests: Triaxial shear test results reproduced with permission from Professor Raymond (Raymond and Davies, 1978)

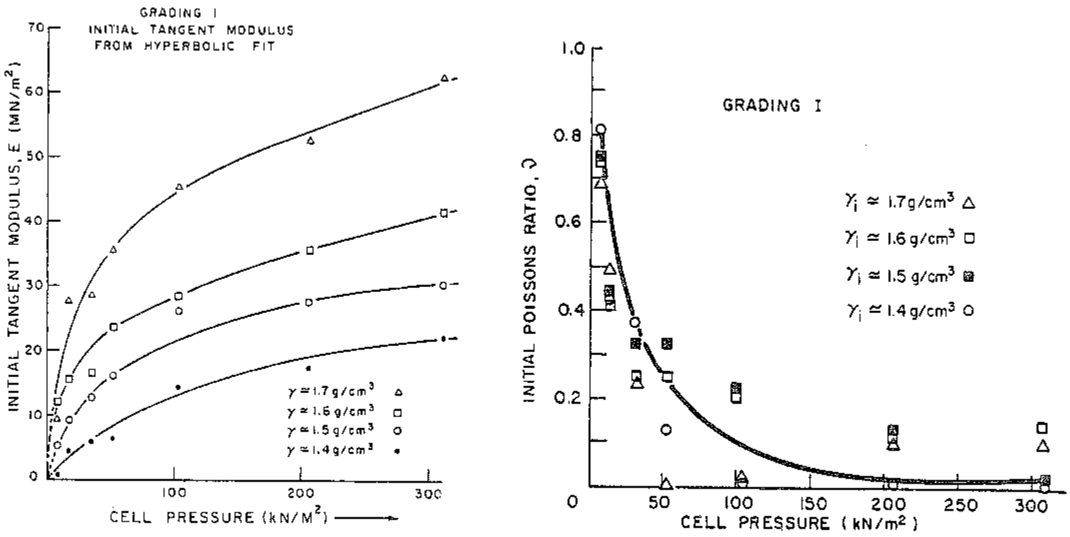

Figure 6-2: Triaxial shear tests, relationships between cell pressure and initial tangent modulus and initial Poisson's ratio for ballast reproduced with permission of Professor Raymond (Raymond and Davies, 1978)

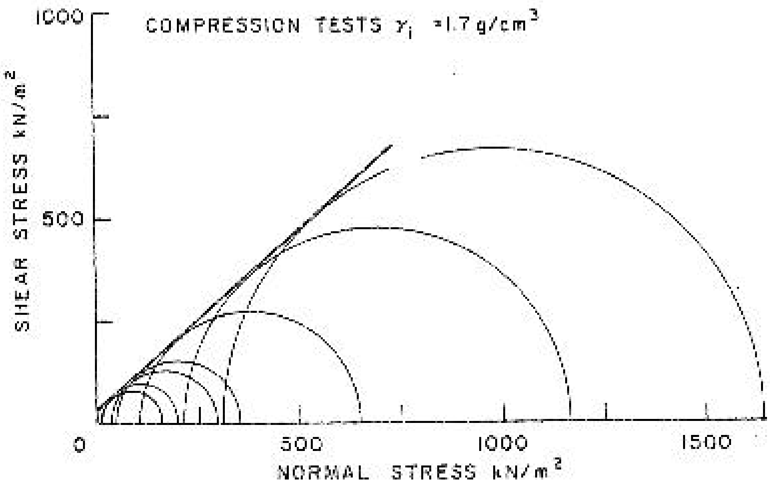

Figure 6-3: Triaxial shear test, Mohr circle reproduced with permission of Professor Raymond (Raymond and Davies, 1978)

The intercept in Figure 6-3 was attributed to dilatancy, changing friction angle or particle interlock due to compaction. Similar findings were reported by Indraratna (2002) who carried out large scale (300 mm × 600 mm) triaxial tests on ballasts used on railways in Australia.

Indraratna and Salim (2002) further proposed a mathematical model for the behaviour of the ballast that accounted for particle breakage and dilatancy to explain changes to the peak friction angle with increasing confining pressure. Figure 6-4 illustrates the behaviour that the model accounted for, no precise data points are provided and no absolute value may be scaled from the figure which is to show trends only. The possibility that the internal friction angle of the ballast may increase at low confining pressures has implications for the resistance that a shoulder of ballast can provide. This will be further investigated in Chapter 7.

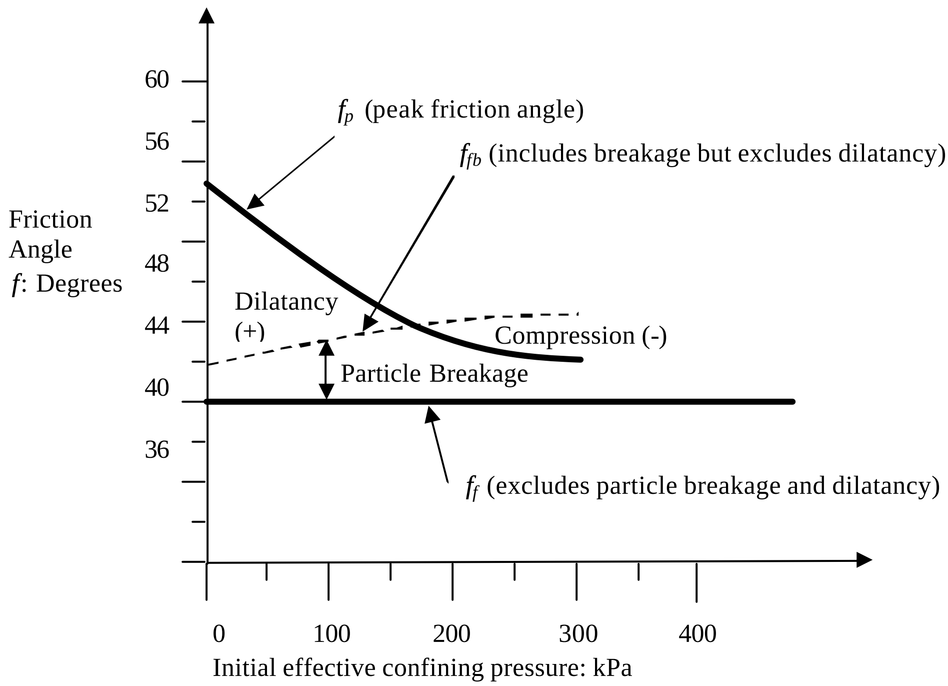

Figure 6-4: Effect of particle breakage, dilatancy and confining pressure on the friction angle of latite basalt (d_{50} = 37.0mm) (Indraratna and Salim, 2002)

Fair (2003) carried out drained monotonic, 100,000 cycle and post cyclic monotonic tests on 236 mm diameter by 455 mm high specimens of wet and dry nominal 50 mm sized ballast from (then) Railtrack stockpiles at Bardon Quarry. For cyclic load tests the maximum load applied was 11 kN, or 250 kPa considered similar to real track conditions. Some tests were also damped by means of a wooden disc on the top and rubber plate at the base of the cylinder which was intended to simulate the railway environment. The resilient moduli[8] were calculated at key numbers of loading cycles, results are presented in Table 6-1.

Specimen	**Cell (kPa)**	**Average Resilient Modulus for Cycles (MPa)**						
		100	**1k**	**10k**	**100k**	**500k**	**1M**	**1.8M**
T24 (dry)	40	211	259	313	298	-	-	-
T38	40	215	252	284	313	-	-	-
T57	40	197	221	272	364	-	-	-
T25	90	275	317	347	356	-	-	-
T36	90	301	326	354	378	-	-	-
T37	90	300	326	368	369	-	-	-
T61	140	353	379	398	385	-	-	-
T62	140	360	367	357	386	-	-	-
T64	140	350	386	410	432	-	-	-
T77	240	548	601	693	-	-	-	-
T65	140	357	-	-	-	-	-	-
T66	140	370	431	-	-	-	-	-
T67	140	342	376	391	-	-	-	-
T75	90	318	335	361	403	385	316	-
T42	90	273	295	327	373	385	258	233
T69 (damped)	140	213	217	227	259	-	-	-
T80 (wet)	40	182	212	251	219	-	-	-
T83	90	230	262	305	-	-	-	-
T78	140	281	268	282	246	-	-	-

Table 6-1: Vertical resilient modulus from cyclic triaxial tests (Fair, 2003)

Figure 6-5 takes the data presented by Fair (2003) shown in Table 6-1 and plots the mean resilient modulus for each group of data with the same testing conditions (cell pressure, wet/dry, damped).

[8] The resilient modulus neglects plastic strain, Elastic track system models (e.g. Geotrack) commonly assign the resilient modulus as the Young's modulus as these models are not capable of allowing plastic strain.

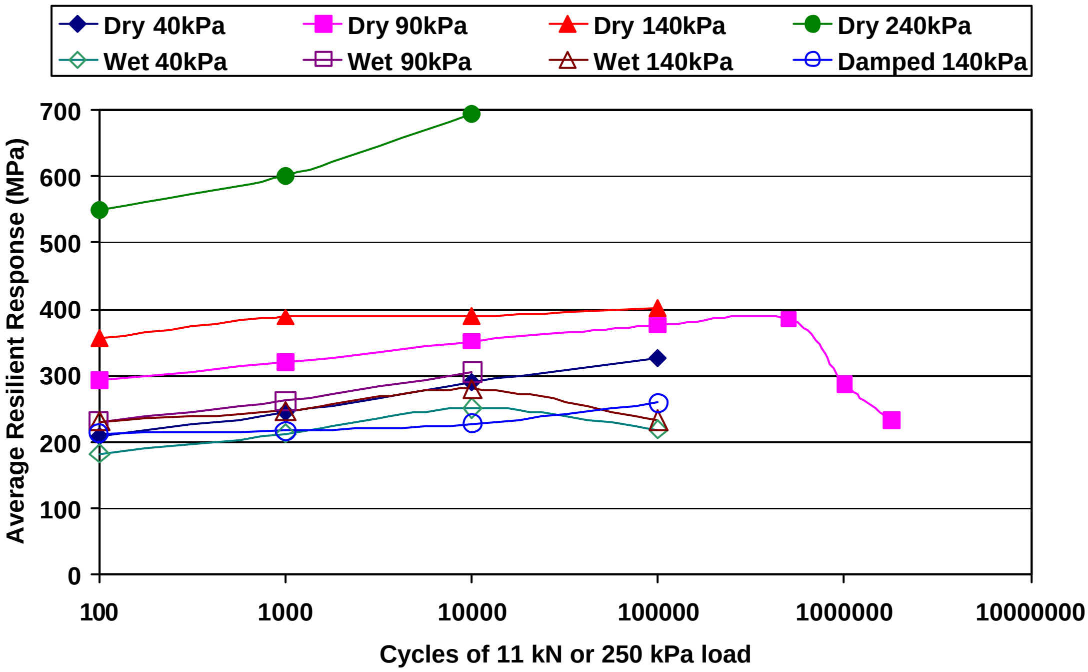

Figure 6-5: Vertical resilient modulus plotted against load cycles, mean of data from triaxial tests reported by Fair (2003)

Figure 6-5 shows that the resilient modulus may vary with the number of cycles, perhaps reflecting changing structure, and whether the ballast is wet or dry. Up to 100,000 load cycles the resilient modulus generally increases (so observed deflection within the cycle would decrease) unless the specimen is wet in which case it has already begun to lose some stiffness. After a certain number of cycles it is expected that the ballast should become life expired and material behaviour begins to degrade, this is only apparent for samples T75 and T42 in Fair's data. The term life expired may be taken to refer to the manifestation of a critical weakening of the particles due to the build up of fractures within the particles caused by the repeated cyclic loading and an increase in the rate of particle breakage.

Although these results are insightful there are significant differences between the loading of the ballast in all these triaxial tests and train/track loading of ballast. The triaxial cells confine the ballast at a constant stress in both horizontal axes. In contrast, on actual track laterally away from the track the ballast is unconfined and as each axle passes, vertical load and horizontal confining stresses vary in approximate proportion to the vertical load. Furthermore the confining stresses applied in these tests are substantially higher than on real track (as the results of the laboratory tests carried out for this research will demonstrate later) and ballast would probably be expected to remain in service longer than the 1M to 1.8M cycles that apparently caused the ballast to become life-expired in these tests.

Triaxial testing is a well established method of determining the properties of granular materials and is usually sufficient in more traditional civil applications where load is static, long term and applied to a soil consisting of a large number of particles. However, changes occurring in the structure of soil materials are more difficult to quantify and such changes take on an increased importance when grain sizes are relatively large in comparison to the volume occupied by the material.

The importance of fabric structure has been demonstrated for certain types of sands, for example, the locked sand investigated by Cresswell and Powrie (2004) showed a peak friction angle of 60° in triaxial tests at a confining pressure of 50 kPa owing to its fabric structure. This is almost double the critical state friction angle (31°) of the unstructured material. Similar behaviour has been observed in triaxial tests on ballast (Indraratna et al., 1998); these showed a very non linear failure envelope, with a peak friction angle of 65° at 30 kPa and in excess of 80° at 1 kPa. Such very high peak strengths indicate that the contribution of fabric structure to the behaviour of ballast is hugely significant.

However, it is very difficult to measure structural changes occurring on an inter-particle scale within the ballast layer. In contrast deflection measurements at the boundaries of the ballast layer can be made relatively easily and much research has focused on evaluating the vertical plastic strain and resilient behaviour.

In addition to measuring vertical load/deformation behaviour, the testing apparatus developed in this research was equipped with pressure plates in the inside walls to record horizontal confining stress in a vertical plane across the track at mid sleeper spacing where it would not normally be possible to obtain data. In this Chapter, amongst other things, the data from these load cells will be examined for evidence of the development of structure with vertical loading cycles.

6.2. Confining stress within the ballast layer, laboratory and finite element data

6.2.1. Background

While we know that the lateral failure resistance improves with traffic, the fundamental mechanism by which this occurs is not fully understood. It is thought that changes to confining stress may reflect changes in structure that occur with load cycles.

To further investigate this, a description of the changes in the measured horizontal confining stress and vertical to horizontal earth pressure ratio in the ballast layer during the first 100 vertical load cycles common to each test is presented and an interpretation of the data is made with the aid of a finite element model of the testing apparatus.

6.2.2. Methods

Methods: laboratory tests

Pressure plates were placed on the inside of the testing apparatus as shown in Figure 6-6 to measure the confining stress within the ballast during the first 100 vertical loading cycles in each test.

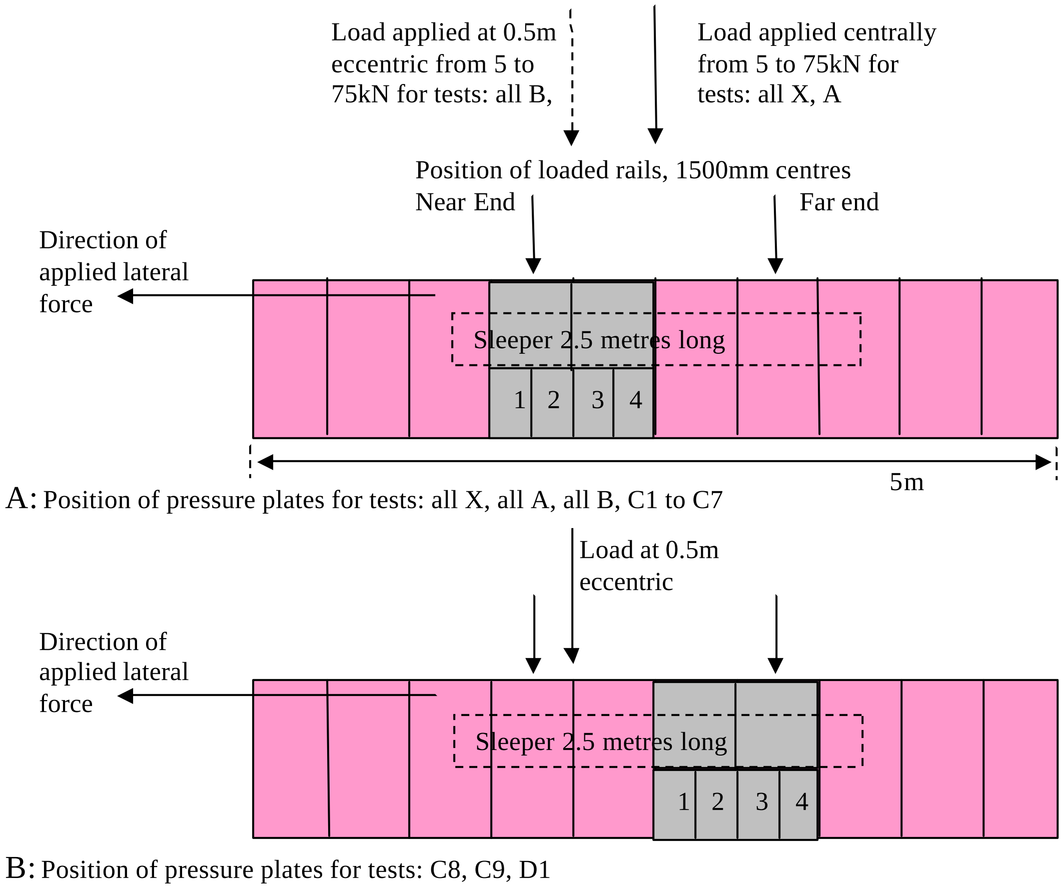

Figure 6-6: Position of pressure plates, elevation from inside the testing apparatus

Methods: finite element model

A finite element model of the laboratory experiment was set up to evaluate vertical stress as shown in Figure 6-7 and Figure 6-8.

The finite element model permits comparison of the experimentally measured horizontal confining stress with the finite element calculated vertical stress. Hence, changes with load cycles in the earth pressure ratio (earth pressure coefficient) can be deduced. The earth pressure ratio is defined in Equation 6-1.

$$K = \frac{s'_h}{s'_v}$$ **Equation 6-1**

The finite element model was not used to calculate directly the horizontal confining stress because the earth pressure coefficient is highly dependent on Poison’s ratio which, for a ballast has been shown to vary with stress state e.g. see Figure 6-2. reproduced from Raymond and Davies (1978). Further complexity in the behaviour of the earth pressure ratio is introduced if the soil is anisotropic; however, ballast particles are angular and rotund and recently placed ballast on railway has minimal loading history, and is consequently not bedded or laminated in any way that would imply anisotropic behaviour.

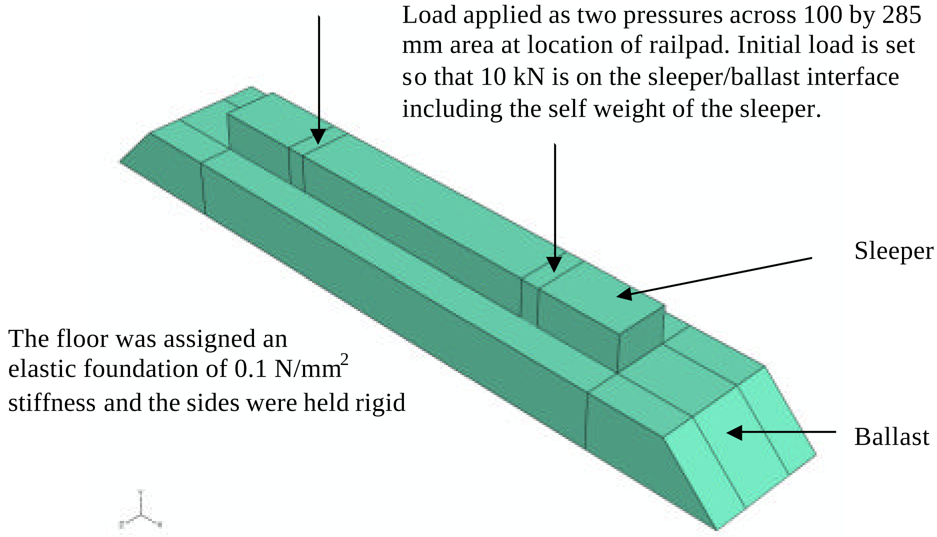

Figure 6-7: Finite element model, general view showing partitions

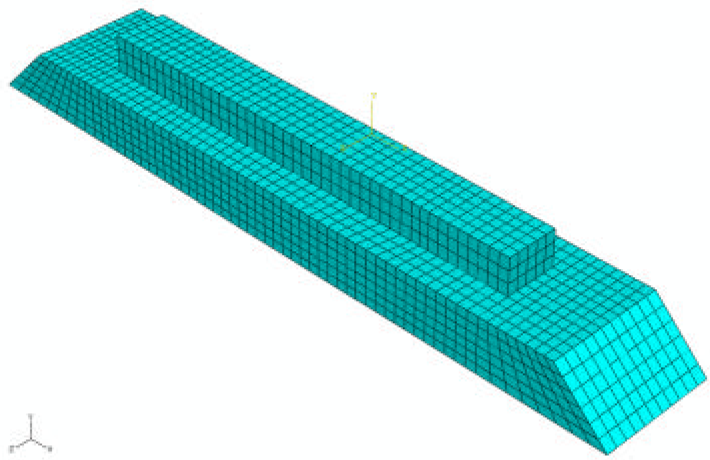

Figure 6-8: Finite element model, view showing mesh

Elastic material properties were assigned as shown in Table 6-2. The dimensions of the component parts of the finite element model are shown in Table 6-3. The finite element model was evaluated for the four load cases shown in Table 6-4 using linear hexahedral elements of type C3D8R (ABAQUS, 2007).

Material properties	Young's modulus N/mm^2	Poisson's ratio	Self weight per volume and as a total for the volume modelled	
			N/mm^3	kN
Ballast	300	0.3	0.000015	10.5
Sleeper	34000	0.3	0.000022	3.1

Table 6-2: Material properties

The material properties were assigned after consideration of tests such as those by Fair (2003), and finite element models such as those by (Grabe, 2002) and (Powrie et al., 2007). A rigidly supported base was found to result in a vertical sleeper deflection of 0.11 mm therefore the base was assigned an elastic foundation so that the vertical deflection would attain a realistic value (~1 mm).

Preliminary variations of the modelling parameters chosen demonstrated that the vertical stress was largely insensitive to changes in Young's modulus and Poisson's ratio in the ballast layer over the probable range of material properties.

Dimensions	Width (mm)	Height (mm)	Length (mm)
Sleeper	285	200	2500
Ballast top	650	300	3300
Ballast base	650		3900

Table 6-3: Dimensions of material components of model

Load cases evaluated	Pressure far pad (N/mm^2)	Pressure near pad (N/mm^2)	Load far pad (kN)	Load near pad (kN)	Total load at sleeper base (there is also a 3 kN weight of sleeper) (kN)	Corresponds to laboratory tests (a 5 kN dead load is present at the sleeper base).
elastic1	0.123	0.123	3.5	3.5	7	5 kN centrally applied laboratory load
elastic2	1.351	1.351	38.5	38.5	77	75 kN centrally applied laboratory load
elastic3	0.041	0.205	1.2	5.8	7	5 kN 0.5 m eccentric applied laboratory load
elastic4	0.450	2.251	12.8	64.2	77	75 kN 0.5 m eccentric applied laboratory load

Table 6-4: Load cases evaluated

Note that there is a 3 kN self weight sleeper load so that the load at the sleeper/ballast interface varies between 10 and 80 kN as in the laboratory experiments.

6.2.3. Results vertical and horizontal confinement stress, experimental and finite element data

Results: Experimental

The confining stress has been measured at the minimum and maximum points of each load cycle in the graphs presented in Figure 6-9 to Figure 6-20, as a mean across all four pressure plates and individually. These Figures show results from selected tests (chosen from the test runs shown in Table 4-2) to show characteristic behaviour. Summary data from all tests is presented in Table 6-5 and Table 6-6.

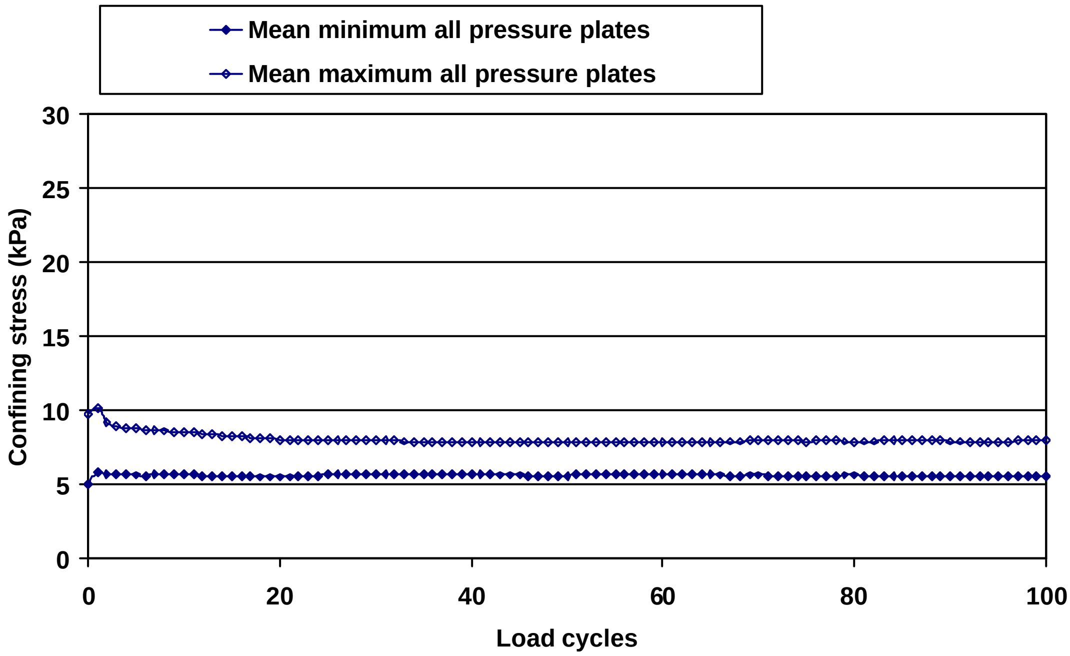

Figure 6-9: Comparison of cyclic minimum and maximum measured confining stress, as mean for all plates when the load is central, plates in initial position, test 1A

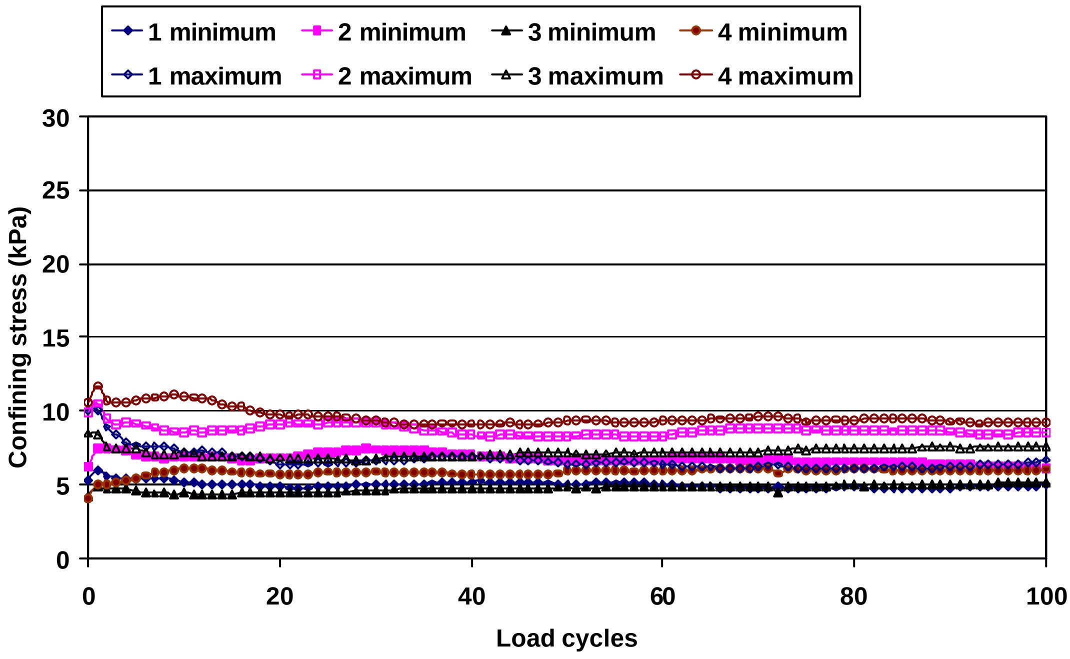

Figure 6-10: Comparison of cyclic minimum and maximum measured confining stress, for each plate when the load is central, plates in initial position, test 1A

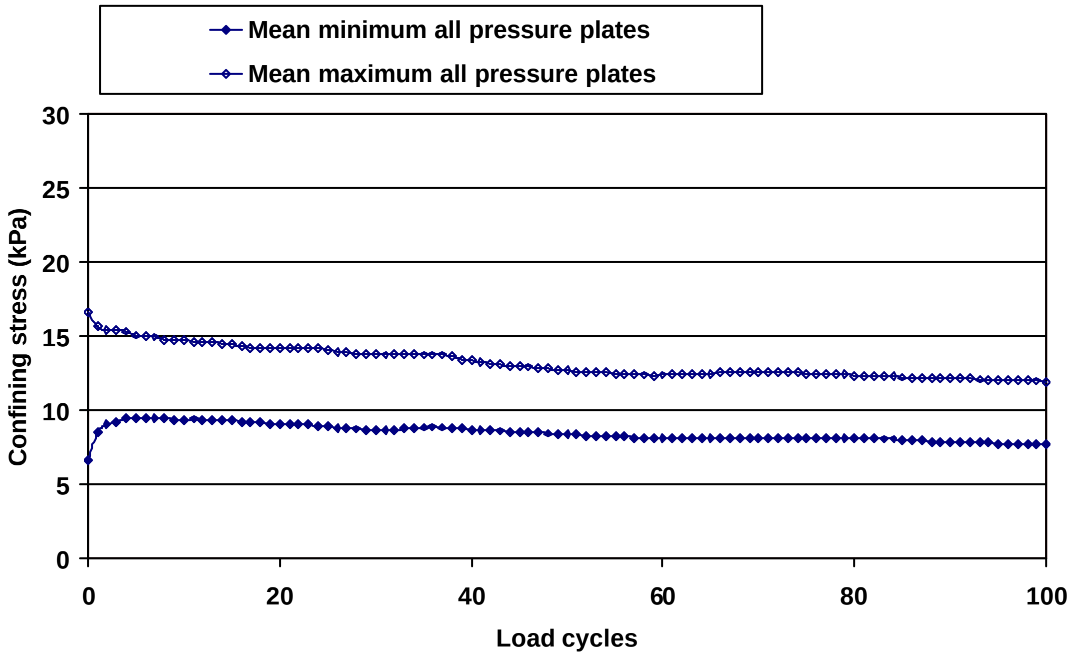

Figure 6-11: Comparison of cyclic minimum and maximum measured confining stress, as mean for all plates when the load is central, plates in initial position, test 3A

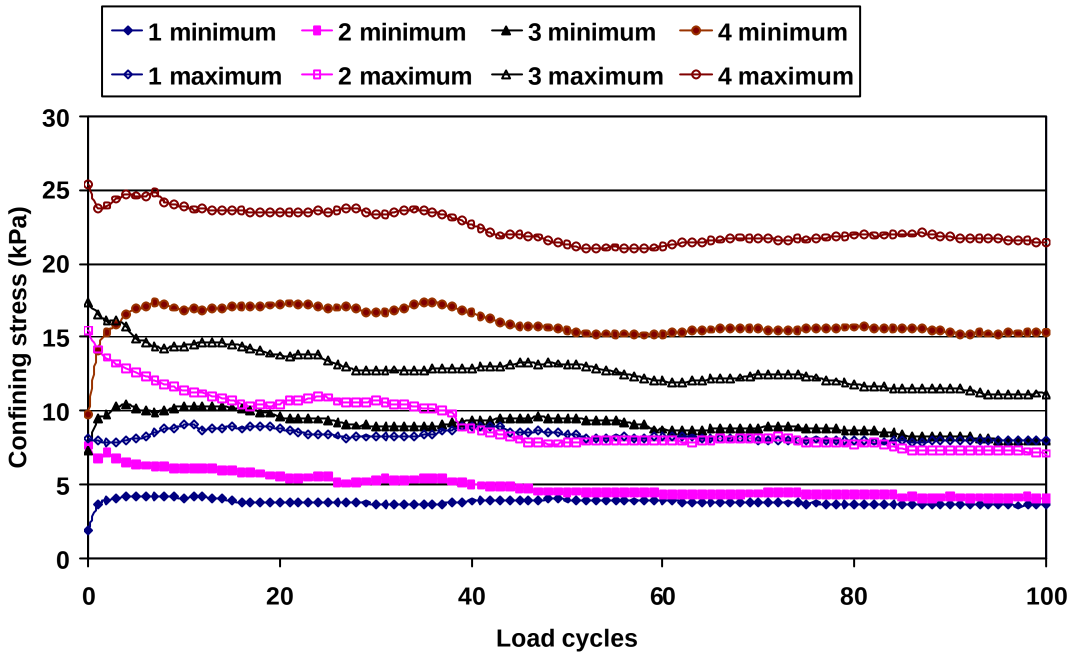

Figure 6-12: Comparison of cyclic minimum and maximum measured confining stress, for each plate when the load is central, plates in initial position, test 3A

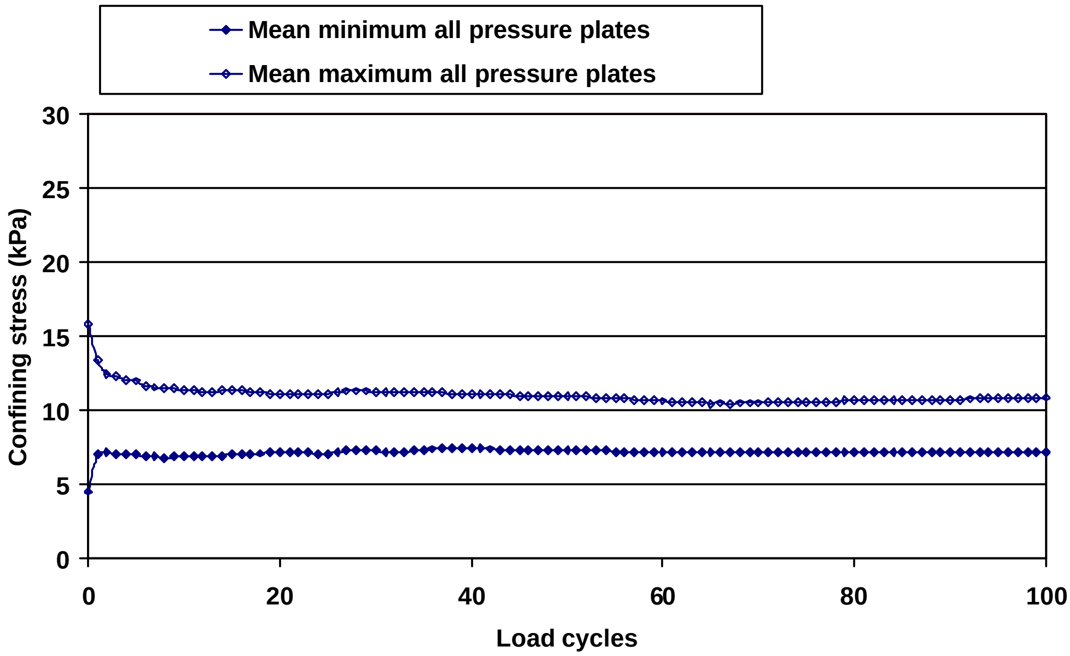

Figure 6-13: Comparison of cyclic minimum and maximum measured confining stress, as mean for all plates when the load is eccentric, plates in initial position, test 2B

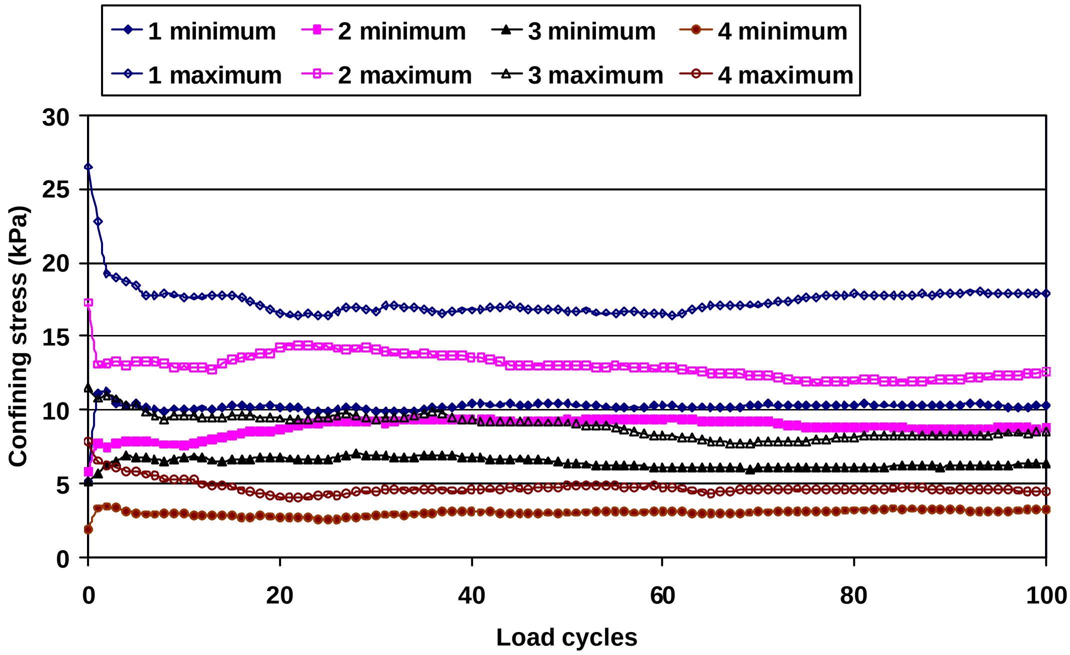

Figure 6-14: Comparison of cyclic minimum and maximum measured confining stress, for each plate when the load is eccentric, plates in initial position, test 2B

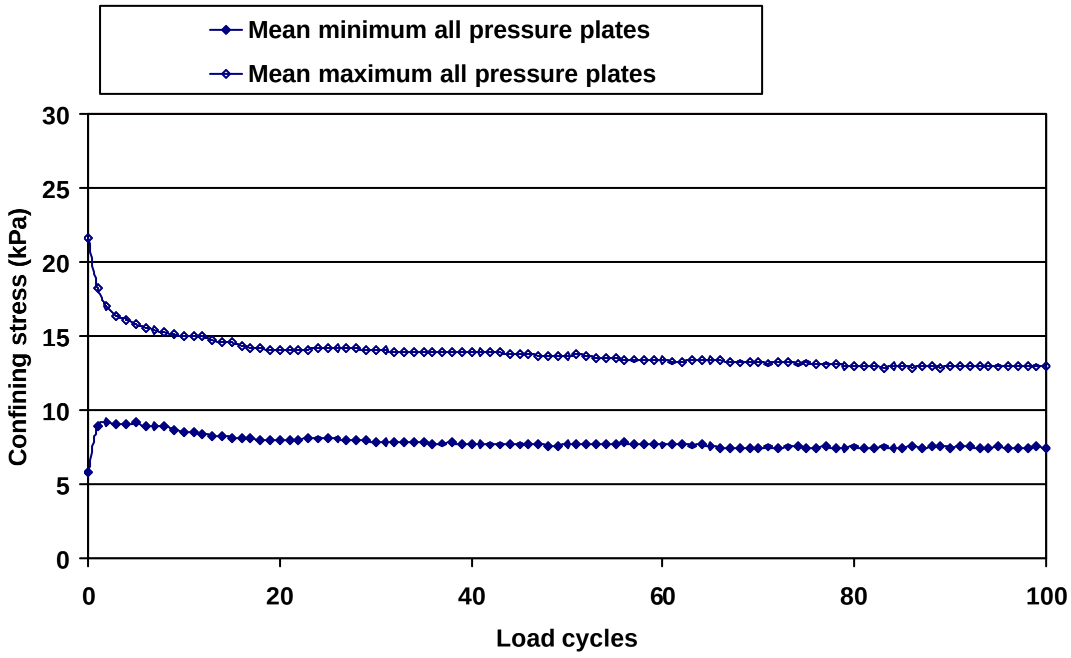

Figure 6-15: Comparison of cyclic minimum and maximum measured confining stress, as mean for all plates when the load is eccentric, plates in initial position, test 3B

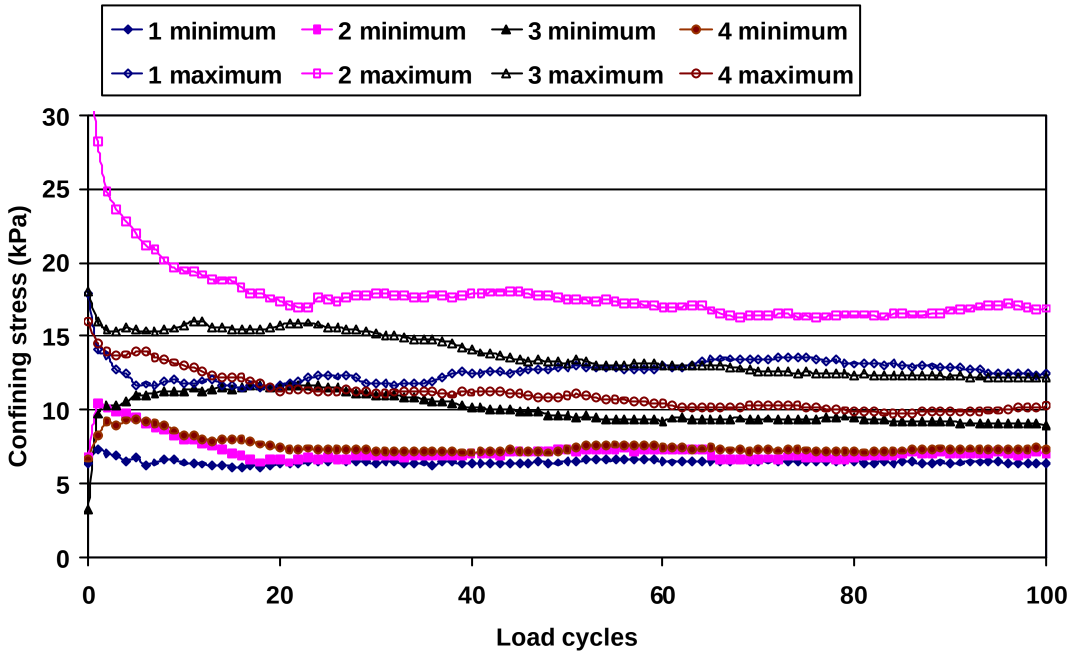

Figure 6-16: Comparison of cyclic minimum and maximum measured confining stress, for each plate when the load is eccentric, plates in initial position, test 3B

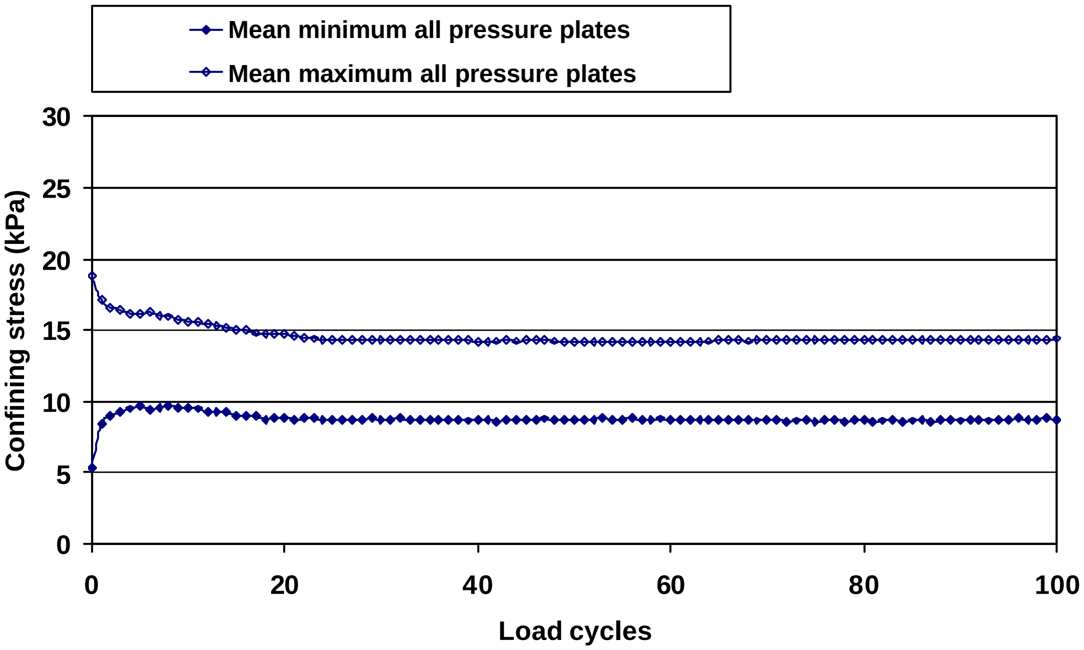

Figure 6-17: Comparison of cyclic minimum and maximum measured confining stress, as mean for all plates when the load is eccentric, plates in initial position, test 6C

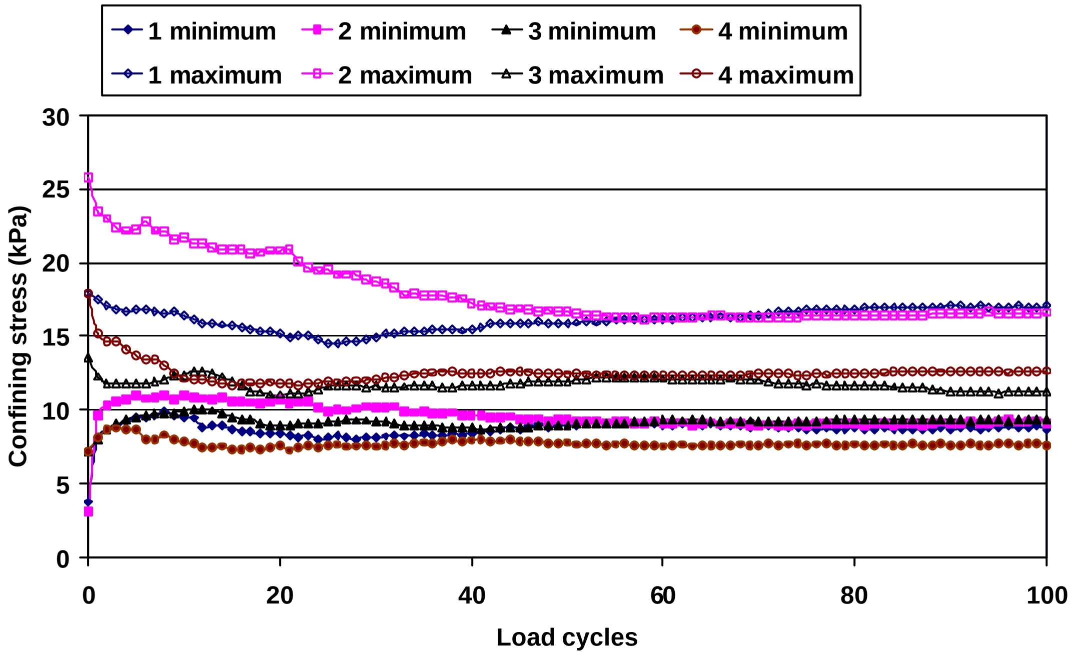

Figure 6-18: Comparison of cyclic minimum and maximum measured confining stress, for each plate when the load is eccentric, plates in initial position, test 6C

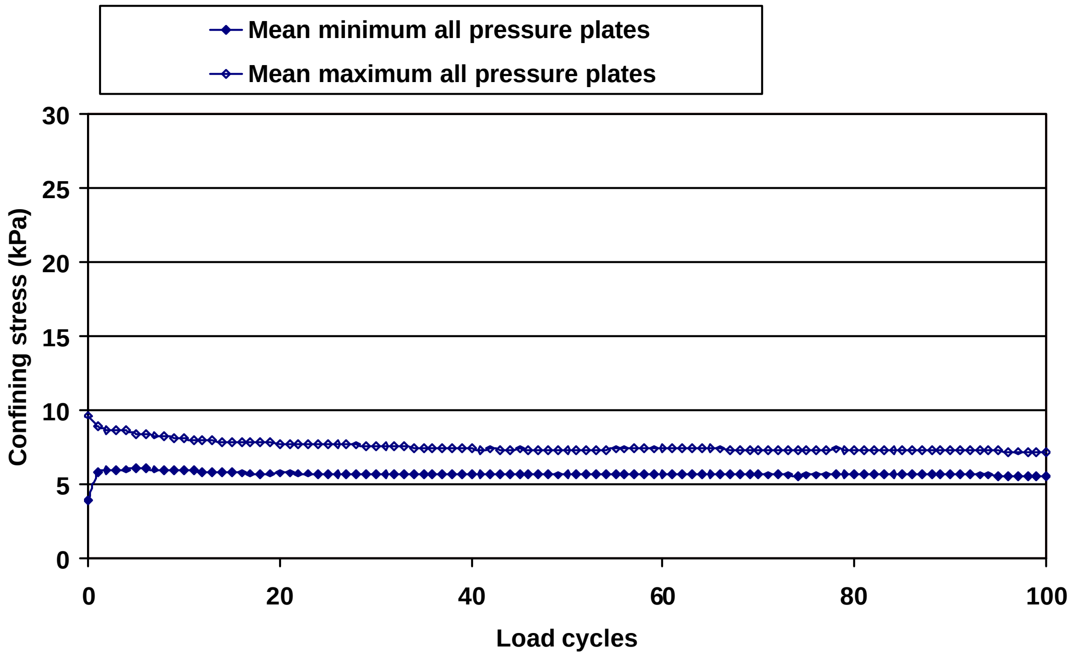

Figure 6-19: Comparison of cyclic minimum and maximum measured confining stress, as mean for all plates when the load is eccentric, plates in secondary position, test 9C

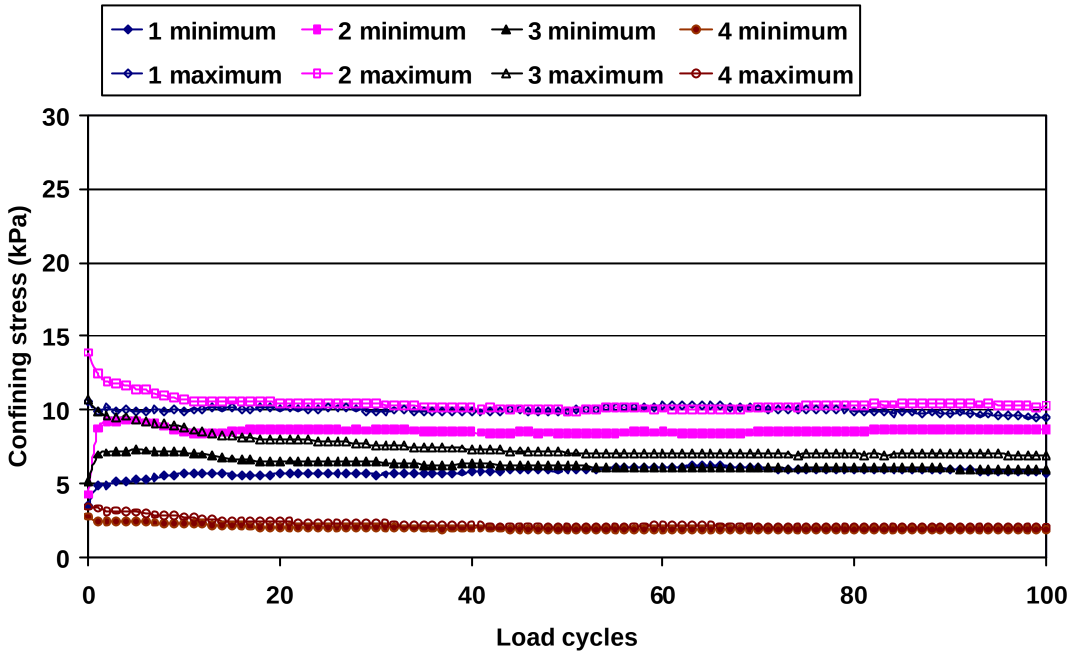

Figure 6-20: Comparison of cyclic minimum and maximum measured confining stress, for each plate when the load is central, plates in initial position, test 9C

	Minimum mean (Pa)	Maximum mean (Pa)	Mean of minimum and maximum means (Pa)
Initial 10kN	3491	6643	4738
Initial 80kN	10706	17582	14195
Final 10kN	5242	10649	7104
Final 80kN	7997	14254	10790

Table 6-5: Summary of measured confining stress for centrally loaded tests, mean for all tests pressure plates in initial position, (test runs X and A)

	Minimum mean (Pa)	Maximum mean (Pa)	Mean of minimum and maximum means (Pa)
Initial 10kN	2939	7022	4856
Initial 80kN	14046	23071	18425
Final 10kN	5581	12172	7982
Final 80kN	10141	19209	13428

Table 6-6: Summary of measured confining stress for eccentric loaded tests, mean for all tests pressure plates in initial position, (test run B, C1 to C7)

Results: Finite element model

The vertical stress was evaluated in the finite element model along the sides of the test rig passing across the position of the pressure plates. Data at key depths is presented in Figure 6-21, Figure 6-22 and Figure 6-23. Vertical stress contour plots are also shown in Figure 6-24.

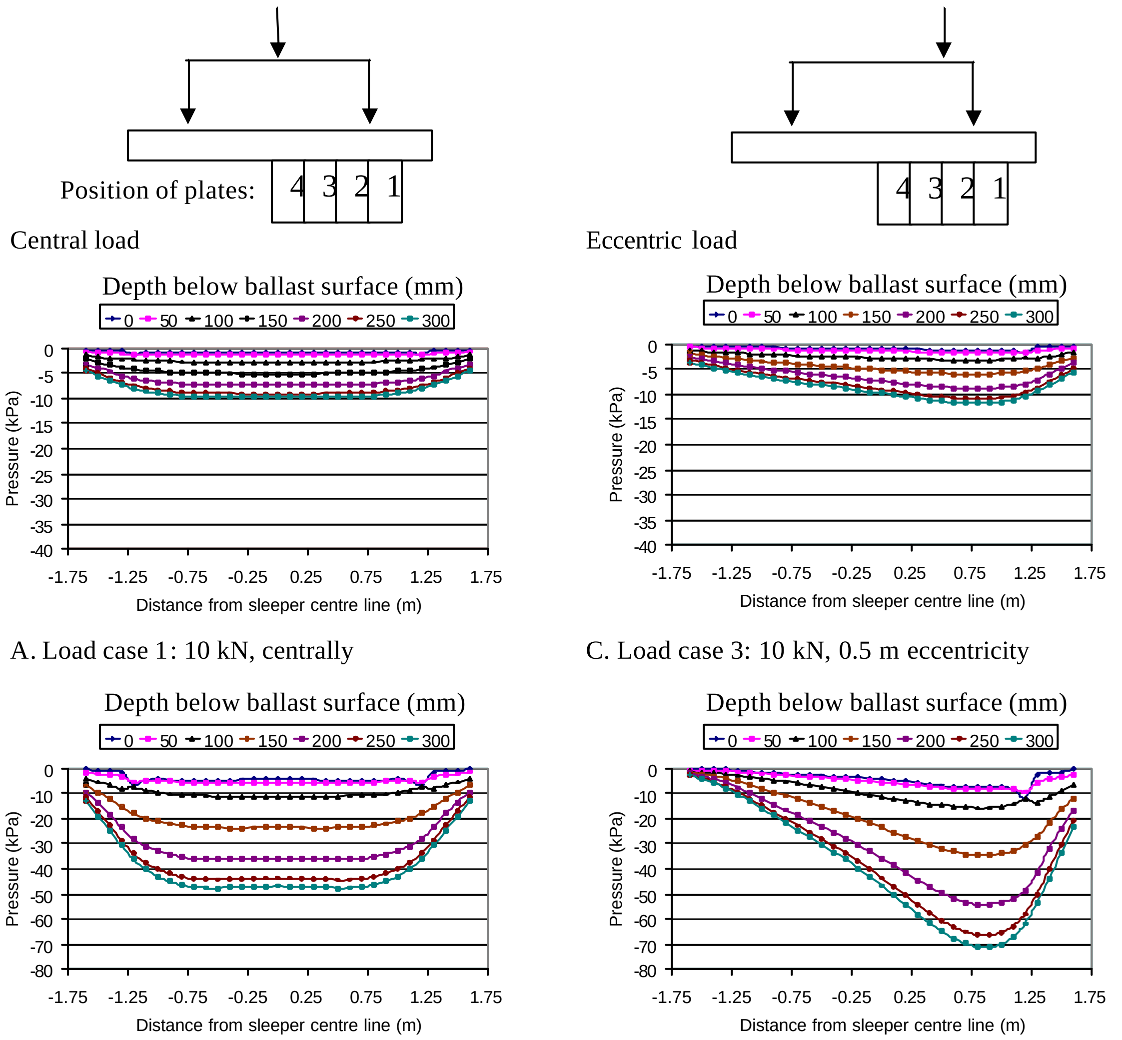

A. Load case 1: 10 kN, centrally

C. Load case 3: 10 kN, 0.5 m eccentricity

B. Load case 1: 80 kN, centrally

C. Load case 4: 80 kN, 0.5 m eccentricity

Figure 6-21: Finite element modelled vertical stress across the track at key depths along the sides of the testing rig, 0=ballast surface, 300=ballast base

In Figure 6-21, showing the vertical stress at key depths along the edge of the testing apparatus, it is possible to discern the remnants of the w shaped stress distribution immediately beneath the sleeper incorporated into Geotrack for the centrally loaded cases 1 and 2. For load cases 3 and 4 where the load is eccentrically applied the increase in stress to one side of the sleeper dominates and no w-shaped distribution can be seen.

Figure 6-22 and Figure 6-23 show the vertical stress along a line vertically down the middle of each plate, to the nearest 100 mm from the sleeper centre line (100 mm, 400 mm, 700 mm, and 900 mm) for all load cases and for both locations of the plates. These stresses have been averaged to produce the maximum and minimum stesses per plate and as a mean for all plates summarised in Table 6-7 and Table 6-8.

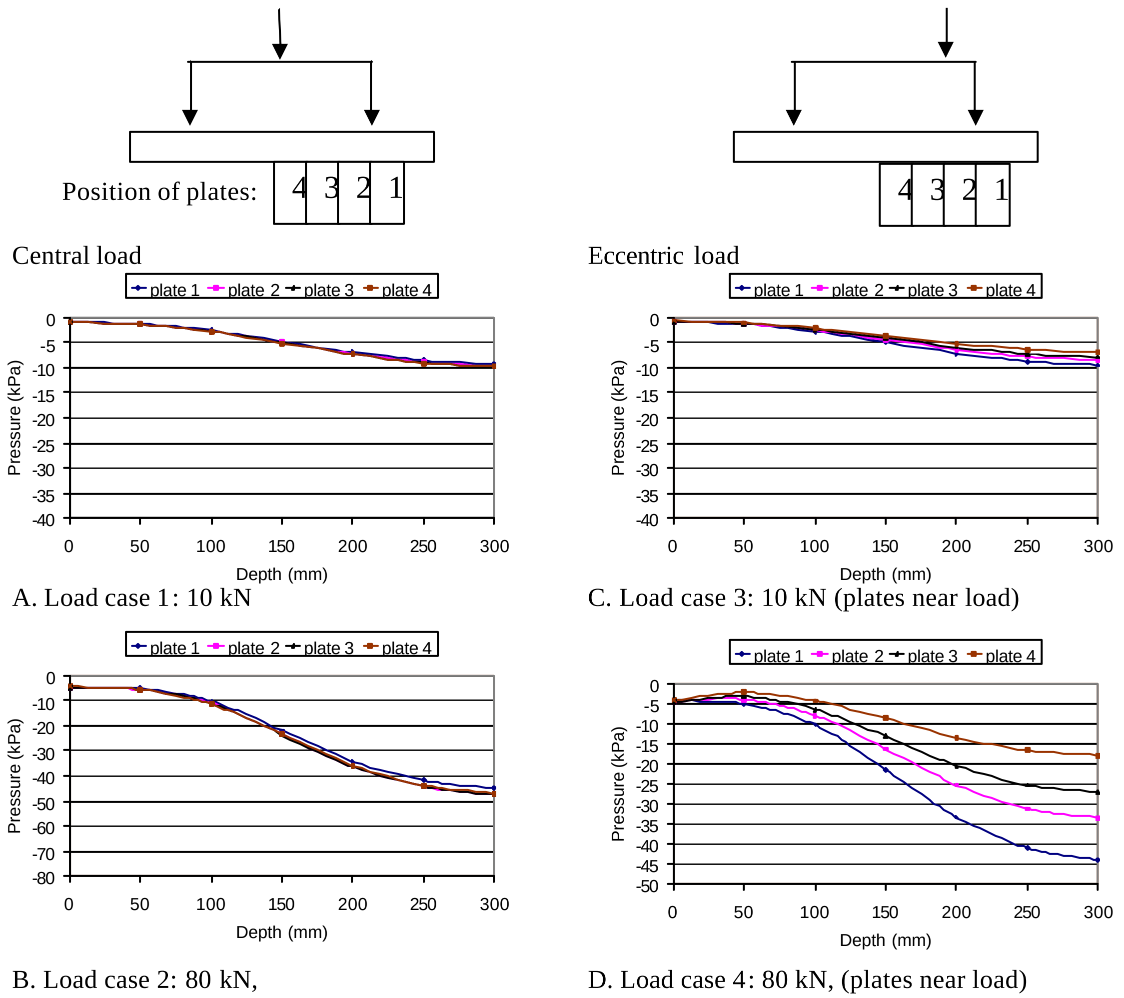

Figure 6-22: Vertical stress over the depth of the pressure plates in their initial positions

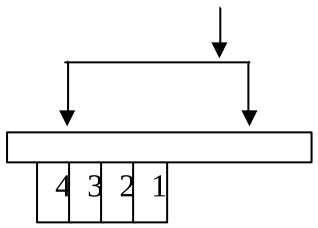

Position of plates:

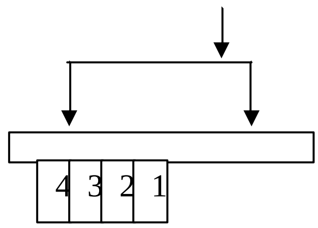

Eccentric load

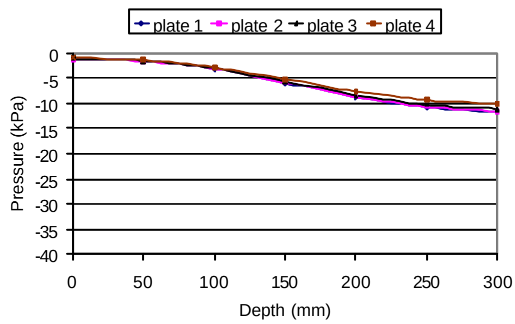

A. Load Case 3 (plates away from load)

Eccentric load

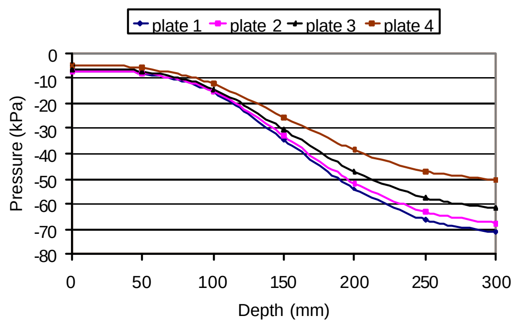

B. Load case 4 (plates away from load)

Figure 6-23: Vertical stress over the depth of the pressure plates in their secondary positions for asymmetric loading

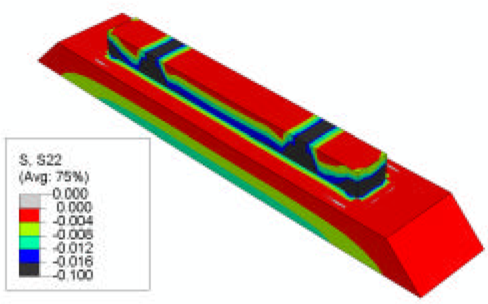

A. Load case 1: 10 kN, central

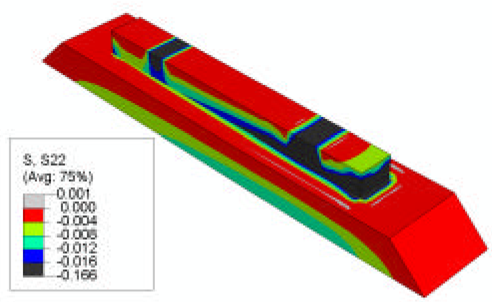

C. Load case 3: 10 kN, eccentric

The contours are from 0 to 16 kPa in steps of 4 kPa with areas outside this range in black and grey grey

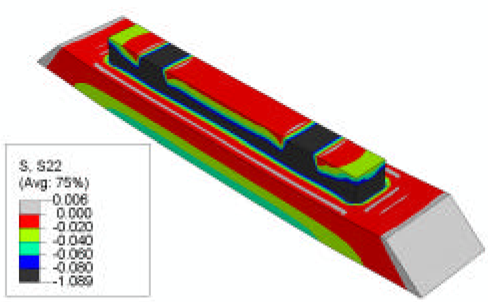

B. Load case 2: 80 kN, central

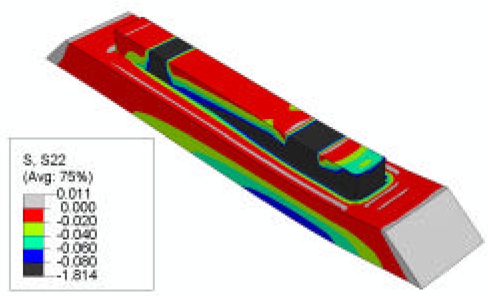

D. Load case 4: 80 kN, eccentric

The contours are from 0 to 80 kPa in steps of 20 kPa with areas outside this range in black and grey

Figure 6-24: Finite element model, vertical stress contour diagrams

In Figure 6-24 the most rapid change in stress, identifiable by the close stress contours, occurs as the load transfers from the railpads through the sleeper onto the ballast. Once it reaches the ballast the load spreads and stress reduces rapidly with depth and width from the sleeper.

Load case	**Plate 1**	**Plate 2**	**Plate 3**	**Plate 4**	**Mean**
	Pa	Pa	Pa	Pa	Pa
1, 10 kN central load	-4874	-5111	-5155	-5165	-5076
2, 80 kN central load	-23034	-24487	-24513	-24264	-24075
3, 10 kN eccentric load	-6080	-6047	-5814	-5337	-5820
4, 80 kN eccentric load	-36276	-34762	-31749	-26142	-32232

Table 6-7: Mean pressure per plate from finite element data, plates in initial position

Load case	**Plate 1**	**Plate 2**	**Plate 3**	**Plate 4**	**Mean**
	Pa	Pa	Pa	Pa	Pa
3, 10 kN eccentric load	-4993	-4495	-4174	-3667	-4332
4, 80 kN eccentric load	-22492	-17248	-14073	-9381	-15799

Table 6-8 – Mean pressure per plate from finite element data, plates in second position

6.2.4. Interpretation, experimental and finite element data, vertical and horizontal confining stress

In this section, general trends in the experimental measured confining stress with cycles are highlighted and a comparison is made with the finite element calculated vertical stress at the location of the pressure plates by evaluating the earth pressure ratio for some of the tests.

In Figure 6-9 to Figure 6-20 it can be seen that measured stress for each individual pressure plate varied significantly within each test and from test to test. However, taking the pressure as a mean for all pressure plates in each test eliminates much of this variation. For this reason, to identify general trends, the mean data across all pressure plates will be considered. Figure 6-25 shows a box and whisker plot of all tests where the load was centrally applied for the mean measured confining stress across all plates for the initial and final loading cycles.

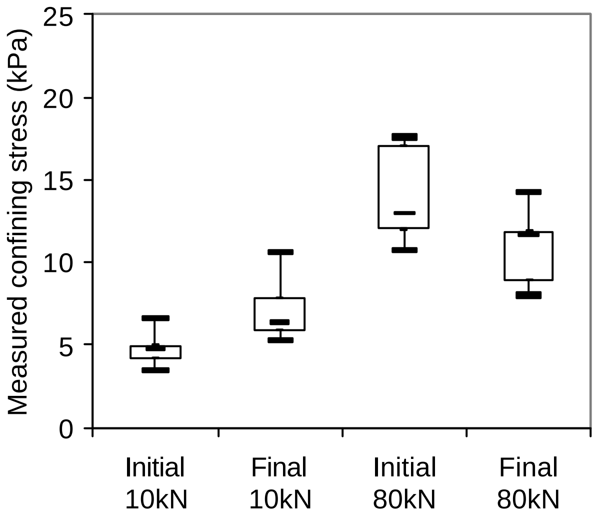

Figure 6-25: Box and whisker plot of measured confining stress at cycle 1 and cycle 100 for centrally loaded tests, pressure plates in initial position, (tests X, A)

Figure 6-25 demonstrates some trends:

- The confining stress increases from its initial value at 10 kN of load from a median of 4.8 kPa to 6.4 kPa after 100 load cycles.
- The maximum confining stress when 80 kN of applied load is present reduces from a median of 13.0 kPa to 11.7 kPa after 100 cycles.

Although not evident from Figure 6-25, most of the changes in confining stress occur during the first few loading cycles.

Figure 6-26 shows a box and whisker plot of data for the tests when the load was eccentrically applied at a 0.5 metre offset, here the load is closer to the plates and the confining stress is generally higher than in Figure 6-25. Figure 6-27 shows the same for data after the plates have been relocated to the opposite side of the sleeper centre line away from the eccentric load. There are only two tests in this data but the same broad trends can still be seen at a generally lower level of stress.

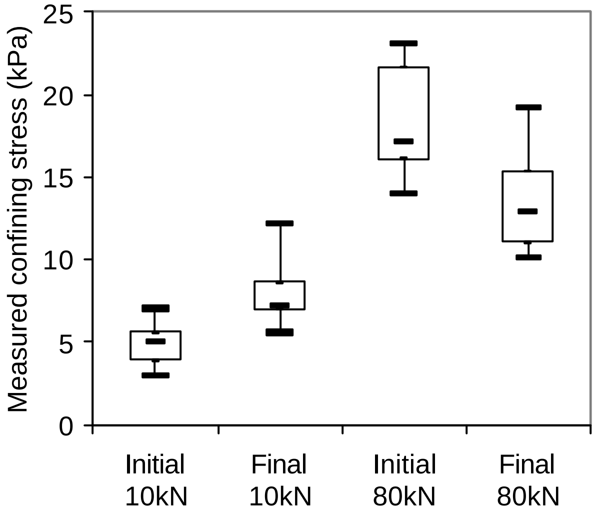

Figure 6-26: Summary statistics of measured confining stress for eccentric loaded tests, pressure plates in initial position, (tests B, C1 to C7)

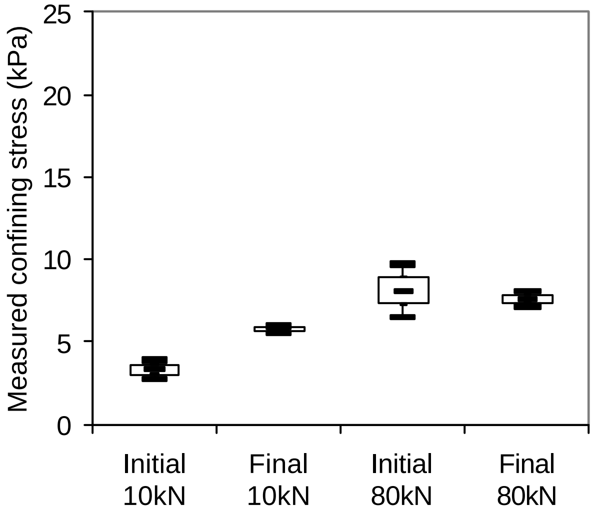

Figure 6-27: Summary statistics of measured confining stress for eccentric loaded tests, pressure plates in initial position, (tests C8 and C9)

The vertical stress calculated in the finite element analysis for each load case is plotted against the measured horizontal confining stress in Figure 6-28, Figure 6-29 and Figure 6-30 for three characteristic tests representing the two loading cases and the two positions of the pressure plates (for the central loading case the pressure plate results for the two positions should be similar). The earth pressure ratio, at key numbers of cycles during the load increase phase of each step (10 to 80 kN) is shown in Table 6-10. Also shown on the Figures are lines to represent the active (K_a) and passive (K_p) earth pressure ratio as defined in Equation 6-2 and Equation 6-3 and shown in Table 6-9 for friction angles of 40° and 45°.

$$K_a = \left[\frac{1-\sin f'}{1+\sin f'}\right] \qquad \textbf{Equation 6-2}$$

$$K_p = \left[\frac{1+\sin f'}{1-\sin f'}\right] \qquad \textbf{Equation 6-3}$$

Friction angle	K_a	K_p
40°	0.17	5.83
45°	0.22	4.60

Table 6-9: Key earth pressure ratios

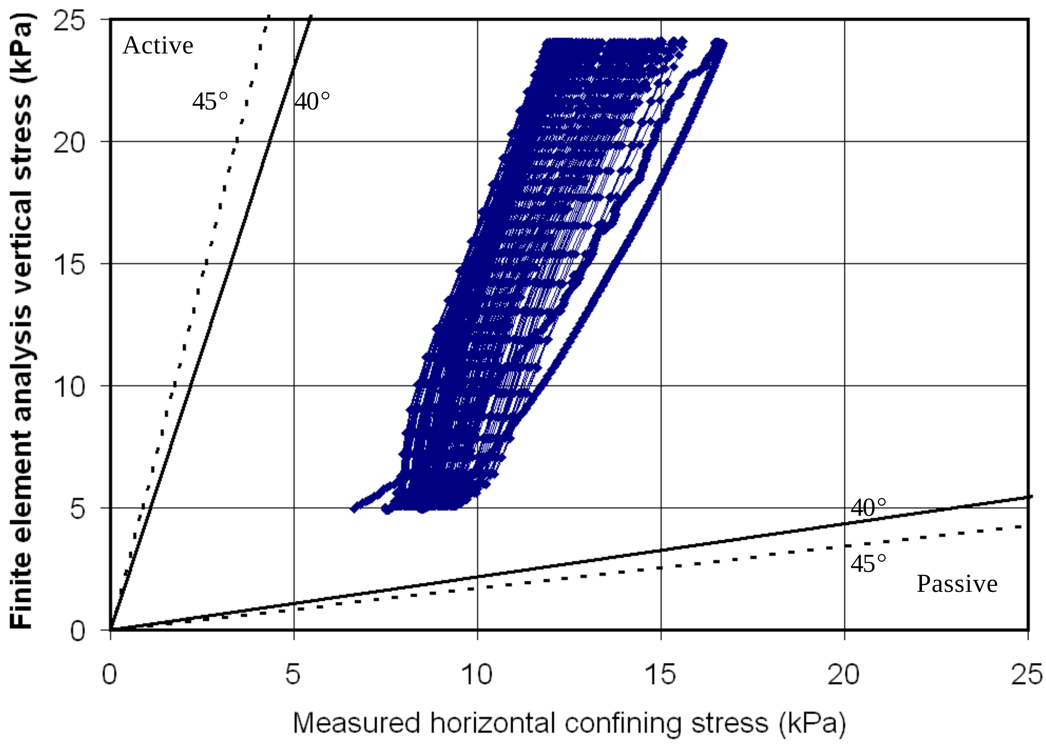

Figure 6-28: Finite element calculated vertical stress plotted against measured horizontal confining stress as average across pressure plates (centrally loaded test 3A)

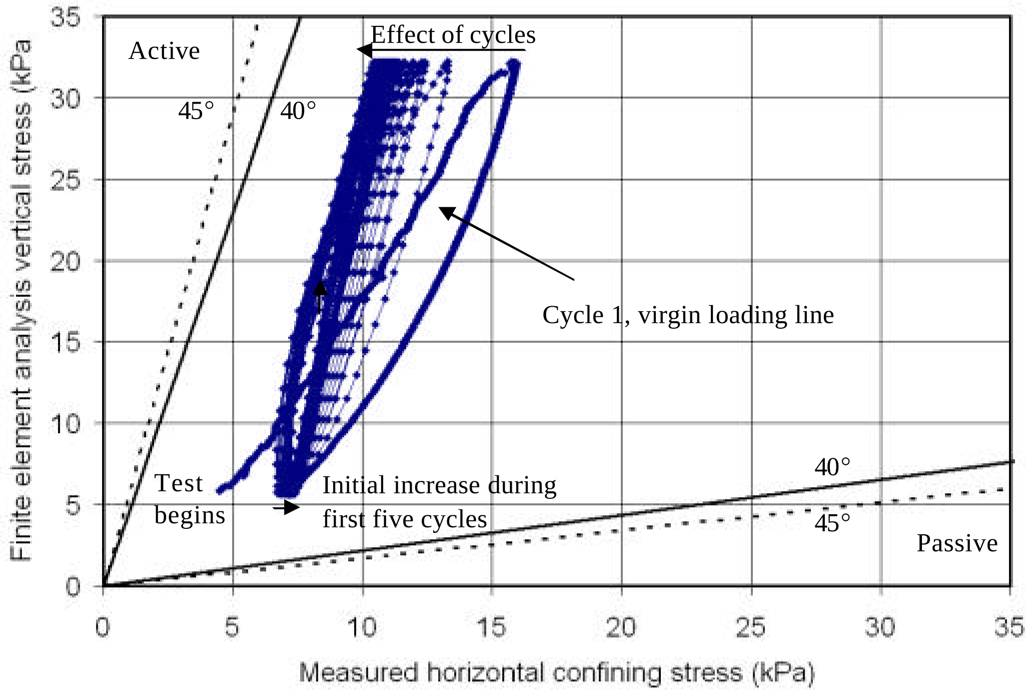

Figure 6-29: Finite element calculated vertical stress plotted against measured horizontal confining stress as average across pressure plates (eccentrically loaded test 2B, plates near to load)

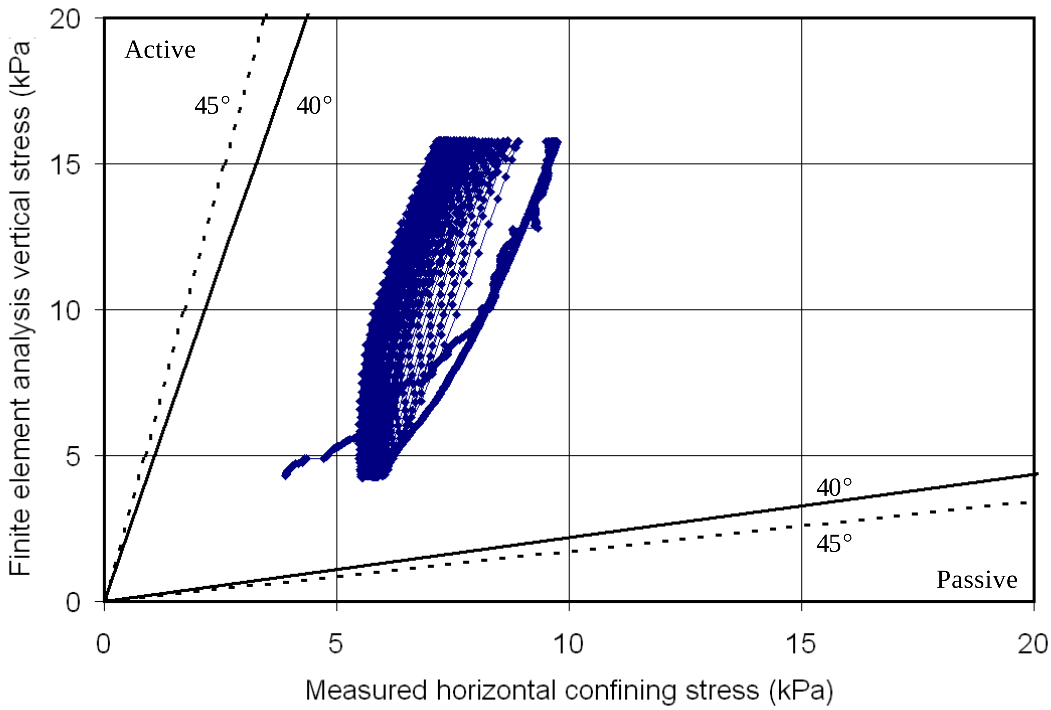

Figure 6-30: Finite element calculated vertical stress plotted against measured horizontal confining stress as average across pressure plates (eccentrically loaded test 9C, plates away fr om load)

Cycle	Ratio during load step 3A			Ratio during load step 2B			Ratio during load step 9C		
	min	**max**	**mean**	**min**	**max**	**mean**	**min**	**max**	**mean**
	(Max load)	**(Min load)**		**(Max load)**	**(Min load)**		**(Max load)**	**(Min load)**	
0	1.34			0.77			0.76		
1	0.69	1.34	0.93	0.48	0.80	0.61	0.60	0.97	0.75
2	0.64	1.66	0.92	0.41	1.21	0.61	0.56	1.31	0.76
5	0.64	1.86	0.98	0.38	1.24	0.68	0.54	1.36	0.76
10	0.61	1.84	0.96	0.35	1.20	0.63	0.52	1.32	0.73
50	0.53	1.65	0.85	0.34	1.28	0.59	0.46	1.28	0.68
100	0.50	1.52	0.80	0.34	1.26	0.59	0.45	1.25	0.67

Table 6-10: Summary of earth pressure ratio at key numbers of cycles, tests 3A, 2B and 9C

The pressure plates for test 2B were located nearest to the eccentric load, so the vertical finite element calculated stress and measured confining stress changed over the greatest range. Because of this, trends are more clearly identifiable and Figure 6-29 is annotated; the measured confining stress is shown at its lowest value when the test begins, as the vertical load is applied, following the virgin loading line the confining stress reaches its maximum. Subsequent cycles show the cyclic peak confining stress reducing whereas the cyclic minimum changes little after the first five cycles of load. Similar behaviour can be seen in Figure 6-28 and Figure 6-30.

These general trends are reflected in the earth pressure ratio, the earth pressure ratio appears to begin close to unity as each test begins and reduces over the initial loading cycle manifested by a curving upwards of the initial load line in Figure 6-28, Figure 6-29, and Figure 6-30, thereafter this trend is reinforced with subsequent cycles having an increasingly reduced earth pressure ratio at peak load i.e. it moves towards the active condition. The earth pressure ratio at minimum load increases during the initial 5 cycles moving towards the passive condition but then appears to stabilise with little change occurring over the remaining 95 cycles. The behaviour at minimum load is in some ways similar to known behaviour of over consolidated soils where it has long been recognised that horizontal earth pressures can exceed vertical ones (Brooker and Ireland, 1965). However, in contrast to tests carried out by Brooker and Ireland (1965) in which normally consolidated reformed clays were consolidated in an oedometer which was set up to prevent radial strain, the initial loading line in these tests is not linear. This is perhaps because the ballast is able to strain horizontally in order to relieve horizontal confining stress by moving towards the active case. In the experiments carried out by Brooker and Ireland it was demonstrated that the earth pressure ratio increases with increasing over consolidation ratio, they further proposed that the value of earth pressure ratio should curve to reach an asymptote with the passive earth pressure as the OCR increases. If this were related to ballast, it may be reasonable to expect that heavier axles would lead to higher unloaded earth pressure ratios. However, the ability of the ballast to sustain higher earth pressure ratios is likely to be limited because it is able to strain horizontally. It is also worth noting that within the paper by Brooker and Ireland a reference is made to Jaky (1948) who put forward a relation for the value of earth pressure coefficient (K_0) for normally consolidated soils.

$$K_0 = 1 - \sin f'$$ **Equation 6-4**

Brooker and Ireland note that this relation applies better to cohesionless soils. Applied to a soil with a friction angle of 45°, about that thought to be present in ballast this gives a K_0 value of 0.71. Although there is variation in the initial value of K_0 shown in Table 6-10, this can be explained by an inconsistent sleeper/ballast contact which becomes more consistent with loading cycles.

Stewart et al (1985) carried out a test to determine residual horizontal stresses in ballast in a specially constructed rig. The ballast was confined within a steel box with plan dimensions of 300 mm (ends) by 600 mm (sides) divided into four vertical tiers each 100 mm deep with instrumentation to measure the confining stress within each tier. In the experiment an angular traprock (AREA No. 4 gradation) ballast was placed into the steel box and a cyclic vertical load ranging up to 4000 lb (~18 kN) was applied through a sleeper segment of plan dimensions 225 mm by 290 mm. During the tests horizontal pressures on side and end panels in each tier were measured over 10,000 load cycles. Figure 6-31 and Figure 6-32 have been reproduced from similar charts produced by Stewart (1985). The original figures are small and no absolute values are given so these reproductions can only be considered accurate to the nearest 2 kPa.

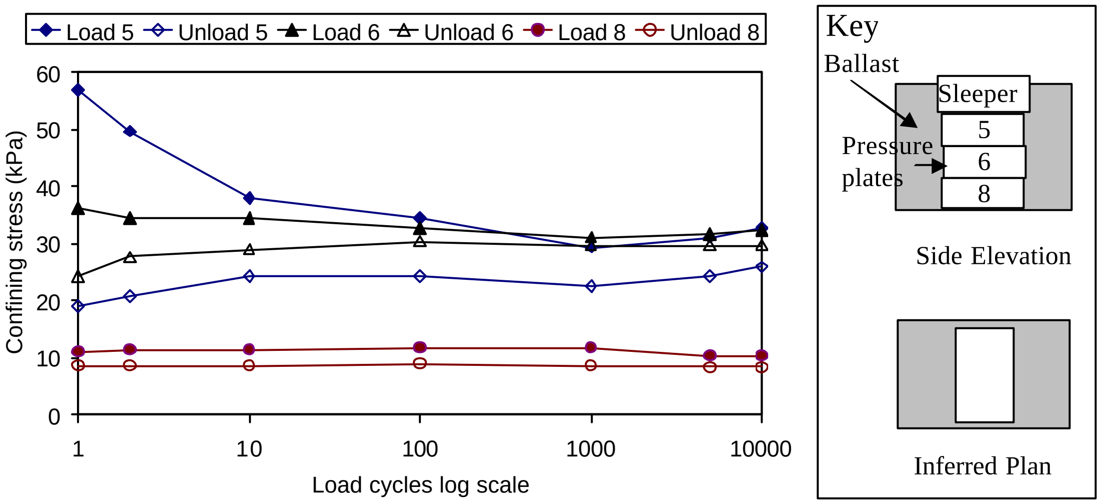

Figure 6-31: Horizontal stresses on side panels after Stewart (1985)

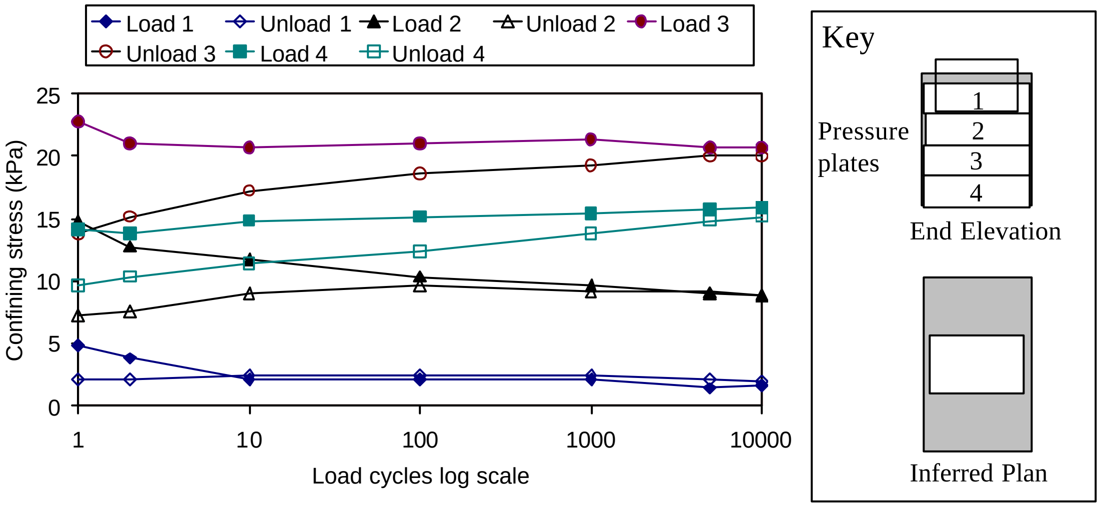

Figure 6-32: Horizontal Stresses on end Panels after Stewart (1985)

In Figure 6-31 the pressure panels occupy approximately one third each in height of the 300 mm depth of ballast beneath the sleeper. Initially the upper of the two trend lines on the graph for each tier represents the loaded case and the lower line the unloaded case, these lines tend to converge with loading cycles. The end panels are further away from the part sleeper. This allows the load some opportunity to spread and explains the lower horizontal stresses measured in the end panels (Figure 6-31) than in the side panels (Figure 6-32).

In Stewart's tests the range of confining stress per loading cycle seems to stabilise at or shortly after 100 load cycles, with limited convergence thereafter to 10,000 cycles. The confining stress in the tests for this research appears to undergo similar convergence during the first 100 load cycles. However, Stewart's tests differ from those carried out for this research in that they confined the ballast from straining horizontally.

6.3. Summary of Chapter 6

Development of confining stress in the laboratory during the first 100 load cycles was measured:

- It was shown that the range of confining stress from minimum to maximum during cycles narrowed with increasing numbers of cycles over the 100 cycles tests.
- Comparison to finite element vertical stress showed that the earth pressure ratio underwent changes during the 100 load cycles. In particular the data was conclusive in identifying a reducing ratio at maximum load with movement towards the active earth pressure ratio. At minimum load the earth pressure ratio increased during the initial 5 cycles in line with expected behaviour of over consolidated soils.

Although structure in ballast was not directly measured, the changes in measured confining stress with loading cycles are considered powerful indicators that changes are occurring to the structure of the ballast. These changes are thought to lead to the increased lateral resistance measured on real track after trafficking. There is potential to research this further and some of the recommendations for further research at the end of this report will address this.

7. Characterising the pre-failure behaviour of the sleeper/ballast interface

This chapter focuses on in-service behaviour due to combined cyclic vertical, lateral and moment loading with the objective to:

- Characterise single sleeper interface properties (pre-failure) for use with dynamics models e.g. ADAMS/Rail (MSC software, 2008).

This Chapter is divided into two main sections:

- Geophone monitoring on the WCML, characterising lateral sleeper movement on low radius curves of the WCML during passage of Pendolinos at high speed.
- Lateral pre-failure response; examining laboratory data for pre-failure response for different cyclic VHM loading regimes following the 100 vertical load cycles and making comparison with the geophone data.

At the end of the Chapter a summary draws together the findings from each section.

7.1. In-service behaviour of the sleeper/ballast interface: Geophone measurements

7.1.1. Background & Methods

As described in Chapter 5, geophones were used to measure sleeper deflections on low radius curves of the WCML. Five geophones were available to measure horizontal sleeper movements; these were used to measure movement both along and lateral to the track. The longitudinal movements were much smaller than the vertical and lateral deflections and are not considered relevant to the objectives of the current research. The longitudinal results are not used in this report, although some of these data are reported in (Priest et al., 2008).

The geophones were only able to measure movement perpendiculuar to the direction of gravity and do not give absolute lateral sleeper movements in the plane of cant. However, the difference is small due to the low cant angle (5.7°) and so the measurements taken are considered to indicate pre-failure sleeper ranges of movement in the plane of cant closely enough without correction for the effects of cant.

Site names and sleepers are identified in accordance with the diagrams presented in Chapter 5 and Appendix B.

7.1.2. Results

Four sleepers were identified across the three monitoring sites at Weedon where measurements were taken of the vertical deflection at both the high and low sleeper ends as well as the lateral movement, two sleepers were at site 1 where the track had recently been tamped and a sleeper each from sites 2a and 2b where the sleepers were inspected and appeared to be in good contact with the surrounding ballast in the crib, and shoulder. It should be noted however, that some sleepers near to those monitored at sites 2a and 2b were observed to be in poor contact with the crib and shoulder ballast. Again, as with the vertical data reported in Chapter 5, some data are taken from different Pendolino trains but the difference in speed and weight of the different trains is minimal and does not introduce any significant discrepancy into the results. However, the small differences in speed do mean that the peaks and troughs sometimes do not align when plotted on the same deflection/time graph.

Figure 7-1 to Figure 7-6 show the deflection/time data in graph form. Two different pairs of graphs are shown for the two sleepers at site 1 for different trains over the same two sleepers (train 1 and train 2), and there is one graph each from sites 2a and 2b. To make comparison easier the data has been adjusted to the same train speed, approximately 110 mph in each case. Also, the scale on the ***x*** and ***y*** axes is identical for all reported data to make visual comparison easier. The lateral deflection is reported on the right hand scale and offset lower in order to make the graphs clearer.

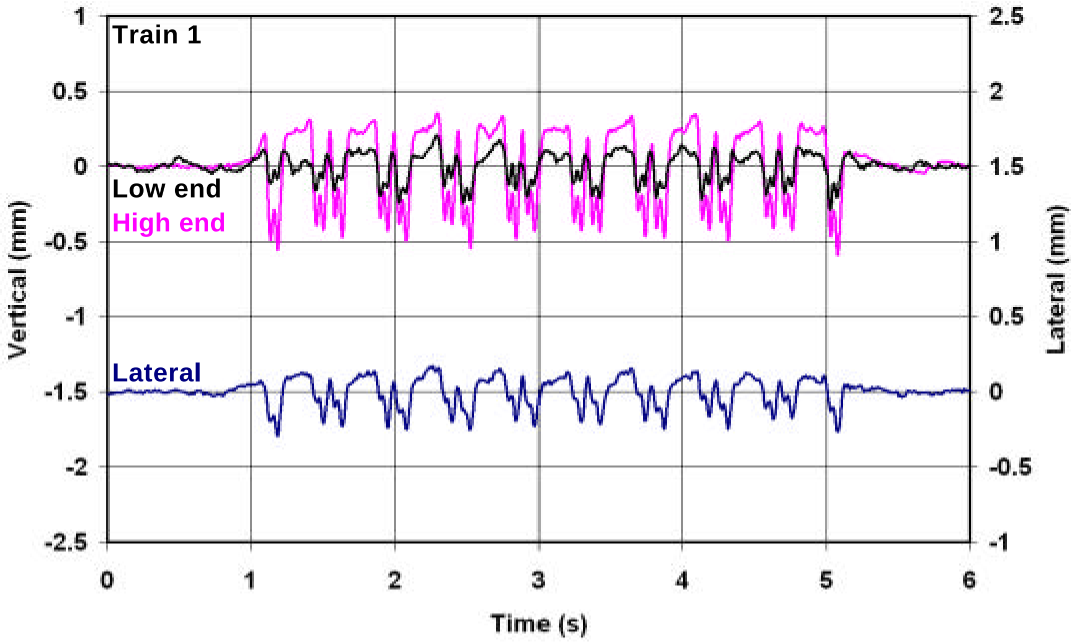

Figure 7-1: Deflection /time graph for passage of a Pendolino train at site 1, sleeper K, set up 3, data from set up 3, run 14, channels 6, 4, and 8

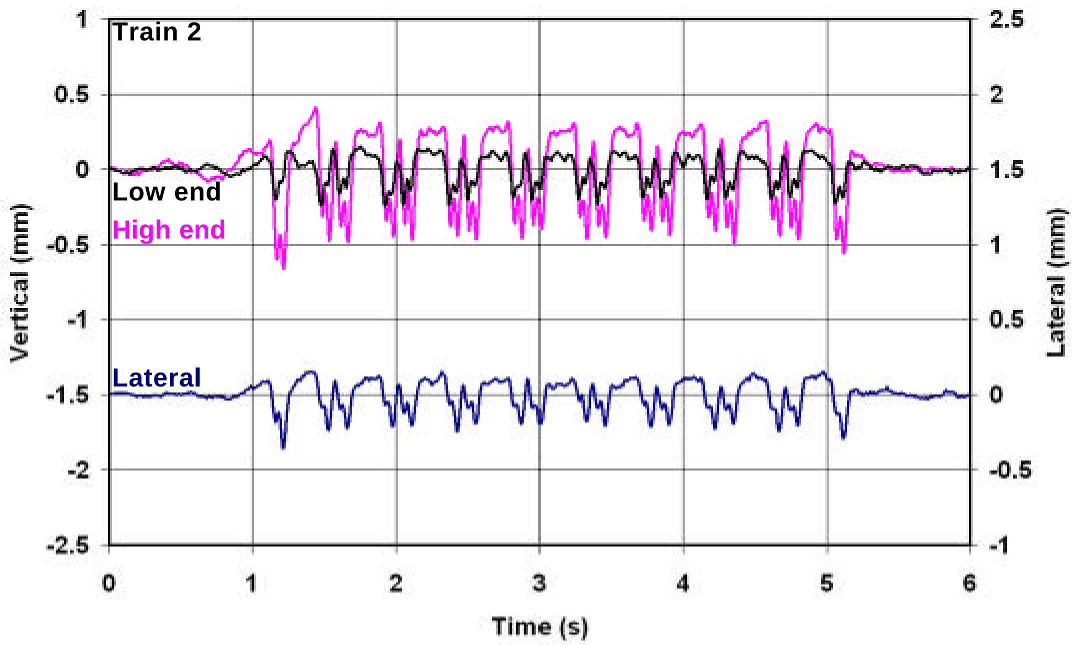

Figure 7-2: Deflection /time graph for passage of a Pendolino train at site 1, sleeper K, data from set up 3, run 17, channels 6 and 8 with high end deflection from run 1, set up 1, channel 4

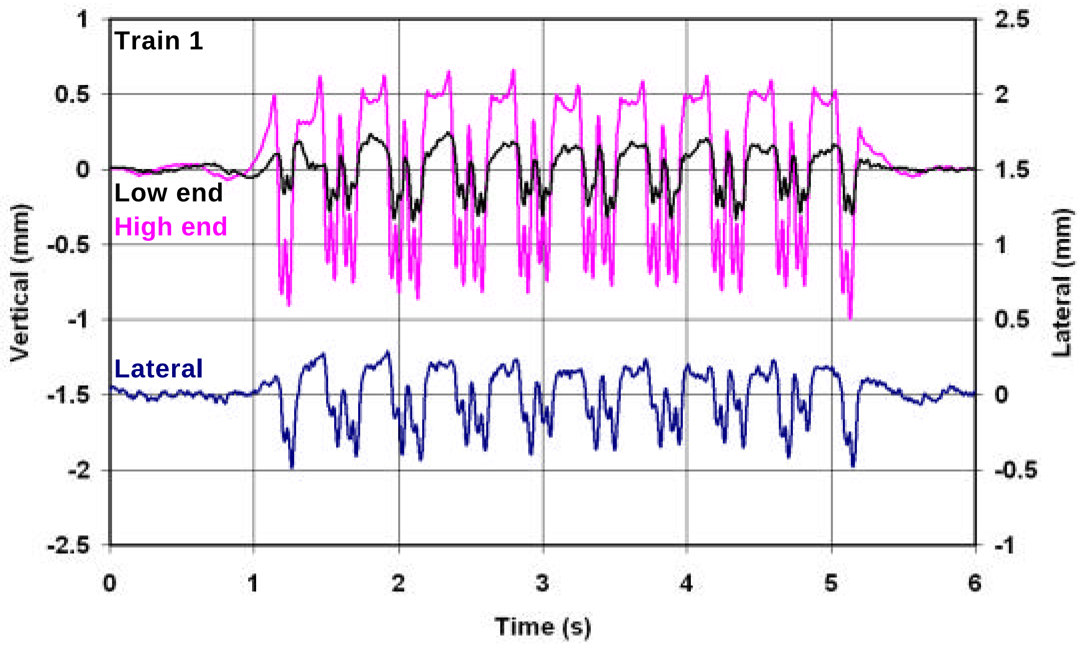

Figure 7-3: Deflection /time graph for passage of a Pendolino train at site 1, sleeper Q, data from set up 3, run 14, channels 2 and 7, with high end deflection taken from run 1, set up 1, channel 1.

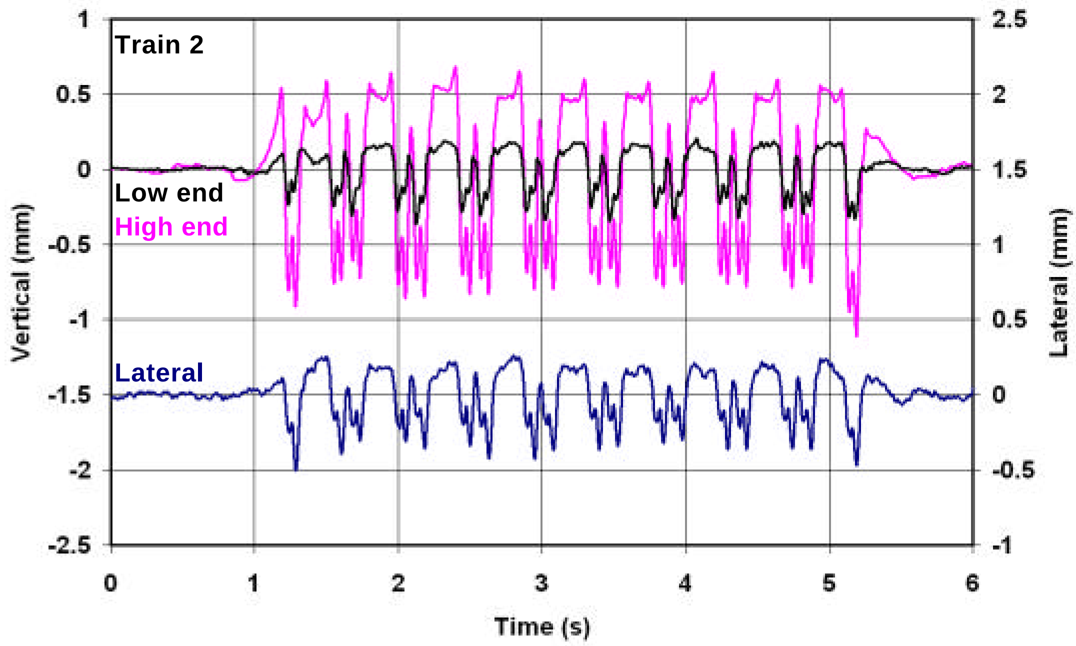

Figure 7-4: Deflection /time graph for passage of a Pendolino train at site 1, sleeper Q, data from set up 3, run 17, channels 2, 7 and 9

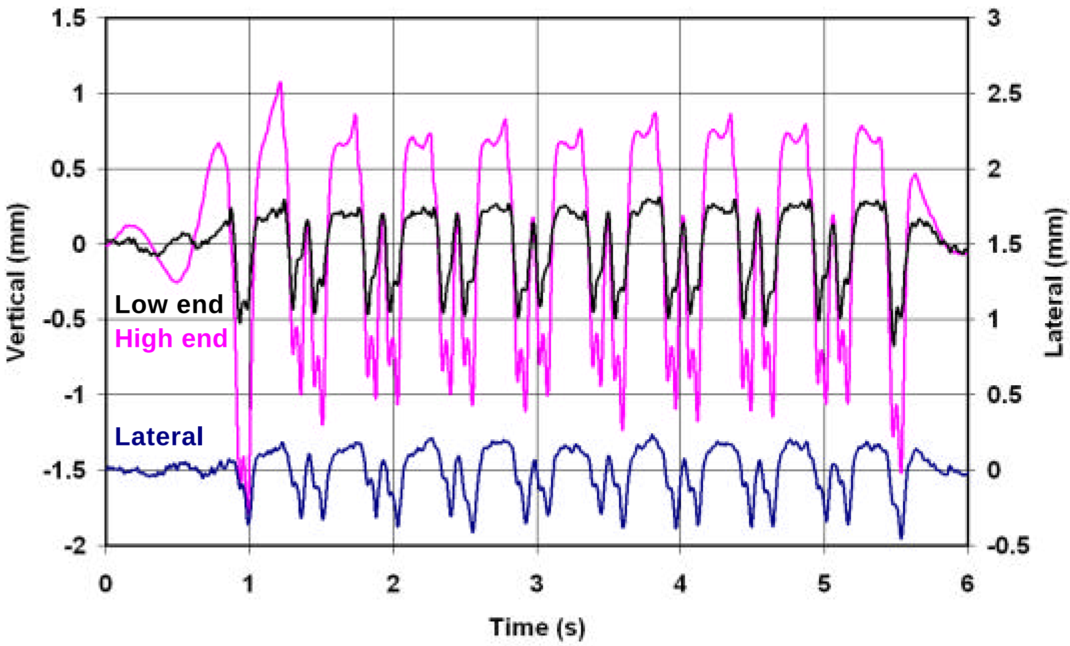

Figure 7-5: Deflection /time graph for passage of a Pendolino train at site 2a, data from set up 5, run 14, channels 2 and 6 with the low end data from setup 4, run 12, channel 10.

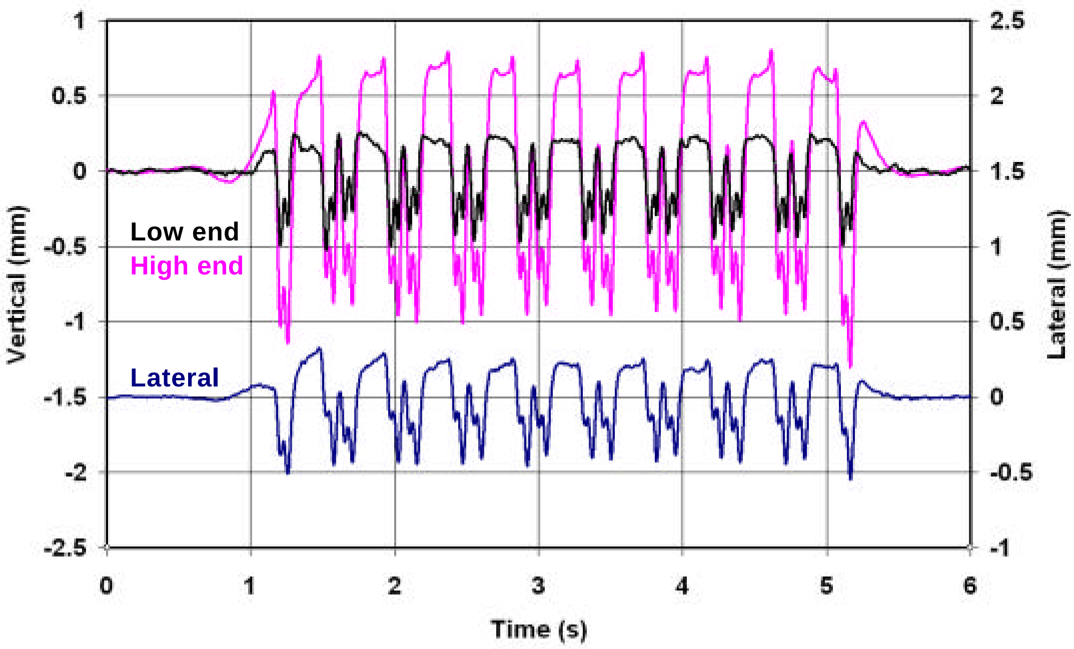

Figure 7-6: Deflection/time graph for passage of a Pendolino train at site 2b, data from set up 3, run 8, channels 1, 2, and 3

7.1.3. Interpretation

Figure 7-1 to Figure 7-6 share some common features. In particular if the variation in lateral deflection with time is examined it can be seen that the second axle of each bogie has a greater deflection than the first axle, often by a significant proportion. Recovery between axles of the same bogie is also not full.

The variation in vertical deflection with time of the high sleeper end also shows the same general behaviour although the tendency of the sleeper to deflect more under the second axle is less pronounced.

In contrast the low end sleeper deflection with time shows a reverse tendency in that the vertical deflection for the first axle on each bogie is greater than the second axle. This would seem to suggest that the forces are not distributed evenly into each axle.

The use of vehicle/track dynamic interaction models can explain this behaviour. Bezin (2008) has shown, by means of computer simulation, that the observation can be explained as a direct consequence of the bogie yaw rotation stiffness resistance (secondary suspension) and the axles yaw stiffness (primary suspension):

While curving, due to the wheel-rail contact conicity, the axles naturally tend to shift away from the central position on the track, to a shifted equilibrium position where contact forces are balanced. The bogie steering resistance reacts to this natural behaviour and produces unequal lateral forces at the wheel-rail contact between the front and rear axles of the bogie explaining the difference in measured sleeper lateral deflection between axles on the same bogie. Additionally, the axles lateral movements mean that the rolling radius increases on one side (contact towards the flange of the wheel) while it reduces on the opposite side (contact towards the outside of the wheel) this compresses the primary (axle) suspension on one side and uncompresses on the other, explaining the differences for the measured vertical deflections. Since the front and rear axles have been rotated by the secondary suspension onto opposite rails the higher peak in vertical deflection occurs on opposite sides of the track for the two axles of a bogie.

These trends can more clearly be seen taking the deflection/time plot for a two bogies on adjacent cars as shown in Figure 7-7.

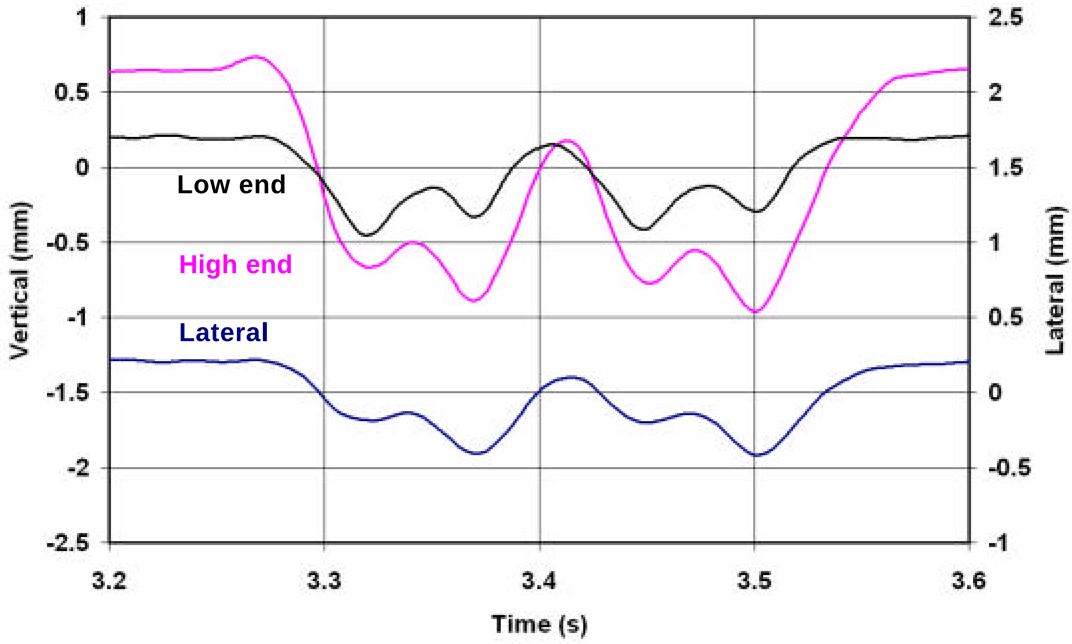

Figure 7-7: Close up of deflection/time plot for two bogies on adjacent cars taken from passage of a Pendolino train at site 2b, data from set up 3, run 8, channels 1, 2, and 3

Figure 7-8, Table 7-1 and Table 7-2 summarise the deflection/time data for axle 7 from each of the four sleepers shown in Figure 7-1 to Figure 7-6. It should be noted however, that axle 7 is the first axle of a bogie and the deflections shown are for the range of movement from the trough prior to axle 7 to the peak deflection for axle 7. Larger ranges of movement may be obtained by considering the trough prior to bogie passage and the peak during bogie passage (i.e. axles 7 and 8 together).

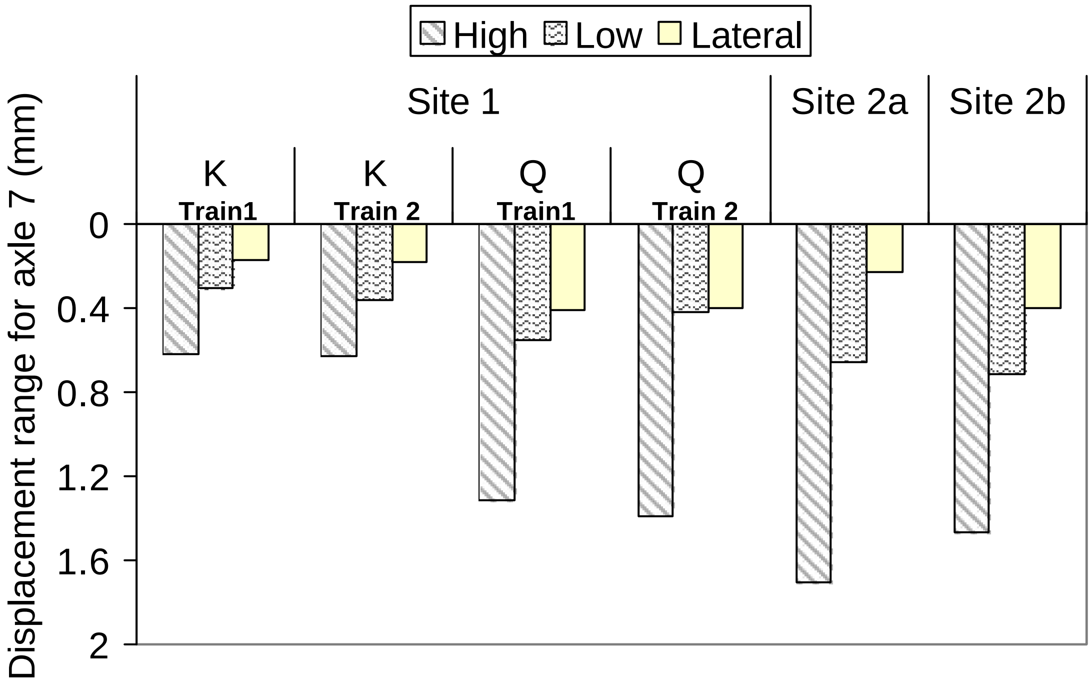

Figure 7-8: Bar chart to compare displacement range for axle 7 at sites 1, 2a and 2b

	Deflection for axle 7 (mm)				
	Sleeper K		**Sleeper Q**		
Train	1	2	1	2	Mean
High	0.62	0.63	1.32	1.39	0.99
Low	0.31	0.36	0.55	0.42	0.41
Ratio H/L	2.00	1.75	2.40	3.31	2.37
Lateral	0.17	0.18	0.41	0.4	0.29

Table 7-1: Summary of displacement ranges for axle 7 on sleepers K and Q at site 1

	Deflection for axle 7 (mm)		
	Site 2a	**Site 2b**	**Mean**
High	1.71	1.47	1.59
Low	0.66	0.72	0.69
Ratio H/L	2.59	2.04	2.315
Lateral	0.23	0.4	0.315

Table 7-2: Summary of displacement ranges for axle 7 on sleepers at sites 2a and 2b

Examining the combined vertical and lateral deflection behaviour shows that the lateral behaviour shows the same trends previously outlined in Chapter 5, sleepers give consistent magnitudes of deflection for different Pendolino trains travelling at the same speed whilst comparison of sleepers seemingly subjected to similar loads can have varied response.

Restating the results from the static analysis of forces on the railheads at sites 1 and 2 previously presented in Chapter 5 Table 5-4:

Site	**Cant (mm)**	**Radius (m)**	**High rail vertical force (kN)**	**Low rail vertical force (kN)**	**Lateral (kN)**
1	150	1230	92	56	14
2	150	1025	99	49	20

Table 7-3: Forces on the rails normal to the track and lateral to the track relative to the plane of cant

It is clear that significantly more lateral load would be expected to reach the sleepers at site 2 than at site 1. However, as with the vertical deflection this is only partly reflected in the lateral deflection from the geophone data. Sleeper Q at site 1 shows a higher lateral deflection than the sleeper at site 2a despite the lower likely load. This means that the general trends described in Chapter 5 can also be applied to the lateral sleeper deflection behaviour.

7.2. Pre-failure behaviour of the sleeper/ballast interface: Laboratory results

7.2.1. Background

In this section results from laboratory tests relating to the pre-failure response of the sleeper/ballast base contact area to cyclic vertical, horizontal and moment loading are presented.

In addition, by examining the load/deflection behaviour of the laboratory data a mathematical relation is proposed to describe the pre-failure behaviour, which has the potential to be used in a train/track interaction model such as ADAMS/Rail (MSC software, 2008).

However, before the laboratory results are presented it is useful to review the known behaviour of granular materials subjected to shear loads and consider how closely elastic theory is able to model this.

Consider an element of ballast in contact with the sleeper across its top surface (Figure 7-9) where the ***z***-axis is along the length of the track, the ***x***-axis is laterally across the track, the ***y***-axis is vertical and d corresponds to the sleeper lateral deflection due to shear stress alone.

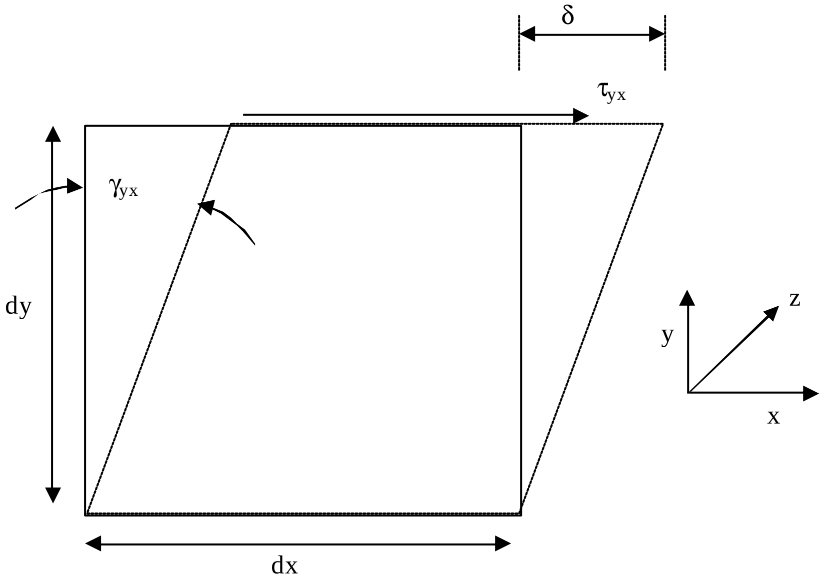

Figure 7-9: Idealised sleeper/ballast interface element in pure shear

The symbol g denotes shear strain and t shear stress.

The element is in plane strain therefore:

$$e_z=0$$

$$\gamma_{xz}=0$$

$$\gamma_{yz}=0$$

The lateral deflection on the sleeper would then depend on the shear modulus ***G*** so that the shear force and shear strain would be related by:

$$t_{yz} = Gg_{yz}$$ **Equation 7-1**

To determine ***G*** for a material in plane strain, tests are required to measure the deflection at the top of the element d for a known shear force such that the shear strain may be determined:

If ***D*** is the depth of ballast, and the shear strain is small:

$$g_{yz} = \frac{d}{D}$$ **Equation 7-2**

In a linear elastic medium, ***G*** would be constant and the relationship between shear strain and shear stress would be linear.

However, ***G*** is known to vary with strain in granular materials as shown in Figure 7-10. It is also highly probable that ***G*** varies with depth of granular medium.

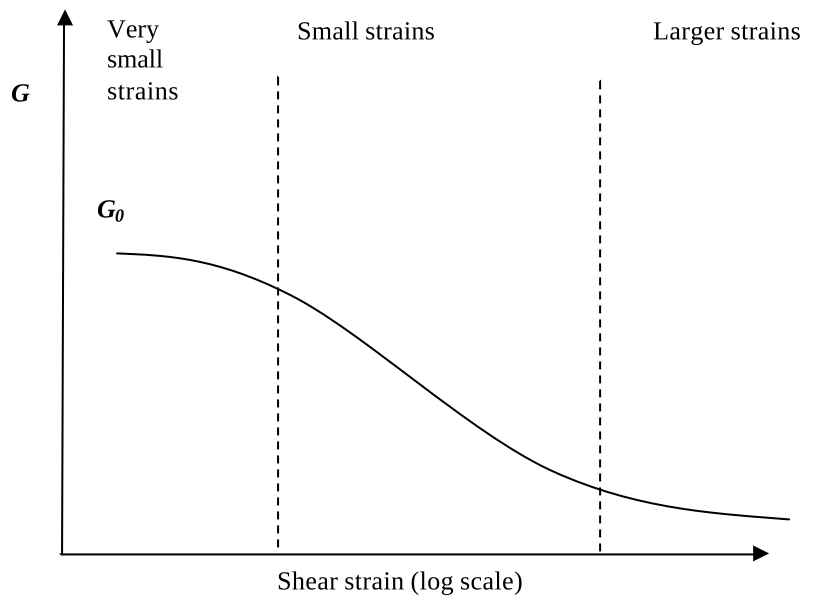

Figure 7-10: Idealized stiffness/strain curve after Atkinson & Sallfors (1991)

To make use of the relationship shown in Figure 7-10 both G_0 and a function for the reduction in shear modulus (***G***) with shear strain are required.

G_0, the initial value of the shear modulus at very low deflections, is thought to be related to the mean effective confining pressure ***p'***. Many researchers have developed equations of the form:

$$G_0 = A_0 p'^{n_o}$$ **Equation 7-3**

Where ***A*** and ***n_0*** are dimensionless constants for a particular material. Different versions of this equation may be traced back in the literature for a number of decades e.g. Hardin (1978). Furthermore it can be shown, using Hertzian contact theory, that for an assembly of spheres in contact with linear elastic properties the bulk modulus is related to a one third power of the pressure (Wroth and Houlsby, 1985). For a linear elastic material the bulk modulus may be considered to behave similarly to the shear modulus so that only the constant ***A_0*** would change in Equation 7-3 and the power ***n*** could be 1/3. For angular particles ***n*** is suggested to be 0.5 (Wroth and Houlsby, 1985).

Rampello et al, (1994b), in a report of a conference panellist discussion stated that many researchers have included the void ratio and the over-consolidation ratio of the medium into Equation 7-3:

$$G_0 = S.f(e)OCR^k p'^{n_o}$$ **Equation 7-4**

Where, ***S***, ***k*** and ***n_0*** are constants, ***f(e)*** is a function of the void ratio, ***OCR*** is the over consolidation ratio. The ***OCR*** and ***f(e)*** are arguably both measures of the quality of inter-particle grain contacts; therefore Rampello et al. (1994a) proposed that the void ratio can be eliminated so simplifying the expression:

$$G_0 = S.OCR^m p'^{n_o}$$ **Equation 7-5**

For a medium such as railway ballast the void ratio and over consolidation ratio may be considered as more or less constant for a particular type of ballast after being freshly placed. Therefore Equation 7-3 is sufficient to describe expected ballast shear behaviour for the particular ballast used in the experiments since no comparison is made to other types of ballast or compaction method. Furthermore a value at or near 0.5 for ***n*** should be expected.

One way to model the variation of ***G*** with shear strain is to use a hyperbolic function (Hardin and Drnevich, 1972), (Diakoumi, 2007), i.e.

$$G_{sec} = \frac{1}{A + Bg}$$ **Equation 7-6**

Where $\boldsymbol{A}$ and $\boldsymbol{B}$ may be found experimentally such that the general form of behaviour of reducing $\boldsymbol{G}$ with strain matches Figure 7-10.

Train loading causes changes in mean effective stress ($\boldsymbol{p'}$) while simultaneously causing shear strains at the sleeper/ballast interface. Thus for a ballast undergoing train loading, $\boldsymbol{G}$ would be expected to vary as shown in Figure 7-11.

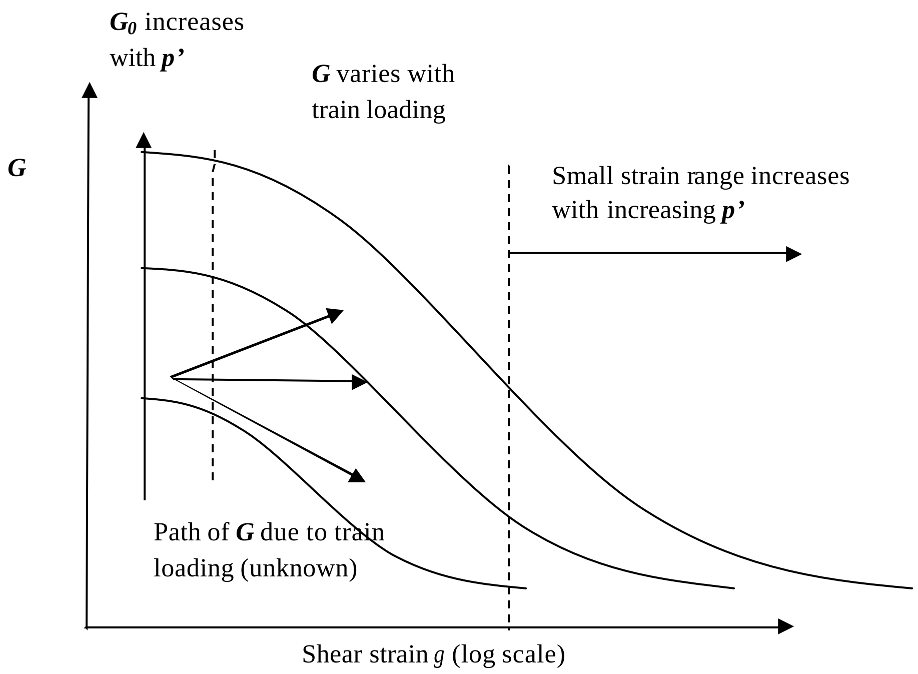

Figure 7-11: Stiffness/strain graph to show conceptualization of the effect of train loading

Initially as the train approaches a sleeper neither vertical load nor lateral deflection are present. As the train nears the sleeper, vertical load and lateral load are transferred to the sleeper/ballast interface in proportions which depend on the relative vertical and lateral stiffnesses of the track system. This means that the behaviour crosses over different lines of expected behaviour of $\boldsymbol{G}$ vs. g for fixed values of $\boldsymbol{p'}$. The increase in vertical load acts to increase the value of $\boldsymbol{G}$ whilst the deflection due to increasing lateral load acts to reduce the value of $\boldsymbol{G}$. Exactly how the proportions of these two effects interact to give the measured value of $\boldsymbol{G}$ has been investigated by cyclic load tests in the laboratory.

Simpson (1992) suggested that the reduction in $\boldsymbol{G}$ with log strain might be proportional to the plastic strain, in effect placing an inverse scale from 0 to 100% plastic strain from $\boldsymbol{G_0}$ to the final limiting value of $\boldsymbol{G}$. However, most researchers have considered that the very small strain region shown in Figure 7-10 corresponds to fully elastic behaviour.

It has been suggested that the strain levels dividing the very small, small, and larger strain levels in Figure 7-10 would be around 0.001% and 1% respectively (Atkinson and Sallfors, 1991). Lo Presti (1995) suggested an elastic limit of 0.001% for any kind of uncemented soil. In the tests reported here it was not possible to obtain reliable information for strains below 0.001% (corresponding to 0.003 mm of movement). For the track system, tension in the rails acts to return displaced sleepers to their starting position after axle passage so other factors are involved in determining the proportion of plastic strain remaining. Determining plastic strain goes beyond the scope of the current research.

7.2.2. Methods and Results, pre-failure laboratory tests

Laboratory tests were carried out in accordance with the methods set out in Chapter 4. In this Chapter the data for single load/unload cycles of lateral vertical and moment load are presented.

Cyclic tests were not carried out on all test set-ups partly due to difficulties in tuning the hydraulic rams. Consequently most cyclic data is from the later test set-ups. The test results presented are intended to cover a variety of loading conditions and demonstrate key aspects of behaviour.

Figure 7-12 to Figure 7-15 present graphs of lateral load plotted against lateral deflection on different test set-ups to compare the effect of cycling the lateral load with different magnitudes of vertical load and moment load present. Because failure is likely to occur near to a particular ratio of vertical to lateral load all tests were carried out so that the peak lateral load was not more than 1/3 of the constant vertical load considered safely below the likely failure ratio. In later sections graphs of stress ratio (equivalent to loading ratio) against deflection are plotted.

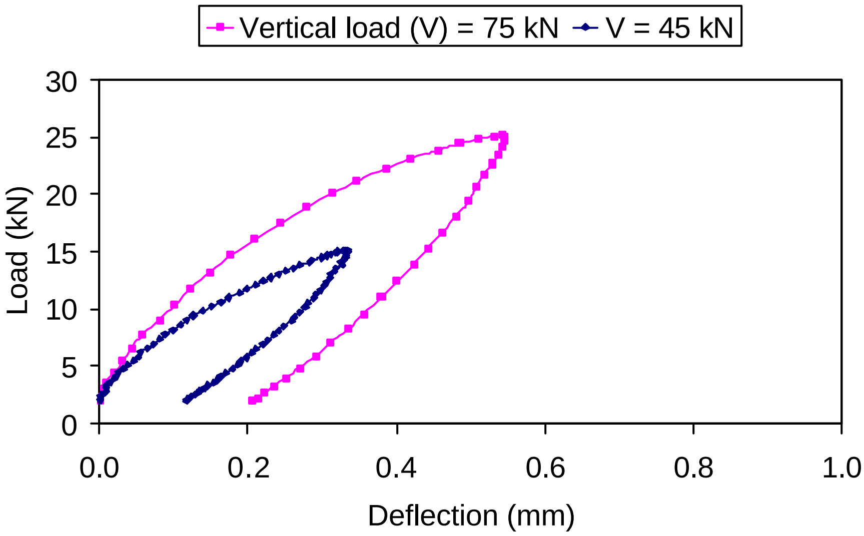

Figure 7-12: Load/deflection graph vertical load central (1A), first load/unload cycle only

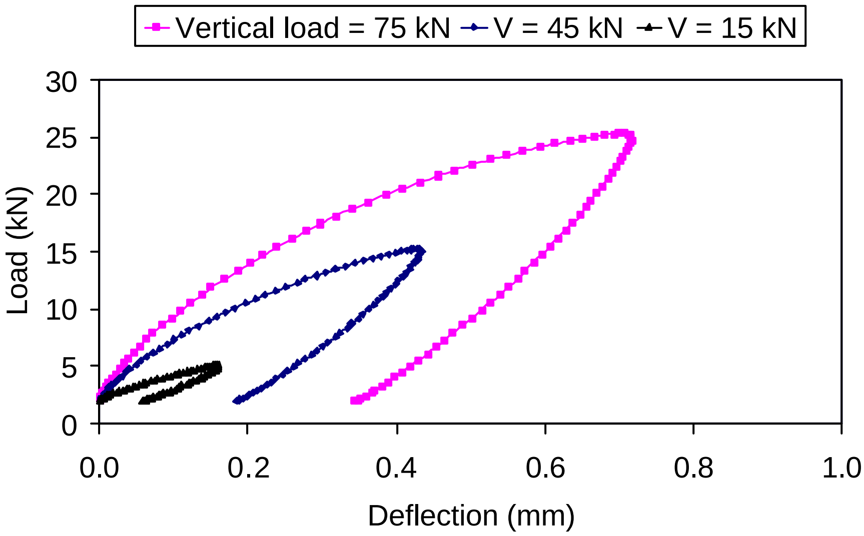

Figure 7-13: Load/deflection graph for eccentric vertical load (7C), first load/unload cycle only

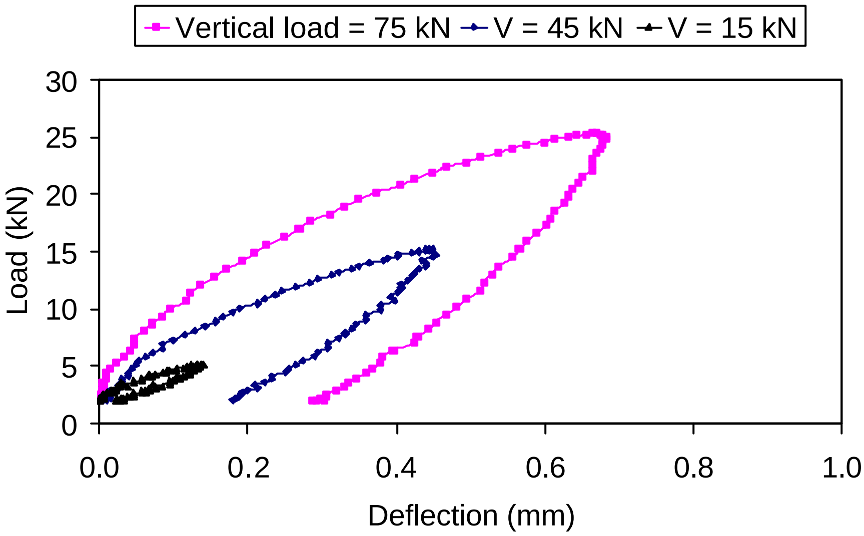

Figure 7-14: Load/deflection graph for eccentric vertical load (5C), first load/unload cycle only

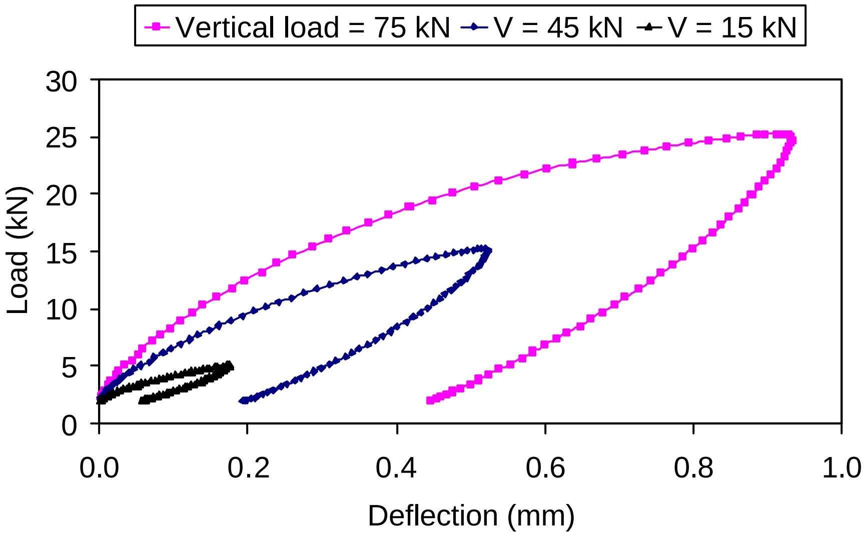

Figure 7-15: Load/deflection graph for eccentric vertical load (8C), first load/unload cycle only

Table 7-4 and Figure 7-16 summarise the peak deflection and the deflection at the end of cycle 1, termed the residual deflection, shown in Figure 7-12 to Figure 7-15.

Test set-up	Load (Vertical:Lateral) and mm of deflection					
	75:25	75:2	45:15	45:2	15:5	15:2
	Peak	Residual	Peak	Residual	Peak	Residual
1A	0.544	0.205	0.333	0.116	-	-
5C	0.683	0.287	0.453	0.179	0.141	0.023
7C	0.717	0.344	0.432	0.185	0.158	0.062
8C	0.933	0.446	0.522	0.192	0.173	0.056
max	0.933	0.446	0.522	0.192	0.173	0.062
min	0.544	0.205	0.333	0.116	0.141	0.023
range	0.389	0.241	0.189	0.076	0.032	0.039
mean	0.719	0.321	0.435	0.168	0.157	0.047

Table 7-4: Summary of cyclic deflection data

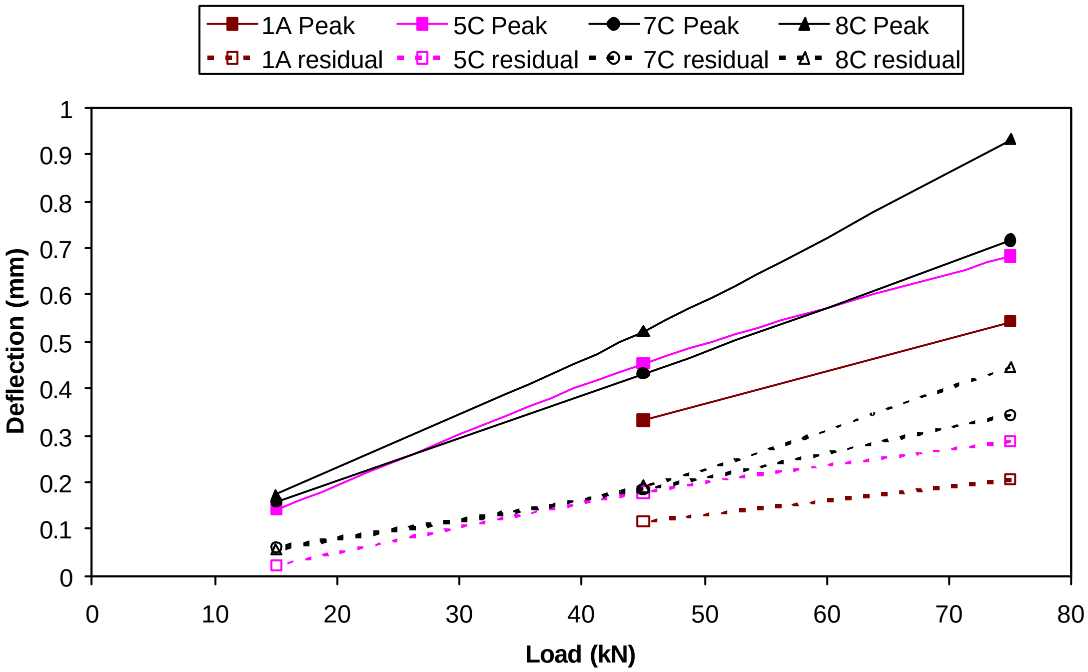

Figure 7-16: Deflection/load plot for vertical load held constant during each test

It is clear from these data that there is a significant variation between tests, for the tests at 75 kN vertical load and 25 kN lateral load, the minimum peak deflection is just below 60% (set-up 1A) of the maximum peak deflection (set-up 8C). This is entirely consistent with the geophone measurements, where it has been shown that the lateral deflection varies significantly from sleeper to sleeper even though loading is expected to be similar. In Figure 7-8 it can be seen that sleeper Q deflects more than twice as much as sleeper K due to the same train loading i.e. that sleeper K's lateral deflection was less than 50% of sleeper Q's.

It is considered coincidental that the lowest peak lateral deflections occur for the only pre-failure testing with centrally applied load (1A). More data would be required to determine whether the lower recorded values compared to the tests with moment load were due to moment load or whether they can be attributed to variation between test set-ups. In this report the presence or lack of moment load and its possible influence on the pre-failure behaviour of the sleeper/ballast interface will not be further explored. In Chapter 8 it will be shown that the failure behaviour of the sleeper/ballast interface due to possible magnitudes of train loading is not influenced by moment load.

So far all the graphs have shown tests where the vertical load was maintained at a constant value. However, true train loading varies both the vertical and lateral load. Therefore two tests, shown in Figure 7-17, were carried out at 0.1 Hz where the vertical and lateral loads were applied in a sinusoidal wave form for one cycle. The slower rate and single cycle were imposed due to safety considerations. Table 7-5 shows the loading regimes imposed for these two tests. The ratios of load were selected so that the vertical load would never exceed four multiples of the lateral load.

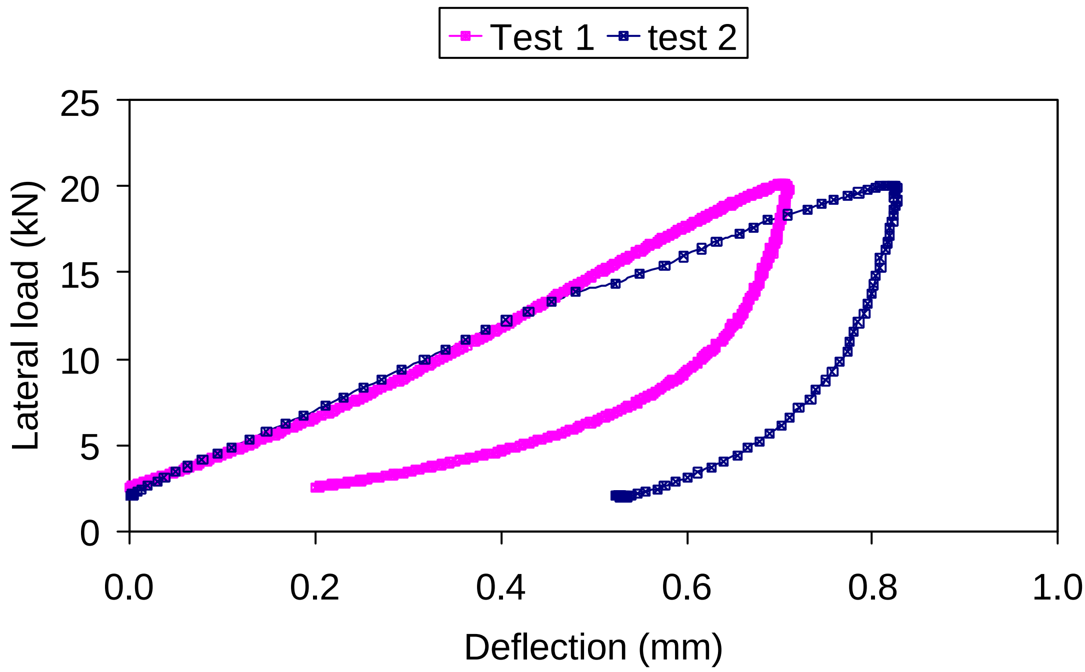

Figure 7-17: Tests where vertical and lateral load were simultaneously cycled. Test 1 was carried out on set up 1A with the vertical load centrally applied, test 2 was carried out on set-up 8C with the vertical load applied at a 0.5 m eccentricity.

Test	Vertical load kN	Lateral load kN
1 Eccentric load on set-up 8C	10:85	2.5:20
2 Central load on set-up 1A	15:75	2:20

Table 7-5: Loading regimes imposed for the two tests where vertical and lateral load were simultaneously cycled

Figure 7-17 shows markedly different load/deflection behaviour to that observed when the vertical load was constant (e.g. shown in Figure 7-15). In particular the load deflection lines during the increasing load phase are almost linear. Test 2 shows some evidence of a small slip near to 0.5 mm of deflection on the loading line which perhaps helps to explain the larger final deflection at the end of the test. Test 1 shows better recovery at the end of the loading cycle.

7.2.3. Interpretation

Comparison of laboratory experimental measurements with trackside geophone data

The geophone measurements at sites 1, 2a and 2b gave a range of lateral deflections for lateral loads at the railhead which were estimated to be 14 kN and 20 kN at sites 1 and 2 respectively (Table 5-4). In Chapter 3 the proportion of lateral load reaching a sleeper was estimated to be in the range 34 to 60%. Taking the median load proportion of 47% and the summary deflection data from Table 7-1 and Table 7-2 and the mean wheel to rail forces shown in Table 7-3, an estimate of the deflection and corresponding load can be made:

- At site 1 a mean deflection of 0.29 mm for a probable mean axle load of 7 kN was measured
- At site 2a and 2b a mean deflection of 0.32 mm for a probable mean axle load of 10 kN was measured

In the laboratory, the two tests where the vertical and lateral loads were simultaneously cycled are considered the most appropriate for comparison to the geophone data, for these tests:

- Test 1 gave a deflection of 0.7 mm for a load step of 17.5 kN
- Test 2 gave 0.8 mm for a load step of 18 kN

Taking the load/deflection behaviour to be linear during the loading phase the gradients of the geophone and laboratory tests can be compared as shown in Table 7-6.

Data source	Deflection (mm)	Load step (kN)	Gradient (kN/mm)
Site 1	0.29	7	24.1
Site 2	0.32	10	31.3
Laboratory simultaneous cyclic test 1	0.7	17.5	25.0
Laboratory simultaneous cyclic test 2	0.8	18	22.5

Table 7-6: Comparison of gradient over initial load step geophone and laboratory data

The mean gradients of the load/deflection lines shown in Table 7-6 are similar, and confirm that the behaviour in the laboratory is reasonably representative of track behaviour.

Evaluation of test data in context of known behaviour of granular materials

In the results section, the behaviour seen in the laboratory tests was described. To help further interpret this behaviour, in this subsection the apparent shear modulus, $\boldsymbol{G}$, is evaluated with respect to stress and strain in the laboratory data. The behaviour of $\boldsymbol{G}$ is then compared with that for a linear elastic medium and also with the known behaviour of granular materials. Data used are shown in Table 7-7. These data were chosen as representative of all the loading cases tested and because they were carried out on the same test set-up. In this section a relationship between shear modulus and load path is fitted to the experimental data and is presented for potential use in train/track dynamic interaction models.

Source data	Lateral load	Vertical load	Duration of loading step	G_{tan} evaluated over
Figure 7-15	2 to 25kN	75kN	1s	0.1s
Figure 7-15	2 to 15kN	45kN	1s	0.1s
Figure 7-15	2 to 5 kN	15kN	1s	0.1s
Figure 7-17 Test 1	2.5 to 20kN	10 to 85kN	5s	0.5s

Table 7-7: Selected tests evaluated in this section and evaluation of G_{tan}

Figure 7-18 shows two different methods used to evaluate the shear modulus. The secant shear modulus $\boldsymbol{G_{sec}}$ relates the current shear stress and shear strain to the intial values whereas $\boldsymbol{G_{tan}}$ is an estimate of the instantaneous shear modulus and is estimated from test data over small increments of change in shear stress and shear strain as shown in Table 7-7.

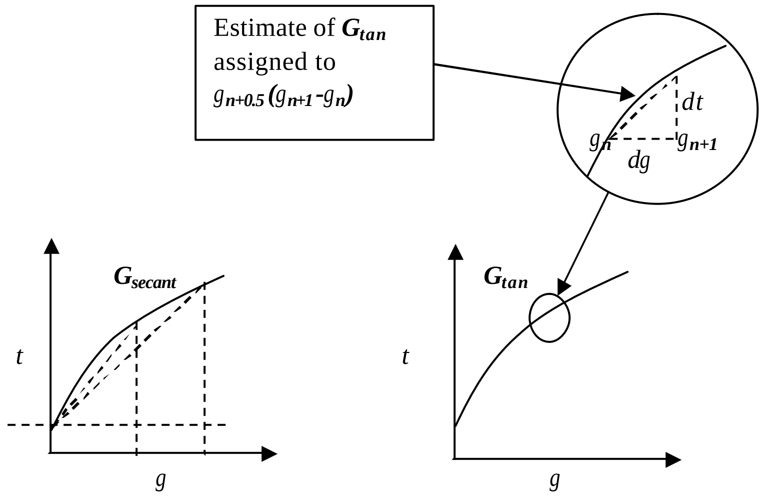

Figure 7-18: Key to calculation of shear moduli

To evaluate the shear modulus the lateral force is converted to a shear stress by dividing it by the area of the footprint of the sleeper (taken as 2500 mm × 300 mm although the sleeper base width is in fact slightly less at 285 mm not 300 mm (Tarmac, 2005)), and the deflection is converted to a shear strain by dividing by the depth of ballast (300 mm). The shear modulus is only evaluated over the loading step. It is also acknowledged that the shear stress and shear strain will spread with increasing depth below the sleeper base. The method of evaluating shear modulus is therefore an approximation.

Figure 7-19 plots the shear stress against deflection for the chosen cycles of load. These lines are identical to the lateral/load deflection lines previously shown with the vertical scale adjusted. Figure 7-21 shows the secant shear modulus against the shear strain and Figure 7-21 shows an estimate of G_{tan} with shear strain.

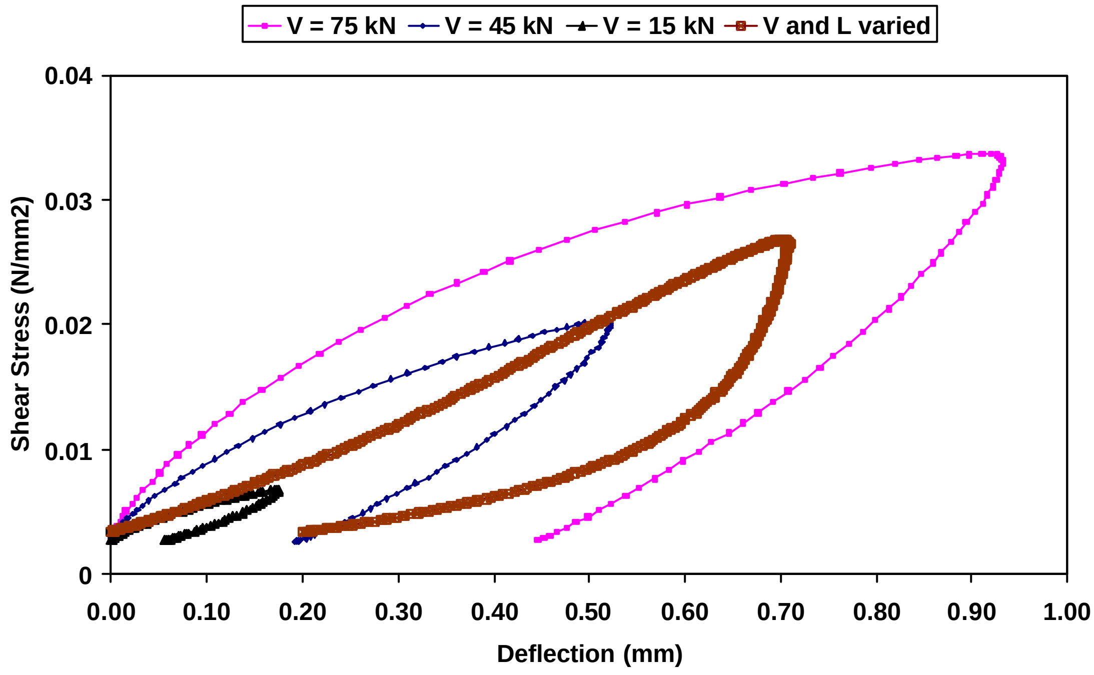

Figure 7-19: Shear stress/deflection graph

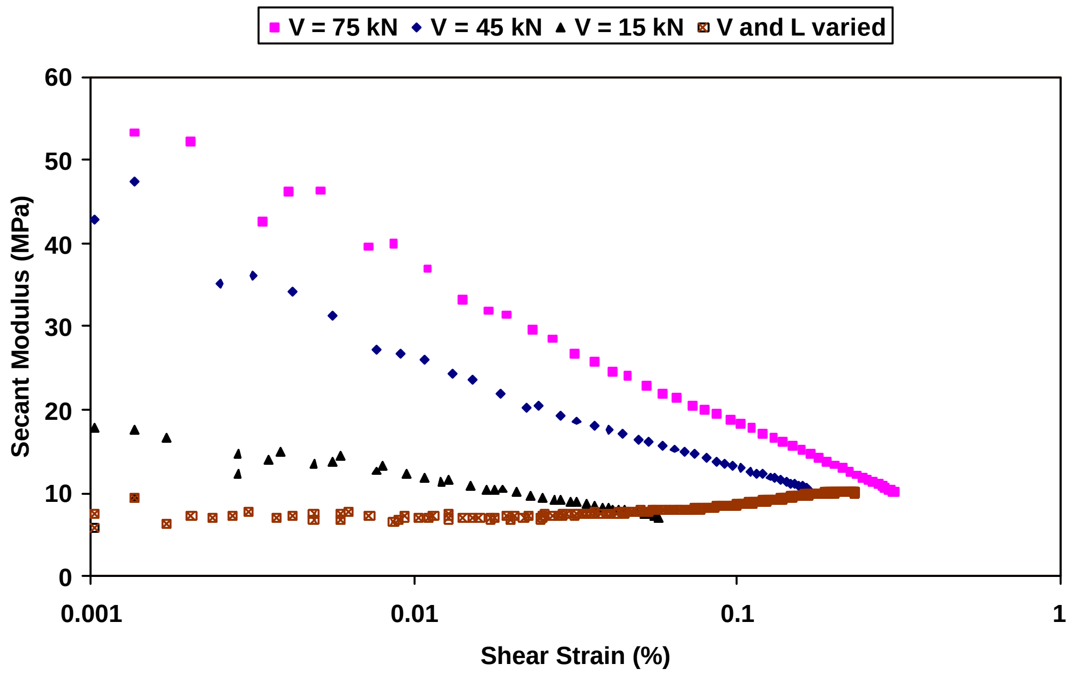

Figure 7-20: Shear strain/secant shear modulus graph

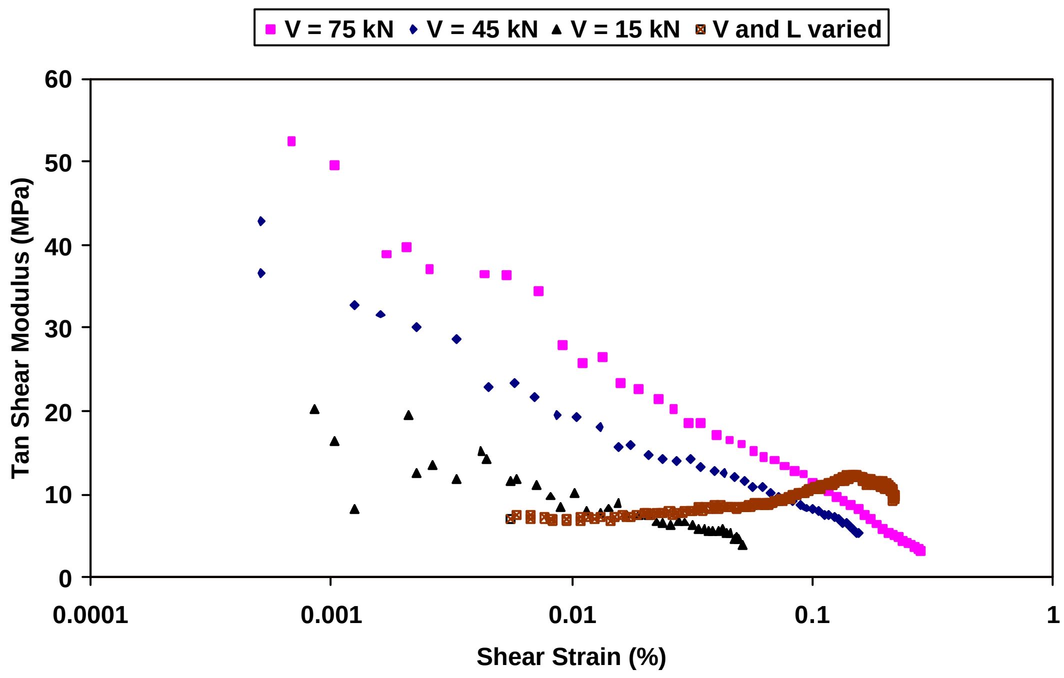

Figure 7-21: Shear strain against estimate of tangent shear modulus

At very low strains approaching 0.001% (0.003×100/300) the LVDTs do not provide accurate data. This is evident in Figure 7-20 and Figure 7-21 where the initial values of G_{sec} at very low strains move both up and down with increasing shear strain before settling into a trend of more or less linear change in G_{sec} with logarithm of increasing shear strain. The value of G_0 in both graphs follows expected behaviour in that it is higher for tests where the initial vertical loading is greater (i.e. proportional to a power of ***p'***). For the test where the vertical and lateral load were simultaneously cycled (denoted V and L varied in the legend), initially there is little vertical stress present, G_0 is low and G_{sec} and G_{tan} alter little during the loading phase, consistent with the linear load/deflection observed previously (Figure 7-17).

These graphs fit well with the known shear behaviour of granular materials shown in Figure 7-10. It appears that the tests place the behaviour in the very low and low shear strain categories (below 1%). However, the very low shear strain behaviour is on the limit of the accuracy of the LVDTs used (a 0.001% shear strain corresponds to 0.003 mm of movement) and therefore the values of G_0 implied by the graphs can only be considered approximate.

Recalling Equation 7-3 which relates the value of G_0 to the mean effective stress, ***p'***, if it is assumed that ***p'*** is proportional to $\sigma_{v'}$ Equation 7-3 may be rewritten:

$$G_0 = A_0 \sigma_v'^{n_o}$$ **Equation 7-7**

and the values of G_0 obtained in the current research using the G_{sec} method fit reasonably well using an equation:

$$G_0 = 290 \sigma_v'^{0.76}$$ **Equation 7-8**

Where the constants have been evaluated using regression analysis and the R^2 value is 0.992 indicating a strong fit to the data. Note that although there are only three data points from the laboratory experiments an additional point of (0, 0) is implied by equation 7-7.

Using the same regression analysis method G_{tan} can be fit using a relation:

$$G_0 = 220 \sigma_v'^{0.68}$$ **Equation 7-9**

and an R^2 value of 0.993 again indicates a close fit top the data.

The values of G_0 for both G_{sec} and G_{tan} are similar and may be summarised as shown in Table 7-8 where the value of G_0 has been calculated as the mean for all the measurements up to 0.005% strain from the data for G_{sec} (corresponding to 0.015 mm) and as a mean up to 0.0025% strain for the data corresponding to G_{tan}.. The estimates of G_0 thus obtained differ slightly because of the calculation methods (which are both likely to underestimate G_0 at low strains) and the inaccuracy of the LVDTs at low strains. Using Equation 7-8 the values of G_0 obtained are also shown in Table 7-8. The powers of 0.57 and 0.76 compare with the power of 0.5 proposed by Wroth and Houslby (1985) for angular particles. Equation 7-8 and Equation 7-9 imply that for Test 1 shown in Table 7-5 where the vertical and lateral load were cycled simultanesoulsy and vertical load began at 10 kN, an initial shear modulus of 11 MPa and 12 MPa would be expected using each equation respectively. The first measurements of G_{tan} and G_{sec} shown on figure 7-20 and 7-21 imply a G_0 of just below 10 MPa. However, the lateral and vertical load has already increased by the time any estimates of G_0 can be made using the methods described.

Test	Vertical stress, s_v', (N/mm^2) (sleeper footprint taken as 2500 mm ´ 300 mm)	G_0 by secant modulus (MPa)	G_0 by tangent modulus (MPa)	G_0 by $290 s_v'^{0.76}$	G_0 by $220 s_v'^{0.68}$
V = 75 kN	0.1	48	45	50	46
V = 45 kN	0.06	36	35	34	32
V = 15 kN	0.02	15	15	15	15

Table 7-8: Comparison of estimates of G_0 by secant method, tangent method and fitted formula

Now that G_0 has been estimated it is also acknowledged that the previous value of Young's modulus used in the finite element model of the experiment shown in Table 6-2 (300 MPa), although justified from the literature, is probably an overestimate of the value. For example given a Poisson's ratio of 0.3 the Young's modulus for an elastic medium with a shear modulus of 50 MPa would correspond to 130 MPa [$E=2G(1+n)$]. However, this would have negligible impact on the assessment of vertical stress previously carried out.

From the graphs produced so far, it is clear that the measured sleeper deflection is highly load path dependent, higher constant vertical loads give rise to greater values of G_0 which then reduce at different rates with deflection. Increasing vertical and lateral load simultanesouly at a similar ratio gives significantly reduced G_0 which then appears to remain similar with deflection.

For the specific case of train loading of sleepers it would be advantageous to capture more precisely the behaviour of G with load path by means of formulae that might then be used in track system models to represent accurately the lateral response of the sleeper/ballast interface.

A graph of the ratio of shear stress to vertical stress (equivalent to lateral load divided by vertical load both at the sleeper ballast base contact area) and measured deflection is shown in Figure 7-22:

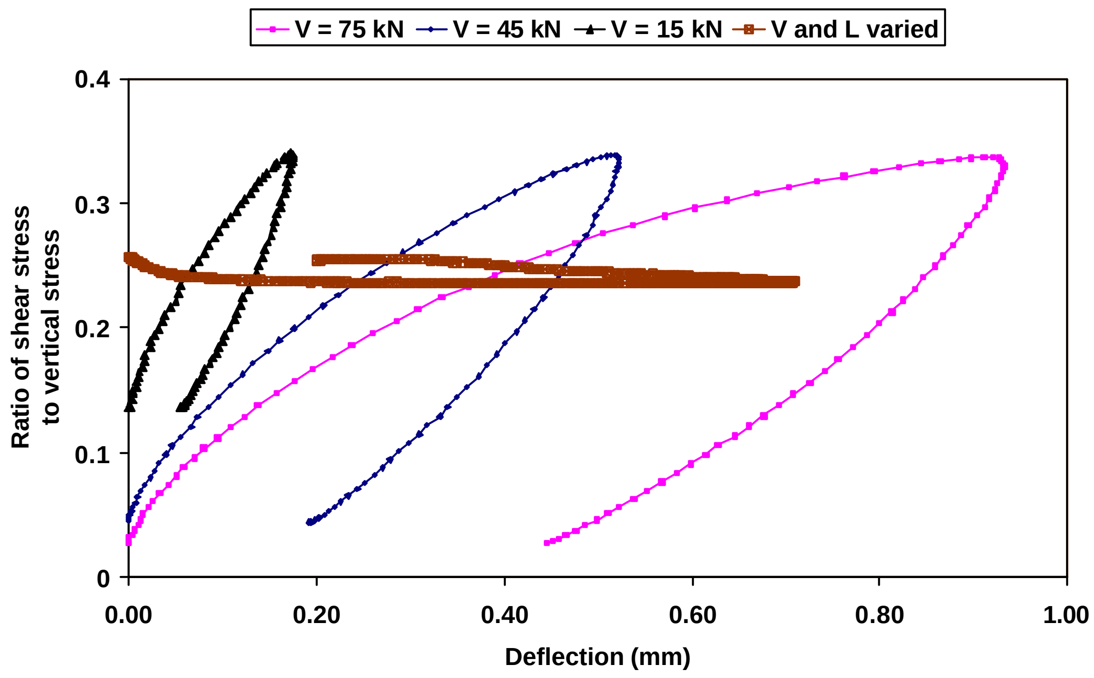

Figure 7-22: Stress ratio/deflection graph, comparison of different tests over initial loading cycle

Figure 7-22 shows that the shape of the load/unload lines of stress ratio/deflection are similar when the vertical load is held constant. However they vary in terms of deflection. The true train loading is more likely to follow a path with a more or less constant stress ratio, similar to that shown in Figure 7-22 for the V and L varied line.

Figure 7-23 shows a graph of the tangent shear modulus against the ratio of shear stress to vertical stress.

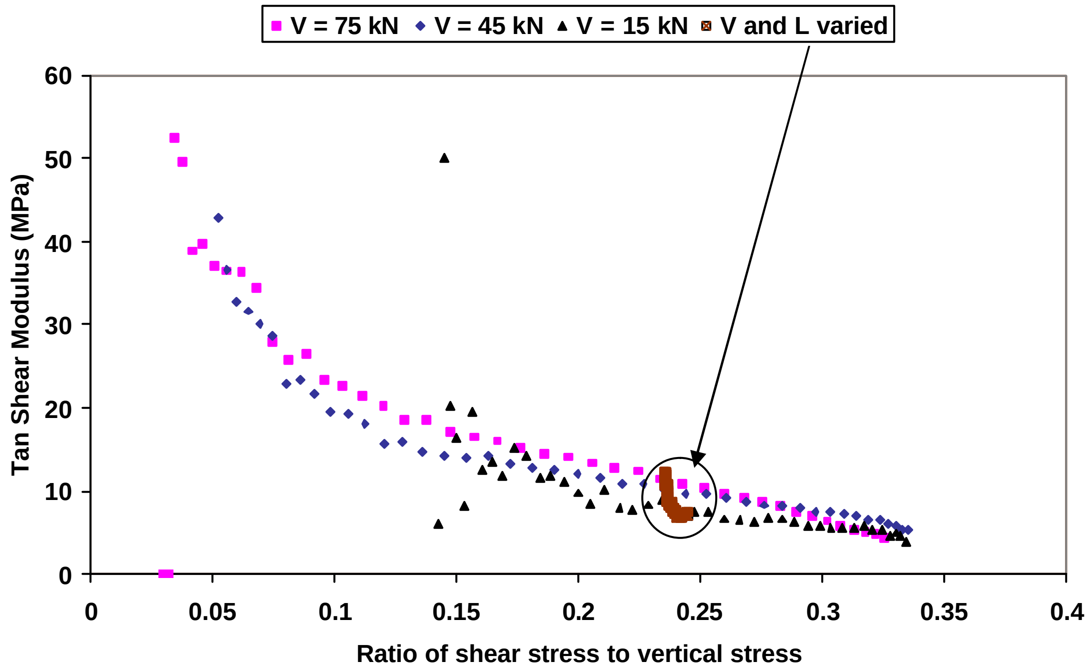

Figure 7-23: Ratio of stresses/estimate of tangent shear modulus during loading step

Figure 7-23 shows that G_{tan} appears to follow a similar path when plotted against stress ratio for the constant vertical load tests. For the test with L and V varied Figure 7-23 shows that there was a slow reduction in G_{tan} over the course of the loading step, although for most of the loading step this remained close to the value crossed over by the other tests at the same loading ratio.

Figure 7-23 may be modified by inverting the ratio of stresses as shown in Figure 7-24.

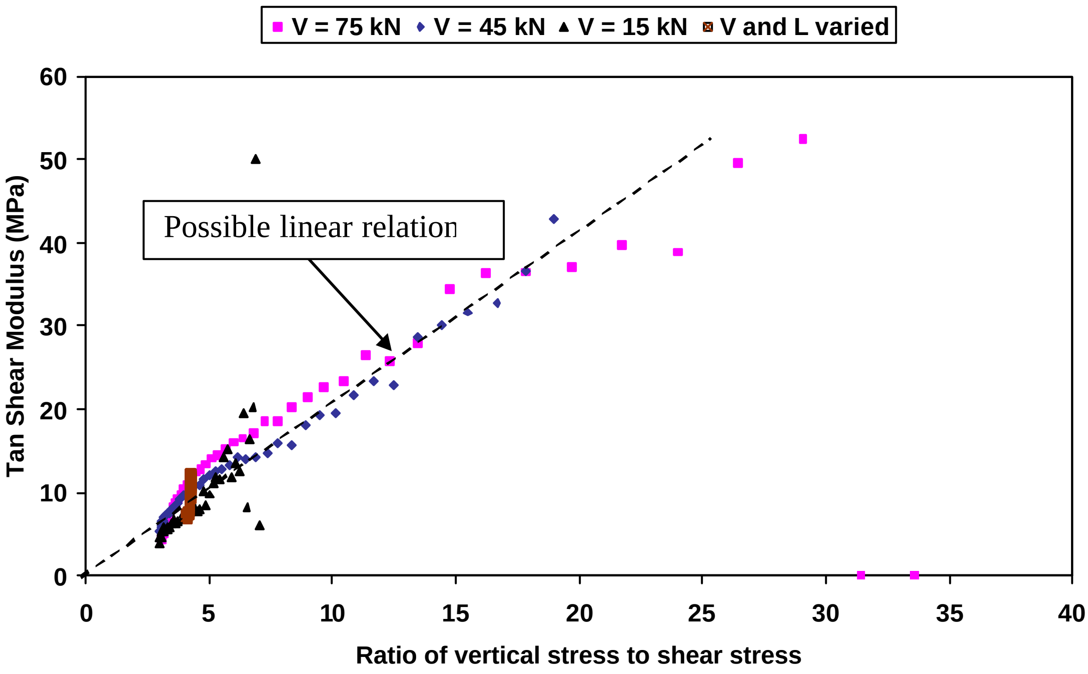

Figure 7-24: Inverted ratio of stresses/estimate of tangent shear modulus during loading step

From inspection of Figure 7-25 it is proposed that:

$$G_{\tan} = A\frac{s_v}{t_{yz}} \qquad \textbf{Equation 7-10}$$

Where $\boldsymbol{A}$ is a constant having units of force per unit area.

Given that:

$$G_{\tan} = \frac{Dd\,t_{yz}}{dd} \qquad \textbf{Equation 7-11}$$

It is possible to relate the deflection d to the way in which the sleeper/ballast interface is loaded:

$$\frac{Dd\,t_{yz}}{dd} = A\frac{s_v}{t_{yz}} \qquad \textbf{Equation 7-12}$$

Rearranging:

$$dd = \frac{Dt_{yz}dt_{yz}}{As_v}$$ **Equation 7-13**

For specific cases where $s_{\boldsymbol{v}}$ is a known function of $t_{\boldsymbol{yz}}$ some useful relationships can be found:

When the vertical stress is constant:

$$d = \frac{Dt_{yz}^{\ 2}}{2As_v}$$ **Equation 7-14**

When the vertical stress is always 3 multiples of the shear stress:

$$d = \frac{Dt_{yz}}{6A}$$ **Equation 7-15**

In the general case Equation 7-13 may be solved by summing small increments of loading:

$$d_1 = \frac{Dt_1(t_1 - t_0)}{As_{v1}}$$ **Equation 7-16**

$$d_2 = \frac{Dt_2(t_2 - t_1)}{As_{v2}} + d_1$$ **Equation 7-17**

$$d_3 = \frac{Dt_3(t_3 - t_2)}{As_{v2}} + d_2$$ **Equation 7-18**

And so on…

Using this method of summing small increments of loading it is possible to make predictions and compare with actual behaviour:

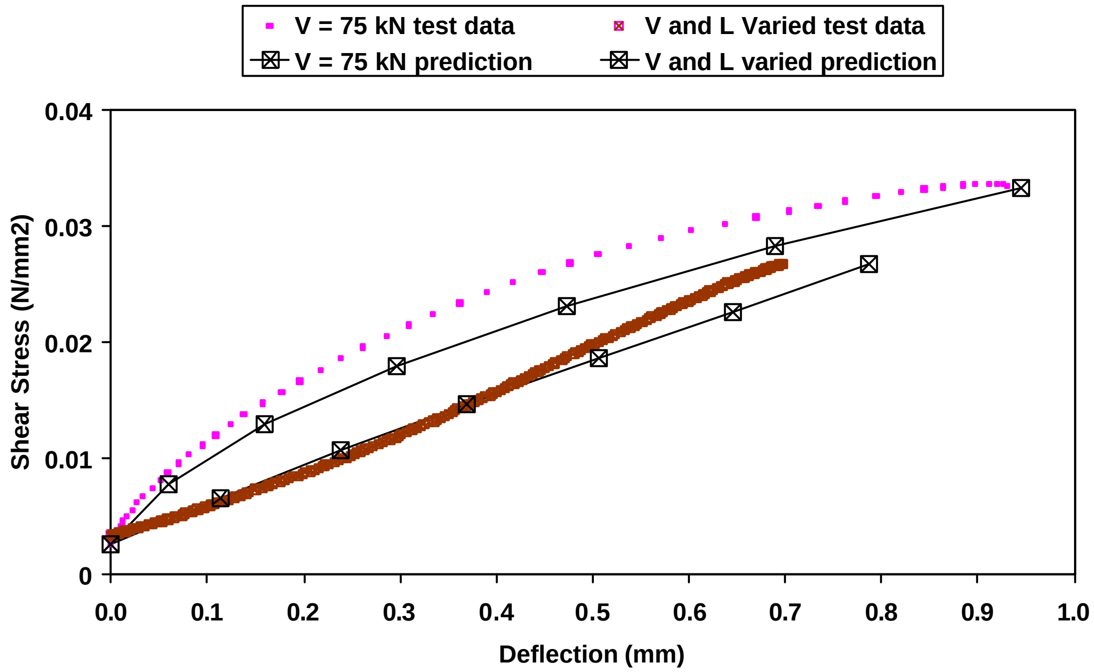

Figure 7-25: Stress ratio/deflection graph, fit of proposed relationship to actual data part 1, thick black lines show the estimates

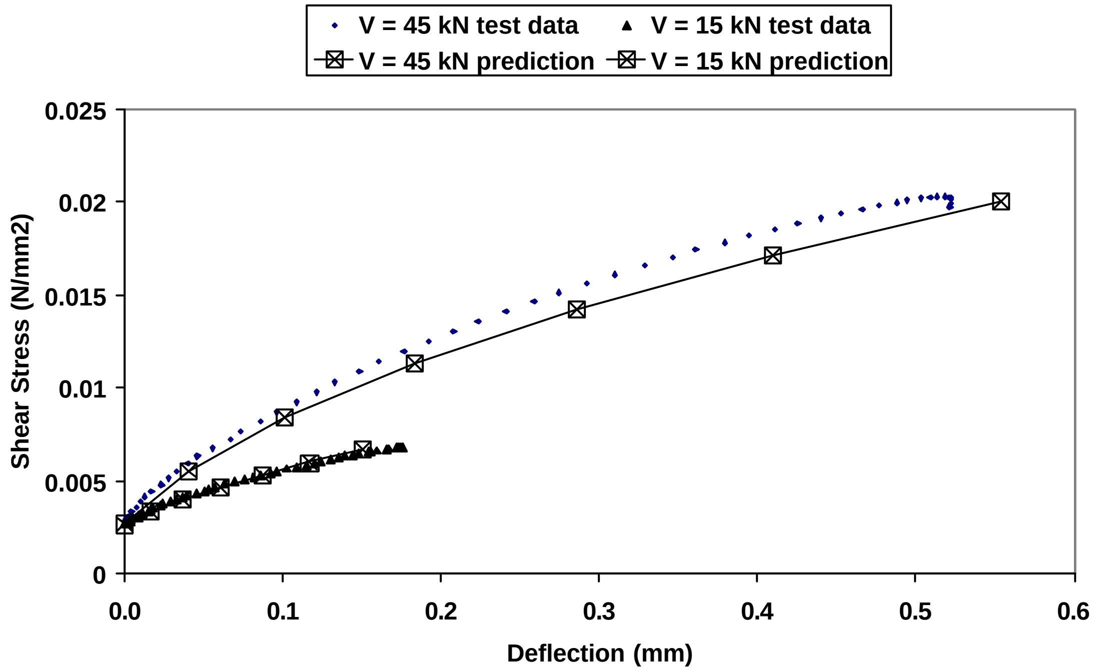

Figure 7-26: Stress ratio/deflection graph, fit of proposed relationship to actual data part 2, thick black lines show the estimates

The constant ***A*** has the value 2 in Figure 7-25 and Figure 7-26. A was determined by a visual trial and improvement method. For dimensional consistency this has units of mm^2 per N.

7.3. Summary of Chapter 7

Geophone measurements have characterised combined vertical high and low end and lateral sleeper movements and confirmed that the lateral behaviour shows the same trends as observed in the vertical behaviour described in Chapter 5. i.e. individual sleepers show consistency of response to comparable loading events but sleepers nearby show varied ranges of deflection.

Compared to the behaviour of actual track (geophone measurements), the laboratory experiments have shown similar ranges of sleeper lateral movement and also identified variation between different set-ups compatible with variations over a number of nearby sleepers shown in the geophone data.

Laboratory experiments have shown that pre-failure lateral behaviour is load path dependent. This is important because it was identified in Chapter 2 that current track vehicle interaction models do not account for load path dependency.

The pre-failure behaviour of the sleeper/ballast interface in the laboratory has been assessed by converting the measurements to shear moduli. The relationship between changes in shear modulus with shear strain has been shown to be comparable to that reported for granular materials in the literature.

A relationship has been proposed that could be used in a train/track interaction model for the increasing lateral load/deflection behaviour of the interface, which would have low requirements for computing power and takes into account load path dependency. Unloading behaviour is more complex but it would be possible to further present an equation of unload behaviour fitted to the laboratory data to model the hysteresis. Further refinements to account for unload/reload behaviour when loading does not return to zero between axles could be achieved by switch functions. It is recognised that in reality the sleeper/ballast lateral behaviour may also be influenced by depth of ballast, and some inherent variability of the sleeper to ballast contact. Also, the relationship proposed is not supported by theoretical modelling; further work to use fundamental soil models to derive load path dependent shear behaviour goes beyond the scope of the current research. However, the current research does demonstrate that there are applications for such research and supports the case for future research into the pre-failure behaviour of granular materials subject to dynamic loading events.

8. Failure of the sleeper/ballast interface, experimental results and geotechnical calculations

In this Chapter, the load at failure of the sleeper/ballast interface is investigated through laboratory experiments and the contributions from each of the three contact areas are assessed. This Chapter addresses the research objectives set out at the end of Chapter 1 which were to:

- Quantify the failure envelope of the sleeper/ballast base contact for a single sleeper in combined VHM loading.
- Quantify the resistance available from the crib and shoulder sleeper/ballast contact areas both experimentally and by calculation.

To assess failure at the sleeper ballast interface it is necessary first to define what is meant by this. Failure at the sleeper/ballast interface can be defined by different criteria:

- Unacceptable lateral deflections of the track during in-service loading may be considered as any that give rise to long term trends of plastic deflection.
- Track may also buckle and in this case sleeper/ballast resistance is important over greater deflection ranges.

The level of deflection which would give rise to long term trends of plastic deflection is likely to depend on a number of variables including sleeper, rail and ballast type. Esveld (2001) reported research by Netherlands railways where actual track had been displaced laterally by a tamping machine up to 5 mm in the presence of the self weight of the tamping machine. These tests identified a point beyond which displacement became non-recoverable. Although Esveld did not identify a value for this he goes on to use a value of 2 mm in a numerical simulation. In Chapter 7 it was identified that the lateral response is load path dependent. In the simpler cases, where the vertical load was constant during lateral cyclic loading tests, the range of movement with a lateral load up to 1/3 of the vertical load increased with increased vertical load. When the lateral load was cycled in an approximate 1/4 proportion to the vertical load, greater deflection ranges were observed for the same peak vertical load. The laboratory experiments were not able to identify non recoverable ranges of movement because they differed from real track in that there were no continuous rails to help return the sleeper to its original position.

In this Chapter, failure at the sleeper/ballast interface will be considered to have occurred for sleeper movements of more than 2 mm relative to the initial position of the sleeper with the 2 kN lateral seating load and appropriate vertical load present. 2 mm is chosen because it is beyond the range of movements measured by the geophones on the WCML and is beyond the range of pre-failure movements measured in the laboratory under the loading regimes investigated as defined in Chapter 4 and 7. In reality 1 mm of movement might be taken to indicate failure. However, for assessing the resistance at failure it is more important to be certain that failure has occurred than to precisely identify the deflection at which failure occurs because resistance is not expected to alter significantly within a few mm from the actual point at which failure occurs.

The primary cause of rail buckling is a rail temperature above the installation temperature causing longitudinal compression forces. Track misalignment and lifting forces prior to and after train axle loading can also influence the occurrence of buckles (ERRI committee D202 report 3, 1995). When assessing the buckling behaviour of track, knowledge of lateral resistance at the sleeper/ballast interface over a range of movement encompassing likely actual movements is desirable. An appropriate range of movement is considered to be about 100 mm.

Therefore it would be of interest to learn the lateral resistance of the sleeper ballast interface in the range of movement 2 to 100 mm.

In this Chapter the resistance of the sleeper/ballast interface is assessed over a deflection range of up to 90 mm. This is because in some tests the initial positioning of the sleeper and the fact that the ram had a travel of only 150 mm meant that deflection up to 100 mm was not always possible.

The Chapter is divided into 3 main sections:

1. Base contact: experimental results are presented and failure is assessed for combined VHM loading
2. Shoulder

3. Crib

In sections 2 and 3 on the Shoulder and Crib the increase in measured resistance compared with the mean resistance for base contact only tests is presented, and geotechnical calculations are developed, these are then compared to each other and results from the literature.

At the end of the Chapter a summary draws together relevant findings.

8.1. Base contact, VHM failure

8.1.1. Background

Butterfield and Gottardi (1994) presented an empirically derived equation relating the resistance of a granular medium to foundation loads from combinations of lateral, vertical and moment load. Their results showed that vertical and moment loads could reduce the lateral resistance so that it may be less than the normally assumed case of linearly increasing lateral resistance with vertical load.

In this section laboratory experiments of the resistance with deflection for a single sleeper on ballast with no shoulder or crib ballast are presented.

Using parameters defined from these tests the formulae proposed by Butterfield and Gottardi are applied to the case of a railway sleeper on ballast. The calculated failure envelopes are then compared with the experimental results.

8.1.2. Methods

Following the experimental methods described in Chapter 4, all tests set-ups were ultimately subjected to a constant vertical load while the lateral load was applied to pull the sleeper across the ballast at a specified rate of movement.

The vertical load was applied at either zero or 0.5 m eccentricity to produce a moment and the sleeper was pulled at a rate of 0.25 mm/s or 0.5 mm/s. During the test, data were logged at 10 Hz so that a data reading was taken at least every 0.05 mm of deflection at the railhead where the load was applied.

It is known that traffic increases the lateral stability of the track and leads to the peak resistance being reached after only a small deflection (ERRI committee D202 report 3, 1995); this state may take many cumulative tonnes of traffic to develop. Exactly how many tonnes of traffic is not clear but evidence from data reported by Esveld (2001) points to it being in the hundreds of thousands. In the tests carried out for this research the intention was to evaluate the resistance for an initial condition of freshly laid/tamped track ballast; therefore there was a concern that cyclic lateral testing would alter load/displacement behaviour making comparison between test set-ups impossible because different test set-ups had had different numbers of lateral cyclic loads applied. However, as will be seen in the results reported, there is no evidence that the relatively few numbers of applied cyclic lateral loads have had any discernable effect over the range of cycles used across all the test set-ups. In the most extreme case a test set-up had had 160 lateral load cycles applied whereas other tests, had had only 10 static lateral cycles applied.

8.1.3. Results

Results for six tests are reported covering a range of VHM loading combinations. Tests 1A, 2A and 3A were for a centrally placed and maintained vertical load and tests 1B, 2B and 3B were for a vertical load applied at an offset of 0.5 m from the centreline of the sleeper toward the direction from which the lateral actuator applied its pull. The rail heads are 1.5 m apart so that the vertical load in test run B was applied at 2/3 of the maximum possible offset. Also, because the lateral load was applied onto the railhead there is an additional moment load in all the tests due to the height of the railhead above the sleeper/ballast interface. This was measured to be at a vertical eccentricity of 0.33 m relative to the sleeper base incorporating the sleeper, the BS113A rail, and the pad. Note that the rail was inclined at 1:20 so the loading beam and bracket made contact at most eccentric locations vertically and horizontally normal to the railhead.

Test	Vertical load (kN)	Position of vertical load
1A	75	Central
2A	45	Central
3A	15	Central
1B	45	0.5m offset
2B	15	0.5m offset
3B	30	0.5m offset

Table 8-1: Key to tests reported

Figure 8-1, Figure 8-2 and Figure 8-3 show the lateral load/deflection graphs over different deflection ranges for each of the tests. The text on the right side of each load/deflection line indicates the test I.D and the vertical load. Table 8-2 and Table 8-3 show key values from these load/deflection graphs.

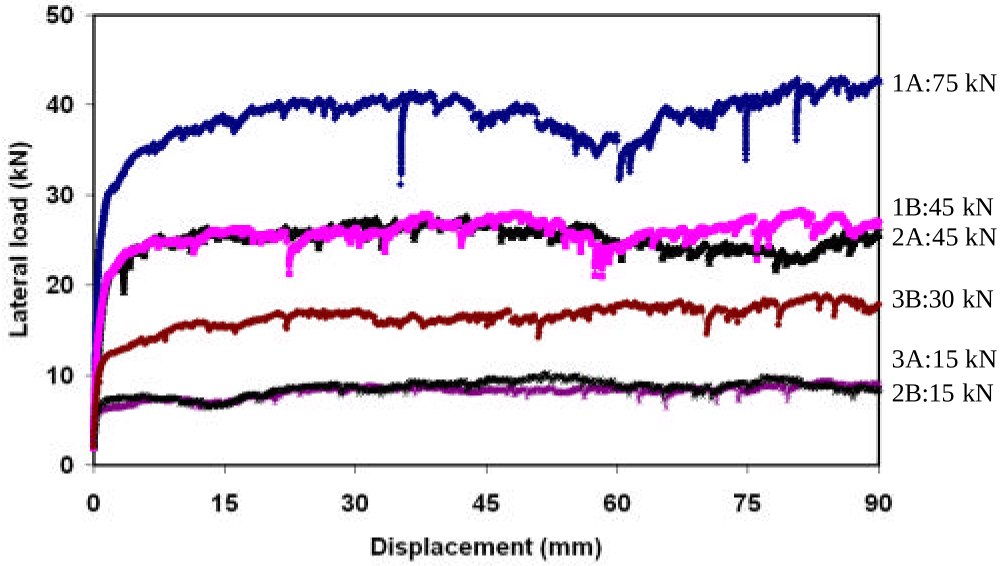

Figure 8-1: Lateral load/displacement graph up to 90 mm

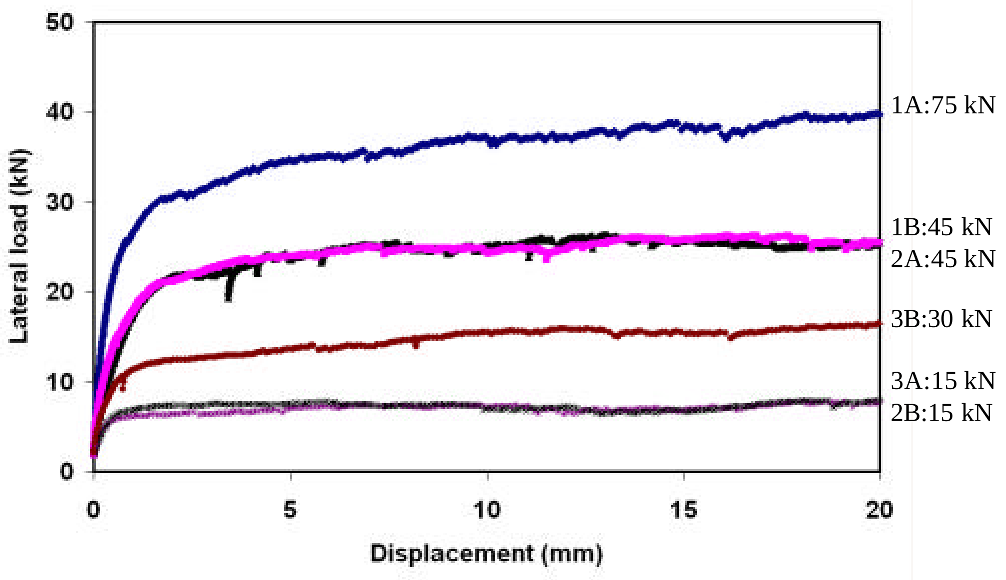

Figure 8-2: Lateral load/ displacement graph up to 20 mm

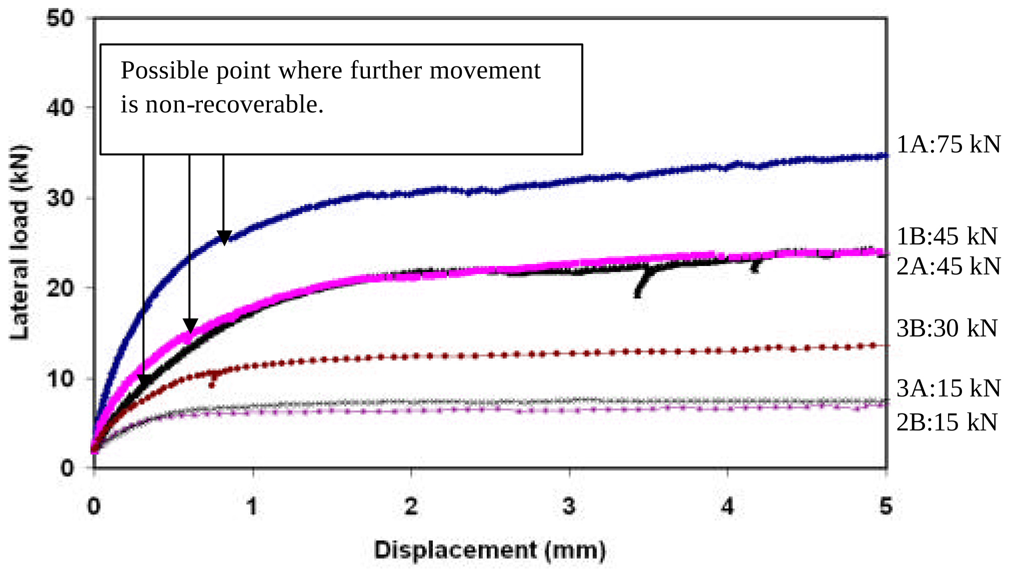

Figure 8-3: Load/ displacement graph up to 5 mm

Test	Vertical load (kN)	Lateral load (kN) on sleeper at:							
		0.5 mm	1 mm	2 mm	3 mm	5 mm	mean 2 to 20	mean 20 to 90mm	peak 2 to 90 mm
1A	75	21.5	26.6	30.4	31.9	34.7	36.5	39.4	43.0
2A	45	12.0	17.5	21.7	21.9	23.7	24.7	25.4	27.6
3A	15	5.7	6.2	6.4	6.5	7.0	7.1	7.2	7.8
1B	45	13.8	17.8	21.2	22.6	23.9	25.5	26.1	28.2
2B	15	6.1	6.8	7.3	7.5	7.5	7.1	8.9	10.2
3B	30	9.2	11.2	12.4	12.7	13.6	15.6	17.0	18.8

Table 8-2: Load at key displacements

Test	Vertical load (kN)	Ratio (lateral load/vertical load) at:							
		0.5 mm	1 mm	2 mm	3 mm	5 mm	mean 2 to 20	mean 20 to 90 mm	peak 2 to 90 mm
1A	75	0.29	0.35	0.41	0.43	0.46	0.49	0.53	0.57
2A	45	0.27	0.39	0.48	0.49	0.53	0.55	0.56	0.61
3A	15	0.38	0.41	0.43	0.43	0.47	0.47	0.48	0.52
2B	15	0.31	0.40	0.47	0.50	0.53	0.57	0.58	0.63
3B	30	0.41	0.46	0.49	0.50	0.50	0.48	0.59	0.68
1B	45	0.31	0.37	0.41	0.42	0.45	0.52	0.57	0.63
mean		0.33	0.40	0.45	0.46	0.49	0.51	0.55	0.61
median		0.31	0.39	0.45	0.46	0.48	0.50	0.57	0.62
max		0.41	0.46	0.49	0.50	0.53	0.57	0.59	0.68
min		0.27	0.35	0.41	0.42	0.45	0.47	0.48	0.52

Table 8-3: Ratio at key displacements

In Figure 8-1 it is possible to identify some variability in each load/displacement line. Occasionally large reductions in the load occur, followed by rapid return towards the previous value of load. These are thought to be due to ballast breakage or rearrangement events; that is, particles of ballast fracturing or crushing, rolling or sliding. During tests noises likely to be associated with such breakage/movement events accompanied the large reductions in load.

Figure 8-2 and Figure 8-3 show that initially, over a small range of deflection, the load/displacement graphs do not exhibit any behaviour that might be associated with breakage/rearrangement of particles. The load/displacement lines initially show a rapid rate of increase in load with displacement with this rate reducing with further increasing load/displacement as the load appears to tend towards a limiting value with increasing deflection. Tests with higher vertical load have greater movements before breakage/rearrangement events are evident in the load/displacement graphs. The first evidence of breakage/rearrangement events could be considered to be where failure occurs, i.e. a displacement beyond which all further displacement is non-recoverable and these locations have been tentatively marked for some of the load displacement lines in Figure 8-3. These points are below the 2 mm limit previously ascribed to the pre-failure zone.

Figure 8-4 and Figure 8-5 show the loading ratio (L/V) plotted against displacement for different displacement ranges for all 6 tests. Individual tests are not identified due to the difficulty in distinguishing the data points. However, some clear trends can be seen.

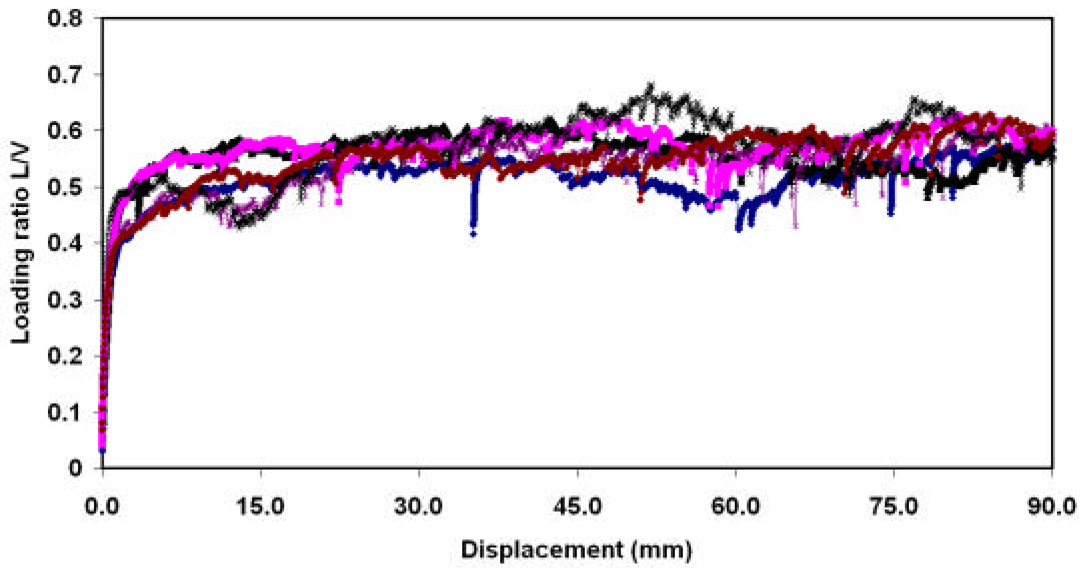

Figure 8-4: Loading ratio/displacement graph up to 90mm, all six tests

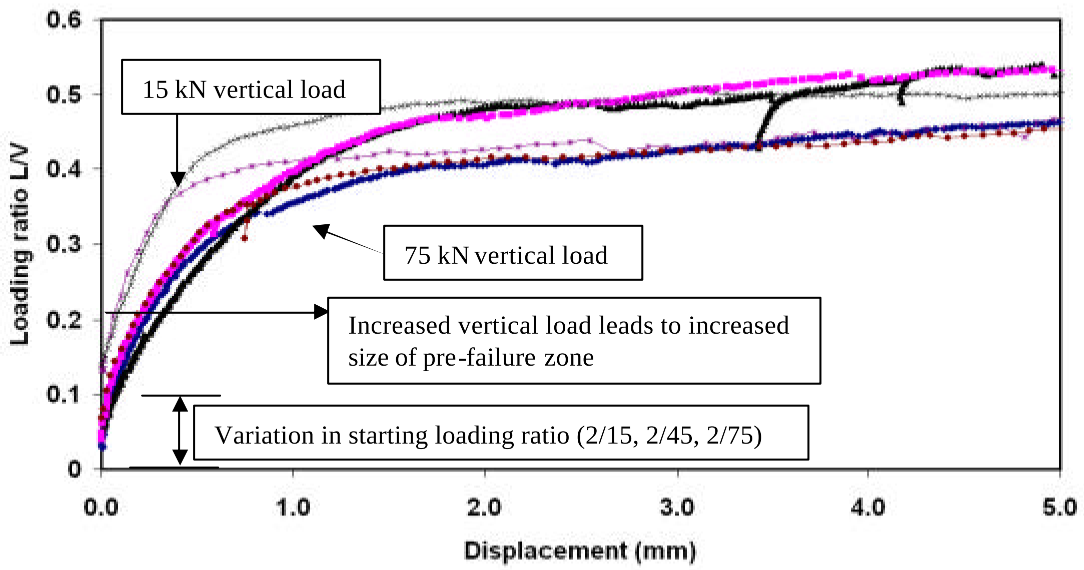

Figure 8-5: Loading ratio/displacement graph up to 5mm, all six tests

In Figure 8-4 it can be seen that all 6 tests move towards a limiting (failure) loading ratio regardless of the magnitude of the constant vertical load and its eccentricity.

In Figure 8-5 the initial loading ratio at zero displacement varies between different tests. This is because while the lateral load is always initially 2 kN the vertical load is varied between tests and the displacements measured from a zero datum at the initial applied load. However, even allowing for this small difference it is still the case that tests with larger vertical loads have larger pre-failure displacements with increasing loading ratio. Figure 8-6 illustrates this behaviour.

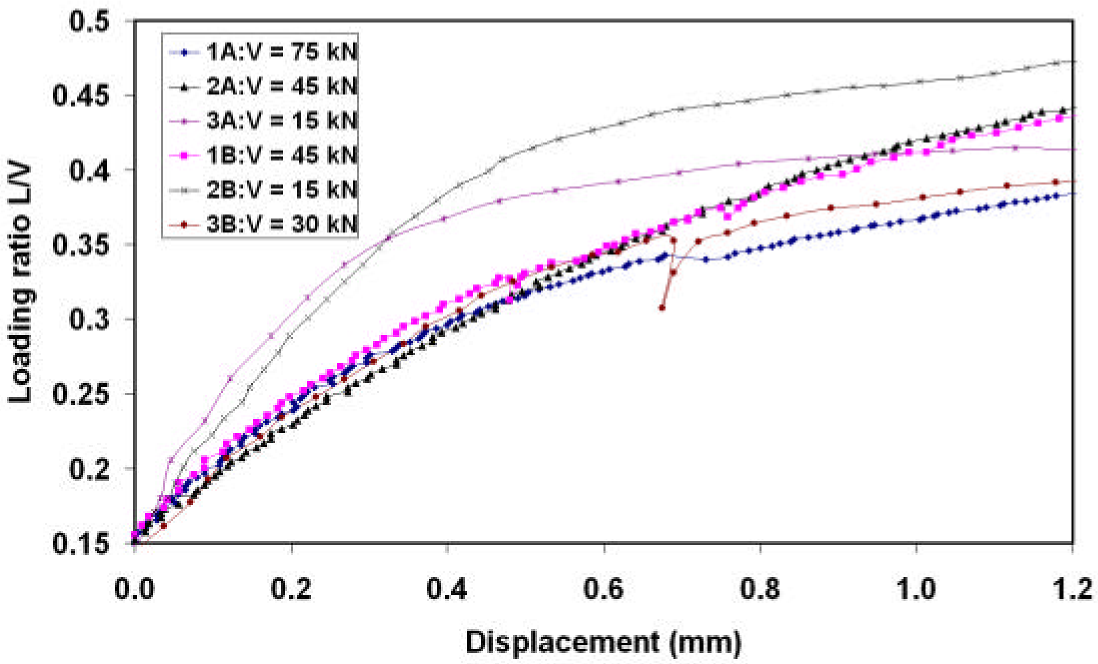

Figure 8-6: Loading ratio/displacement graph up to 1.2 mm, all six tests, loading ratio has been migrated to 0.15 for zero displacement in all tests to permit easier comparison of the loading ratio/displacement behaviour at low displacements

In Figure 8-6 all the tests have been migrated to a common zero displacement at a loading ratio of 0.15. In Figure 8-6 the two tests carried out at 15 kN vertical load deflect less at lower loading ratios and reach higher loading ratios sooner than the tests carried out at 45 kN and 75 kN of vertical load.

These tests appear to indicate that the lateral load at failure is insensitive to the eccentricity of the vertical applied load, i.e. that the moment component of loading has a negligible effect on the ultimate lateral failure load within the range of load cases investigated.

To further characterise the likely behaviour of the sleeper/ballast interface, an average, a minimum and a maximum load/displacement line may be produced from all the tests. In Figure 8-7 the data are sampled every 0.05 mm from each test and the mean, maximum and minimum loading ratio from all tests are plotted.

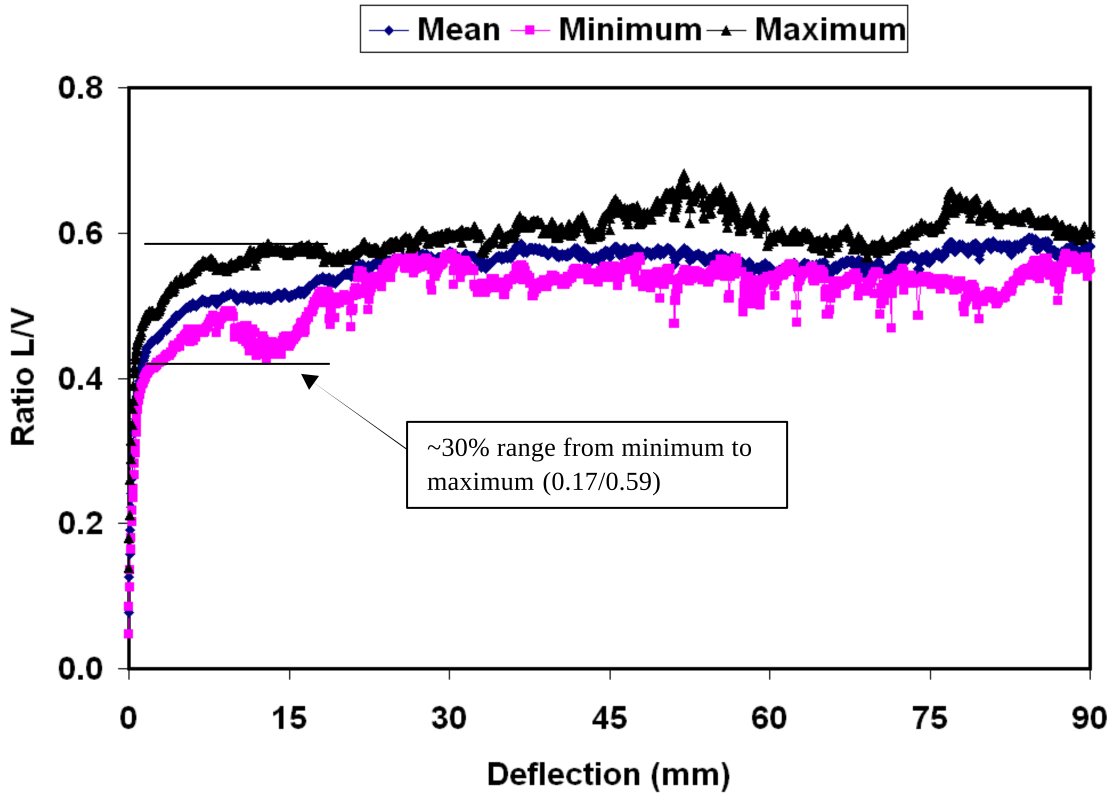

Figure 8-7: Loading ratio displacement graph, mean, maximum and minimum up to 90mm

Figure 8-7 demonstrates that, although all tests appear to converge towards the same limiting value after 2 mm of displacement there is significant variation at specific displacements. The range from maximum to minimum can vary by as much as approximately 30% in the extreme case from these tests.

8.1.4. Interpretation of test data and comparison with calculations

Based on these tests and the cyclic loading tests reported in Chapter 6, the sleeper/ballast base contact has a pre-failure behaviour zone that increases with increasing constant vertical load. In all tests the range of this zone in terms of deflection does not extend beyond 2 mm.

At 2 mm of deflection the median ratio of vertical to lateral load is about 0.45 or 24° (Table 8-3).

The ratio of vertical to lateral load then tends to a limiting ratio at larger deflections of about 0.57 (median value at 20 to 90 mm mean, all tests Table 8-3).

Sudden falls in the load/deflection graphs appear to be due to breakage/rearrangement events with the overall trend quickly reasserting itself.

The ultimate failure load can be calculated using the equations proposed by Butterfield and Gottardi (1994) giving the failure of a shallow foundation under combined vertical (V), horizontal (H) and moment (M) loading. The main equations are summarised below and all the symbols used were described at the beginning of this report:

$$\left[\frac{H/V_{\max}}{t_h}\right]^2 + \left[\frac{M/BV_{\max}}{t_m}\right]^2 - \left[\frac{2C\dfrac{M}{BV_{\max}}\dfrac{H}{V_{\max}}}{t_h t_m}\right] = \left[\frac{V}{V_{\max}}\left(1-\frac{V}{V_{\max}}\right)\right]^2 \qquad \textbf{Equation 8-1}$$

$$V_{\max} = s'_f\,BL = N_g s_g\,(0.5gB - \Delta u)BL \qquad \textbf{Equation 8-2}$$

$$\frac{H}{t_h} = \frac{V(V_{\max} - V)}{V_{\max}} \qquad \textbf{Equation 8-3}$$

$$\frac{M/B}{t_m} = \frac{V(V_{\max} - V)}{V_{\max}} \qquad \textbf{Equation 8-4}$$

Where:

$$N_q = K_p e^{p \tan f} \qquad \textbf{Equation 8-5}$$

$$K_p = \left(\frac{1+\sin f'}{1-\sin f'}\right) \qquad \textbf{Equation 8-6}$$

$$t_h = \tan d \qquad \textbf{Equation 8-7}$$

$$N_g = (N_q - 1)\tan(1.4f') \text{ (Meyerhof, 1963)} \qquad \textbf{Equation 8-8}$$

$$S_g = 1 + 0.1K_p(B/L) \text{ (Meyerhof, 1963)} \qquad \textbf{Equation 8-9}$$

For a fuller explanation the reader is referred to Powrie, (2004).

By estimating the relevant material parameters, it is possible to plot the failure envelope for a G44 sleeper on Network Rail specification railway ballast. The main difficulty in using these equations is in deciding on a value for $\boldsymbol{t_m}$, which corresponds to the initial tangent to the failure surface on the graph of ***V*** against ***M/B*** (Figure 8-9). The difficulty arises because t_m can only be found experimentally and the tests so far carried out indicate that not enough moment loading has been applied to cause a moment loading failure and hence to determine the value of t_m. Therefore it has only been possible to indicate a minimum value for t_m, by ensuring that all test results reported here fall along the edge or within the failure envelope. This may represent a significant underestimate of t_m.

The calculations to plot the failure envelopes are not fully set out here but the parameter values used are summarised in Table 8-4 and the failure envelopes, which do not incorporate any factors of safety, are illustrated in Figure 8-8 and Figure 8-9. Table 8-5 shows the values of combined vertical, horizontal and moment loading present in the laboratory tests, these are also plotted onto Figure 8-8 and Figure 8-9. Note that the horizontal load also contributes to moment loading at the base of the sleeper due to the vertical offset of the load application point (see Figure 4-8).

Symbol	Value adopted	Units	Description
B	2.5	m	Sleeper length
L	0.285	m	Sleeper width
g	16	kN/m3	Bulk unit weight of ballast
u	0	-	Pore water pressure
f	0.785	radians	Friction angle of ballast (45°)
k_p	5.828	-	Passive pressure coefficient
N_q	134.87	-	Bearing capacity factor
N_g	262.74	-	Analogous to the bearing capacity factor found from Meyerhof formula
s_g	6.112	-	Shape factor taken as the value for s_q from Meyerhof formula
d	0.431	radians	Measured angle between soil and structure here taken as the 2 mm median ($\tan^{-1}0.45$ or 24°)
t_h	0.45	-	Tangent to failure surface on graph of V against H when V=O
t_m	0.259	-	Tangent to failure surface on graph of V against M/B when V=0 Taken as a lower bound from these tests
V_{max}	9154	kN	Maximum bearing capacity

Table 8-4: Values used in Butterfield's equations

Test	Vertical load (V)	Horizontal eccentricity	Horizontal load (H)	Vertical eccentricity	Moment (M)	M/B
	kN	(m)	(kN)	(m)	(kNm)	(kN)
1A	75	0	30.41	0.33	10.03513	4.014051
2A	45	0	21.66	0.33	7.149393	2.859757
3A	15	0	6.39	0.33	2.10903	0.843612
1B	45	0.5	21.18	0.33	29.49005	11.79602
2B	15	0.5	7.33	0.33	9.917367	3.966947
3B	30	0.5	12.37	0.33	19.08124	7.632496

Table 8-5: VHM combinations at failure for the laboratory tests, the horizontal loads shown are the actual loads from the test at 2 mm of deflection

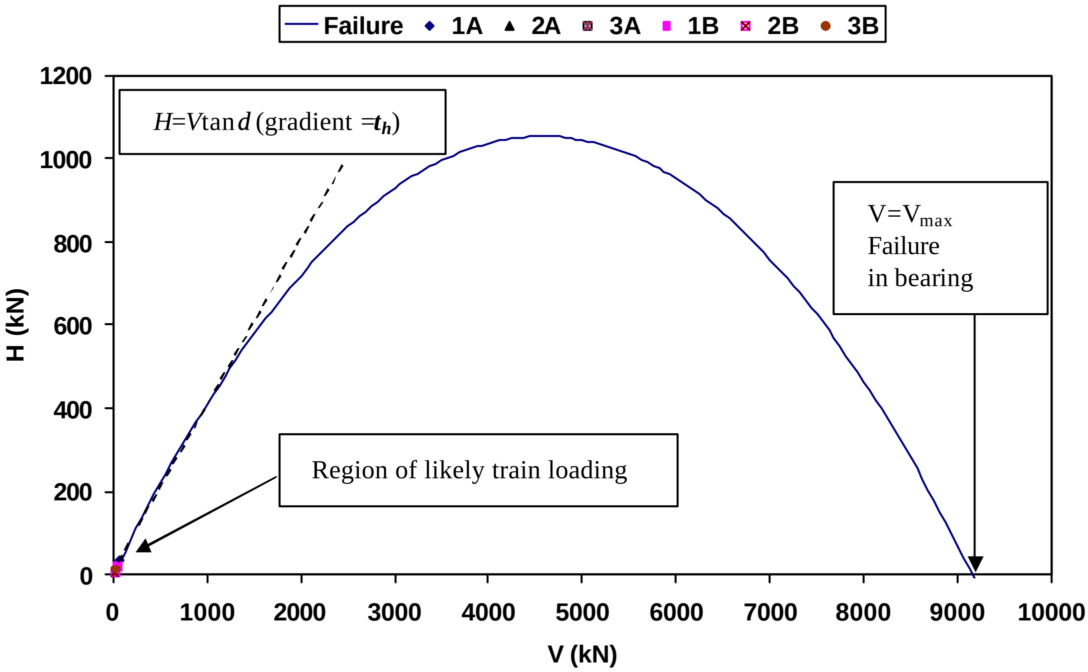

Figure 8-8: Vertical, horizontal loading failure envelope

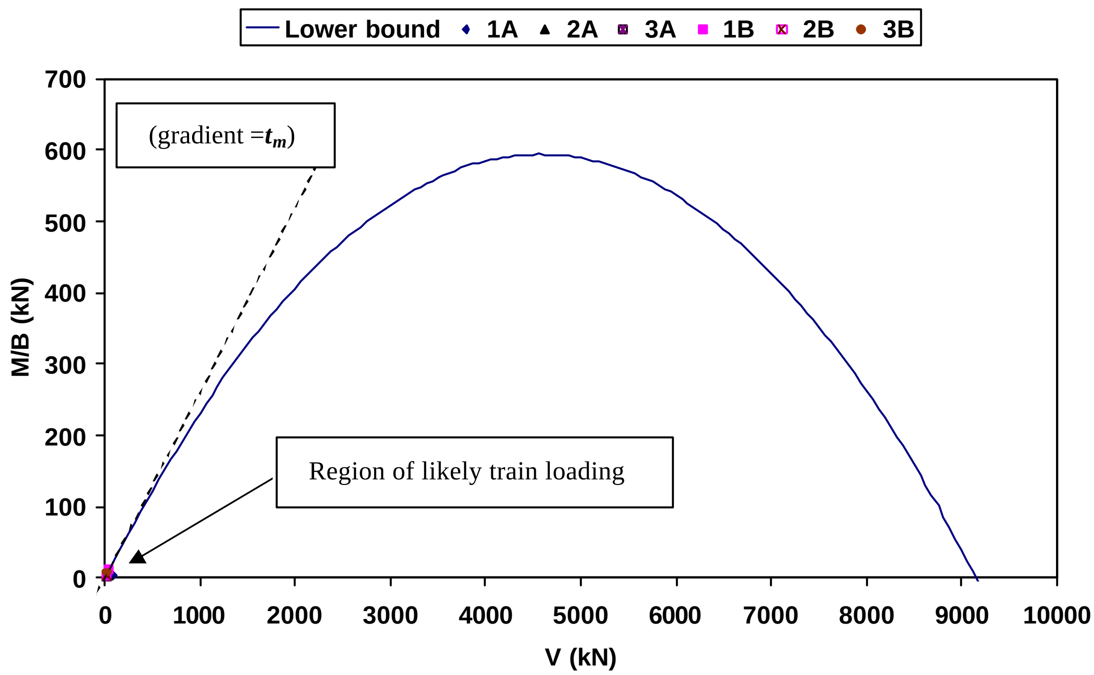

Figure 8-9: Vertical, moment loading failure envelope

The value of $\boldsymbol{V_{max}}$ is highly sensitive to the the internal angle of friction of the ballast, for example at 40° $\boldsymbol{V_{max}}$ reduces to 2688 kN from 9154 kN at 45°. However, even for a lower internal angle of friction of 40°, the following observations are valid.

Figure 8-8 confirms that the vertical to lateral loading ratio for sliding failure remains more or less constant for any likely magnitude of train-applied vertical load. In Figure 8-9 it can be seen that even with the lower bound estimate for $\boldsymbol{t_m}$ from these tests, the failure envelope remains close to linear in the likely region of train loading.

The lower bound estimate $\boldsymbol{t_m}$ from these tests may also be compared to a range of possible values: A minimum value for $\boldsymbol{t_m}$ may be estimated by assuming that there is no effect from moment loading when the eccentricity of a vertical load $\boldsymbol{V}$ on a strip foundation of width $\boldsymbol{B}$ from the centre is less than $\boldsymbol{B}/6$. This corresponds to the well known middle third rule where, provided a vertical load remains within the middle third, pressure is distributed across the full width $\boldsymbol{B}$ with no contact lost. It then follows that by replacing $\boldsymbol{M}$ with $\boldsymbol{VB}/6$ in Equation 8-4, at low values of $\boldsymbol{V}$, the minimum value for $\boldsymbol{t_m}$ is 0.167. A maximum value for $\boldsymbol{t_m}$ may then be estimated by assuming that the maximum eccentricity of a vertical load is $\boldsymbol{B}/2$. Similarly $\boldsymbol{M}$ may be replaced with $\boldsymbol{VB}/2$ in Equation 8-4, hence, at low values of $\boldsymbol{V}$, the maximum value of $\boldsymbol{t_m}$ is 0.5.

The lower bound value determined in these tests of 0.259 then places the true value of t_m in the range 0.259 to 0.5.

8.2. Shoulder

8.2.1. Background

If a sleeper moves into the shoulder ballast under the action of an applied force (Figure 8-10 & Figure 8-11) there is a resistance to movement. This resistance is difficult to quantify as it is necessary to know properties of the material, the volume of ballast involved in resisting an applied force, the size of any movement required to mobilise the resistance and the mechanism of potential failure

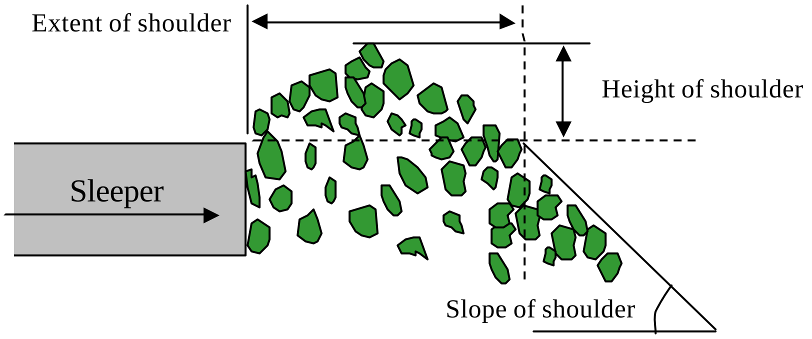

Figure 8-10: Elevation to show shoulder ballast involved in resisting applied lateral load and the terminology used in this report

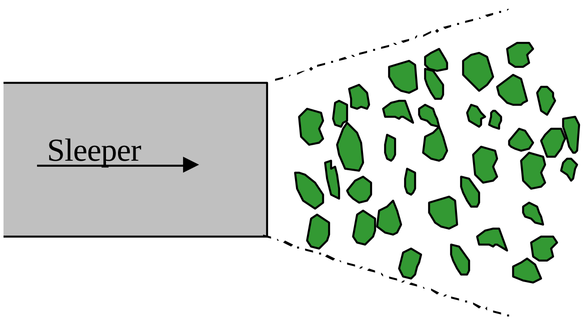

Figure 8-11: Plan to show shoulder ballast involved in resisting lateral load

To evaluate the effect of different sizes of shoulder on lateral resistance, experiments have been carried out in which the size of shoulder is varied. In this section, the results of these tests are presented and then interpreted by comparison with limit equilibrium analyses carried out on the shoulder using widely accepted principles in the field of geotechnical engineering.

8.2.2. Methods

Nine tests were carried out with shoulder ballast present as shown in Table 8-6.

Test set up	Extent of shoulder (mm)	Shoulder height (mm)	Measured slope of shoulder	Vertical load applied (kN)
1C	400	0	41.5°	15
2C	200	0	45.0°	15
3C	200	0	42.8°	45
4C	600	0	42.8°	15
5C	400	125	45.9°	15
6C	400	62.5	40.9°	30
7C	400	0	43.9°	15
8C	300	0	41.4°	15
9C	400	125	37.6°	15

Table 8-6: Key to shoulder ballast tests carried out

The extent of shoulder column in Table 8-6 shows the lateral extent level with the sleeper top and, if present, the height of any heaped ballast above the sleeper top. When ballast was heaped above the sleeper top level the shoulder was profiled so as to have an isosceles triangle shape and the dimension given is for the height at the middle of the isosceles triangle. These definitions are shown in Figure 8-10.

Images of some of the shoulders prior to testing are shown in Figure 8-12. In all cases the ballast was permitted to fall away at its natural angle of repose from the lateral limit of each shoulder. The natural angle of repose of the ballast was measured for each test and found to be within the range 37.6° to 45.9° with a mean of 42.4°. The measured angles were considered to underestimate fractionally the true angle of repose due to the tendency of fallen ballast to roll out at the toe. Once each shoulder had been prepared a vertical load was applied and maintained whilst the sleeper was moved under position control into the shoulder for a distance of at least 80 mm on all tests at 0.5 mm/s. The load and displacement of the sleeper were recorded at 10 Hz giving a resolution to the nearest 0.05 mm, the accuracy limit for the large range LVDT used was 0.015 mm. Most tests were carried out with a vertical load of 15 kN.

A B C

Figure 8-12:(a) Test 5C before (b) Test 2C before (c) Test 7c before

The testing apparatus measures the total applied lateral load. To assess the shoulder resistance, an estimate of the ratio of lateral to vertical load when only base ballast is present was made using the results from test series A and B in which no shoulder (or crib) ballast was present. This was then subtracted from the measured loading ratio for tests in which shoulder ballast was present to eliminate the contribution from base contact. The remaining ratio is multiplied by the vertical load for each test to estimate shoulder contribution.

Due to locally irregular load/deflection response within tests, this can result in highly varied estimates of shoulder resistance over the full displacement range. This variation is thought to be largely caused by the noise level from the base contact resistance and is not a true reflection of variations in shoulder resistance. Using the lowest practical vertical load (15 kN) minimises noise error. Different vertical loads are not expected to influence shoulder resistance.

8.2.3. Results

In most of the tests, as the sleeper displaced into the shoulder, ballast was observed to fall down the natural slope of ballast beyond the lateral extent of the shoulder. Exceptions to this were tests 4C and 9C. In test 4C the lateral extent of 600 mm appeared to have passed a threshold beyond which up to 100 mm of shoulder displacement was accommodated by hunching of the ballast as shown in Figure 8-13. In test 9C the angle of ballast repose was particularly shallow at 37.6 and this rather low value meant the ballast remained stable despite the displacement of the sleeper. This test also gave a comparatively high estimate of shoulder contribution. It may therefore be deduced that there are potential benefits to placing the ballast at less than the angle of repose.

Figure 8-13: Photos of test 4C before and after. Hunching is clearly visible. The length of level beyond the sleeper end is 600mm in both photos

Figure 8-14, Figure 8-15, and Figure 8-16 show the mean increase in resistance plotted against sleeper displacement[9] at every 0.05 mm of displacment tests for the same shoulder size have been averaged (see Table 8-6).

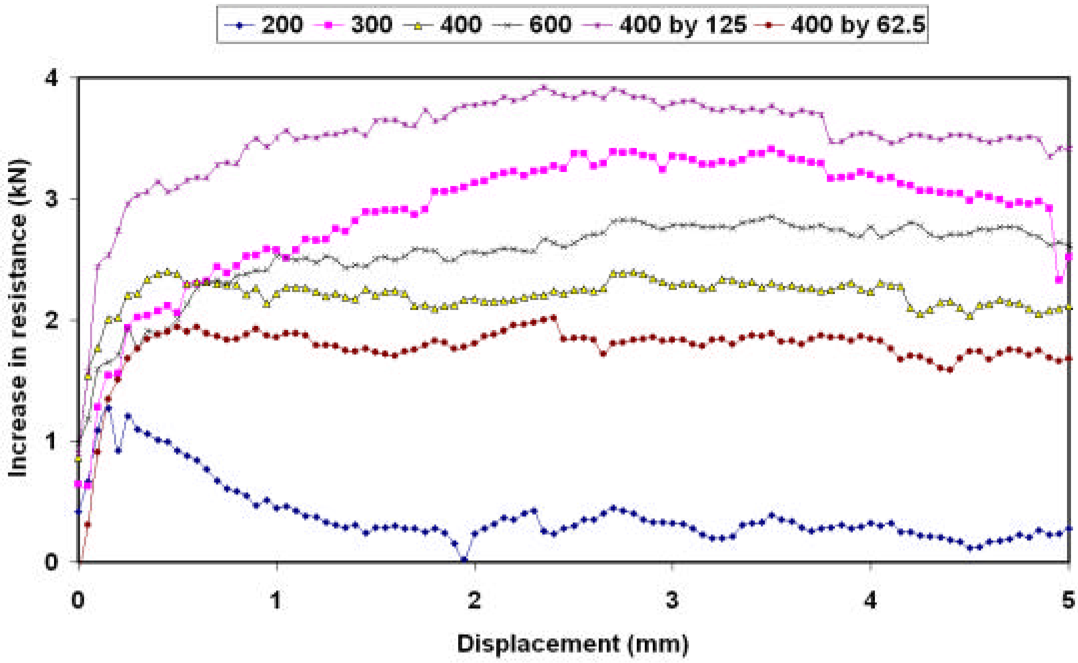

Figure 8-14: Low displacement range shoulder resistance/displacement graph to compare tests with different sized shoulders

---

[9] The term displacement implies a permanent movement whereas the term deflection has been used to describe the pre-failure range of movement

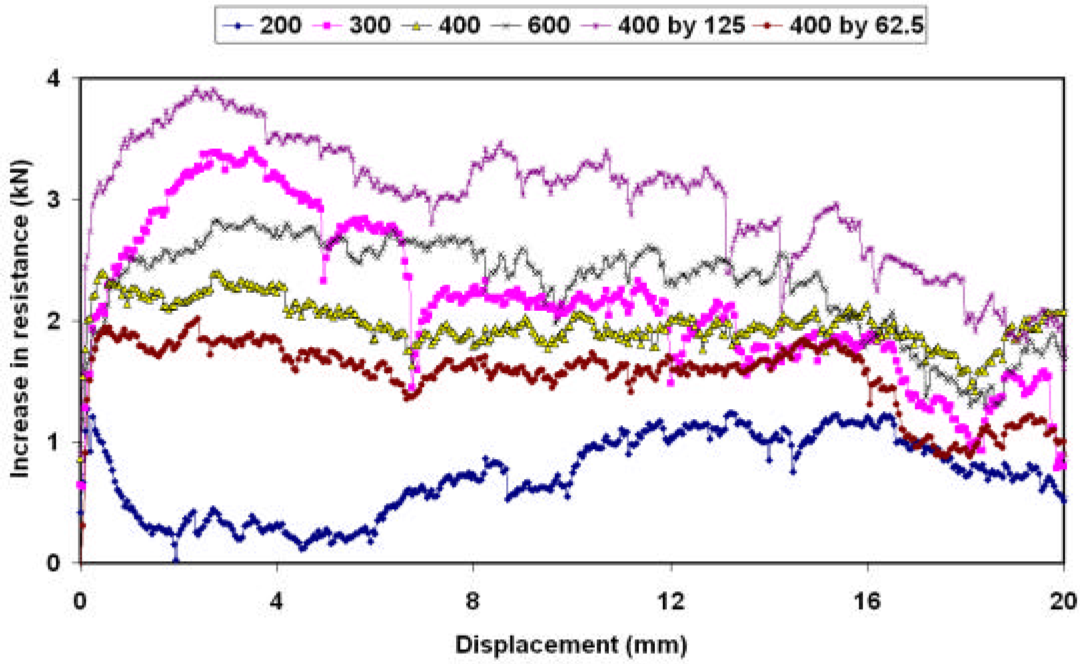

Figure 8-15: Medium displacement range increase in resistance/displacement graph to compare tests with different sized shoulders

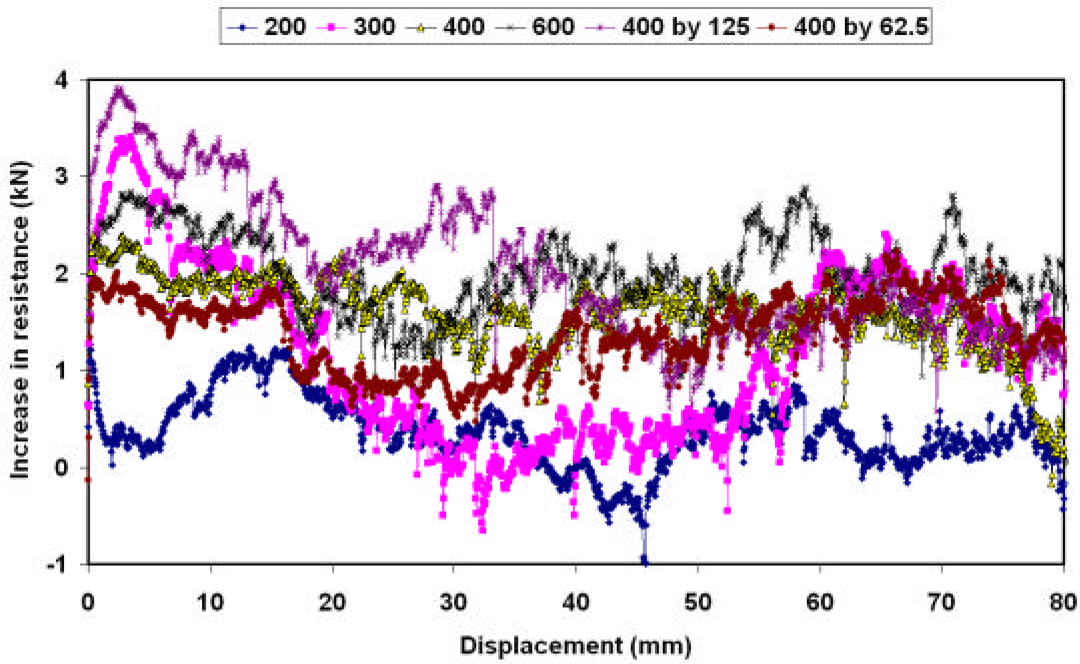

Figure 8-16: Large displacement range increase in resistance/displacement graph to compare tests with different sized shoulders

In Figure 8-14, Figure 8-15, and Figure 8-16 a trend for larger shoulders to give higher resistance is apparent. In Figure 8-14 the largest shoulder size (600 mm), shows the greatest loading ratio over the deflection range 0 to 5 mm. Evaluating shoulder contribution at greater displacement becomes more difficult. At larger displacements the shoulder becomes progressively less effective as its lateral extent is reduced by ballast falling off the end. This is illustrated in Figure 8-16 where at greater deflections different tests converge and cross over.

8.2.4. Interpretation

Test Results

Calculating the increase in resistance due to the presence of a shoulder is sensitive to the displacement at which the calculation is made. However, this sensitivity is probably more a result of variations in the resistance due to base resistance than to actual variation in the shoulder resistance though shoulder resistance would perhaps be expected to decrease with increasing displacement as ballast falls from the shoulder.

Given the difficulties in evaluating the shoulder resistance it was decided that a characteristic value of shoulder resistance was most meaningful when calculated by taking the mean increase in loading ratio (Lateral load/vertical load) over the displacement range of movement from 2 mm to 20 mm and multiplying this by the vertical load. This has advantages of:

- Eliminating variation due to ballast breakage, rearrangement or slippage events.
- Eliminating the pre-failure range of movement of the sleeper on base contact below 2 mm.
- Avoiding the fall-offs in resistance that occur at deflections generally beyond 20 mm due to ballast falling off the shoulder.

Table 8-7 summarises the increase in shoulder resistance at key displacements and as a mean over the displacement range 2 to 20 mm.

	Increase in resistance (N) compared to mean of test series A and B								
Shoulder size	**Mean 2 to 20**	**5**	**10**	**15**	**20**	**30**	**50**	**80**	**Test(s)**
200	899	136	635	1671	420	321	-52	-1574	2C and 3C
300	2150	2513	2119	1670	796	-7	508	2009	8C
400	1973	2117	2015	2016	2071	1336	1670	1567	1C and 7C
600	2317	2608	2305	2389	1692	1485	1934	2337	4C
400 by 62.5	3092	3358	3239	3477	2010	1290	2335	3235	6C
400 by125	2976	3414	3175	2854	1610	2258	842	1387	5C and 9C

Table 8-7: Summary of key increases in resistance for shoulders, means of same size shoulder tests

Tests 3C and 6C contain greater degrees of uncertainty due to the effect of the greater vertical load applied during testing.

Figure 8-17 shows the increase in shoulder resistance from 2 mm to 20 mm.

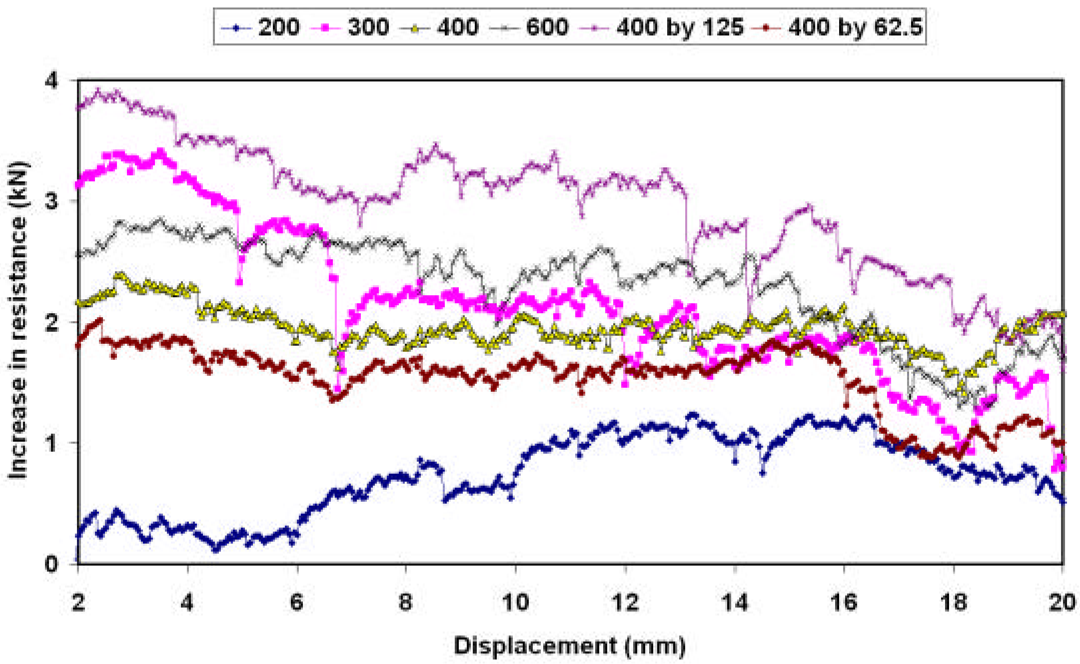

Figure 8-17: Increase in resistance/displacement graph to compare effects of shoulder over range considered most relevant for evaluation

Figure 8-18 shows a bar chart of increase in shoulder resistance at key displacements and as the mean increase from 2 mm to 20 mm for different shoulder sizes.

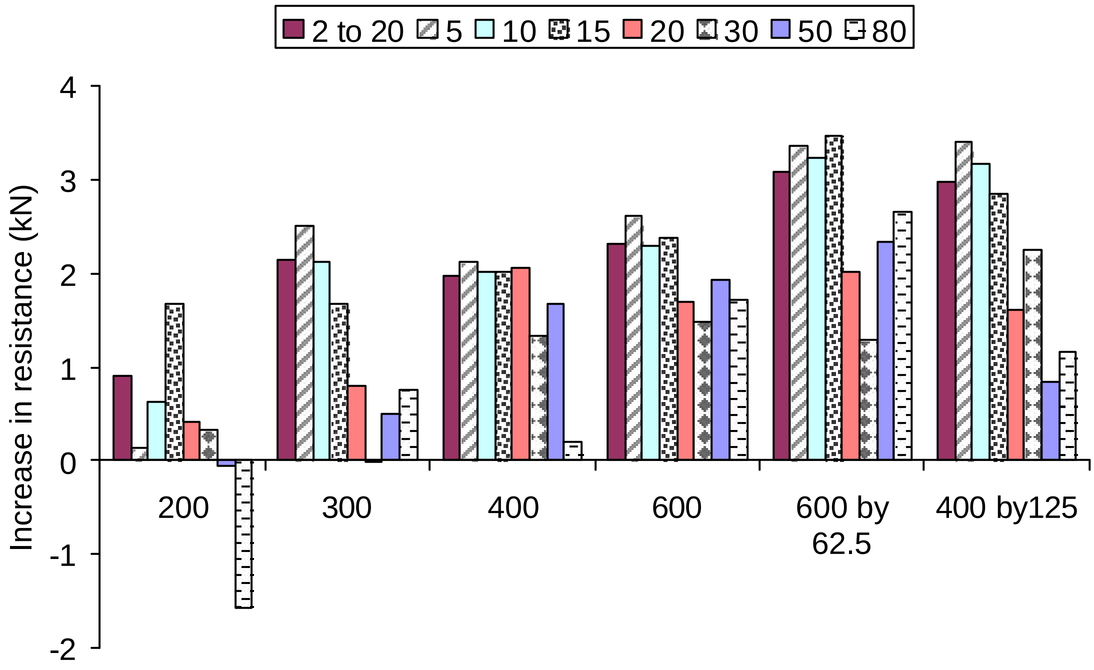

Figure 8-18: Bar chart to show increase in resistance due to shoulder (from Table 8-7)

Inspecting Figure 8-18, it can be seen that trends are partly obscured by variability in the tests. In particular it is inconsistent that the 300 mm size of shoulder appears to give a greater resistance than the 400 mm size at lower deflections. This is most likely caused by base ballast resistance contribution varying from the estimate of mean base ballast contribution. Tests with a 400 mm shoulder were carried out twice with a low vertical load of 15 kN and the mean estimates of shoulder resistance from these tests are considered the most reliable. In general it can be seen that increasing the shoulder extent and height increases the resistance.

Calculated shoulder resistance

A calculation will now be set out to quantify the shoulder resistance. The calculation follows the well established limit equilibrium method with the assumed mechanism of failure shown in Figure 8-19. Initially the calculation will be carried out as for plane strain, but modification for the finite area of the sleeper end and sideways spread of the mechanism is then required.

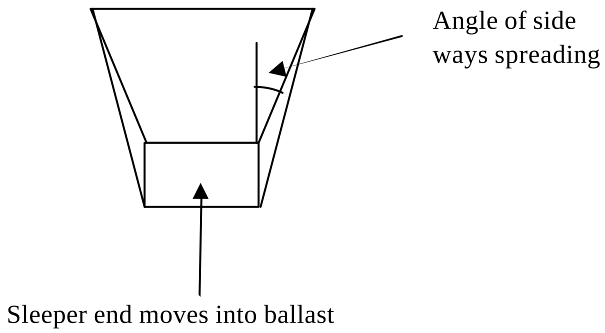

Figure 8-19: Diagram of shoulder failure wedge in 3D

Figure 8-20 shows the simplified geometry of the assumed failure mechanism and the symbols used which are then described below.

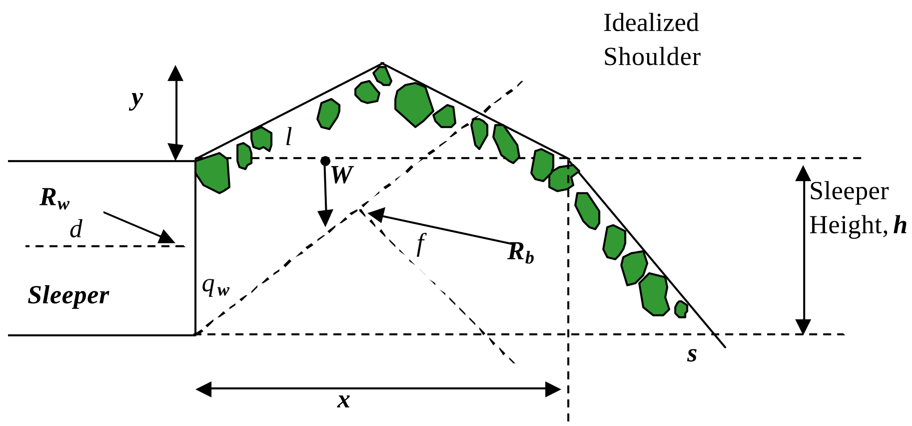

Figure 8-20: Assumed failure mechanism of shoulder ballast in plane strain

Where:

W =	the weight of the wedge
$\boldsymbol{R_w}$ =	the reaction at the sleeper/ballast shoulder contact
$\boldsymbol{R_b}$ =.	the reaction on the base of the slip surface within the ballast
l =	angle of heaped ballast
s =	Slope angle of the ballast as it falls away from the shoulder, the maximum value this can take is equivalent to the internal angle of friction for the ballast (estimated to be 45°)
y =	the height of the shoulder above the level of the sleeper top
x =	extent of ballast shoulder adjacent to sleeper top

h =	height of sleeper
q_w =	the angle that provides the least resistance and is found by trial and improvement
f	Internal angle of friction within the ballast
d =	the angle of friction between the sleeper and the ballast

In Figure 8-20 the reaction forces on the slip surfaces represent the combined normal and shear force for each surface.

The forces shown in Figure 8-20 can be represented in force diagrams as shown in Figure 8-21 A and B. where f is the internal angle of friction of the ballast.

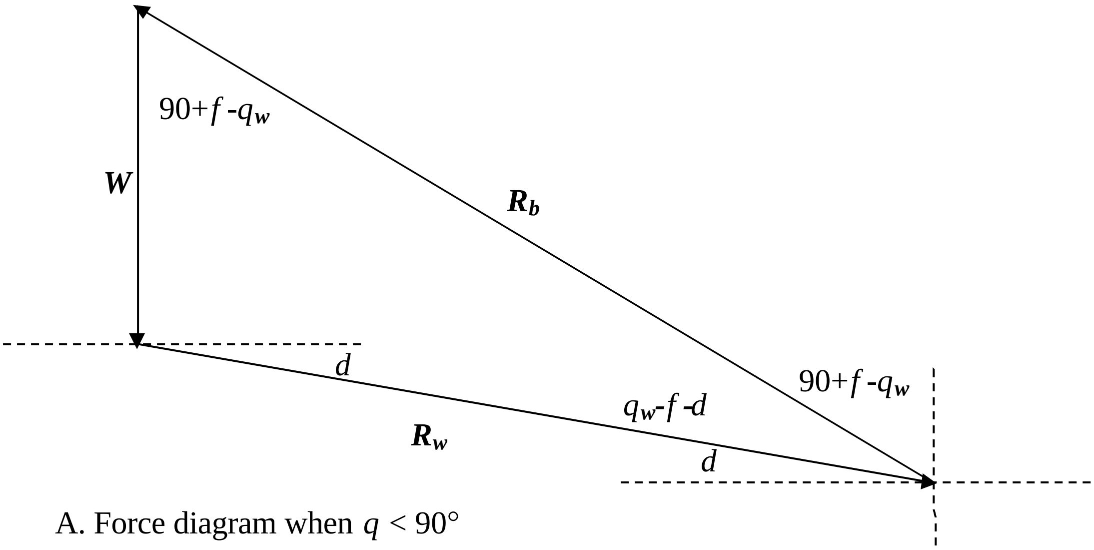

A. Force diagram when q < 90°

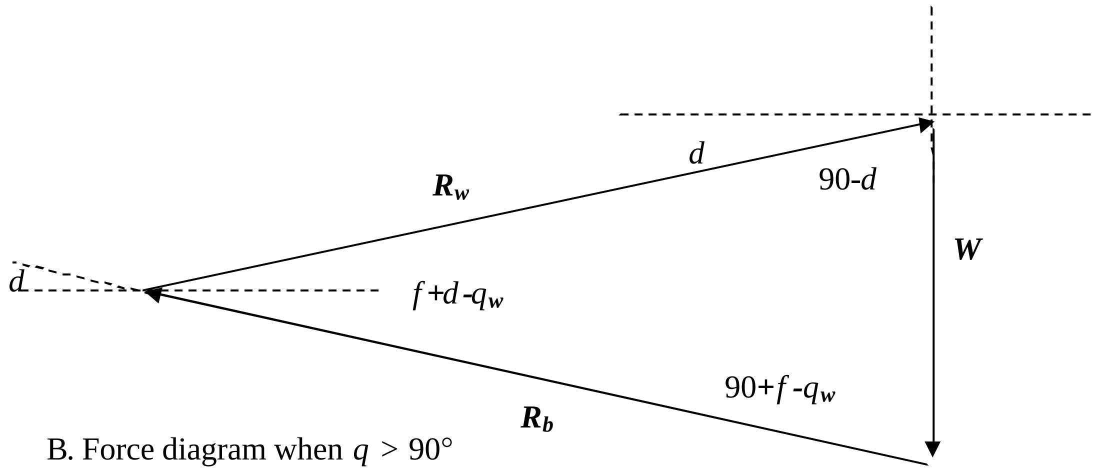

B. Force diagram when q > 90°

Figure 8-21: Force diagram for wedge failure mechanism when wedge angle < 90° and > 90°

The cases A and B occur because as the wedge angle passes 90° the direction of wall friction reverses. If the wall friction angle d is a fixed value this leads to a discontinuity in the calculated forces as the wedge angle q approaches and passes 90°. This would represent a sudden and unnatural reversal in the direction of forces. To accommodate a smooth transition it is proposed that as q increases to 90°, d will reduce to zero at $q = 90$ before again increasing as q passes 90°. The rate at which d changes as a function of q is unknown. To resolve the forces d will be taken as $0.5 \times (90 - q)$ until it reaches its maximum value of 24° ($Tan^{-1}0.45$). In fact it will be shown that, for the shoulder sizes evaluated, the failure wedge angle is so close to 90° that were the failure to occur at 90° the force would be similar, in this regard the need to accurately find the true angle of wall friction when the wedge angle is close to 90° is trivialised because at 90° there is no wall friction.

The force diagrams can be solved using the sine rule because one side (***W***) and all angles (f, d, q) are inputs to the calculation. The lateral force on the sleeper is then $\boldsymbol{R_w}\cos d$.

Note that the maximum ballast/sleeper friction interface angle (24°) has been taken as equivalent to the sleeper base/ballast angle found in these experiments as the median at 2 mm of displacement. However, the sleeper base is rougher than the sleeper ends as it is the sleeper base that is the open face during the pre-cast concrete fabrication process, again this has limited influence on the resultant forces calculated because the wedge angle is so close to 90°.

Consideration of the force diagrams shown in Figure 8-21 reveals several limitations on the validity of the shape of the wedge. The calculation is invalid when the following inequalities are true:

- $\theta \leq \phi + d$
- $\theta \geq 90 + f$

Both limiting inequalities correspond to the physical situation that all forces are vertical and so no lateral force is generated.

In addition to the forces in the lateral plane of movement shown in Figure 8-20 forces are also present on the sides of the wedge as shown in Figure 8-22.

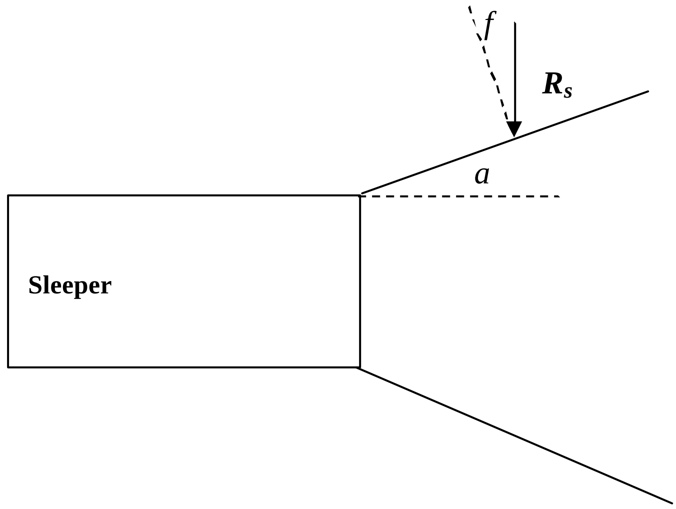

Figure 8-22: Plan view of failure wedge

In the case where $a = f$ the side force(s) $\boldsymbol{R_s}$ are normal to the direction of movement and therefore do not contribute to lateral force on the sleeper/ballast shoulder contact area. This assumes that all friction will be mobilised laterally on this interface with no contribution to vertical forces. In any case it will be a conservative assumption in that the side forces will not contribute to the calculated resistance.

It is now possible to use the method to find a shoulder resistance for sleeper movement on horizontal track. The calculation can be solved by careful discretisation of different areas of cross section for a range of failure angles q to determine the volume of ballast of density r involved in the failure wedge and hence to determine the weight $\boldsymbol{W}$ of the wedge. Two different types of cross section have been evaluated as shown in Figure 8-23.

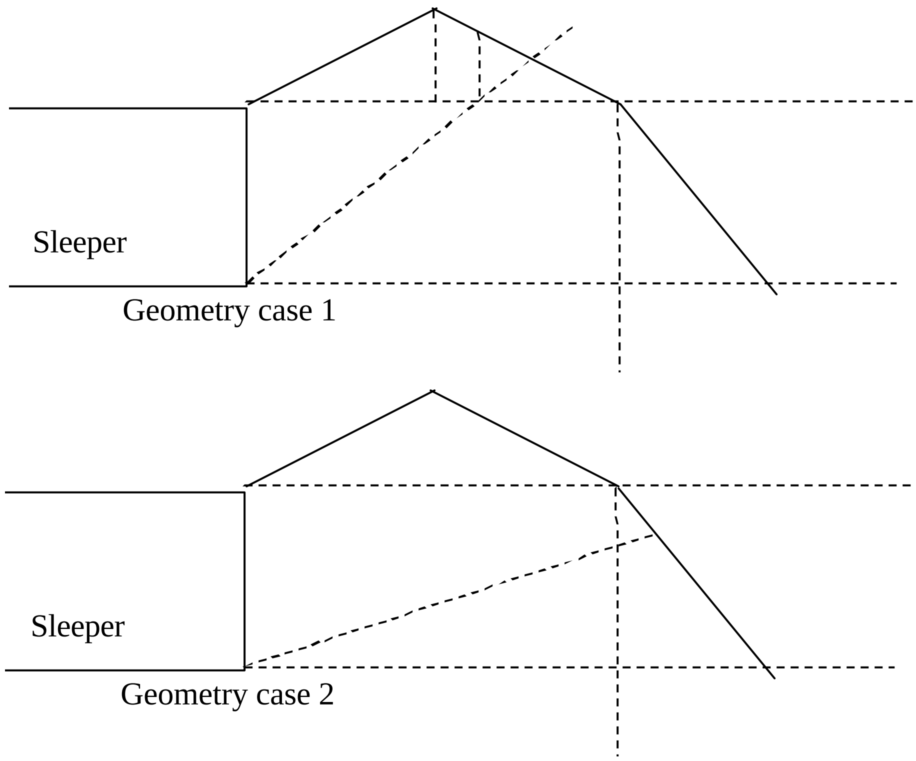

Figure 8-23: Geometries evaluated to calculate shoulder resistance

A complex discretisation of the 3D spreading of the failure wedge is also necessary.

The values used to calculate the forces are shown in Table 8-8.

Symbol	Values	Description	Units	Notes
h	0.21	Height of sleeper	m	0.21 at end (Tarmac G44)
w	0.29 and 0.65m	width sleeper and sleeper spacing	m	0.20 top to 0.29 base (Tarmac G44)
r_b	1,500	Density of ballast	kg/m^3	1,600 value for granite gneiss (Chang et al., 1980)
x	0.2 to 0.6	Extent of shoulder base	m	Based on values used on Network Rail (RGS, 2003, pp.table 1).
y	0 to 0.125	Height top	m	
d	0 to 24	Angle friction ballast/sleeper	°	Permitted to mobilise equal to $0.5\times(90\text{-}q\,)$until it reaches its maximum value of ~24° found from tests of base ballast L/V ratio
q	Varied	Angle wedge for shoulder	°	adjust for minimum resistance
l	0 to 32	Angle of heap	°	Set for each test
f	45 to 55	Angle friction ballast	°	Measured angle of repose lab tests, to maximum including dilation
s	45 and 34	Slope angle	°	In the lab tests this was allowed to be at the natural angle of repose of the ballasy ~45°. Additionally an angle of 34° has been evaluated corresponding to a slope of 1V to 1.5H

Table 8-8: Values used to calculate shoulder resistance

For a ballast internal friction angle of 45° the force diagrams in Figure 8-21 are valid only when 60°< q <135°. This means that most cases evaluated are for geometry case 2 because the crossover angle is close to or less than 60°.

The variations of shoulder resistance with angle of wedge for an internal ballast friction angle of 45° and a shoulder slope angle of 45° are shown in Figure 8-24 and the minimum resistance values and corresponding angles are shown in Table 8-9. The calculations are to the nearest 5° for q_w.

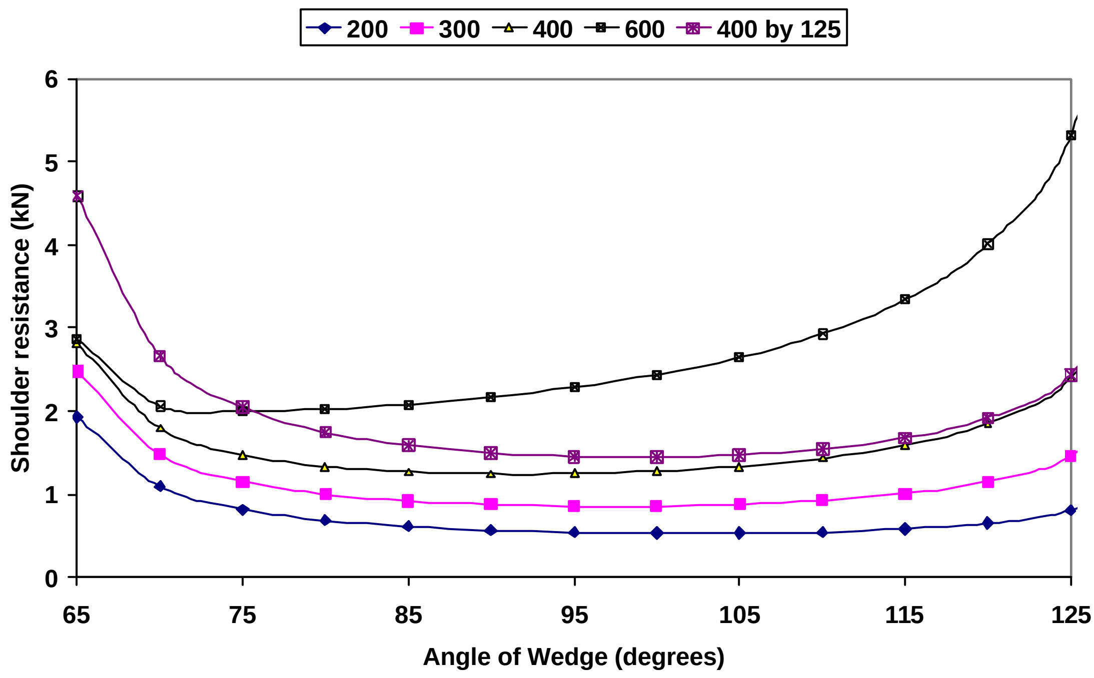

Figure 8-24: Angle of wedge failure mechanism plotted against failure load for a friction angle and sideways spreading angle of 45° and a slope angle of 45°

Extent (x)	Heap (y)	Angle	load	Geometry case	Geometry crossover angle
(mm)	(mm)		(N)		
200	0	100°	530	2	55.0°
300	0	95°	856	2	43.6°
400	0	90°	1244	2	63.2°
600	0	75°	2002	2	70.9°
400	125	100°	1445	2	63.2°

Table 8-9: Results of shoulder resistance calculations, friction angle and sideways spreading angle 45°, slope angle 45°

The friction angle was estimated to be 45° based on the natural angle of repose of the ballast. However, evidence to justify a greater value was presented by Indraratna and Salim (2005) who carried out triaxial tests on a ballast with a basic friction angle of 44°. They found that at low confining stress an apparent friction angle of 55° was obtained from measurements which was attributed to dilation. Therefore the shoulder resistance calculation has been carried out again for a friction angle of 55° to test the sensitivity of the calculated resistance; results are shown in Figure 8-25 and Table 8-10.

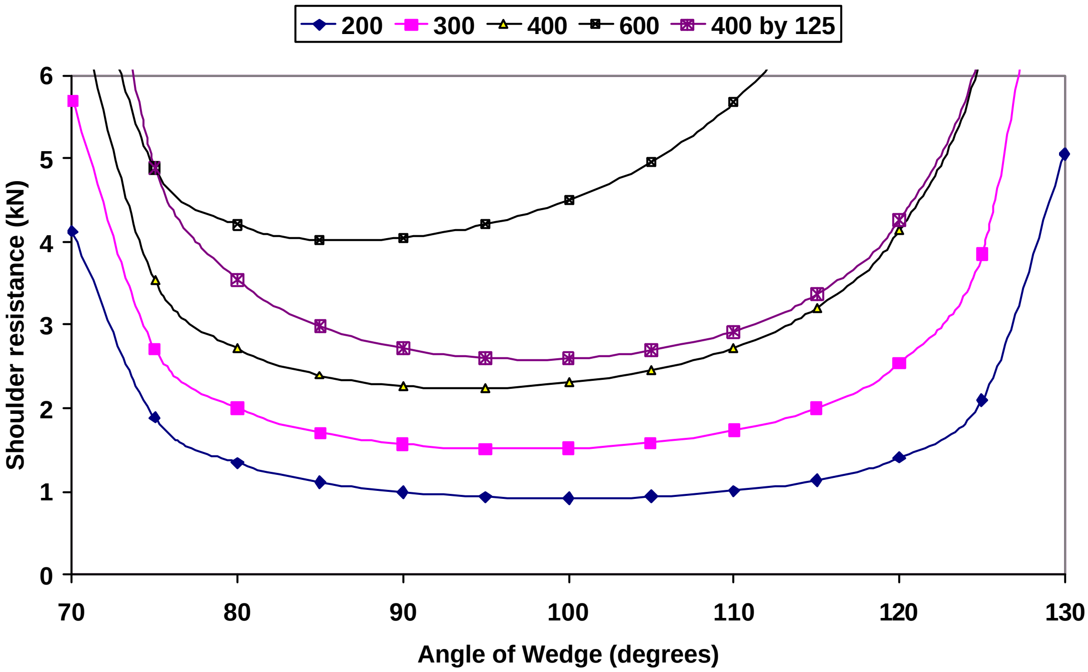

Figure 8-25: Angle of wedge failure mechanism plotted against failure load for a friction angle and sideways spreading angle of 55° and a slope angle of 45°

Extent (x)	Heap (y)	Angle	load
(mm)	(mm)		(N)
200	0	100°	919
300	0	95°	1513
400	0	95°	2244
600	125	85°	4019
400	62.5	100°	2595

Table 8-10: Results of shoulder resistance calculations, friction angle and sideways spreading angle 55°, slope angle 45°

In addition to varying the angle of friction calculations were carried out for a reduced slope angle (*s*) of 34°. This would correspond to a 3 along to 2 down slope. Results of these calculations are shown below:

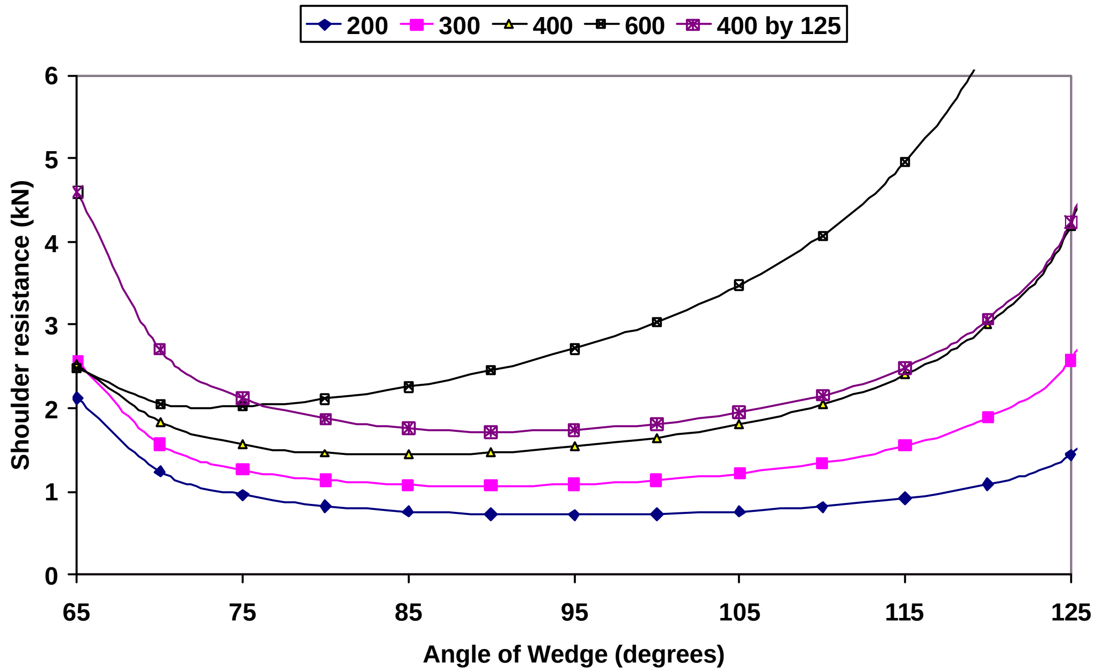

Figure 8-26: Angle of wedge failure mechanism plotted against failure load for a friction angle and sideways spreading angle of 45° and a slope angle of 34°

Extent (x)	**Heap (y)**	**Angle**	**load**
(mm)	(mm)		(N)
200	0	95°	721
300	0	90°	1068
400	0	85°	1439
600	125	75°	2025
400	62.5	90°	1721

Table 8-11: Results of shoulder resistance calculations friction angle and sideways spreading angle of 45° and a slope angle of 34°

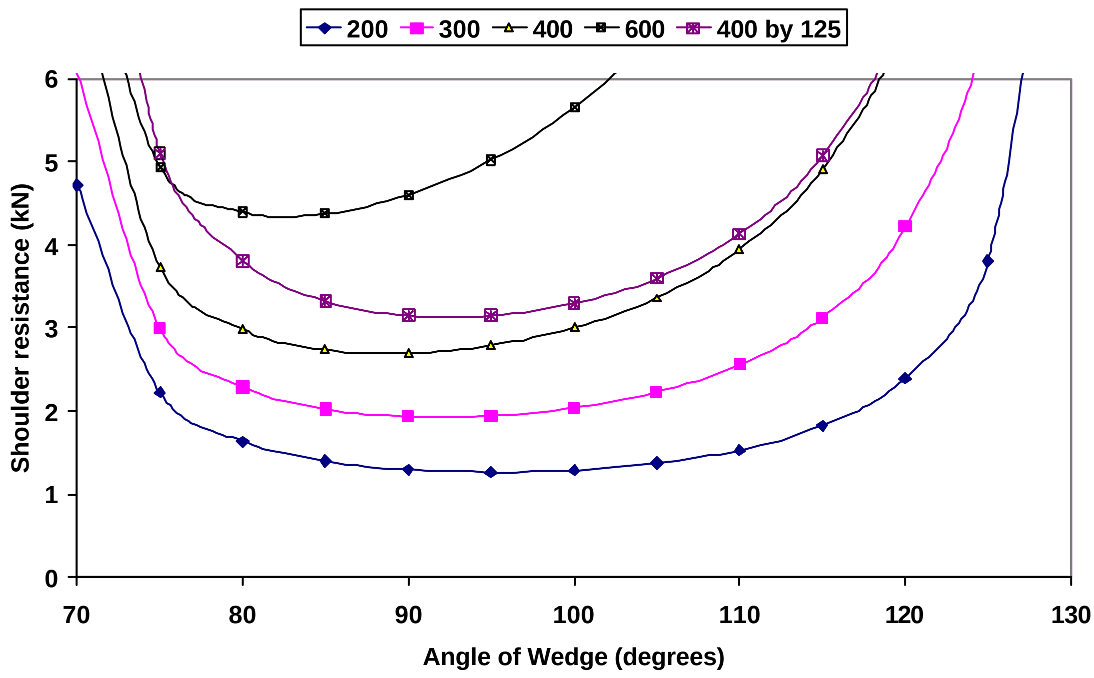

Figure 8-27: Angle of wedge failure mechanism plotted against failure load for a friction angle and sideways spreading angle of 55° and a slope angle of 34°

Extent (x)	Heap (y)	Angle	load
(mm)	(mm)		(N)
200	0	95°	1266
300	0	90°	1933
400	0	90°	2696
600	125	85°	4374
400	62.5	90°	3146

Table 8-12: Results of shoulder resistance calculations friction angle and sideways spreading angle of 55° and a slope angle of 34°

The bar chart shown in Figure 8-28 compares all the calculated resistances for each size of shoulder.

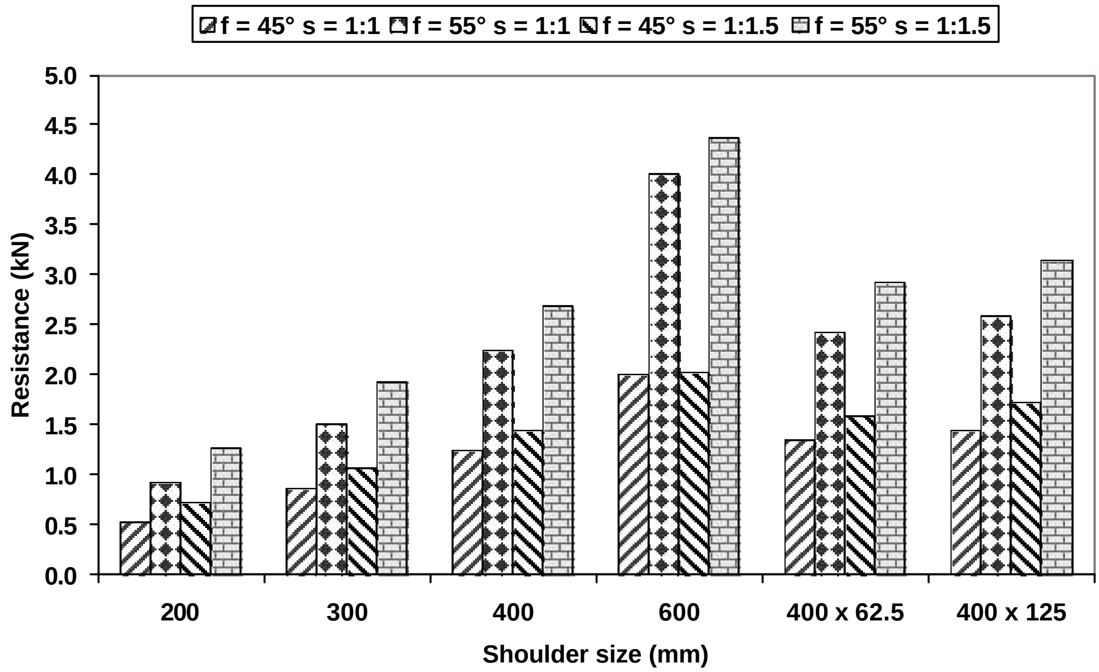

Figure 8-28: Bar chart to compare calculated shoulder resistance for friction angles of 45° and 55° and slope angles of 45° and 34°

Figure 8-28 demonstrates the large differences in calculated shoulder resistance that occur when the friction angle is increased from 45° to 55°. A small increase is also apparent when the slope angle is reduced from 45° to 34°. It is also noted that reducing the slope angle can force the wedge failure angle (q_w) to reduce, but perhaps more importantly a reduced slope angle is likely to have the additional benefit of maintaining the magnitude of shoulder resistance with displacement because ballast will be less likely to fall from the shoulder.

Comparing the estimated shoulder resistance from the laboratory tests to the calculated shoulder resistance

In comparing the test results to the calculated results there is an issue that if the angle of sideways spreading is too great then the edges of the wedge hit the sides of the testing rig. For example, for α = 45° this occurs after 0.5×(0.65-0.285) = 0.1825 m of shoulder lateral extent.

It could perhaps be argued that a contribution in frictional resistance from the sides of the testing rig compensates for a loss of resistance due to reduced size and hence weight of a failure wedge.

In Figure 8-29 a bar chart compares the experimental results to the calculated shoulder resistance for different sizes of shoulder. The calculated results are for a shoulder slope of 45°, similar to the shoulders tested.

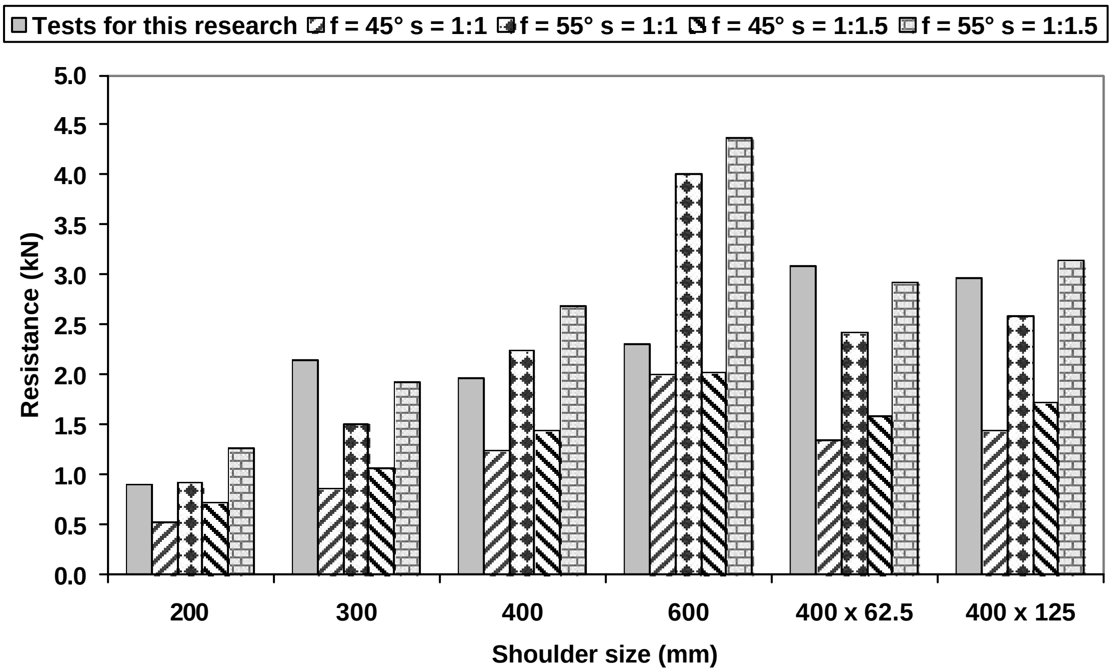

Figure 8-29: Comparison of experimentally measured shoulder resistance as a mean over the range 2 mm to 20 mm of displacement with calculated values of shoulder resistance

In Figure 8-29 the calculated shoulder resistance values show an increasing resistance with shoulder size, the experimental results show the same general trend. The experimentally estimated shoulder resistance is usually within the range of calculated values for the estimated possible range of friction angles with a side slope of 45°. Exceptions to this, as previously mentioned, are possibly due to shallower than usual slope angles in the tests which could have accounted for small increases in measured resistance. All the experiments incorporate a level of uncertainty due to the variability in the sleeper base contribution.

8.3. Crib

8.3.1. Background

Crib ballast is present on either side of the sleepers in a real railway track. The width of the crib ballast varies depending on the size of the sleeper and the sleeper spacing. Resistance to movement of the sleeper is due to the frictional contact between the sleeper and the crib ballast and within the crib ballast itself. The horizontal and vertical stresses within the ballast provide the normal force on the sleeper and within the ballast to mobilise the frictional resistance. If the sleeper is forced to move laterally, two modes of failure for the crib ballast can be identified. Either the sleeper/ballast crib contact area fails in sliding or a slip plane develops within the ballast, probably level with the base of the sleeper as shown in Figure 8-30 and Figure 8-31. It is likely that at a particular width between adjacent sleepers the modes of failure cross over from failure of sleeper/ballast contact to failure within the ballast with narrower spacing being required for the latter. Note that in both failure cases the base contact ballast is assumed to fail in sliding with the sleeper.

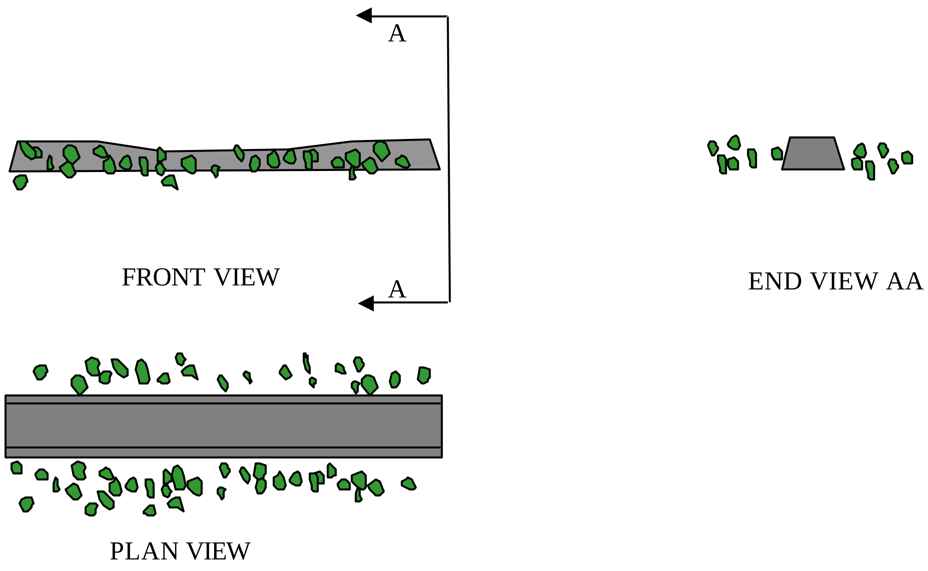

Figure 8-30: Crib contact area

Slip surface sleeper/ballast

Slip surface within ballast

Figure 8-31: The two possible slip surfaces identified

Assuming that confining stress within the ballast and at the sleeper/ballast crib contact may be similar, it can be deduced that cross over between the two failure modes occurs when:

$$(\boldsymbol{s}\text{-}\boldsymbol{b}) \tan f = 2\boldsymbol{h} \tan d \qquad \textbf{Equation 8-10}$$

Where $\boldsymbol{s}$ is the sleeper spacing, $\boldsymbol{b}$ is the sleeper width at the base, $\boldsymbol{h}$ is the effective height of the sleeper, f is the angle of shearing resistance within the ballast and d is the angle of shearing resistance between the sleeper crib surface and the ballast.

Therefore when $(\boldsymbol{s}\text{-}\boldsymbol{b}) \tan f < 2\boldsymbol{h} \tan d$ failure would be within the ballast and when $(\boldsymbol{s}\text{-}\boldsymbol{b}) \tan \phi > 2\boldsymbol{h} \tan d$ failure would be at the sleeper/ballast crib contact area.

From the previous tests on the base sleeper/ballast contact area it is known that the angle of shearing resistance between the sleeper base and the ballast is 24° and that the angle of repose for the ballast considered to be the same as the angle of internal shearing resistance is about 45°. However the sleeper surface contact with the crib is smooth concrete rather than the roughened underside of the sleeper and the friction interface angle will be less than 24°.

In reality the stresses on the sleeper and within the ballast may differ. Compaction of the crib ballast may lead to greater horizontal confining stress than would be expected from the purely geostatic case. In addition the presence of shoulder ballast beyond the crib may further complicate such a simplistic approach. However, in the tests reported in this section no shoulder ballast is present.

Taking values of s, b and h of 0.65 m, 0.285 m and 0.2 m respectively for G44 sleepers on the WCML, (s-b) tan 45° = 0.365 and 2h tan 24° = 0.18. (Note that while elsewhere a value of 0.3 m is taken for b, the sleeper width, here it is more appropriate to use the value accurate to the nearest mm). Therefore, in the tests reported here, failure would be expected by the development of a slip surface between the sleeper and ballast crib contact area.

8.3.2. Results

Results are presented for two tests in which crib ballast was placed adjacent to the sleeper on either side up to the level of the sleeper top surface. No shoulder ballast was present. The sleeper base is flat but the top surface is raised at either end, so the level of ballast is slightly lower adjacent to the middle of the sleeper compared to the sleeper ends.

To confirm the type of failure occurring, paint was sprayed across the crib ballast and sleeper top surface in lines so that any movement of sleeper relative to ballast would be identifiable in photographs taken before and after each test. Photographs from one of the tests to show the characteristic behaviour are shown in Figure 8-32, Figure 8-33 and Figure 8-34.

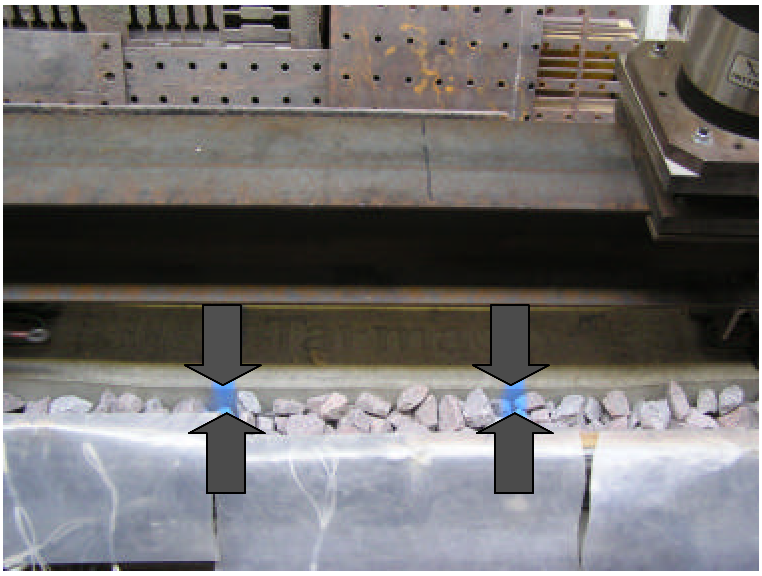

Figure 8-32: Photographs before lateral pull test, middle of sleeper

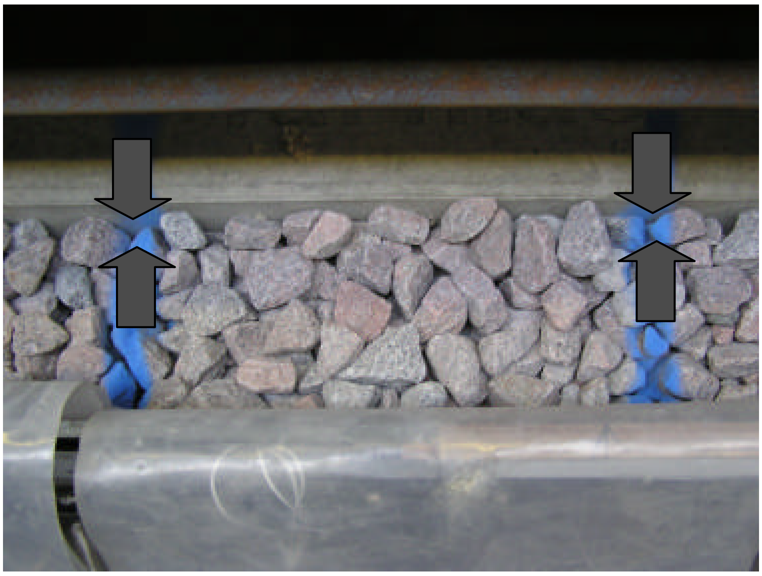

Figure 8-33: Photographs before lateral pull test, middle of sleeper, close up

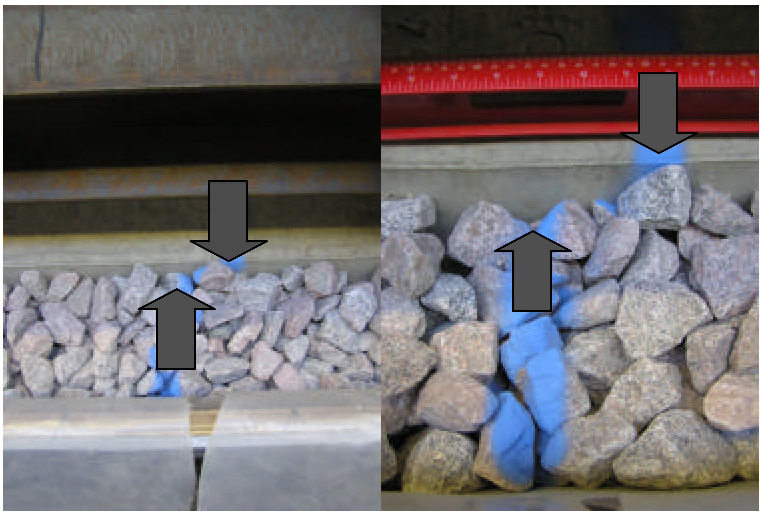

Figure 8-34: Photographs after lateral pull test, middle of sleeper, close up

The photographs confirm that the sleeper has moved relative to the ballast by approximately the same distance the sleeper was pulled laterally (~90 mm). This is taken to confirm that failure occurred by the sleeper sliding against the crib ballast.

Figure 8-35, Figure 8-36 and Figure 8-37 show graphs of the increase in resistance/displacement over different ranges of displacement.

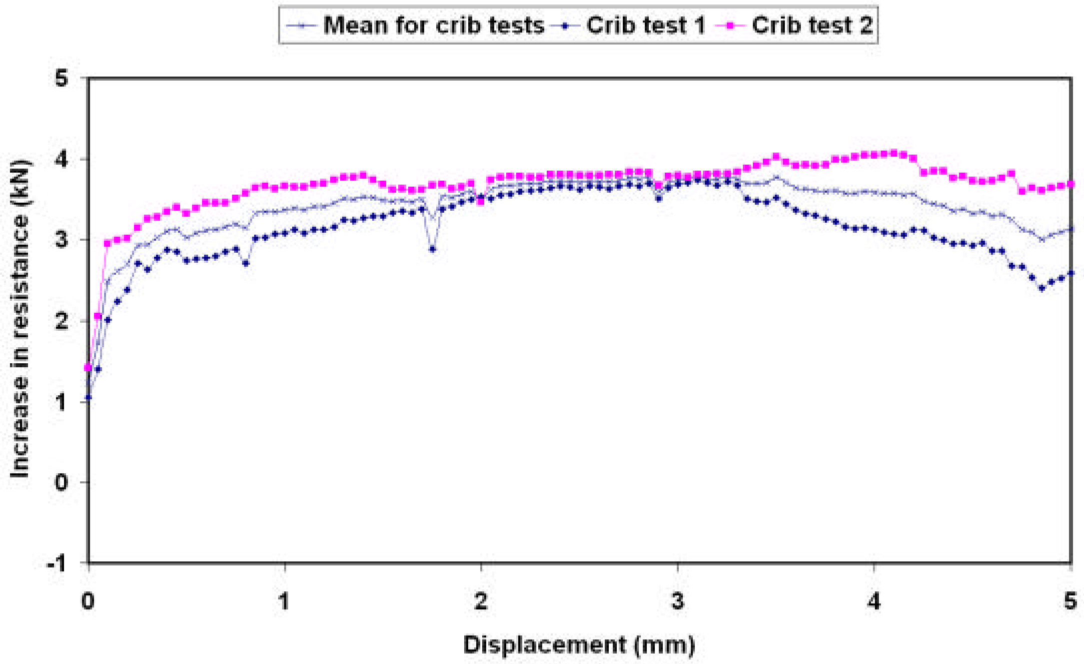

Figure 8-35: Low range increase in resistance/displacement graph for tests where crib ballast is present

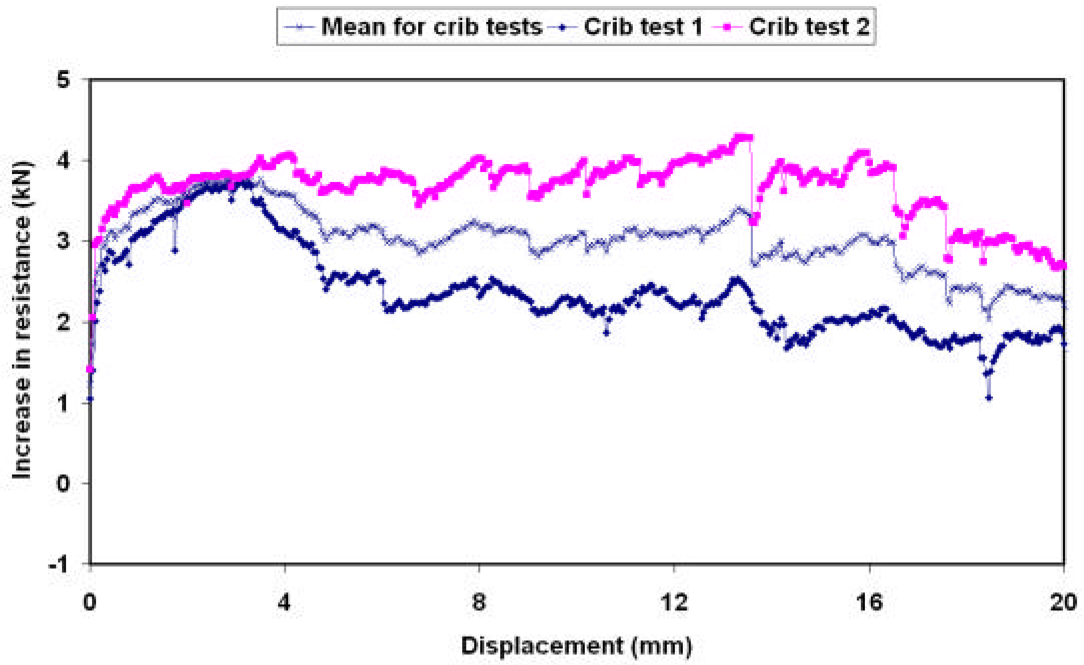

Figure 8-36: Medium range increase in resistance/displacement graph for tests where crib ballast is present

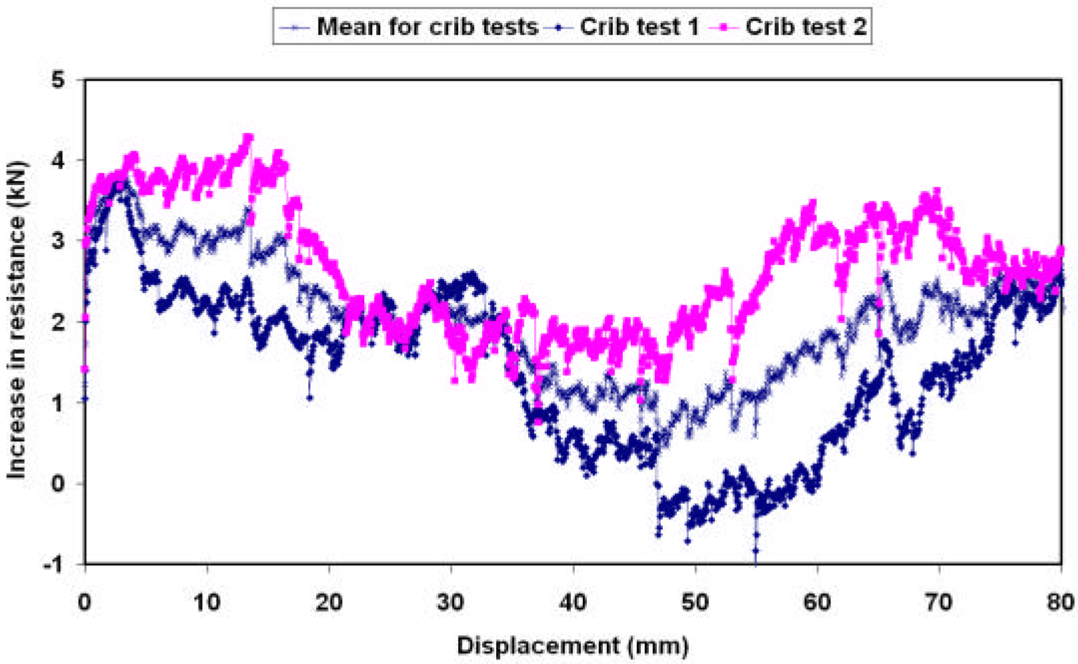

Figure 8-37: Large range increase in resistance/displacement graph for tests where crib ballast is present

These graphs confirm the increase in resistance due to the presence of crib ballast but again, as with previous tests, highlight the locally highly erratic response of the sleeper/ballast interface.

8.3.3. Interpretation

The mechanism (though not necessarily the magnitude) of crib resistance, in contrast to the shoulder resistance, should be largely independent of sleeper movement over the range tested. Figure 8-38 shows a bar chart of the increase in resistance due to the presence of crib ballast for both tests and as a mean for both of these tests.

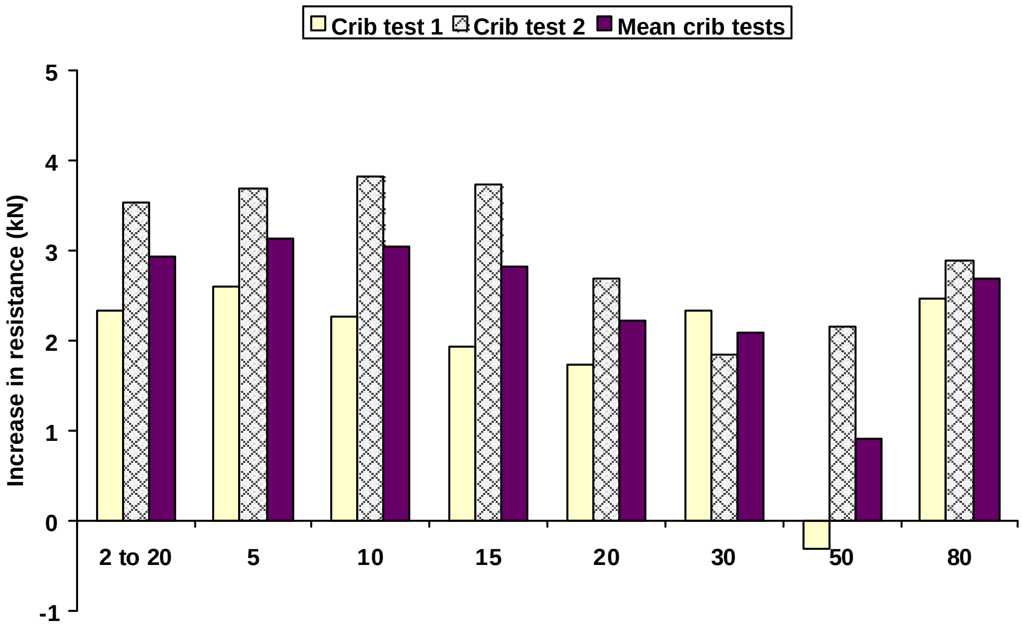

Figure 8-38: Comparison of measured crib resistance as a mean over a range of deflections and at specific deflections

By inspection of Figure 8-38, it is clear that there is some variation when the increase in resistance is evaluated at different deflections with a trend of slightly reducing resistance beyond 15 mm notwithstanding individual results which contradict this at specific deflections. This reduction in magnitude of crib resistance is thought to be due to destructurisation of the ballast contact matrix as the deflection of the sleeper increases.

Table 8-13 gives the values used in the bar chart shown in Figure 8-38.

Increase in resistance (N) compared to mean of test series A and B								
Test	**Mean 2 to 20**	**5**	**10**	**15**	**20**	**30**	**50**	**80**
Crib 1D	2339	2588	2258	1926	1736	2327	-323	2459
Crib 2D	3531	3689	3823	3721	2683	1833	2156	2892
Mean 1D and 2D	2935	3138	3040	2823	2209	2080	917	2676

Table 8-13: Increase in sleeper resistance due to crib ballast

Given the known size of the crib sleeper/ballast contact area and the angle of friction between sleeper and ballast from previous base sleeper/ballast tests, it is possible to estimate the horizontal confining stress in the crib ballast. This can then be compared to the mean geostatic vertical confining stress and a stress ratio deduced.

The experimentally determined resistance values in Table 8-13 are converted to horizontal confining stress as shown in Table 8-15 taking the contact area of the crib sleeper/ballast as $2m^2$ ($2.5\times0.2\times2$) and the sleeper/ballast friction ratio as $\tan d = 0.45$.

Estimate of horizontal confining stress in crib ballast (N/m^2)								
Test	**Mean 2 to 20**	**5**	**10**	**15**	**20**	**30**	**50**	**80**
Crib 1D	2543	2813	2454	2094	1887	2530	-351	2673
Crib 2D	3839	4009	4156	4044	2916	1993	2344	3144
Mean 1D and 2D	3191	3411	3305	3069	2401	2261	996	2908

Table 8-14: Estimated horizontal confining stress in crib ballast

The mean geostatic vertical stress in the crib can be approximated by taking a unit weight of 15 kN/m^3 for the ballast and a mean depth of 0.1 m so that σ_v = 1.5 kPa. Therefore the earth pressure ratio can be calculated to be as shown in Table 8-15.

Earth pressure ratio s_h/s_v								
Test	**Mean 2 to 20**	**5**	**10**	**15**	**20**	**30**	**50**	**80**
1D	1.70	1.88	1.64	1.40	1.26	1.69	-0.23	1.78
2D	2.56	2.67	2.77	2.70	1.94	1.33	1.56	2.10
mean	2.13	2.27	2.20	2.05	1.60	1.51	0.66	1.94

Table 8-15: Summary data for ratio of vertical to horizontal confining stress in the ballast

According to this calculation, the horizontal confining stress in the crib is the major principal stress and is approximately twice the mean vertical geostatic stress as a mean from 2 to 20 mm of displacement. The greater horizontal stress compared to the geostatic case is thought to be caused during testing; as the sleeper moves relative to the ballast the particles in contact with the sleeper are rotated and lock into place. It is also relevant to note that in Chapter 6, where the horizontal stress due to vertical cyclic loads was evaluated, a locked in earth pressure ratio of 0.5 developed after 100 load cycles in test 3A. In test 3A the major principle stress was vertical and there was no crib ballast present so the ballast was open at the surface level with the top of the pressure plate used. These findings indicate that the major principal stress may not be more than twice the minor principal stress in a layer of ballast open at the surface.

Having deduced the likely earth pressure ratio it is now possible to revisit Equation 8-10 which may be modified to include the maximum likely earth pressure ratio $\boldsymbol{K_{max}}=s_{\boldsymbol{h}}/s_{\boldsymbol{v}}$ = 2.0.

$$(\boldsymbol{s}\text{-}\boldsymbol{b})\tan f = \boldsymbol{K_{max}}\, 2\boldsymbol{h}\tan d \qquad \textbf{Equation 8-11}$$

Therefore in these tests $(\boldsymbol{s}\text{-}\boldsymbol{b})\tan f = 0.365$ and $\boldsymbol{K_{max}}\, 2\boldsymbol{h}\tan d = 0.356$. This is (just) consistent with a failure mechanism of sleeper on ballast. The spacing would need to be reduced such that $(\boldsymbol{s}\text{-}\boldsymbol{b})\tan 45° < 0.356$ for a slip surface to develop within the ballast, i.e. the sleeper spacing would need to be reduced to 0.64 m or less. A more realistic value for d, which is currently overestimated based on the interface friction angle of the roughened base of the sleeper, would reduce further $\boldsymbol{K_{max}}\, 2\boldsymbol{h}\tan d$.

8.4. Comparison with previous sleeper/ballast lateral resistance tests

Lateral sleeper resistance tests are scarce in published literature and data are rarely presented so as to isolate resistance due to crib, shoulder and base sleeper/ballast contact areas.

Most tests tend to focus on individual sleeper resistance on unloaded track. Typically a global value of resistance is quoted and then it is often suggested that the shoulder accounts for a certain proportion of this resistance, e.g. Lichtberger (2007a) & (2007b).

Investigations have been carried out into the effects of type of sleeper type, sleeper spacing, and sizes of crib and ballast shoulder. However, many research findings are confined to internal reports with only second-hand or anecdotal accounts finding their way into freely available published literature. For example ERRI (1995) reported that the sleeper crib and base ballast contribute approximately 1/3 each to the lateral resistance of the sleeper on unloaded track based on an unpublished BR report by Shenton (1973).

Lateral resistance tests take different forms, and while some investigate the resistance of the sleeper/ballast interface (Selig and Waters, 1994) others report data on the resistance provided by the track system as a whole (Esveld, 2001).

Computers have also been used to try and quantify ballast shoulder resistance, Kabo (2006) carried out finite element modeling of a sleeper bay of track of dimensions very similar to that in the laboratory tests carried out for this research. Kabo reported resistance in the presence of a 15 kN vertical load for different sizes of shoulder as a peak resistance within up to 50 mm of deflection; however no test data was reported for shoulder absence so it is difficult to infer absolute values for shoulder contribution. Kabo's tests showed that increasing the lateral extent of the shoulder significantly increased the resistance but that increasing the height actually reduced the resistance. Kabo's results are more likely to highlight difficulties in applying FEM techniques to model ballast than any real effects of changing shoulder height.

In this section, where possible, published data have been taken for physical tests on freshly laid ballast. There follows a summary of selected published results with the most relevant compared to the test data from this research for shoulder and crib contribution.

Shoulder

ERRI (1995) reported data from an ORE report of 1976 (ORE D 117/RP 8, 1976). These data were presented as a graph of the % change in resistance due to increasing shoulder size (100% is assumed to be the resistance when no shoulder is present). A sketched reproduction of this graph is shown in Figure 8-39.

It is possible to estimate the shoulder resistance for increasing shoulder lateral extent provided that a base sleeper/ballast contact resistance value can be estimated to apply to the percentage increases in resistance that can be read from Figure 8-39. This has been achieved by taking a global sleeper resistance value of 8.3 kN corresponding to the 50% less than value in the summary table of lateral resistance for just tamped ballast (shown in Table 2-1, ERRI, 1995a) and assuming this corresponds to a 300 mm shoulder. For the 300 mm shoulder the resistance is calculated by dividing the total resistance (8.3 kN) by the median total % (estimated from Figure 8-39, e.g. 120% for 300 mm shoulder), then multiplying by 100 to obtain the non shoulder contribution. The shoulder contribution is then the difference between the global and non-shoulder value. Similarly the contributions from different sizes of shoulder can be estimated. These assumptions result in 6.9 kN of resistance for a sleeper with no shoulder present and is assumed to include crib as well as base sleeper/ballast contact area contributions.

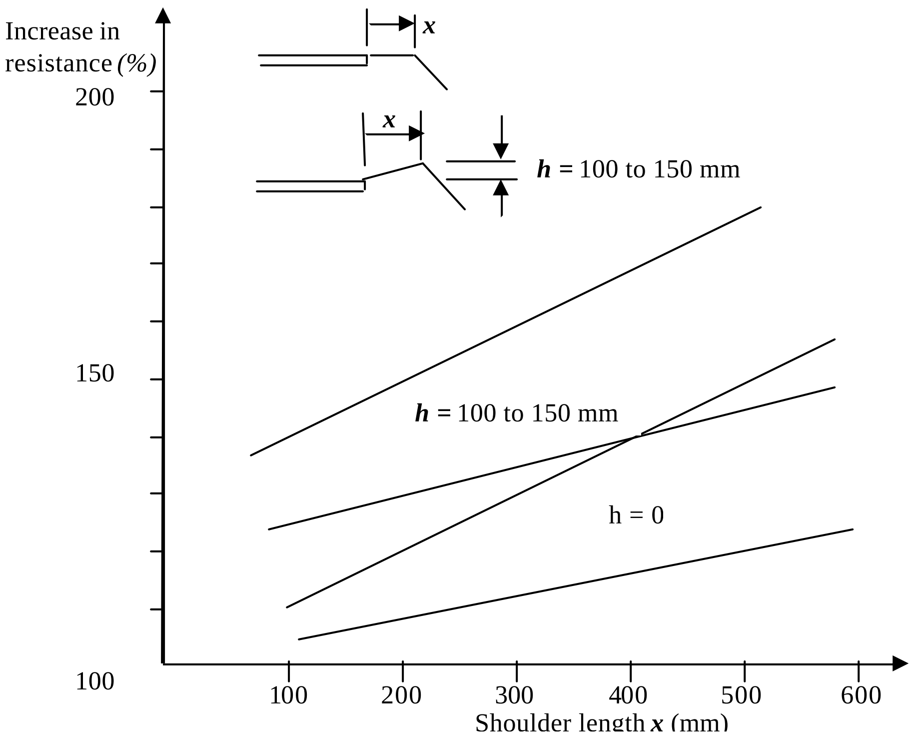

Figure 8-39: % increase in shoulder resistance against shoulder sketched from ERRI (1995a)

The definition of heaped shoulder ballast shown in Figure 8-39 is different from the definition adopted in this research; this means that comparison of experimentally measured heaped shoulder resistance to ERRI's reported data is more problematic. To obtain an estimate of shoulder contribution it will be assumed that ***x-h*** in Figure 8-39 is equivalent to the ***x*** in this research, thus an estimate for a shoulder size of 125 mm heap is possible by reading off the % increase in shoulder resistance within the shaded region for h = 100 mm to 150 mm at the ***x*** point 275 mm (400 - 125).

Results of these calculations are shown in Table 8-16.

	Increase due to shoulder presence scaled from graph (%)			**Resistance (N)**		
Shoulder size	**Median**	**Min**	**Max**	**Median**	**Min**	**Max**
200	114	106	118	968	415	1245
300	120	110	128	1383	692	1937
400	126	114	138	1798	968	2628
600	138	122	158	2628	1522	4012
400 by 125	141	130	155	2836	3804	2075

Table 8-16: Inferred shoulder resistance

A bar chart shown in Figure 8-40 shows the inferred maximum and minimum ERRI values of shoulder resistance and compares them with the results from the tests for this research.

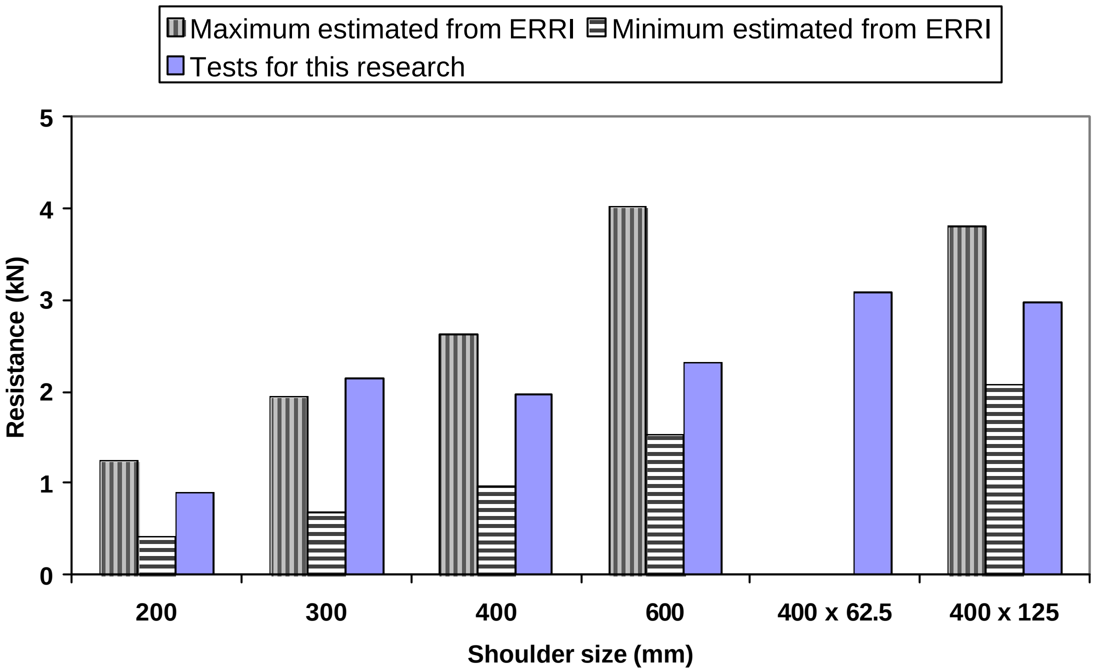

Figure 8-40: Comparison of experimental shoulder resistance with values extrapolated from ERRI (1995a) and calculated values.

In Figure 8-40 it can be seen that the laboratory tests gave shoulder resistance within the range of those inferred from the ERRI report except for the test at 300 mm of resistance which is slightly higher.

Figure 8-41 plots the inferred ERRI sleeper resistance with the theoretically calculated shoulder resistance for friction angles of 45° and 55° and ballast slopes of 1:1 and 1:1.5 for increasing lateral extent of the shoulder level with the top of the sleeper.

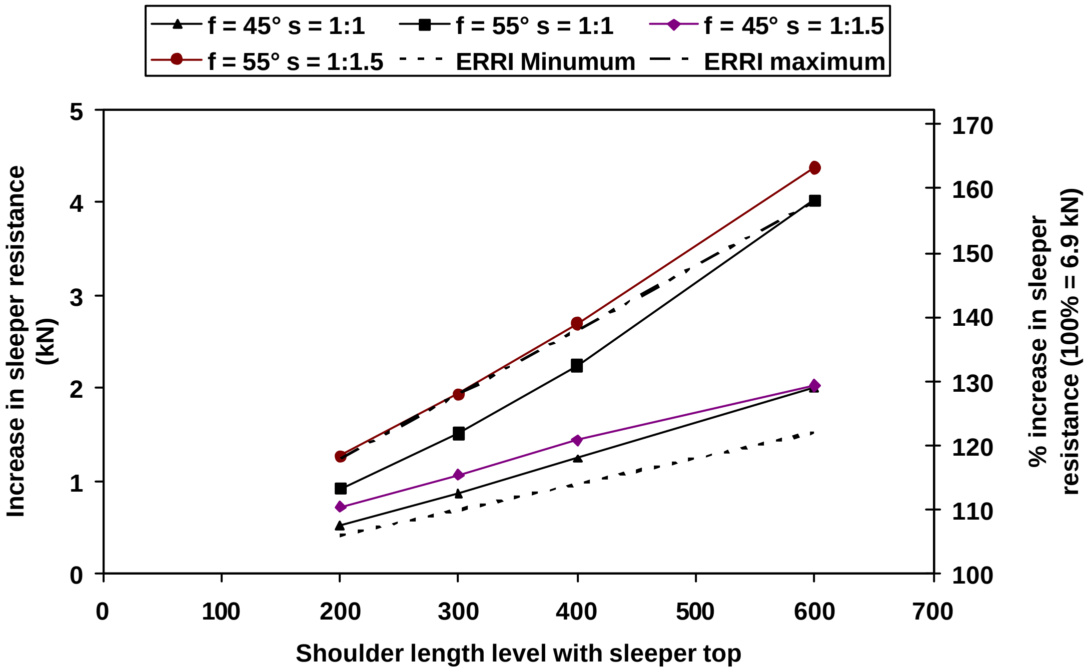

Figure 8-41: Comparison of theoretically calculated shoulder resistance with results inferred from ERRI (1995a)

In Figure 8-41 the theoretical values of shoulder resistance are generally within the region of ERRI results and these also show that changes in internal angle of friction of ballast and side slope of ballast can explain the variation within the ERRI data. Also note that the theoretical lines are not quite linear because the wedge block angle changes slightly as the shoulder extent increases.

In addition to using experimental data to assess shoulder resistance by using a mean estimate of the contribution of base contact resistance, estimates of the maximum and minimum possible base contact contributions can be used from tests runs A and B to quantify the potential uncertainty in the experimental values of shoulder resistance. This is shown in Figure 8-42 for increasing lateral extent of shoulder (no heaped results are included).

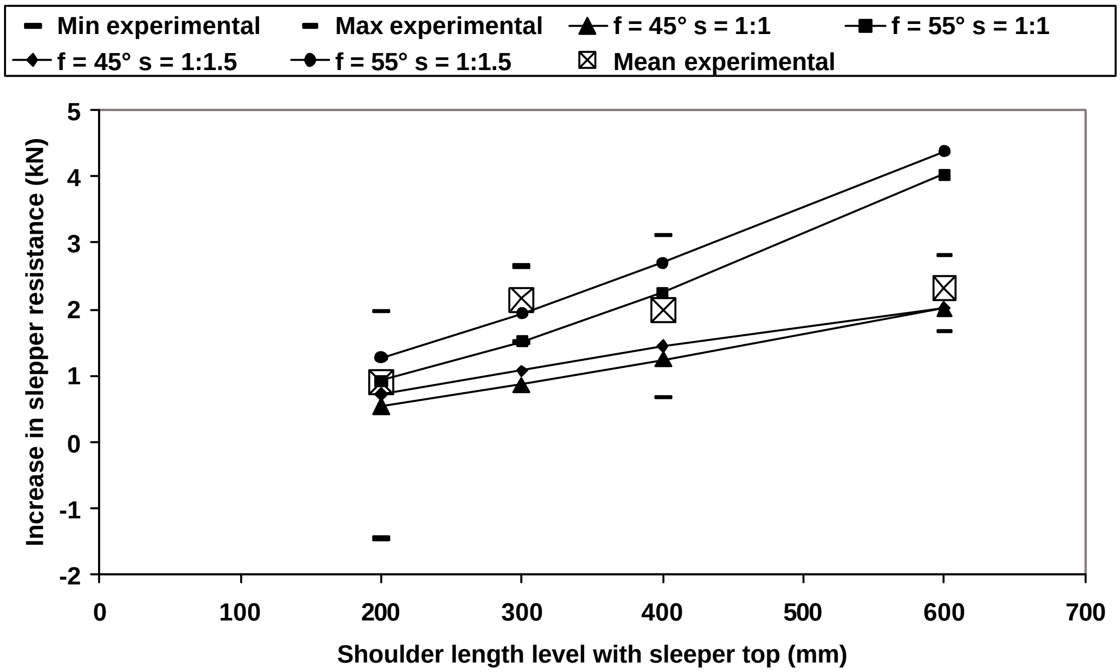

Figure 8-42: Resistance/shoulder extent graph showing possible range of shoulder resistance inherent in laboratory tests

Figure 8-42 shows the high level of variation possible associated with the resistance contribution from the base contact from the experimental data. The large potential variation for the 200 mm shoulder is partly caused because of the larger vertical load present in one of the two tests at this shoulder size (test 3C).

Crib

Crib resistance from the ERRI data may be estimated by applying the 1/3 rule from the unpublished BR research (Shenton, 1973) to the same estimate of typical sleeper resistance in the ERRI data outlined previously of 8.3kN. This corresponds to an estimated crib resistance of 2.76kN.

A further estimate of crib resistance can be made from research carried out in the USA. Selig and Waters (1994) reported typical data from lateral tie push tests (LTPT). LTPTs involve detaching a sleeper from the rails and using a reaction beam connected to the rails to push the sleeper a set amount, typically 1 to 6.4 mm laterally and recording the resistance. Selig and Sluz (1978) show a graph that indicates 3000 N to 4000 N produces a lateral movement of 0.1 inches for an unloaded wooden sleeper subject to a horizontal load after maintenance of the track (Selig and Sluz, 1978). Selig and Waters

(1994) show a graph that indicates crib resistance is approximately half the total resistance, and shoulder resistance is approximately one quarter of the total resistance on freshly laid unloaded track (Selig and Waters, 1994, pp.8.13). In the USA shoulder sizes are typically 300 mm level with the sleeper top (AREA, 2003). Therefore it may be deduced that the maximum shoulder resistance for a 300 mm lateral extent may reach 1000 N and the crib resistance may be at most 2000 N.

In the current research, the mean crib resistance for two tests was found to be 2993 N. This compares favourably with the estimate from the ERRI data and appears somewhat higher than the estimate made using American based research. However, the American research was for wooden sleepers which may also have been smaller in size and on significantly different ballast and will have different interface properties.

8.5. Summary of Chapter 8

8.5.1. Base resistance

In test runs A and B, the ratio of vertical to lateral load of centrally and eccentrically loaded sleepers was found to be the same. Justification for this finding was made using the Butterfield failure envelopes where it was shown that train loading was likely to fall within the linear region of the combined VHM failure envelopes. However, care is needed in applying this finding to specific cases of train loading where, in addition to the exact combination of vertical, horizontal and moment loading to be considered, arrangement and types of ballast and sleepers may also differ.

8.5.2. Shoulder resistance

Test run C comprised 9 tests with varying shoulder size. Tests gave varied results over the full range of deflection up to 90 mm. A mean resistance derived by taking the mean loading ratio from 2 mm to 20 mm of deflection was found to be advantageous in eliminating test variability inherent when resistances were calculated from loading ratios at specific deflections.

A calculation was presented which appeared to provide a reasonable estimate of shoulder contributions to resistance by comparison with shoulder resistance inferred from ERRI data and the experimental data. The calculations were used to present a chart which has the potential to be used for the specification of shoulder sizes (Figure 8-41).

8.5.3. Crib resistance

Two tests were carried out to quantify the crib sleeper/ballast resistance and a mean value of 2935 N was obtained. This compared favourably with estimates from the literature. Furthermore calculations showed that an inferred earth pressure ratio of 2 was consistent with the measured earth pressure ratios found in vertical loading tests where the major and minor principal stress planes were reversed. The earth pressure ratio of 2 was also consistent with the observed failure mechanism of sleeper/ballast slip.

9. Conclusions and further research

9.1. Conclusions

The **aim** of this research was to develop a fuller understanding of the mechanical behaviour of the sleeper/ballast interface. Specific objectives were set out at the end of Chapter 1; these are reprinted in italic below and addressed in turn:

- *To quantify likely magnitudes of Pendolino train loading for normal and extreme conditions by summing the effects of curving forces, wind load and static axle loads on low radius curves of the WCML (Chapters 2 and 3).*

Calculations have identified likely normal and extreme magnitudes of load transferred to individual sleepers on low radius curves for Pendolino trains travelling at their current maximum operating cant deficiency. In the course of this the importance of the relative stiffness of the normal and lateral axes of the track system was also identified.

- *To characterise the in-service (pre-failure) behaviour of the sleeper/ballast interface due to likely Pendolino train loading (Chapters 5 and 7).*

The behaviour of the sleeper/ballast interface during in-service pre-failure loading has been characterized using geophone field data and laboratory testing. Analysis of these results has shown that while the resilient response of individual sleepers is consistent it may differ in magnitude from different experimental test set-ups and nearby sleepers on real track where the sleepers are apparently supported by similar arrangements of ballast and loaded similarly.

- *To quantify the development of confining stress within the ballast at the end of an initial 100 Pendolino axle loads on freshly prepared ballast and assess its impact on sleeper/ballast interface behaviour (Chapter 6).*

Changes occur to the confining stress within the ballast during cyclic vertical loading. Using experimental and finite element modelling it was shown that the earth pressure ratio moves towards the active case at peak load and the passive case at minimum load with increasing loading cycles. This behaviour allows the sleeper to bed into the ballast and is evidence that long term changes to the structure of the ballast are occurring with load cycles.

- *To characterise single sleeper interface properties (pre-failure) for use with vehicle/ track dynamic models (Chapter 7).*

Individual sleeper interface properties have been evaluated by laboratory experiments and it has been found that the pre-failure behaviour of the sleeper/ballast interface is load path dependent. A relationship has been fitted to the experimental data that has the potential to be used in vehicle/track dynamic interaction models.

- *To quantify the failure envelope of the sleeper/ballast base contact for a single sleeper in combined VHM loading (Chapter 8).*

Combined vertical, horizontal and moment loading failure envelopes have been plotted for the sleeper/ballast interface and moment loading has been shown to have negligible impact on the failure of the sleeper/ballast interface within the likely range of train loading.

- *To quantify the resistance available from the crib and shoulder sleeper/ballast contact areas both experimentally and by calculation (Chapter 8).*

Experimental results for the failure of the sleeper/ballast base contact have found that the mobilised friction angle at 2 mm of displacement as a median of all tests is 24°, as a mean of the resistance from 20 to 90 mm this tends to 30°. The contribution to lateral resistance from the shoulder and crib has been shown to be dependent on sleeper displacement and an evaluation of changes in resistance with displacement has concluded that at specific displacements results can be highly varied due to ballast breakage/rearrangement events. However, the resistance is most consistent when taken as a mean from 2 to 20 mm of displacement. A method to calculate the contribution to sleeper lateral resistance from different sizes of shoulder ballast has been presented and results proven to be reasonable by comparison with the experimental results in this research and results in the literature. A chart has been presented which has the potential to be used as the basis for shoulder size specification. Contributions to sleeper lateral resistance from crib ballast have been measured and observations of the failure mechanism have permitted calculations to deduce the earth pressure ratio at failure and hence the minimum spacing for the failure mechanism to develop.

- *To address the implications of the findings of the research (Chapter 9).*

Two key implications of the research are identified:

1. The ability to calculate the lateral sleeper/ballast resistance from the shoulder has the potential to bring scientific method and design to shoulder specification rather than stated shoulder sizes for given circumstances such as those currently incorporated within Network Rail codes. A chart was presented in Chapter 8 which could be used for this.
2. Comparison of shoulder and crib resistance to literature was hampered by a lack of published and freely available data and inconsistency in methods of reporting sleeper resistance from the three contact areas. Therefore it is recommended that a universal method of reporting sleeper lateral resistance tests be adopted which identifies the shoulder and crib ballast dimensions, the type of sleeper and ballast and differentiates where possible between contributions from the three sleeper/ballast contact areas. The vertical load present should also be included so that a coefficient of friction of the sleeper to ballast may be calculated. Averages should be taken at key deflections and ranges of deflections. In this research the resistance at 2 mm, the mean from 2 to 20 mm and the mean from 20 to 90 mm were found to be important ways to characterise sleeper lateral resistance.

9.2. Further research

Consideration of the behaviour of the track system has shown that in relation to a wheel load applied to the rail, the lateral resistance of an individual sleeper depends on the vertical load present. However, the lateral load present depends on the lateral stiffness. Investigation into the global lateral and vertical stiffness of the track system are recommended. Improved understanding of the interaction between the global vertical and lateral stiffness and the contributions from the component parts of the track system could enable designers to specify rail sections, pads and sleepers which contribute to an optimum vertical and lateral global stiffness for lateral resistance. This would potentially minimise the occurrence of rail buckles and may have implications for the design life of ballast.

It has been found experimentally that the sleeper/ballast interface mobilised friction angle is about 24° at 2 mm of deflection, this is less than the internal angle of friction of the ballast and therefore there is a potential to increase the lateral failure resistance of the sleeper ballast interface by roughening of the sleeper base. Currently the type G44 sleeper (and others) is cast into an upside down mould leaving the base open to the atmosphere. This has the effect of roughening the base in comparison to the top surface of the sleeper which is flattened by the mould. It is suggested that further roughening could be achieved by incorporating ridges into the casting of the sleeper base. Further research is recommended into different ways of achieving this and on the implications for ballast life.

It is known that the lateral resistance of the sleeper ballast interface improves with trafficking and it was shown experimentally that changes in the earth pressure ratio occur with loading cycles. Therefore research is recommended into the changes in structure that occur within ballast during cyclic loading over the full life cycle to improve fundamental understanding of the mechanical behaviour of ballast. During the current research ideas were developed within the infrastructure research group at the University of Southampton, and a research project is due to start shortly (University of Southampton, 2008).

Over the course of this research findings were made that, with hindsight, could have altered testing arrangements and testing procedures. In particular it was shown that the contribution from sleeper base contact to global sleeper resistance is highly variable and this presented difficulties in calculating the contribution from shoulder and crib from measurements of global sleeper/ballast lateral resistance. Tests could be planned which eliminated this source of potential variation, for example by replacing the base contact ballast with a material of consistent frictional response. Such tests would be valuable in deducing the true variation present in the contribution to sleeper lateral resistance of given sizes of shoulder and crib ballast.

Further research to reproduce load path dependent behaviour using constitutive models of soil in finite element or other analyses methods would be of benefit in validating either the relation proposed as part of this research or in developing further relations that could be used to take account of load path dependent behaviour. More accurate modelling of load path dependent behaviour in rain/track interaction models (e.g. Vampire, ADAMS/rail) could be used to carry out investigations to better understand the relative importance of the relative lateral and vertical stiffness of the track system and variations therein on sleeper loading and to investigate the behaviour of track systems with the incorporation of track flaws such as hanging sleepers.

10. References:

ABAQUS, Inc. (2007) *ABAQUS version 6.7-1 Documentation*. ABAQUS, Inc. Rising Sun Mills,166 Valley Street, Providence, RI 02909-2499, Tel: +1 401 276 4400, Fax: +1 401 276 4408, E-mail: support@Abaqus.com http://www.abaqus.com

Adegoke, C. W., Chang, C. S. & Selig, E. T. (1979) STUDY OF ANALYTICAL MODELS FOR TRACK SUPPORT SYSTEMS. *Transportation Research Record,* Vol.733, Mechanics of Track Support, Piles and Geotechnical Data**,** pp.12-20.

Alias, J. (1984) La voie ferrée, techniques de construction et d'entretien, deuxieme edition, Eyrolles, 61 boulevard Saint Germain - 75005 Paris.

Alsthom (2008) *The new PENDOLINO.* Available from: http://www.transport.alstom.com/_eLibrary/brochure/upload_55552.pdf [Accessed June 2008]

AREA (2003). *Manual for railway engineering*. Washington, Washington.

Atkinson, J. H. & Sallfors, G. (1991) Experimental determination of soil properties, *10th European conference on soil mechanics,* Florence. Vol.3, pp.915-956.

Baker, C. J., Jones, J. & Lopez-Calleja, F. (2003) Measurements of the cross wind forces on trains, *Proceedings of the World Congress on Railway Research,* WCRR 2003 Edinburgh International Conference Centre. pp.486-492.

Baker, C. J., Jones, J., Lopez-Calleja, F. & Munday, J. (2004) Measurements of the cross wind forces on trains. *Journal of Wind Engineering and Industrial Aerodynamics,* Vol.92**,** pp.547.

Barton, M. E. (1994) Cohesive sands: The natural transition from sands to sandstones, *Proceedings of the conference on Geotechnical engineering of hard soils - soft rocks,* Athens, Greece. pp.367-374. A.A. Balkema

Bathurst, R. J. & Raymond, G. P. (1987) Geogrid Reinforcement of Ballasted Track. *Transportation Research Record,* Vol.1153**,** pp.8-14.

BBC (2004) *Tilting train breaks speed record.* Available from*:* http://news.bbc.co.uk/1/hi/uk/3671680.stm [Accessed January 2008]

BBC (2007) *French set new rail speed record.* Available from*:* http://news.bbc.co.uk/1/hi/world/europe/6521295.stm [Accessed January 2008]

Bezin, Y. (2008) *Emails concerning the behaviour of Pendolino tilting trains when curving*

Boucher, D. L. S. & Selig, E. T. (1987) Application of Petrographic Analysis to Ballast Performance Evaluation. *Transportation Research Record,* Vol.1131, Performance of Aggregates in Railroads and Other Track Performance Issues**,** pp.15-25.

Bowness, D., Lock, A. C., Powrie, W., Priest, J. A. & Richards, D. J. (2007) Monitoring the dynamic displacements of railway track. *Proceedings of the Institution of Mechanical Engineers, Part F (Journal of Rail and Rapid Transit),* Vol.221**,** pp.13-22.

Bowness, D., Lock, A. C., Richards, D. J. & Powrie, W. (2005a) Innovative remote video monitoring of railway track displacements, *Advances in Experimental Mechanics IV,* Southampton, UK. pp.417. Trans Tech Publications

Bowness, D., Powrie, W., Richards, D., Lock, A. & Clayton, C. (2005b) Report on Field Observations of the Performance of Railway Track, Location, Crewe. Rail Research UK, School of Civil Engineering & the Environment, University of Southampton.

British Transport Commission (1958). *Soil Mechanics Laboratory Interim Report, Individual Test Report, Lateral Moment of Resistance of Track*. The Chief Civil Engineer's Office British Railways - Western Region, Soil Mechanics Laboratory, 66 Porchester Road, Paddington, W2.

British Railways Board GM/TT0088 (1993). *Group Standard: Permissible Track Forces for Railway Vehicles*. Group Standards, Railway Technical Centre, Derby.

British Standards Institution BS EN 13674-1 (2003). *Railway applications - Track - Rail - Part 1*. British Standards Institution, London, UK.

Brooker, E. W. & Ireland, H. O. (1965) Earth pressures at rest related to stress history. *Canadian Geotechnical Journal,* Vol.II.

Brown, S. F. (1996) The use of geosynthetics in pavement engineering, *Proceedings of the 1996 1st European Geosynthetics Conference*, Maastricht, Neth. pp.47.

Brown, S. F. & Pappin, J. W. (1981) Analysis of Pavements With Granular Bases. *Transportation Research Record,* Vol.810**,** pp.17-23.

Burmister, D. (1945) The General Theory of Stresses and Displacements in Layered Systems. *Journal of Applied Physics,* Vol.16**,** pp.89-94.

Burrow, M. P. N., Bowness, D. & Ghataora, G. S. (2007a) A comparison of railway track foundation design methods. *Proceedings of the Institution of Mechanical Engineers, Part F (Journal of Rail and Rapid Transit),* Vol.221**,** pp.1-12.

Burrow, M. P. N., Chan, A. H. C. & Shein, A. (2007b) Deflectometer-based analysis of ballasted railway tracks. *Proceedings of the Institution of Civil Engineers, Civil Engineering,* Vol.160**,** pp.169-77.

Butterfield, R. & Gottardi, G. (1994) A complete three-dimensional failure envelope for shallow footings on sand *Géotechnique,* Vol. 44(1) pp.181-184.

Chang, C. S., Adegoke, C. W. & Selig, E. T. (1980) GEOTRACK Model for Railroad Track Performance. *Journal of The Geotechnical Engineering Division, ASCE,* Vol.106**,** pp.1201-1218.

Chrismer, S. M. & Richardson, G. (1986) In-Track Performance of Geotextiles at Caldwell, Texas. *Transportation Research Record,* Vol.1071**,** pp.72-80.

Corbet, S. (2003) Use of geosynthetics in transportation projects, *Transportation Geotechnics, Proceedings of the Symposium,* Nottingham, United Kingdom. pp.25. Thomas Telford Services Ltd, London, E14 4JD, United Kingdom

Cox, S. J. & Grassie, S. L. (1983) New Dynamic Model of Railway Track Incorporating Flexible Sleepers. Engineering Department, Cambridge University, UK.

Cresswell, A. & Powrie, W. (2004) Triaxial tests on an unbonded locked sand. *Geotechnique,* Vol.54**,** pp.107.

DeltaRail (2006) *http://www.vampire-dynamics.com/.* Available from: [Accessed

Department for Transport (2004) *Government White paper, The Future of Rail*. London UK, Crown Copyright, HMSO

Diakoumi, M. (2007) Relative soil/wall stiffness effects on retaining walls propped at the crest. *Ph.D thesis* University of Southampton.

Dyson, M. (2005) Train Design, Vehicle Track Interaction – Track vs Trains. IMechE, One Birdcage Walk, Westminster, London, SW1H 9JJ.

Dyson, M. (2006) Emails Concerning Pendolino Testing

European Rail Research Institute, committee D202 (1995). Improved knowledge of forces in CWR track (including switches), Report 2, Review of existing experimental work in behaviour of CWR track. European Rail Research Institute, Arthur van Schendelstraat 754, NL - 3511 MK UTRECHT.

European Rail Research Institute, committee D202 (1995). *Improved knowledge of forces in CWR track (including switches), Report 3, Theory of CWR track stability.* European Rail Research Institute, Arthur van Schendelstraat 754, NL - 3511 MK UTRECHT.

Esveld, C. (2001) *Modern Railway Track*, Zaltbommel, MRT Productions.

Fair, P. (2003) The geotechnical behaviour of ballast materials for railway track maintenance. *Thesis (Ph.D.),* University of Sheffield.

Fermer, M. & Nielsen, J. C. O. (1995) Vertical interaction between train and track with soft and stiff railpads - full-scale experiments and theory. *Proceedings of the Institution of Mechanical Engineers, Part F: Journal of Rail and Rapid Transit,* Vol.209**,** pp.39-47.

Gonzalo, R. & Witczak, M. W. (1981) Comprehensive Evaluation of Laboratory Resilient Moduli Results for Granular Material. *Transportation Research Record,* Vol.810**,** pp.23-33.

Grabe, P. J. (2002) Resilient and permanent deformation of railway foundations under principal stress rotation. *Thesis (Ph.D.)-University of Southampton, Nov 2002.,* University of Southampton, UK.

Green, C. (2005) Research to the Rescue UK Rail Research Conference, *Rail Research UK Workshop,* York, UK.

Hardin, B. O. (1978) The nature of stress strain behvaiour for soils, Proceedings of the ASCE geotechincal engineering division special conference on earthquake engineering and soil dynamics, Pasadena, Calif. pp.3-90. ASCE, New York, NY

Hardin, B. O. & Drnevich, V. P. (1972) Shear modulus and damping in soils: design equations and curves. *American Society of Civil Engineers, Journal of the Soil Mechanics and Foundations Division,* Vol.87 SM7**,** pp.667-692.

Harris, N. R., Schmid, F. & Smith, R. A. (1998) Introduction: Theory of tilting train behaviour. *Proceedings of the Institution of Mechanical Engineers, Part F: Journal of Rail and Rapid Transit,* Vol.212**,** pp.1.

Harwood, N. (2005) Emails Concerning Pendolino Technical Data for West Coast Mainline

Hunt, G. A. (2000) EUROBALT optimises ballasted track. *Railway Gazette International,* Vol.156**,** pp.813.

Indraratna, B., Ionescu, D. & Christie, H. D. (1998) Shear behavior of railway ballast based on large-scale triaxial tests. *Journal of Geotechnical and Geoenvironmental Engineering,* Vol.124**,** pp.439.

Indraratna, B., Khabbaz, H. & Salim, W. (2004) A laboratory study on improvement of railway ballast using geosynthetics, *Geotechnical Special Publication,* Los Angeles, CA, United States. pp.617. American Society of Civil Engineers, Reston, VA 20191-4400, United States

Indraratna, B. & Salim, W. (2002) Modelling of particle breakage of coarse aggregates incorporating strength and dilatancy. *Proceedings of the Institution of Civil Engineers: Geotechnical Engineering,* Vol.155**,** pp.243.

Indraratna, B. & Salim, W. (2005) *Mechanics of Ballasted Rail Tracks, a Geomechanical Perspective,* London, UK, Taylor & Francis Group plc.

Jaky, J. (1948) Pressure in silos. Second international conference on soil mechanics and foundation engineering. Rotterdam.

Kabo, E. (2006) A numerical study of the lateral ballast resistance in railway tracks. *Proc. Imech E. Journal of Rail and Rapid Transit,* Vol.220, Part F:.

Kalker, J. J. (1979) Survey of wheel-rail rolling contact theory. *Vehicle System Dynamics,* Vol.8**,** pp.317.

Kennedy, J. & Prause, R. (1978) Development of Multilayer Analysis Model for Tie-Ballast Track Structures. *Transportation Research Record,* Vol.694, Railroad Track and Electrification Studies**,** pp.39-47.

Klassen, M., Clifton, A. & Waters, J. (1987) Track Evaluation and Ballast Performance Specifications. *Transportation Research Record,* Vol.1131, Performance of Aggregates in Railroads and Other Track Performance Issues**,** pp.35-44.

Kuethe, A. M. & Chow, C.-y. (1998) *Foundations of aerodynamics : bases of aerodynamic design,* New York ; Chichester, J. Wiley.

Kuwano, J., Nakamura, Y. & Hashimoto, S. (1999) Anisotropy of small-strain stiffness and creep of Toyoura sand under various stress conditions, *Eleventh Asian Regional Conference on Soil Mechnaics and Geotechnical Engineering,* pp.53 to 56. Balkema, Rotterdam

Lacy, H. S. & Pannee, J. (1987) Use of Geosynthetics in The Design of Railroad Tracks. *Transportation Research Record,* Vol.1131**,** pp.99-106.

Li, D. & Selig, E. T. (1998a) Method for railroad track foundation design. I: Development. *Journal of Geotechnical and Geoenvironmental Engineering,* Vol.124**,** pp.316-322.

Li, D. & Selig, E. T. (1998b) Method for railroad track foundation design. II: Applications. *Journal of Geotechnical and Geoenvironmental Engineering,* Vol.124**,** pp.323-329.

Lichtberger, B. (2007a) The lateral resistance of the track (Part1). *European Railway Review***,** pp.88 - 91.

Lichtberger, B. (2007b) The lateral resistance of the track (Part2). *European Railway Review***,** pp.68 - 71.

Lo Presti, D. (1995) General report: Measurement of shear deformation of geomaterials in the laboratory, *Proceedings of the 1st conference on pre-failure deformation of geomaterials,* Sapporo, Jpn. Vol.2, pp.1067 to 1088. A.A. Balkema

Lo Presti, D. C. F. L., Jamiolkowski, M., Pallara, O., Cavallaro, A. & Pedroni, S. (1997) Shear modulus and damping of soils. *Geotechnique,* Vol.47**,** pp.603-617.

McDowell, G. R., Harireche, O., Konietzky, H., Brown, S. F. & Thom, N. H. (2006) Discrete element modelling of geogrid-reinforced aggregates. *Proceedings of the Institution of Civil Engineers: Geotechnical Engineering,* Vol.159**,** pp.35.

MSC software (2008) *ADAMS/rail.* Available from: http://www.mscsoftware.com/assets/1708_ADM6_02DAT_RAIL_CIN_r4.pdf [Accessed July 2008]

Network Rail RT/CE/C/039 (2003). *Company Code of Practice: Formation Treatments, Issue 2, Dec 2003*. Network Rail, 40 Melton Street, London, W1 2EE.

O'Reilly, M. P. & Brown, S. F. (1991) *Cyclic loading of soils : from theory to design,* Glasgow, Blackie.

ORE D 117/RP 8, October (1976). A study of the factors influencing the resistance to transverse displacement of unloaded track.

Office of Rail Regulation & Railtrack (2000) *West Coast Route Modernisation Joint Costs Assessment Overview Paper.* Available from: http://www.rail-reg.gov.uk/upload/pdf/wcm-jointcost.pdf [Accessed October 2008]

Office of Rail Regulation (2008) *West Coast Route Modernisation Project.* Available from: http://www.rail-reg.gov.uk/server/show/ConWebDoc.5687 [Accessed October 2008]

Oscarsson, J. (2002) Simulation of train-track interaction with stochastic track properties. *Vehicle System Dynamics,* Vol.37**,** pp.449-469.

Pandrol Rail Fastenings Limited, report No: 41174, (2003). Assessment of Railtrack G44 sleeper assembly incorporating PANDROL Brand Rail Clips type FC1504 and 60UIC to CEN standard modified for 30 tonne axle loads ref (EWR797). Pandrol Rail Fastenings Limited, 63 Station Road, Addlestone, Surrey, KT15 2AR, U.K.

Pandrol Rail Fastenings Limited: Report No. 45111 (2000). Assessment of Railtrack G44 sleeper assembly incorporating PANDROL Brand Rail Clips type FC1504 and BS113A rail to draft CEN Standards. Pandrol Rail Fastenings Limited, 63 Station Road, Addlestone, Surrey, KT15 2AR, U.K.

Powrie, W. (2004) Soil Mechanics: Concepts and Applications, London, Spon.

Powrie, W., Yang, L. A. & Clayton, C. R. I. (2007) Stress changes in the ground below ballasted railway track during train passage. *Proceedings of the Institution of Mechanical Engineers, Part F (Journal of Rail and Rapid Transit),* Vol.221**,** pp.247-61.

Priest, J. A., Le Pen, L., Powrie, W. & Mak, P. (2008) Performance of canted ballasted track during curving of high speed trains*, 1st international conference on transportation geotechnics,* Nottingham, UK. Balkema

Prud'homme, A. & Weber, O. (1973) L'ASPECT TECHNIQUE DES GRANDES VITESSES. LA VOIE ET LES INSTALLATIONS ELECTRIQUES DES LIGNES A GRANDE VITESSE 1, 2. (Technical Aspects of High-Speed Trains. Track and Its Infrastructure. Electric Installations 1, 2). *Travaux***,** pp.26-46.

Rail Safety and Standards Board GC/RT5021 (2003). *Railway Group Standard: Track System Requirements*. Rail Safety and Standards Board, Evergreen House, 160 Euston Road, London, NW1 2DX.

Rail-Safety-and-Standards-Board (2008) *Railway Group Standards Online.* Available from: http://www.rgsonline.co.uk/rail/document_index.html [Accessed March, 2008]

Rail Safety and Standards Board GC/RT5014 (2003). *Railway Group Standard: Trackbed and Track Drainage, Issue 2, June 2003*. Rail Safety and Standards Board, Evergreen House, 160 Euston Road, London, NW1 2DX.

Rail Safety and Standards Board GC/RT5021 (2003). *Railway Group Standard: Track System Requirements*. Rail Safety and Standards Board, Evergreen House, 160 Euston Road, London, NW1 2DX.

Railway Safety GC/RC5521 (2001). Railway Safety Approved Code of Practice: Calculation of Enhanced Permissible Speeds for Tilting Trains. Railway Safety, Evergreen House, 160 Euston Road, London, NW1 2DX

Railway Safety GC/RC5521 (2001). Railway Safety Approved Code of Practice: Calculation of Enhanced Permissible Speeds for Tilting Trains. Railway Safety, Evergreen House, 160 Euston Road, London, NW1 2DX

Rampello, S., Silvestri, F. & Viggiani, G. (1994a) Dependence of small strain stiffness on stress state and history for fine grained soils. The example of Vallericca clay, *Proceedings of the 1st conference on pre-failure deformation of geomaterials,* Sapporo, Jpn. Vol.1, pp.273. A.A. Balkema

Rampello, S., Silvestri, F. & Viggiani, G. (1994b) Panelist discussion: The dependence of G_0 on stress state and history in cohesive soils, *Proceedings of the 1st conference on pre-failure deformation of geomaterials,* Sapporo, Jpn. Vol.2, pp.1155 to 1171. A.A. Balkema

Raymond, G. P. (1978) Design for railroad ballast and subgrade support. *American Society of Civil Engineers, Journal of the Geotechnical Engineering Division,* Vol.104**,** pp.60.

Raymond, G. P. (1982) Track Rehabilitation with Geotextiles, New York, NY, USA. pp.368-381. Assoc of the Nonwoven Fabrics Industry, New York, NY, USA

Raymond, G. P. (1985a) Analysis of Track Support and Determination of Track Modulus. *Transportation Research Record,* Vol.1022**,** pp.80-90.

Raymond, G. P. (1985b) Research on Rail Road Ballast Specification and Evaluation. *Transportation Research Record,* Vol.1006**,** pp.1-8.

Raymond, G. P. & Davies, J. R. (1978) Triaxial Tests on Dolomite Railroad Ballast. *Journal of The Geotechnical Engineering Division, ASCE,* Vol.104**,** pp.737-751.

RDP Electronics Ltd (2008) *Model 53 compression load cell.* Available from: http://www.rdpe.com/uk/slc53.htm [Accessed June, 2008]

Safety and Standards Directorate Railtrack PLC GM/RT2141 (2000). *Railway Group Standard: Resistance of Railway Vehicles to Derailment and Roll-Over*. Safety and Standards Directorate, Railtrack PLC, Railtrack House DP01, Euston Square, London, NW1 2EE.

Safety and Standards Directorate Railtrack PLC, RT/CE/S/006 (2000). *Railtrack Line Specification: Track Ballast and Stoneblower Aggregate.* Railtrack Plc, Railtrack House, Euston Square, London, NW1 2EE.

Selig, E. T. (1980) Ballast Research, *Proceedings, Technical Conference - American Railway Engineering Association,* Chicago, IL, USA. Vol.81, pp.504-520. Am Railw Eng Assoc, Washington, DC

Selig, E. T. & Sluz, A. (1978) Ballast and Subgrade Response to Train Loads. *Transportation Research Record,* Vol.694**,** pp.53-60.

Selig, E. T. & Waters, J. M. (1994) *Track Geotechnology and Substructure Management,* London, Telford.

Shenton, M. J. (1975) Deformation of Railway Ballast under Repeated Loading Conditions. IN KERR (Ed.) *Railroad Track Mechanics and Technology.* Proceedingss of a symposium held at Princeton University, USA, pp. 387-404.

Simpson, B. (1992) Retaining structures: displacement and design. *Geotechnique,* Vol.42**,** pp.541-576.

Song, M.-K., Noh, H.-C. & Choi, C.-K. (2003) A new three-dimensional finite element analysis model of high-speed train-bridge interactions. *Engineering Structures,* Vol.25**,** pp.1611-1626.

Stewart, H. E. (1985) Measurement and Prediction of Vertical Track Modulus. *Transportation Research Record,* Vol.1022**,** pp.65-71.

Stewart, H. E., Selig, E. T. & Norman-Gregory, G M. (1985) Failure Criteria and Lateral Stresses in Track Foundations. *Transportation Research Record,* Vol.1022**,** pp.59-64.

Sussmann, T., Kish, A. & Trosino, M. (2003) Influence of Track Maintenance on Lateral Resistance of Concrete-Tie Track. *Transportation Research Record***,** pp.56.

Tarmac (2005) Rail Products Guide. Tarmac Precast Concrete Limited.

Tayabji, S. & Thompson, M. (1976) Program ILLI-TRACK: A Finite Element Analysis of Conventional Railway Support System. User's Manual and Program Listing. Illinois Univ at Urbana-Champaign Dept of Civil Engineering.

Timoshenko, S. (1927) Proceedings Second International Congress of Applied Mechanics: Methods of Analysis of Statical and Dynamical Stresses in Rails, Zurich. pp.407-418.

Turcke, D. J. & Raymond, G. P. (1979) Three-Dimensional Analysis of Rail Track Structure. *Transportation Research Record,* Vol.733, Mechanics of Track Support, Piles and Geotechnical Data**,** pp.1-6.

University of Southampton (2008) *New Grant Awarded: Development and role of structure in railway ballast.* Available from*:* http://www.civil.soton.ac.uk/news/shownews.asp?newsid=73 [Accessed July 2008]

Watters, B., Klassen, M. & Clifton, A. (1987) Evaluation of Ballast Materials using Petrographic Criteria. *Transportation Research Record,* Vol.1131, Performance of Aggregates in Railroads and Other Track Performance Issues**,** pp.45-63.

Wood, S. (1993a) Further investigations on the use of the DTS after tamping, RR TM 004. Track research unit, British Rail research, PO Box 2, London Road, Derby, DE24 8YB.

Wood, S. (1993b) Use of the DTS after maintenance tamping, RR TM 002. Track research unit, British Rail research, PO Box 2, London Road, Derby, DE24 8YB.

Wroth, C. P. & Houlsby, G. T. (1985) Soil mechanics - Property characterisation and analysis procedure, *XI ICSMFE,* San Francisco. pp.1 to 55.

Yau, J.-D., Lin, C.-L. & Yang, Y.-B. (2000) Dynamic Response of Bridges with Elastic Bearings due to High Speed Trains. IN CHOUW, N. & SCHMID, G. (Eds.) *Wave 2000 Wave propagation, Moving load, Vibration reduction : Proceedings of the international workshop WAVE 2000.* Bochum, Germany, 13 - 15 December 2000, Balkema.

Appendix A: Lateral beam model

Derive Differential Equation

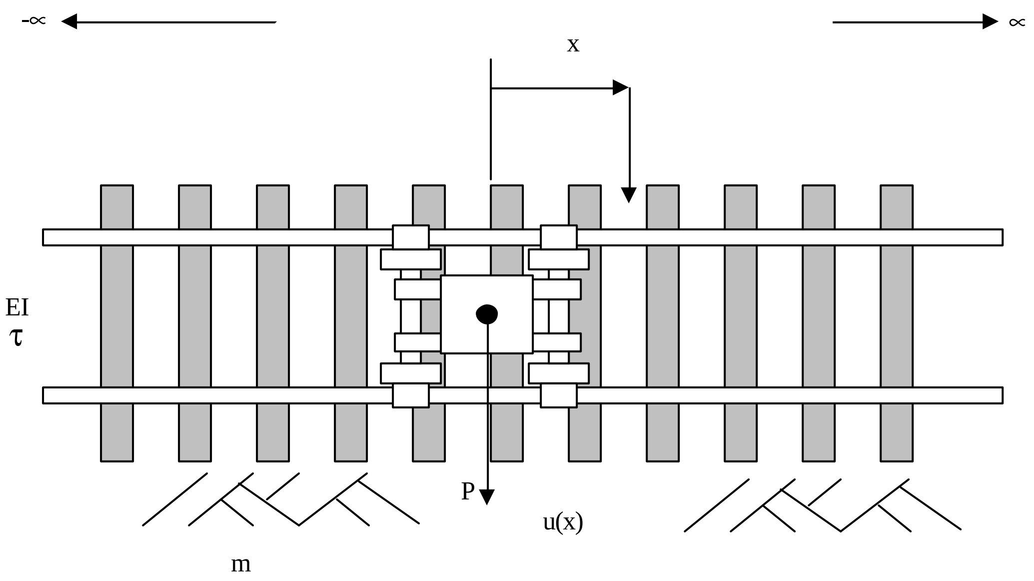

Figure 1: Lateral beam model

P is the lateral load which may be evaluated at the level the axle and summed for the carriages and train.

EI is the bending stiffness of the track in the lateral plane, both rails are lumped together

m is the lateral stiffness coefficient assuming a linear lateral response to load from the ballast sleeper interface made up from the base, shoulder and side contacts.

$u(x)$ is the lateral rail deflection

x is the longitudinal distance from the load

t is the torsional resistance of the sleeper rail fastenings, this may be evaluated per metre run of track.

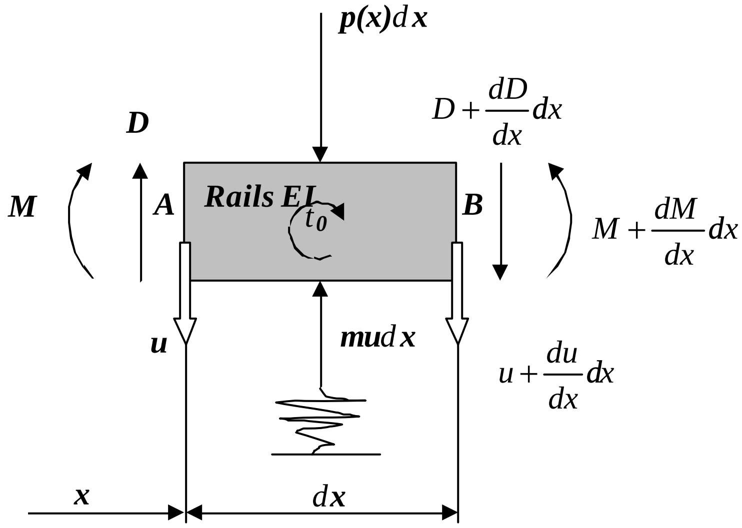

Figure 2: beam element model

From the diagram resolve horizontally,

$$p(x)dx + \frac{dD}{dx}dx = mudx \qquad \textbf{Equation 1}$$

$$p(x) + \frac{dD}{dx} = mu \qquad \textbf{Equation 2}$$

Take moments about A,

$$M + \left[D + \frac{dD}{dx}dx\right]dx + t_0\frac{du}{dx}dx = M + \frac{dM}{dx}dx \qquad \textbf{Equation 3}$$

Neglect dx^2 terms

du/dx is the gradient of the track

D is the shear force

M is the moment

Simplify:

$$D + t_0\frac{du}{dx} = \frac{dM}{dx} \qquad \textbf{Equation 4}$$

Re-arrange:

$$D = \frac{dM}{dx} - t_0 \frac{du}{dx}$$ **Equation 5**

From structures elastic theory it can be found:

$$M = -EI \frac{d^2u}{dx^2}$$ **Equation 6**

Substituting Equation 6 into Equation 5:

$$D = -EI \frac{d^3u}{dx^3} - t_0 \frac{du}{dx}$$ **Equation 7**

Therefore substituting Equation 7 into Equation 2:

$$p(x) - EI \frac{d^4u}{dx^4} - t_0 \frac{d^2u}{dx^2} = mu$$ **Equation 8**

Rearrange

$$p(x) = EI \frac{d^4u}{dx^4} + t_0 \frac{d^2u}{dx^2} + mu$$ **Equation 9**

Because there is no distributed load p, only a point load P for $x > 0$ this equation can be equated to zero and the governing differential equation is:

$$EI \frac{d^4u}{dx^4} + t_0 \frac{d^2u}{dx^2} + mu = 0$$ **Equation 10**

This differential equation is identical to the vertical case when t_0 is taken as zero. With the inclusion of the torsional resistance term we would reasonably expect the deflection to be lower.

Solution

Use D-operator method

$$EID^4 + t_0 D^2 + m = 0$$ **Equation 11**

Find the complementary function

Use the quadratic equation

$$D^2 = \frac{-t_0 \pm \sqrt{4mEI - t_0^2}}{2EI}$$ **Equation 12**

Taking realistic values for t_0 and $4EI$ the rooted term will be negative so,

$$D^2 = \frac{-t_0 \pm \sqrt{-1}\sqrt{t_0^2 - 4mEI}}{2EI}$$ **Equation 13**

This means that D must be a complex number of the form

$$D = a + ib$$ **Equation 14**

And

$$D^2 = (a^2 - b^2) + 2iab$$ **Equation 15**

By inspection

$$(a^2 - b^2) = \frac{t_0}{2EI}$$ **Equation 16**

and

$$2ab = \frac{\sqrt{t_0^2 - 4mEI}}{2EI}$$ **Equation 17**

Now find a and b,

$$a = \pm\sqrt{\frac{\sqrt{4mEI} - t_0}{4EI}}$$ **Equation 18**

$$b = \pm\sqrt{\frac{\sqrt{4mEI} + t_0}{4EI}}$$ **Equation 19**

Check one

$$a^2 - b^2 = \left[\frac{\sqrt{4mEI} - t_0}{4EI}\right] - \left[\frac{\sqrt{4mEI} + t_0}{4EI}\right]$$ **Equation 20**

$$a^2 - b^2 = \frac{\sqrt{4mEI}}{4EI} - \frac{t_0}{4EI} - \frac{\sqrt{4mEI}}{4EI} - \frac{t_0}{4EI}$$ **Equation 21**

$$a^2 - b^2 = \frac{-2t_0}{4EI} = \frac{-t_0}{2EI}$$ **Equation 22**

Check 2

$$ab = \left[\sqrt{\frac{\sqrt{4mEI} - t_0}{4EI}}\right] \times \left[\sqrt{\frac{\sqrt{4mEI} + t_0}{4EI}}\right]$$ **Equation 23**

$$a^2 b^2 = \left[\frac{\sqrt{4mEI} - t_0}{4EI}\right] \times \left[\frac{\sqrt{4mEI} + t_0}{4EI}\right]$$ **Equation 24**

$$a^2 b^2 = \frac{4mEI - t_0^2}{16E^2 I^2}$$ **Equation 25**

$$ab = \frac{\sqrt{4mEI - t_0^2}}{4EI}$$ **Equation 26**

$$2ab = \frac{\sqrt{4mEI - t_0^2}}{2EI}$$ **Equation 27**

Finally

$$D = \pm\sqrt{\frac{\sqrt{4mEI} - t_0}{4EI}} \pm i\sqrt{\frac{\sqrt{4mEI} + t_0}{4EI}}$$ **Equation 28**

With both roots negative the complementary function is of the form:

$$u = e^{-l_1 x}(a\cos l_2 x + b\sin l_2 x) + e^{-l_3 x}(c\cos l_4 x + d\sin l_4 x)$$ **Equation 29**

Substituting the roots (l_n)

$$u = e^{\sqrt{\frac{\sqrt{4mEI}-t_0}{4EI}}x}\left(a\cos\sqrt{\frac{\sqrt{4mEI}+t_0}{4EI}}x + b\sin\sqrt{\frac{\sqrt{4mEI}+t_0}{4EI}}x\right)$$
$$+ e^{-\sqrt{\frac{\sqrt{4mEI}-t_0}{4EI}}x}\left(c\cos\sqrt{\frac{\sqrt{4mEI}+t_0}{4EI}}x + d\sin\sqrt{\frac{\sqrt{4mEI}+t_0}{4EI}}x\right)$$

Equation 30

Factorize:

$$u = Ae^{\sqrt{\frac{\sqrt{4mEI}-t_0}{4EI}}x} + Be^{-\sqrt{\frac{\sqrt{4mEI}-t_0}{4EI}}x}\left(C\cos\sqrt{\frac{\sqrt{4mEI}+t_0}{4EI}}x + D\sin\sqrt{\frac{\sqrt{4mEI}+t_0}{4EI}}x\right)$$

Equation 31

It is now necessary to find the constant terms A, B, C, & D.

Use particular integrals to find constants

When x tends to infinity u is zero therefore A = 0, (B does not because e to a negative as x increases tends to zero).

$$u = Be^{-\sqrt{\frac{\sqrt{4mEI}-t_0}{4EI}}x}\left(C\cos\sqrt{\frac{\sqrt{4mEI}+t_0}{4EI}}x + D\sin\sqrt{\frac{\sqrt{4mEI}+t_0}{4EI}}x\right)$$

Equation 32

To differentiate to find other functions for boundary conditions, we need to use product rule

If $y = uv$ then:

$$\frac{dy}{dx} = u\frac{dv}{dx} + v\frac{du}{dx}$$

Equation 33

Say

$$L_1 = \sqrt{\frac{\sqrt{4mEI}-t_0}{4EI}}$$

Equation 34

$$L_2 = \sqrt{\frac{\sqrt{4mEI} + t_0}{4EI}}$$ **Equation 35**

so

$$u = Be^{-L_1 x}\left(C\cos L_2 x + D\sin L_2 x\right)$$ **Equation 36**

Use the product rule to find u’

$$\begin{aligned} u' &= -Be^{-L_1 x}\left(L_2 C\sin L_2 x - L_1 C\cos L_2 x\right) \\ &+ Be^{-L_1 x}\left(L_2 D\cos L_2 x - L_1 D\sin L_2 x\right) \end{aligned}$$ **Equation 37**

Apply the condition *u*’(0) = 0

$$0 = -B(-L_1 C) + B(L_2 D)$$ **Equation 38**

so

$$D = \frac{-CL_1}{L_2}$$ **Equation 39**

Substitute into *u*’

$$\begin{aligned} u' &= -Be^{-L_1 x}\left(L_2 C\sin L_2 x - L_1 C\cos L_2 x\right) \\ &+ Be^{-L_1 x}\left(L_1 C\cos L_2 x - \frac{L_1}{L_2} C\sin L_2 x\right) \end{aligned}$$ **Equation 40**

The cosine terms now cancel and this leaves:

$$u' = Be^{-L_1 x}\left(-L_2 C\sin L_2 x - \frac{L_1^2}{L_2} C\sin L_2 x\right)$$ **Equation 41**

Take C and $1/L_2$ outside the brackets and consider BC a combined constant E

$$u' = -E\frac{1}{L_2}e^{-L_1 x}\left(L_2^2\sin L_2 x + L_1^2\sin L_2 x\right)$$ **Equation 42**

Continue differentiating:

$$u'' = Ee^{-L_1 x}\left(-L_2^2\cos L_2 x + L_1 L_2 \sin L_2 x\right) + Ee^{-L_1 x}\left(-L_1^2\cos L_2 x + \frac{L_1^3}{L_2}\sin L_2 x\right) \qquad \textbf{Equation 43}$$

$$u'' = Ee^{-L_1 x}\left(\left[-L_2^2 - L_1^2\right]\cos L_2 x + \left[L_1 L_2 + \frac{L_1^3}{L_2}\right]\sin L_2 x\right) \qquad \textbf{Equation 44}$$

Continue differentiating

$$u''' = Ee^{-L_1 x}\left(\left[L_2^3 + L_1^2 L_2\right]\sin L_2 x + \left[L_1 L_2^2 + L_1^3\right]\cos L_2 x\right) + Ee^{-L_1 x}\left(\left[L_2^2 L_1 + L_1^3\right]\cos L_2 x - \left[L_2 L_1^2 + \frac{L_1^4}{L_2}\right]\sin L_2 x\right) \qquad \textbf{Equation 45}$$

$$u''' = Ee^{-L_1 x}\begin{pmatrix}\left[2L_1 L_2^2 + 2L_1^3\right]\cos L_2 x \\ + \left[L_2^3 - \frac{L_1^4}{L_2}\right]\sin L_2 x\end{pmatrix} \qquad \textbf{Equation 46}$$

Use u’’’(0)=P/2EI

Sine terms vanish

$$\frac{P}{2EI} = E\left(\left[2L_1 L_2^2 + 2L_1^3\right]\right) \qquad \textbf{Equation 47}$$

So

$$E = \frac{P}{2EI\left(\left[2L_1 L_2^2 + 2L_1^3\right]\right)} \qquad \textbf{Equation 48}$$

Now take advantage of the engineers bending formula

$$M = \frac{-EIP}{2EI\left(\left[2L_1 L_2^2 + 2L_1^3\right]\right)}e^{-L_1 x}\left(\left[-L_2^2 - L_1^2\right]\cos L_2 x + \left[L_1 L_2 + \frac{L_1^3}{L_2}\right]\sin L_2 x\right) \qquad \textbf{Equation 49}$$

$$M = \frac{-P}{4\left(L_1L_2^2 + L_1^3\right)} e^{-L_1x}\left(\left[-L_2^2 - L_1^2\right]\cos L_2x + \left[L_1L_2 + \frac{L_1^3}{L_2}\right]\sin L_2x\right)$$ **Equation 50**

It could be said that L_1 and L_2 will be close to identical given that 4mEI is >>>>> τ. Let L = L_1=L_2 by approximating τ as zero

$$M = \frac{-P}{8L^3} e^{-L_1x}\left(\left[-2L^2\right]\cos L_2x + \left[2L^2\right]\sin L_2x\right)$$ **Equation 51**

$$M = \frac{P}{4L} e^{-L_1x}\left(\cos Lx - \sin Lx\right)$$ **Equation 52**

Return to original equation for deflection

$$u = Be^{-L_1x}\left(C\cos L_2x + D\sin L_2x\right)$$ **Equation 53**

$$D = \frac{-CL_1}{L_2}$$ **Equation 54**

$$u = \frac{P}{4EI\left(\left[L_1L_2^2 + L_1^3\right]\right)} e^{-L_1x}\left(\cos L_2x + \frac{L_1}{L_2}\sin L_2x\right)$$ **Equation 55**

Again consider L_1 and L_2 as L

$$u = \frac{P}{8EIL^3} e^{-L_1x}\left(\cos Lx + \sin Lx\right)$$ **Equation 56**

Explanation of Boundary Conditions

Boundary conditions for *x*>0 are:

1. **u(μ)=0**
2. **u'(0) =0**
3. ***u''(μ)=0* (not useful)**
4. **u'''(0) =P/2EI**

Condition 1 is intuitive; condition 2 implies that the gradient below the load is zero. Condition 3 that the curvature is zero at great distances from the load

Condition 4 can be demonstrated by considering that adjacent to the horizontal load the shear force *D* is simply half the lateral load *P* so using Equation 5 and substituting for D.

Note: u is deflection, u' gradient, u'' curvature which is a related to moment, u''' shear force.

Since (from Equation 4)

$$\frac{P}{2} + t_0 \frac{du}{dx} = \frac{dM}{dx} \qquad \textbf{Equation 57}$$

Recall Equation 6 and re-arrange:

$$\frac{-1}{EI} M = \frac{d^2 u}{dx^2} \qquad \textbf{Equation 58}$$

Differentiate Equation 58 and substitute Equation 57:

$$\frac{-1}{EI}\left[\frac{P}{2} + t_0 \frac{du}{dx}\right] = \frac{d^3 u}{dx^3} \qquad \textbf{Equation 59}$$

Set x= 0 and this gives:

$$\frac{-1}{EI}\left[\frac{P}{2} + t_0 u'(0)\right] = u'''(0) \qquad \textbf{Equation 60}$$

It has already been observed that $u'(0)$ is zero so the equation reduces to the boundary condition 4 stipulated.

Appendix B: Key to geophone data

Site 1			Site 2a			Site 2b		
Run	Setup	Train	Run	Setup	Train	Run	Setup	Train
1	1	Pendo	1	1	Pendo	1	1	Pendo
2		Pendo	2		Pendo	2		Pendo
3		Pendo	3		3 class 66	3		Pendo
4		Pendo	4		Pendo	4		Pendo
5		Pendo	5		Pendo	5	2	Voyager
6		Pendo	6		Pendo	6		Pendo
7	2	Pendo	7	2	Pendo	7		Pendo
8		Pendo	8		Pendo	8	3	Pendo
9		Pendo	9		Pendo	9		Pendo
10		Voyager	10	3	Pendo	10		Pendo
11		Pendo	11		Pendo	11		Pendo
12		Pendo	12	4	Pendo	12		Pendo
13		Pendo	13		Pendo	13	4	Voyager
14	3	Pendo	14	5	Pendo	14		Pendo
15		Pendo				15		Pendo
16		Voyager				16		Pendo
17		Pendo						

Table 1: Geophone data obtained

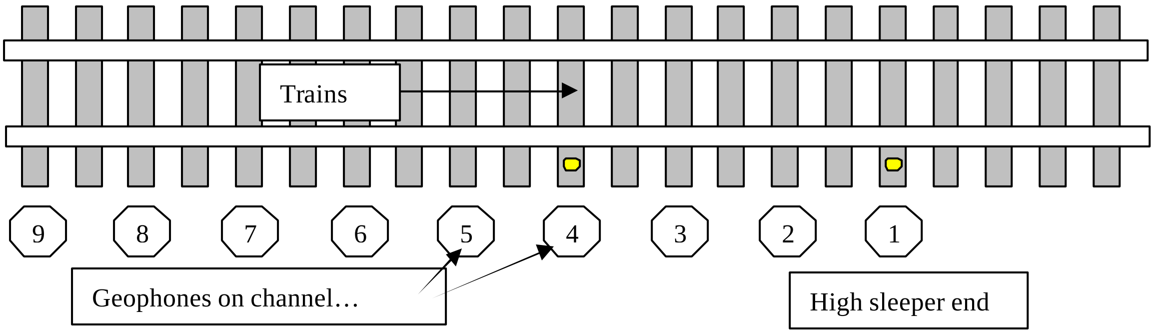

Figure 1: Site 1 Set up 1, 26/2/07

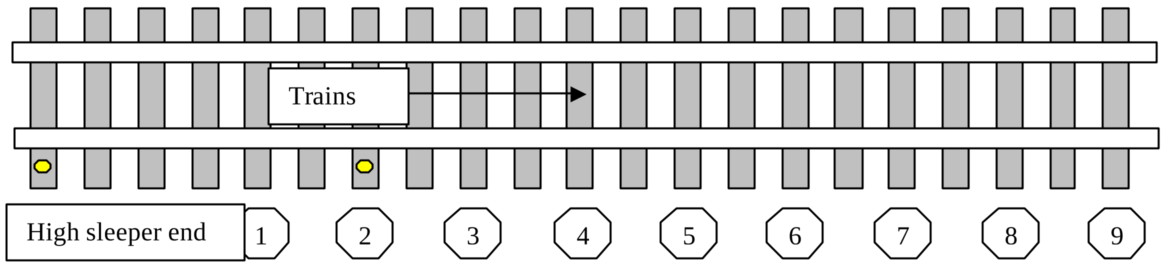

Figure 2: Site 1 Set up 2, 26/2/07

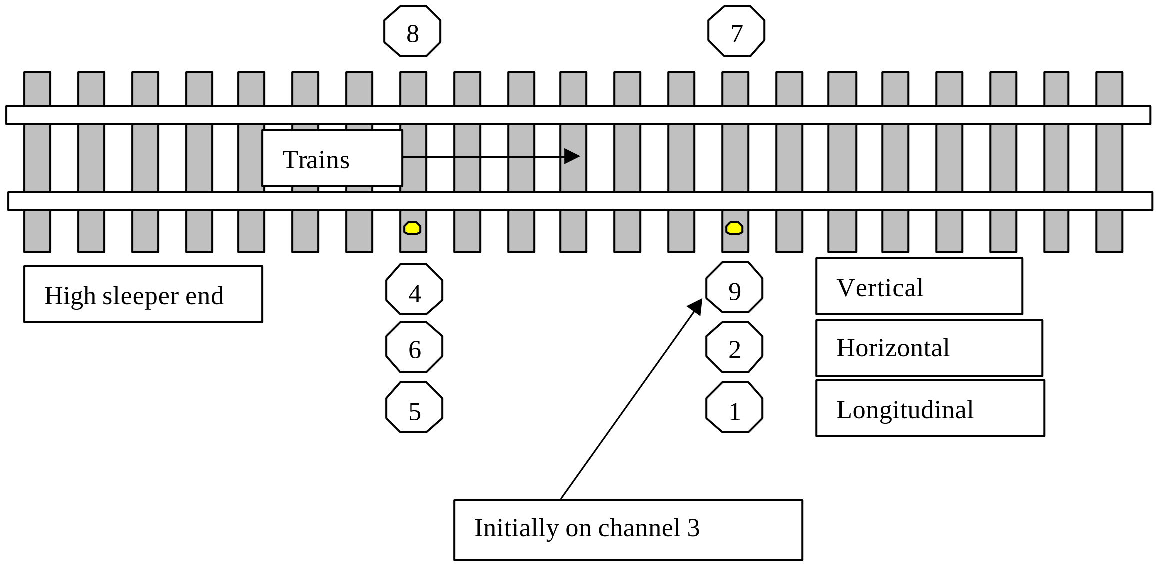

Figure 3: Site 1 Set up 3, 26/2/07

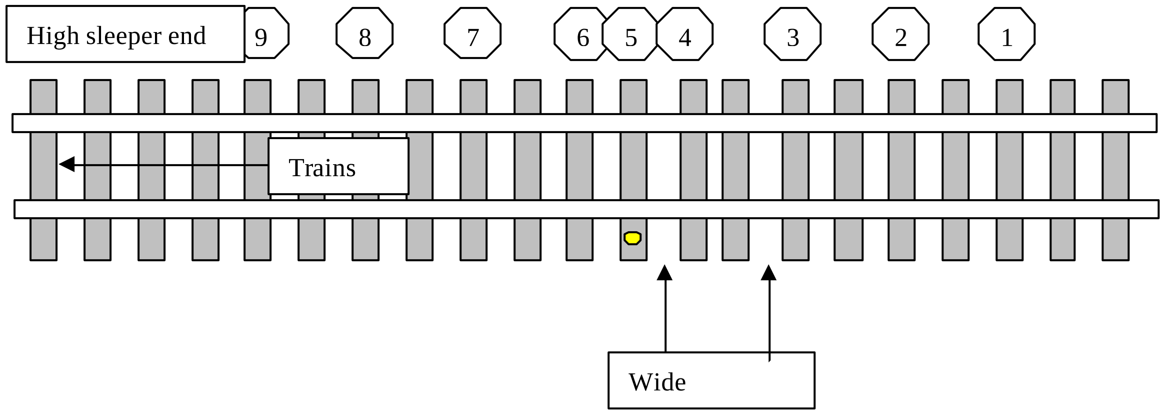

Figure 4: Site 2a Set up 1, 26/3/07

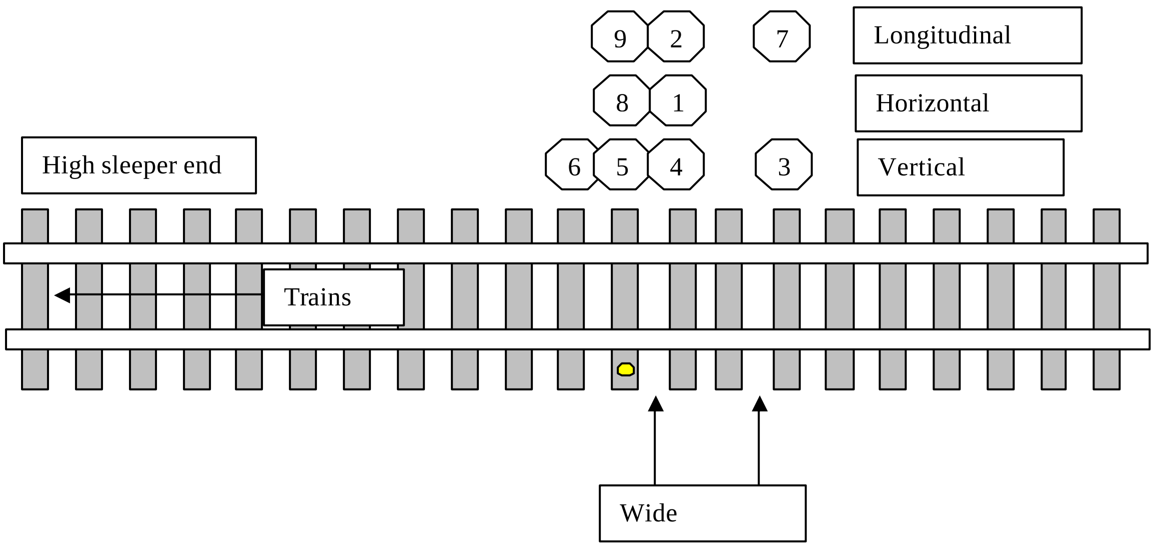

Figure 5: Site 2a Set up 2, 26/3/07

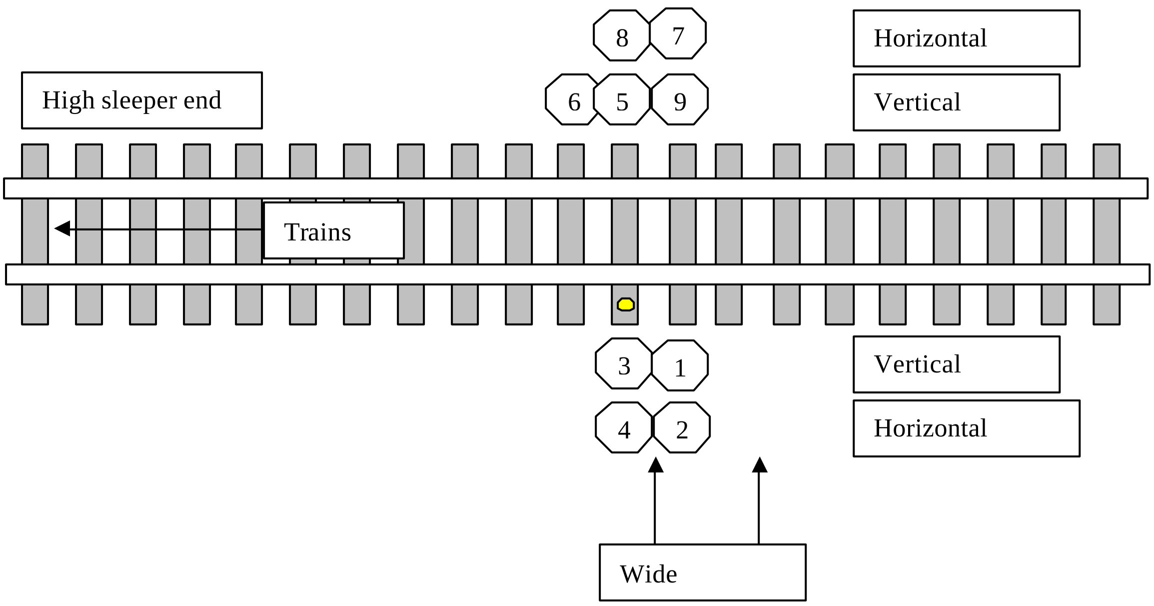

Figure 6: Site 2a Set up 3, 26/3/07

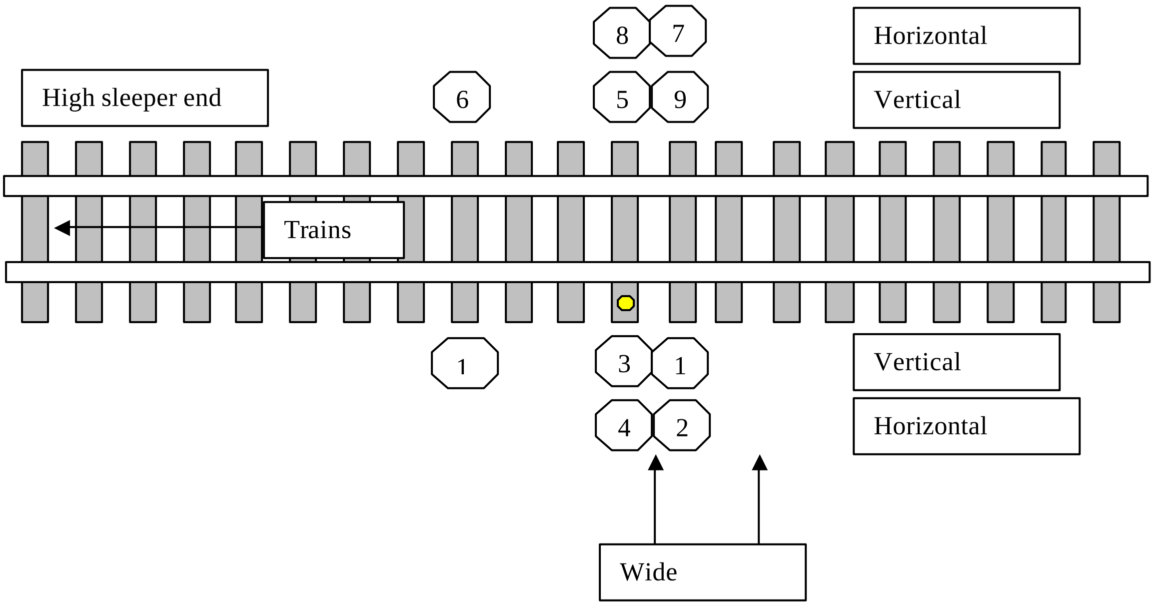

Figure 7: Site 2a Set up4, 26/3/07

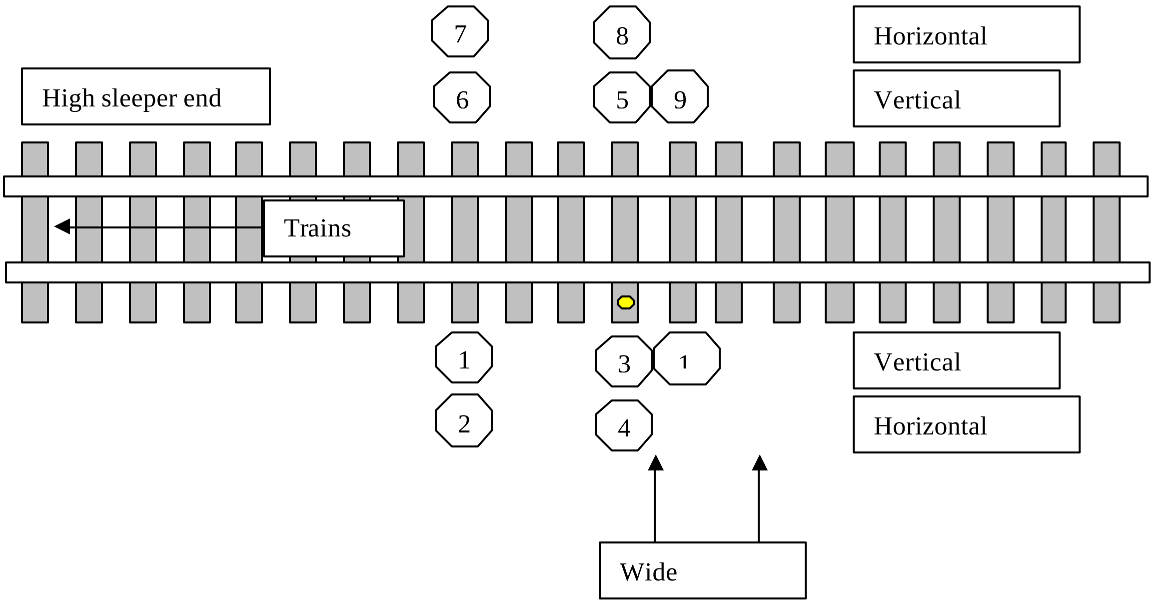

Figure 8: Site 2a Set up 5, 26/3/07

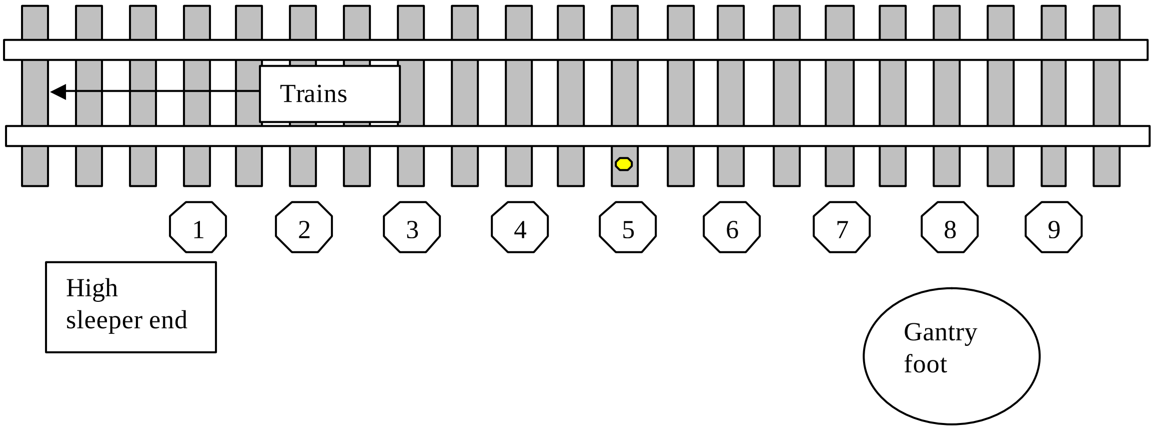

Figure 9: Site 2b Set up 1, 26/3/07

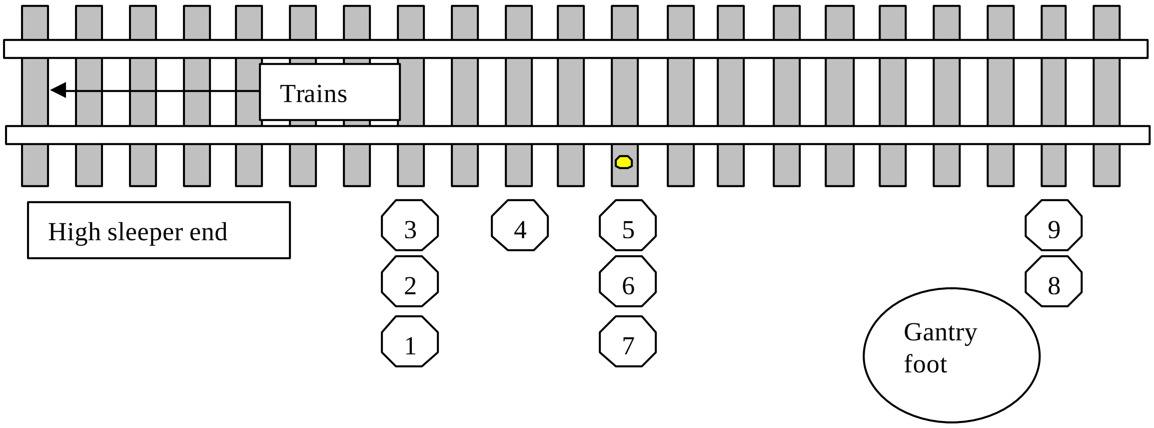

Figure 10: Site 2b Set up 2, 26/3/07

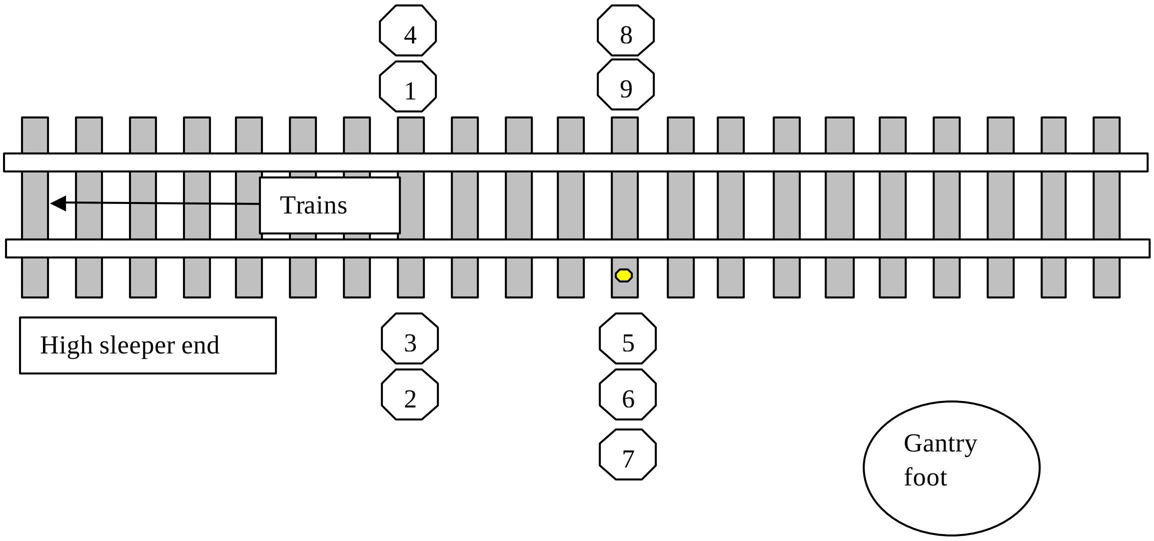

Figure 11: Site 2bSet up 3, 26/3/07

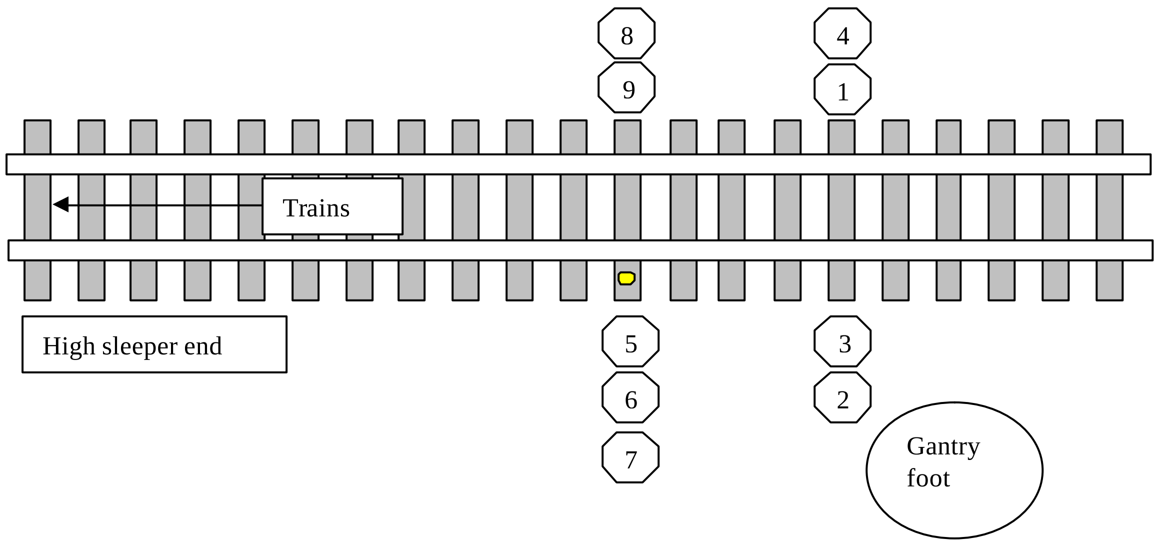

Figure 12: Site 2b Set up 4, 26/3/07